PONTIFICIA UNIVERSIDAD CATÓLICA DE CHILE
FACULTAD DE MEDICINA
CENTRO INTERDISCIPLINARIO DE NEUROCIENCIA

DYNAMICS OF CORTICAL COMPUTATIONS UNDERLYING ATTENTIVE STATES

by

Vicente Nicolás Medel Sierralta

A dissertation submitted to the Neuroscience Program
of Pontificia Universidad Católica de Chile
in partial satisfaction of the requirements for the degree
Doctor of Philosophy in Neuroscience

Supervisor	:	Tomás Ossandón Ph. D.
Co-Supervisor	:	Nicolás Crossley Ph.D.
Committee	:	Ranganatha Sitaram Ph. D.
		María José Escobar Ph. D.
		María Rodríguez Ph.D.

August, 2021

Santiago, Chile

A Emilio

Why should the brain continue
further in the direction of the center?
Why should this order not proceed,
so to speak, out of chaos?
- Ludwig Wittgenstein

Abstract

Spontaneous fluctuations occur at different spatial and temporal scales in the brain. Depending on its scale, these activities can show characteristic hallmarks. From a mesoscale perspective, in spontaneous conditions, cortical neurons fire action potentials in a seemingly stochastic manner, which extrapolated to an entire population shows a dynamical state coined as the asynchronous irregular state. Interestingly, when a local population of balanced excitation and inhibition is recurrently connected, the asynchronous population generates a baseline of stochastic perturbation over the neuron's membrane potential of that local population. These perturbations have been proposed as optimal for information computation and are associated with different states of attention at the behavioral level. Specifically, Locus-Coeruleus Noradrenergic (LC-NE) neuromodulation -which regulates brain states- has been highly implicated in the modulation of desynchronized activity. In this dissertation, we will use a modeling-driven analysis of attentional modulation of local electrophysiological desynchronization, hypothesizing that LC-NE neuromodulation shapes desynchronized background state and the balance between excitation and inhibition. We will show how the complexity of the electrophysiological signals depends on the excitation-inhibition balance of cortical activity, how it tracks behavioral performance, and how it can be related to LC-NE activity and arousal-related neuromodulation. Finally, we show how this complexity fluctuates at different spatial scales with low-dimensionality in attention, and how it is tracked by pupil diameter fluctuations -a non-invasive proxy of LC-NE activity and arousal- in a visuospatial working memory task in humans.

Co-author acknowledgments:

Chapter 1 is a reprint of the material as it appears in the following manuscript uploaded to bioRxiv: Medel, V., Irani, M., Ossandon, T., & Boncompte, G. (2020). **Complexity and 1/f slope jointly reflect cortical states across different E/I balances**.

Chapter 2 is a reprint of the material as it appears in the following manuscript published in British Journal of Anaesthesia: Boncompte, G., Medel, V., Cortínez, I., & Ossandon, T. (2021). **Brain activity complexity has a non-linear relation with the level of propofol sedation**.

Chapter 3 is a original draft: Medel, V., Irani, M., Munn, B., Gonzalez, F., Boncompte, G., Shine, J., Crossley, N. & Ossandon, T. (2021). **Interpreting the neuromodulation of 1/f aperiodic activity through the switch of adaptation currents**.

Chapter 4 is a original draft: Medel, V., Valdés, J., Irani, M., Follet, B., Wainstein, G., Boncompte, G., Castro, S., Lachaux, JP, Crossley, N. & Ossandon, T. (2021). **Attentional rapid state shift is related to transient 1/f aperiodic activity and phasic Arousal in human iEEG and scalp EEG**.

Publications

- **Medel, V.**, Valdés, J., Castro, S., Ossandón, T., & Boncompte, G. (2019). Commentary: Amplification and Suppression of Distinct Brainwide Activity Patterns by Catecholamines. *Frontiers in behavioral neuroscience*, 13, 217.

- Ramirez-Mahaluf, J. P., **Medel, V.**, Tepper, Á., Alliende, L. M., Sato, J. R., Ossandon, T., & Crossley, N. A. (2020). Transitions between human functional brain networks reveal complex, cost-efficient and behaviorally-relevant temporal paths. *NeuroImage*, 219, 117027.

- Brouwer, R. M., Klein, M., Grasby, K. L., Schnack, H. G., Jahanshad, N., Teeuw, J., ... **Medel, V.**, ... & Hillegers, M. (2020). Dynamics of brain structure and its genetic architecture over the lifespan. *bioRxiv*.

- **Medel, V.**, Irani, M., Ossandon, T., & Boncompte, G. (2020). Complexity and 1/f slope jointly reflect cortical states across different E/I balances. *bioRxiv*.

- Boncompte, G., **Medel, V.**, Cortínez, L. I., & Ossandón, T. (2021). Brain activity complexity has a non-linear relation to the level of propofol sedation. *British Journal of Anaesthesia*.

- Wainstein, G., Rojas-Libano, D., **Medel, V.** Alnæs, D., ...Ossandón, T., Crossley, N., Matar, E., & Shine, J. M. (2021). The ascending arousal system promotes optimal performance through meso-scale network integration in a visuospatial attentional task. Accepted in *Network Neuroscience*.

Vita

2015 B. S. in Philosophy *cum laude*, Universidad de Chile, Santiago.

2019 Teaching Assistant, Latin-American Summer School in Computational Neuroscience (LACONEU), Centro Interdisciplinario de Neurociencia de Valparaíso (CINV), Valparaíso.

2019 Graduate Teaching Assistant, Cognitive Neuroscience Course, Centro Interdisciplinario de Neurociencia, Pontificia Universidad Católica de Chile, Santiago.

2021 Ph. D. in Neuroscience, Pontificia Universidad Católica de Chile, Santiago.

Acknowledgments

This work would not have been possible without the direct and indirect help -in science and life- of so many people I have luckily have found myself with.

Thanks to my first mentors in neuroscience, Alain Destexhe and Bartosz Telenczuk, who made me first discover the immense beauty of computational neuroscience and modeling. You have significantly influenced my work. Thanks to the Paris 'beerosophers' for my first of many discussions on philosophy and neuroscience.

Thanks to my supervisors, Tomás Ossandón and Nicolás Crossley, for the many insightful moments, the patience, the teaching, and the support. But most of all, for challenging me to think always profoundly.

I would like to thank my thesis committee, María José Escobar, María Rodríguez and Ranganatha Sitaram for their contributions and rigorous evaluation which undoubtedly improved this dissertation at its different stages.

Thanks to my labmates Daniela Santander, Marcos Domic, Josefina Ihnen, Martín Irani, Catalina Fabar, Joaquín Valdés, Luz María Alliende, Vicente Tiznado, Gonzalo Boncompte, Brice Follet, Nicolás Gravel, Felipe González and Vicente Figueroa, for being fantastic friends and colleagues. All of you have influenced my work, my thinking in such diverse and unique ways. Thanks to my amazing peers Alexandra García, Macarena Tejos, Ángeles Tepper, Carolina González and Sergio Osorio, for their friendship. Also thanks to my friends and collaborators from Valparaíso, Samy Castro, Ruben Herzog, and Carlos Coronel: for the long talks, where tried to solve the mysteries of biophysics, entropy, and the brain.

I'd like to thank my close friends, Miguel Carmona, Javiera Millaqueo, Matías Tapia, Natalia Uribe, Juan Pablo Yañez, Diego Loyola, Facundo Ferreiros, Harijan Fernández, Cristobal Medeiros, Sebastián Soler, Nicolás Candia, Betzabeth Guzman and Lucas Velasco. Without you guys, I would not have been able to grab the courage to move from philosophy to neuroscience. Thanks for the friendship and the intense political and philosophical talks that give sense to all of this. And most important, thanks for showing me that science is still just a tiny part of life. Thanks to Joaquín Valdés, Stephano Labarca, Rodolfo Navarrete and Emiliano Ortiz for their constant support and ageless friendship.

Special thanks to my colleagues Gonzalo Boncompte and Martín Irani for giving confidence to my work and working side-by-side with me. Thanks for your unique and passionate pursuit in understanding cognition and consciousness.

I'd like to thank my international collaborators and friends: Mac Shine, Brandon Munn, Natasha Taylor, Eli Muller and Gabriel Wainstein. It has been a pleasure to start working closely with you and become friends over our collaborations.

I am grateful to NeuroUC for being a genuine center for studying the brain, mind, and cognition from its diverse angles and scales. I am also deeply grateful to ANID for their support to basic scientific research as the one studied in this dissertation, which allowed me to fully dedicate myself to research in the course of my studies.

I am immensely grateful to the open-science community for all the free resources, datasets, codes, and opportunities to learn neuroscience freely, making the inequality gap always smaller. Thanks to countless researchers whose work inspired this dissertation.

Thanks to my loving family: you guys are, at the end, the ones who I most admire. It is beautiful to know with certainty that the diverse paths I could have taken through this part of my life would have reached the same road of love and kindness from you. Thanks to Valentina for loving and caring for our lovely son. Special thanks to my mom Jimena Sierralta, for her immense patience, constant guidance, and inspiration.

Thanks to my fiance, Ivana Gajardo, for her endless love, for choosing me, believing in me, and always helping me be the best version of myself.

Finally, thanks to Emilio Medel: this is dedicated to you.

Contents

Introduction

One of the starting points of the neuroscience of cognition was the quest to find its specific biological mechanisms. Since then, cognitive research has not only become more diverse, but the research focus has also dramatically shifted. There is a growing trend to abandon the study of cognition supported by the strategy of searching for its correlates of single neural activity and an increasing perspective of going beyond the neural doctrine of cognition. Instead, cognition is now more understood as emerging from interactions between distributed networks of neurons.

Our field is at a paradigm shift towards a network comprehension of the brain (Yuste, 2015). There is strong evidence showing that both anatomical and biophysical properties show a distributed connectivity plan (Braitenberg & Schüz, 1998), suggesting that individual neurons become dispensable for the overall circuit function. Importantly, this structural and functional connectivity is characteristic of physical systems that generate emergent properties (Churchland & Sejnowski, 1994), which arise from interactions among the elements but are not present in the individuals.

We interact with the dynamic nature of the world with a high temporal resolution. More than a century ago, in 1890, William James articulated a general idea that underlies dynamical descriptions of human cognition: "Thought is in constant change — no state once gone can recur and be identical with what it was before." In other words, we move continuously from one relatively stable thought to another. The consideration of time or dynamics is fundamental for all aspects of mental activity — perception, cognition, and emotion. This is because one prominent feature of brain activity is the continuous change

of its spatiotemporal organization -the so-called brain states-, which can fluctuate even in a stable environment.

Spontaneous fluctuations of brain states can occur at different spatial and temporal scales in the brain. Depending on its scale, these activities can show characteristic hallmarks. For example, on the one hand, from a macro perspective, spontaneous brain activity shows temporally synchronous and correlated fluctuations across areas that have been modeled as functionally correlated networks (Bullmore & Sporns, 2009). On the other hand, from a more mesoscale perspective, in spontaneous in-vivo conditions, cortical neurons fire action potentials in a seemingly stochastic manner, which extrapolated to an entire neural population shows a rich dynamical state (Brunel et al., 2000). The scientific advances in both macro and meso approaches to cognition have made remarkable discoveries uncovering key features of brain states' spatial and temporal organization. However, a lack of an integrated and multiscale brain theory of cognition is still lacking.

The difficulties in integrating scales are varied. First, there are technical limitations. To simultaneously record large populations of neurons with high temporal and spatial resolution and molecular markers for morphological characterization, we would need invasive methods. Second, ethical limitations surrounding this type of brain imaging make it impossible to perform this type of study on the human brain. An alternative for the second limitation is the study of cognition in animal models. Although it could be argued that higher cognitive functions cannot be addressed in animal models, decades of research of the basic mechanisms of cognition have solved important clues on biological details underlying single neuron and population activity.

The technological advances in neuroimaging have shortened the gap between cognition and its biological underpinnings. This is particularly true for potentials measured at the human scalp, which provide a non-invasive and information-rich window and offer the opportunity to bridge observations across multiple spatial scales in cognitive and systems neuroscience. However, the characterization of the components of scalp potentials is challenging. Neural oscillations are an essential characteristic observed since the early

days of electrophysiological recordings (Berger, 1929). By its periodicity, oscillations can orchestrate local and distributed neural activity and provide a principled framework for the coordination of neural activity. However, oscillatory activity is only one aspect of neural activity, whereas most of the variance in neural recordings can be characterized as aperiodic, complex, and non-linear. From this perspective, our understanding of it remains limited partly because a canonical focus on narrowband oscillations marginalizes non-linear activity to the status of 'background' activity or irrelevant 'noise'. However, this background noise can provide a crucial measure to bridge the gap between biology and cognition to understand the mechanisms underlying attentive states.

A good example for understanding the link between the underlying neural synchrony with neural oscillations observed in the EEG is the stadium metaphor (Biasiucci et al., 2019). Let us imagine that we are outside a stadium with a microphone recording all the sounds occurring in a football match. We cannot know what is occurring at each moment in the match, but we can only infer the match by the sound. For example, when a goal is scored, there is a huge synchronized scream of the football spectators that can be heard from outside the stadium. We can even infer the typical "wave" the travels across the stadium by hearing how the sound comes and goes. In this common metaphor, each subject in the stadium would be dispensable compared to all the emerging activity of the match, which would be assumed as an oscillatory activity reflecting underlying synchronous activity of its elements. In this example, however, the uncoordinated activity would be irrelevant. We argue that asynchronous roars or conversations will generate a background noise that will make it harder or easier to detect prominent synchronous oscillations outside the stadium, depending on the type of context. Moreover, this background activity will also directly impact the match itself, improving the information in the interaction between the football match players (it is not trivial that in pandemic football matches, the game occurs with background noise even though there are no spectators). It is imaginable from this mental experiment that an intense uncorrelated background noise also changes in time. The noise level would likely be low in a very local and unpopular match between

two unknown teams. On the contrary, a big match that is being very boring, it is also possible that background noise is informative of the state of the match.

The phenomenology of noise in electrophysiological signals was first noticed by Hans Berger in 1929 when he characterized the first EEG recording in the awake state. He discovered that brain signals in the awake brain had a noisy low amplitude and high-frequency fluctuation. The background activity that governed awake EEG has been called "desynchronized state" as opposed to the high-amplitude oscillations that appear in other cortical states, such as deep sleep, epilepsy, inattentive arousal, and anesthesia, where the neuronal activity tends to follow stereotyped "synchronous" slow oscillatory patterns (Neske, 2016). As the animals start actively processing information about their world, the EEG starts getting systematically desynchronized.

A foundational work in computational neuroscience and one of the first models of desynchronized state was Van Vreeswijk & Sompolinsky (1996). The authors showed that it is possible to build a theoretical neural network that exhibits chaotic behavior where excitatory and inhibitory neurons fire asynchronously and irregularly. The asynchronous irregular (AI) (Brunel, 2000) is a state of recurrently connected excitatory and inhibitory neural populations that exhibit strong non-linearity of their activity. A characteristic hallmark of this model is that it depends on a dynamic balance between excitation and inhibition where both cancel each other and generate Gaussian fluctuations in the membrane potential (Vm) with a mean close to the spiking threshold. These stochastic perturbations to the membrane potential have been proposed as optimal for information computation (Zerlaut & Destexhe, 2017). From this perspective, E-I balanced networks provide a dynamical system capable of a wide range of computational functions. Moreover, it has been shown by theoretical and experimental work that the brain can fluctuate its local balance from a 'tight' to a 'loose' state (Deneve & Machens, 2016). This suggests two important notions: first, there are dynamical modulations to the local synaptic weights of excitation and inhibition; second, the continuous transition between 'tight' and 'loose' states modulates the baseline stochastic perturbations differently over local neuronal responsiveness.

When studying the mechanism that modulates background activity, it has to be considered what is modulated, i.e., what is the default mode of cortical computations? The slow oscillatory activity appears as a standard start-point, considering its cross-modality phenomenology, ranging from membrane potential to fMRI-BOLD activity. Steriade et al. (1993) showed that slow bistable oscillatory patterns emerge due to recurrent interaction of cortical neurons. This regime fades out when the animals wake up, where the activity tends to a metastable and irregular state (Sanchez-Vives and Mattia, 2014). Experimentally, slow oscillatory activity appears as a default state of the brain, most probably representing the functional aspect of structural connections. Interestingly, with lesions -like an ischemic stroke- slow oscillations persist for years (Butz et al., 2004). Slow oscillations also appear as the default activity in cortical slices in the absence of chemical or electrical stimulation (Sanchez-Vives & McCormick, 2000). From this perspective, it has been proposed that changes of macro-scale connectivity and mesoscale stochastic perturbations in the membrane potential of a population of neurons are both associated with the shaping of the default mode of the cortical activity (Sanchez-Vives, Massimini & Mattia, 2017). One of the main modulators of default cortical activity is the subcortical arousal-related neuromodulation, which can serve as a model to understand the dynamics by which the cortex is kicked out from its synchronous state into an asynchronous, stochastic and fluctuation-driven regime. From this perspective, the modulation of ongoing, balanced network activity may provide a powerful and fast mechanism to control the excitability and responsiveness of interconnected regions of the cortex. Such cellular mechanisms of network activity may be operating in awake animals to rapidly control the gain of neuronal responsiveness in a behaviorally relevant manner.

Perception and cognition are not a consequence of the physical input of the senses alone. The intrinsic dynamics of cortical computations affect the construction of sensory as well as our consciouss perception (Harris & Thiele, 2011). Recently, the link between instantanous fluctuations of both pupil-linked arousal (Pfeffer et al., 2021; Vinck et al., 2015) and neural desynchronization (Marguet & Harris, 2011) have been higlighted as a

source of perceptual variability. In other words, arousal and cortical desynchronization can be thought as two ways of characterizing cortical states, and thus the influence of internal dynamics on perception.

The search for mechanisms that regulate the desynchronization of the network is still an open question, and its relation with pupil-linked arousal is a promising road. Pupil-linked arousal, which is related to locus coeruleus-norepinephrine system (LC-NE) has been shown to influence perception and cognition (Hendler & Nir, 2018; McGinley et al., 2015). The LC-NE has widespread ascending projections to the neocortex (Aston-Jones Cohen, 2005) and controls the transitions of the sleep-wake cycle and changes in arousal, attention, and stress (Lee and Dan, 2012). Interestingly, pharmacological stimulation of the LC-NE system shifts the EEG towards a more desynchronized state with higher background noise (Steriade et al., 1993; Vazey and Aston-Jones, 2014). Indeed, electrical microstimulation in LC causes a desynchronization of cortical EEG, which suggests that the desynchronization of cortical EEG is partially due to LC-NE activation. However, little is known of what biological mechanisms relate the LC-NE system with the desynchronized state and its fluctuations.

Neuromodulation is, by definition, a process that occurs at the microscopic synaptic level. However, its behavioral effects generally manifest in its action at the mesoscopic level of neural populations. From that perspective, some have hypothesized that in a critically stable system such as the cortex, small changes can occur, which putatively shape the mesoscale balance of excitation and inhibition and large-scale functional gradients of activity (Cocchi et al., 2017; Wang, 2020). In this regime, individual neurons would play a democratic role in larger ensembles (Shine et al., 2021).

Altough the relation between LC-NE activity and behavior has been mostly related to the sleep-wake cycle related to arousal (Lee & Dan, 2012), strong evidence has shown that there is an active role in top-down attention. Specifically, the adaptive gain theory (Aston-Jones & Cohen, 2005) proposes that LC-NE activity can exhibit both phasic and tonic modes of activity, which closely track good or poor task performance. Moreover,

computational modeling and experimental results has shown that slow tonic changes have been shown to be related to the global sleep-wake cycle, while changes in the phasic activity have been related to rapid changes in behavior and focused attention (Aston-Jones et al., 1999; McGinley et al., 2015).

The above indicates that cortical states, balance between E/I, LC-NE neuromodulation and cognitive processes such as attention, are tightly intertwined. It is this junction and the question of what brain mechanisms support this junction what forms the central theme of this thesis. In this thesis, we propose to make use of theoretical and computational background to use modeling-driven analytical tools to probe proxies of mesoscale brain mechanisms, such as the balance between E/I, to then test how it changes with attentive/cognitive states. We hypothesize that this relation is supported by LC-NE neuromodulatory mechanism which will change E/I balance shaping mesoscale signals. To test this, we formulated a two step hypothesis procedure to incorporate computational modelling with experimental analysis.

We first hypothesize that asynchronous network state fluctuates and is a crucial signal to understand the complexity of attention. To test this, the *Objective 1* of this thesis focuses on deriving a biologically meaningful proxy of E/I balance -which biophysically determines asynchronous state- in cortical mesoscale activity. *Objective 2* is to probe this computational-driven analysis and test it in a cognitive setting. In **Chapter 1** we make use of neural modeling and simulation to relate two apparently diverse field potential signals (Lempel-Ziv Complexity and the 1/f slope of the power spectrum) as reflecting the cortical state, and thus the balance between excitation and inhibition. In **Chapter 2**, we make use of an open dataset to show that changes in our proxy of balance between excitation and inhibition can track the state of sedation and behavioral performance of subjects with pharmacologically disrupted E/I balance.

We next hypothesize that the balance between excitation and inhibition is dynamically fluctuating due to a varying modulation from LC-NE system. We propose that this would be observed as a multiscale phenomenon that will track optimal behavior and attention.

At the same time, the attentional state will recruit neuromodulation to regulate background cortical computations dynamically. To test this, *Objective 3* focuses on linking our proxy of E/I balance with LC-NE system statically. Then, *Objective 4* of this thesis test how our proxy of E/I balance is linked with LC-NE and behavior in a dynamical and temporally-resolved manner. In **Chapter 3** we show that changes in our proxy of balance between excitation and inhibition can also occur by manipulating spike-frequency adaptation, a mechanism known to depend on K+ channels which regulate the burstiness of neural activity. The dynamic elimination of spike-frequency adaptation by LC-NE system and arousal-related neuromodulation diminishes K+ and increases the burstiness of neural population activity, making the system to enter a highly non-linear state. With computational and experimental data, we show that arousal-related LC-NE neuromodulation shapes E/I balance by shifting adaptation. In **Chapter 4** we show how our proxy of excitation and inhibition changes in time, and is highly coupled to transient attentional recruitment in a visuospatial working memory task. Furthermore, we characterize the temporal dynamics of this fluctuation according to the attentional demand and show that our proxy of balance between excitation and inhibition is maximal at the highest attentional demand, suggesting that this mechanism is under fine top-down control. Moreover, our proxy of excitation and inhibition balance strongly correlates with LC-NE system as addressed by pupil diameter signal, and this relation can be observed as a multiscale low-dimensional signal across the brain.

Bibliography

[1] Yuste, R. (2015). From the neuron doctrine to neural networks. Nature reviews neuroscience, 16(8), 487-497.

[2] Braitenberg, V., Schüz, A. (2013). Cortex: statistics and geometry of neuronal connectivity. Springer Science Business Media.

[3] Churchland, P. S., Sejnowski, T. J. (1994). The computational brain. MIT press.

[4] Bullmore, E., Sporns, O. (2009). Complex brain networks: graph theoretical analysis of structural and functional systems. Nature reviews neuroscience, 10(3), 186-198.

[5] Brunel, N. (2000). Dynamics of sparsely connected networks of excitatory and inhibitory spiking neurons. Journal of computational neuroscience, 8(3), 183-208.

[6] Neske, G. T. (2016). The slow oscillation in cortical and thalamic networks: mechanisms and functions. Frontiers in neural circuits, 9, 88.

[7] Van Vreeswijk, C., Sompolinsky, H. (1996). Chaos in neuronal networks with balanced excitatory and inhibitory activity. Science, 274(5293), 1724-1726.

[8] Zerlaut, Y., Destexhe, A. (2017). Enhanced responsiveness and low-level awareness in stochastic network states. Neuron, 94(5), 1002-1009.

[9] Denève, S., Machens, C. K. (2016). Efficient codes and balanced networks. Nature neuroscience, 19(3), 375-382.

[10] Steriade, M., McCormick, D. A., Sejnowski, T. J. (1993). Thalamocortical oscillations in the sleeping and aroused brain. Science, 262(5134), 679-685.

[11] Sanchez-Vives, M. V., Mattia, M. (2014). Slow wave activity as the default mode of the cerebral cortex. Arch Ital Biol, 152(2-3), 147-155.

[12] Butz, M., Gross, J., Timmermann, L., Moll, M., Freund, H. J., Witte, O. W., Schnitzler, A. (2004). Perilesional pathological oscillatory activity in the magnetoencephalogram of patients with cortical brain lesions. Neuroscience letters, 355(1-2), 93-96.

[13] Sanchez-Vives, M. V., McCormick, D. A. (2000). Cellular and network mechanisms of rhythmic recurrent activity in neocortex. Nature neuroscience, 3(10), 1027-1034.

[14] Sanchez-Vives, M. V., Massimini, M., Mattia, M. (2017). Shaping the default activity pattern of the cortical network. Neuron, 94(5), 993-1001.

[15] Aston-Jones, G., Cohen, J. D. (2005). An integrative theory of locus coeruleus-norepinephrine function: adaptive gain and optimal performance. Annu. Rev. Neurosci., 28, 403-450.

[16] Lee, S. H., Dan, Y. (2012). Neuromodulation of brain states. Neuron, 76(1), 209-222.

[17] Vazey, E. M., Aston-Jones, G. (2014). Designer receptor manipulations reveal a role of the locus coeruleus noradrenergic system in isoflurane general anesthesia. Proceedings of the National Academy of Sciences, 111(10), 3859-3864.

Chapter 1

Complexity and 1/f slope jointly reflect cortical states and E/I balance

Abstract

Characterization of cortical states is essential for understanding brain functioning in the absence of external stimuli. The balance between excitation and inhibition and the number of non-redundant activity patterns, indexed by the 1/f slope and LZc respectively, distinguish cortical states. However, the relation between these two measures has not been characterized. Here we analyzed the relation between 1/f slope and LZc with two modeling approaches and in empirical human EEG and monkey ECoG data. We contrasted resting state with propofol anesthesia, which is known to modulate the excitation-inhibition balance. We found convergent results among all strategies employed, showing that there is an inverse and not trivial monotonic relation between 1/f slope and complexity. This behavior was observed even when the spectral properties of the signals were heavily manipulated, and was consistent at both ECoG and EEG scales. Models also showed that LZc was strongly dependent on 1/f slope but independent of the offset of the signal's spectral power law. Our results show that, although these measures have distinct mathematical origins, they are closely related. We hypothesize that differentially entropic regimes could underlie the link between the excitation-inhibition balance and the vastness of

the repertoire of cortical systems.

Keywords— Cortical States, Lempel-Ziv Complexity, 1/f Slope, Excitation/Inhibition Balance, Anaesthesia, Propofol

1.1 Introduction

Spontaneously occurring patterns of brain activity in the cerebral cortex constitute the so-called cortical states (Harris & Thiele, 2011; Reimer et al., 2014). These are present without a direct link to external stimuli, and constitute the basis of essential cognitive processes like attention (McGinley(Harris & Thiele, 2011; Reimer et al., 2014)) and global states of consciousness (GSC; e.g. sleep, wakefulness and anesthesia; (Bayne et al., 2016; He & Raichle, 2009). One of the most prominent strategies to characterize cortical states has been through the analysis of the spectral properties of their associated field potentials like electroencephalogram (EEG) and local field potential (LFP). In the particular case of attention, it has been shown that both induced (Klimesch et al., 1998) and spontaneous (Boncompte et al., 2016; Iemi et al., 2017) modulations of properties of alpha-band oscillations greatly explain the attentional state of subjects. However, characterization of GSC in terms of the unique properties of their associated cortical states has proven to be more elusive. Traditional spectral characteristics of brain field potentials are unable to fully distinguish between GSC (Purdon & Sampson, 2015). This is well illustrated for the case of anesthetics that equally produce a cease of phenomenological experiences in loss of consciousness, but show diverse spectral neural signatures. For example, transitions from wakefulness to anesthesia induced by propofol increase and frontalize alpha oscillations, while dexmedetomidine anesthesia instead induces spindle-like activity without significant modulations of alpha oscillations (Akeju et al., 2014; Huupponen et al., 2008). In recent years, new methodologies have emerged with promising results, which aim at characterizing background cortical states in general, but also specifically for GSC.

Cortical neurons in awake animals show strong membrane potential fluctuations which cause irregular discharge similar to a Poisson process, known as high conductance states (Destexhe et al., 2003). These states generate the background activity from which high-order processes are computed. It has been shown that irregular firing patterns can be achieved by a neuron with bal-

anced excitatory and inhibitory synaptic activity ((van Vreeswijk & Sompolinsky, 1996); (Brunel, 2000). From this perspective, cortical states depend on global brain variables, such as relative levels of excitation and inhibition (Haider et al., 2006). Moreover, from local circuit activity to whole-brain modeling, the computational characterization of the balance between excitation and inhibition (E/I balance) has shown to modulate information transmission and entropy (Deco et al., 2014; Rubin et al., 2017); (Agrawal et al., 2018). On the other hand, perturbations in the E/I balance has shown to be related with pathological brain activity (Žiburkus et al., 2013) and neuropsychiatric disorders (Haider et al., 2006; Uhlhaas & Singer, 2010); (Rubenstein & Merzenich, 2003); (Sohal & Rubenstein, 2019). A particularly successful way to quantify E/I balance is the slope of the power law decay of spectral power of brain field potentials. Specifically, models have been shown that the background 1/f slope of the power spectral density (PSD) emerges from the sum of stochastic excitatory and inhibitory currents (A. Destexhe et al., 2001; Sheehan et al., 2018); (Gao et al., 2017). Moreover, empirical validation of these models has shown that the E/I balance can be properly inferred from background activity by parameterizing the 1/f shape of the PSD ((Gao et al., 2017); (Trakoshis et al., 2020).

Interest in the detailed informational structure of cortical states have produced a recent surge of information-theory based approaches ((Arsiwalla & Verschure, 2018; Ferenets et al., 2006; Sarasso et al., 2014; Zhang et al., 2001); (Ferenets et al., 2006; Sarasso et al., 2014; Zhang et al., 2001). Data analysis strategies based on Lempel-Ziv complexity (LZc; (Lempel & Ziv, 1976)), like the Perturbational Complexity Index (Massimini et al., 2005)(Casali et al., 2013) have been successful for addressing subject's GSC during dreamless sleep and during anesthesia-induced unconsciousness, with independence of the anesthetic used (Casali et al., 2013). It has been shown that LZc decreases concomitantly with the loss of phenomenological possibilities, which is consistent with theoretical views of consciousness (Tononi & Edelman, 1998). Lempel-Ziv complexity algorithm computes the number of non-redundant segments of a signal (Lempel & Ziv, 1976), which in turn, when applied to brain data, is related to the abundance of the repertoire of brain activity patterns observed (Wenzel et al., 2019). During the transition from wakefulness to sleep or anesthesia, the number of possible experiences and cognitive processes that one can have is greatly reduced, and thus it is coherent that the complexity of brain activity follows the same pattern. In fact, this reduction of the repertoire of brain activity has been seen in rats

at the single neuron level using a myriad of convergent measures of cortical diversity, including LZc (Wenzel et al., 2019) which suggests that LZc can be applied as a multiscale proxy of neural repertoire.

Although 1/f slope and LZc have distant mathematical origins, one coming from spectral analysis and the other one from Information Theory, both have been shown to correlate with GSC (Miskovic et al., 2019; Zhang et al., 2001). We hypothesize that this could be due to an underlying intrinsic relation between E/I balance and the repertoire of activity patterns in cortical systems. Here we employed three complementary approaches to study the possible relation between 1/f slope and LZc and thus implicitly between E/I balance and the abundance of non-redundant repertoire in brain field potentials. We analyzed this relation in a simple inverse Discrete Fourier Transform (iDFT) model, in a cortical field potential model, but also in real human EEG and monkey ECoG anesthesia data. Our results consistently show that there is a non-trivial relation between 1/f slope and LZc in brain field potentials, and suggest that both could be related to the underlying entropy rate of the system.

1.2 Materials and Methods

iDFT Models

To study the relation between the power-law slope of neuronal signals and their complexity in time, we first employed an iDFT modeling strategy. We constructed signals with different 1/f slopes, among other spectral parameters, and analyzed their resulting LZc. Each signal was simulated using 5 seconds of length sampled at 1KHz, which resulted in a Nyquist frequency (Nf) of 500Hz. Each time series was initially constructed in the frequency domain as the product of its amplitude and phase components. The amplitude of each frequency component was set accordingly to a power-law distribution as illustrated in Equation 1:

$$A(f) = O * f^{-}s \tag{1.1}$$

where f is the frequency of each term, A(f) is the amplitude of each frequency component, O is the offset of the curve, the amplitude of the 1 Hz component, and s corresponds to the slope

of the power-law. Each initial phase was randomly assigned from a uniform distribution ($-\pi$ to π). iDFT algorithm (as implemented in Numpy; (Virtanen et al., 2020) was applied to the product of the amplitude (A(f)) and phase components to obtain the time series data according to Equation 2:

$$signal(t) = iDFT(A(f) * exp(i * \theta_0)) \tag{1.2}$$

where i is the imaginary unit, and $\theta 0$ corresponds to the initial phase of each frequency. Only positive frequencies were employed. To better model the spectral properties of physiologically plausible neural signals, in addition to constructing signals using the whole range of possible frequencies (0 to Nf) we also applied two types of constraints to the power-law distribution: an initial frequency (f0) and a final frequency (ff). Both of these are illustrated in Figure 1.1A. Specifically, f0 corresponds to setting all amplitudes of frequencies lower than f0 to the value of f0, thus flattening the curve to the left of f0. On the other hand, applying a ff corresponds to setting the amplitude of every frequency higher than ff to zero. To maintain time series stationarity, a requirement of the LZc algorithm (Lempel & Ziv, 1976; Zhang et al., 2001), all iDFT models were made with a f0 = 1Hz unless otherwise stated. For every set of simulations, we generated a 256 time series with different values of s.

Lempel-Ziv complexity algorithm

To compute the complexity of time series (both simulated and empirical), we used the Lempel-Ziv Complexity algorithm as introduced by Lempel and Ziv (Lempel & Ziv, 1976). This algorithm quantifies the number of distinct and non-redundant patterns of a signal and it can serve as a close analogue of the entropy rate of a signal (Amigó et al., 2004). We implemented the LZ76 algorithm using custom made Python scripts (available in Supplementary Materials). Briefly, every time series was first binarized, assigning a value of 1 for each time point with an amplitude greater than the median of the entire signal (5 s), and zero for those below it. Afterwards, the LZ76 algorithm was applied to the resulting so-called symbolic signal. To quantify the number of non-redundant patterns, a sequential evaluation of the signal is performed. At each point, the algorithm analyzes whether the following segment of the signal can be recreated from the already analyzed signal. In

this sense, if the following sequence is not contained in the previously analyzed signal, then the complexity increases. If the next sequence is already contained in the already analyzed signal, the algorithm advances without increasing the complexity. An illustrative description of the algorithm for two sample sequences can be found in supplementary materials (Supplementary Figure 1). The number of non-redundant patterns in a signal is then normalized to produce the final LZc value, which ranges (asymptotically for long signals) from 0 to 1. The LZ76 algorithm has been widely applied to analyze neural signals, from spike trains to EEG field potentials;, however, it should not be mistaken with the similar Lempel-Ziv-Welch algorithm (Welch, 1984), also recently employed in neurocognitive studies (Schartner et al., 2015). Although these two share commonalities, to our knowledge the link between complexity and entropy rate has only been established for the LZ76 algorithm.

1/f slope vs LZc modeling function

We found that the relation between 1/f slope and LZc in pure power-law iDFT data (Figure 1.1B) closely followed a particular mathematical behavior:

$$LZc(s) = a_1 * exp(-b * ln^2(s^c + 1) \tag{1.3}$$

where s is the slope of the power-law, LZc(s) is the LZc value obtained for a signal with slope s and a_1, b and c are free parameters such that a1 ranges from 0 to 1 and b and c $\in \mathbb{R}_+$. The parameters b and c modify the shape of the curve, while a is a scaling factor. Without this scaling factor, the image of LZc(s) ranges from (0 to 1), while if a_1 is introduced it ranges from (0 to a_1) without changing the internal structure of the curve. While Equation 3.1 appropriately adjusted to pure power-law signals (Figure 1.1B) and iDFT-data generated with a non-trivial final frequency (ff $\neq$ Nq; Figure 1.1D), the LZc values for signals with non-trivial f0 ($>$ 1Hz) did not ranged from 0 to 1 but from a value greater than zero to 1 (Figure 1.1C). Because of this, we designed a similar equation that better reflected the required image of the LZc(s) function for non-trivial f0 cases, introducing a second scaling parameter a_2:

$$LZc(s) = a_1 + (1 - a_2)exp(-b * ln^2(s^c + 1) \tag{1.4}$$

For every fit we employed Equations 3.1 or 3.2 using an algorithm that minimized the squares of the differences between data and models as implemented in the `scipy.optimize.curve_fit` function (Virtanen et al., 2020). Best fit parameters and R_2 values for goodness of fit for all iDFT simulations can be found in Supplementary Table 1 (all $R_2 > 0.98$).

LFP Simulations

To simulate cortical LFP time series we employed the strategy recently developed by Gao et. al. (2017) where LFP time series are constructed based on modeled inhibitory and excitatory conductances. Briefly, inter spike intervals were generated by Poisson processes (Destexhe et al., 2001) with specified average firing rates for GABA-A (inhibitory) and AMPA (excitatory) neurons. This produced binary time series describing firing at each time point. These spike time series were then convoluted with empirically defined conductance kernels for excitatory and inhibitory synapses independently (Alain Destexhe et al., 2003; Gao et al., 2017). Each kernel was constructed as the sum of an exponential growth and an exponential decay function, which were specific for excitatory and inhibitory synapses (CNRGlab; `http://compneuro.uwaterloo.ca/research/constants-constraints/`). Current time series were then obtained by multiplying each conductance by the difference between the resting potential and the typical reversal potential of AMPA and GABA-A receptors. Finally, LFP time series were computed as the sum of excitatory and inhibitory currents (Mazzoni et al., 2015). The particular parameters used in LFP simulations can be found in supplementary material (Table S2) which are based on previous electrophysiological results and modeling of LFP (Gao et al., 2017).

For each particular simulation we manipulated firing rate and E/I balance. Each firing rate was defined as a parameter to generate interspike intervals following a Poisson process. E/I balance, defined as the ratio between mean excitation and mean inhibition conductances, was manipulated by a multiplicative parameter applied only to inhibitory conductances (Gao et al., 2017), such that mean inhibition current was 2 to 10 times greater than the mean magnitude of excitation conductances. Each simulated LFP time series consisted of 5s, and was downsampled to 1KHz to match iDFT simulations. We employed this modeling strategy because it has been shown to capture amplitude and spectral characteristics of synaptic conductances observed in

vivo (Destexhe et al., 2001), and has been previously validated as a tool to infer the E/I balance of cortical tissues (Gao et al., 2017).

Power Spectral Density and 1/f analysis

We employed the same approach to estimate the power-law slope of LFP simulations, human EEG and monkey ECoG data. This consisted in calculating the Power Spectral Density (PSD) by means of Fourier Transforms using Welch's method as implemented in the MNE toolbox (Gramfort et al., 2014; Jas et al., 2018). Afterwards, the power-law 1/f slope and offset were obtained using the *"Fitting Oscillations & One Over f"* (FOOOF) toolbox (Donoghue et al., 2020). Aperiodic offset (O) and slope (s) components are obtained by modelling the aperiodic signal according to Equation 1.1. The FOOOF algorithm decomposes the log power spectra into a summation of narrowband Gaussian periodic (oscillations) and the aperiodic (offset and slope) components for the whole frequency range. The algorithm estimates periodic and aperiodic components, removes the periodic ones and estimates again until only the aperiodic components of the signal remain. This allows for estimation of offset and power-law slope with considerable independence from oscillatory behavior, which is particularly important for empirical signal analysis (Donoghue et al., 2020; Voytek & Knight, 2015). FOOOF toolbox also contains a "knee" parameter, which was not considered as it corresponds to changes in the 1/f slope at higher frequencies, not analyzed in this study. With this we obtained the 1/f slope and offset estimates of each time series. For our analyses we performed the FOOOF fitting using a frequency range from 1 to 70 Hz for simulated and ECoG data, and 1 to 40 Hz in EEG data.

ECoG Data

We used an open ECoG database collected from 2 macaque monkeys (Chibi and George) during wakefulness, propofol anesthesia (5 and 5.2 mg/kg) and recovery ((Yanagawa et al., 2013)). Propofol induced anesthesia was achieved through intravenous propofol injection. Loss of consciousness was defined as the moment when monkeys no longer responded to touch stimuli. The ECoG grid consisted of 128 channels using multichannel ECoG electrode arrays (Unique Medical, Japan). The array was implanted in the subdural space with an interelectrode distance

of 5 mm. Electrodes were implanted in the left hemisphere continuously covering frontal, parietal, temporal and occipital lobes. No further preprocessing than the one used by (Yanagawa et al., 2013)) was applied to this data. Since we were interested in assessing differences between brain states during wakefulness and anesthesia and not in the transitions, we only considered periods of closed-eyes wakefulness and anesthesia. We computed LZc and 1/f slope measures of the times series as mentioned above for each electrode, epoch and subject and then averaged LZc and 1/f slope across epochs. These results are shown in Figure 1.3.

EEG Data

We analyzed an open human propofol anesthesia EEG database (Chennu et al., 2016). We only analyzed data collected during baseline and moderate sedation conditions. In each state, subjects performed an auditory discrimination task. After the task, during closed eyes resting state, EEG data was recorded with high-density 128 electrodes caps and the Net Amps 300 amplifier (Electrical Geodesic Inc., Eugene, Oregon, USA) for 7 minutes. Only channels covering scalp area were retained, which resulted in 91 channels for further analysis. Moderate sedation was induced by target-controlled infusion of propofol, with targeted plasmatic propofol levels of 1.2 mcg/ml. Because the level of propofol sedation is near the anaesthetic threshold of unconsciousness, and not sufficient for deep anesthesia, we collected data from the two subjects who lost the most performance. This was assessed by the number of correct responses in the auditory discrimination task during moderate sedation, as compared to baseline condition. EEG signals were filtered between 0.5 Hz and 45 Hz and segmented into 10-second epochs (ranging from 37 to 40 epochs per subject). Data was re-referenced to the average of all channels. We did not apply any further preprocessing steps beside those described by Chennu et al. (Chennu et al., 2016) for the analysis presented here. Further details of procedures regarding data collection and preprocessing can be consulted in the original paper. Finally, for each epoch (time segment) and electrode we calculated LZc and 1/f slope and then averaged across epochs.

Statistical analysis

Experimental data was visualized using raincloud plot (Allen et al., 2019); van Langen, 2020). Statistical significance was assessed with a Type-1 error threshold of 0.05. All curve fits were carried out using Scipy optimize function. R2 were calculated using custom made scripts. Differences among groups in 1/f slope (Figure 1.3A, B) and LZc (Figure 1.3C, D) were assessed by two-way ANOVAs for each measure. Conscious state (awake vs. anesthesia) and the subject's identity were used as ways. We included both humans and monkey datasets in these ANOVAs. Afterwards, simple main effects for conscious states were performed for each dataset, comparing awake vs. anesthesia for each human and monkey individually. To estimate the relation between 1/f slope and LZc in ECoG and EEG data, for each subject and electrode, we adjusted a linear curve to 1/f slope and LZc data across epochs (time segments). The Pearson product-moment correlation coefficient for each one of these fits were used as the dependent variable in a two-way ANOVA analysis (Figure 1.3E, F). Simple main effects were applied in the same way as for the analysis of each individual measure.

1.3 Results

iDFT Model

In order to analyze the relation between the spectral power-law slope and the LZc, we generated, by means of iDFT, sets of 256 time series with different slopes (e.g. blue trace in Figure 1.1A) ranging from 0 to 2, and calculated the complexity values for each one. We found that, for pure power-law time series, the relation between slope and LZc follows a strict monotonically descending behavior (Figure 1.1B), with lesser complexity values for time series with a steeper slope. This general behavior is expected: slopes near zero reflect white noise (maximal LZc), while on the other hand very high slopes reflect time series with significant power only in low frequencies (periodic signals with minimal LZc). Interestingly, we found that LZc had a one-to-one mapping with 1/f slope. This relation can be robustly adjusted ($R^2 > 0.99$) to an x-inverted asymmetrical sigmoid function (see Methods, Equation 3.1).

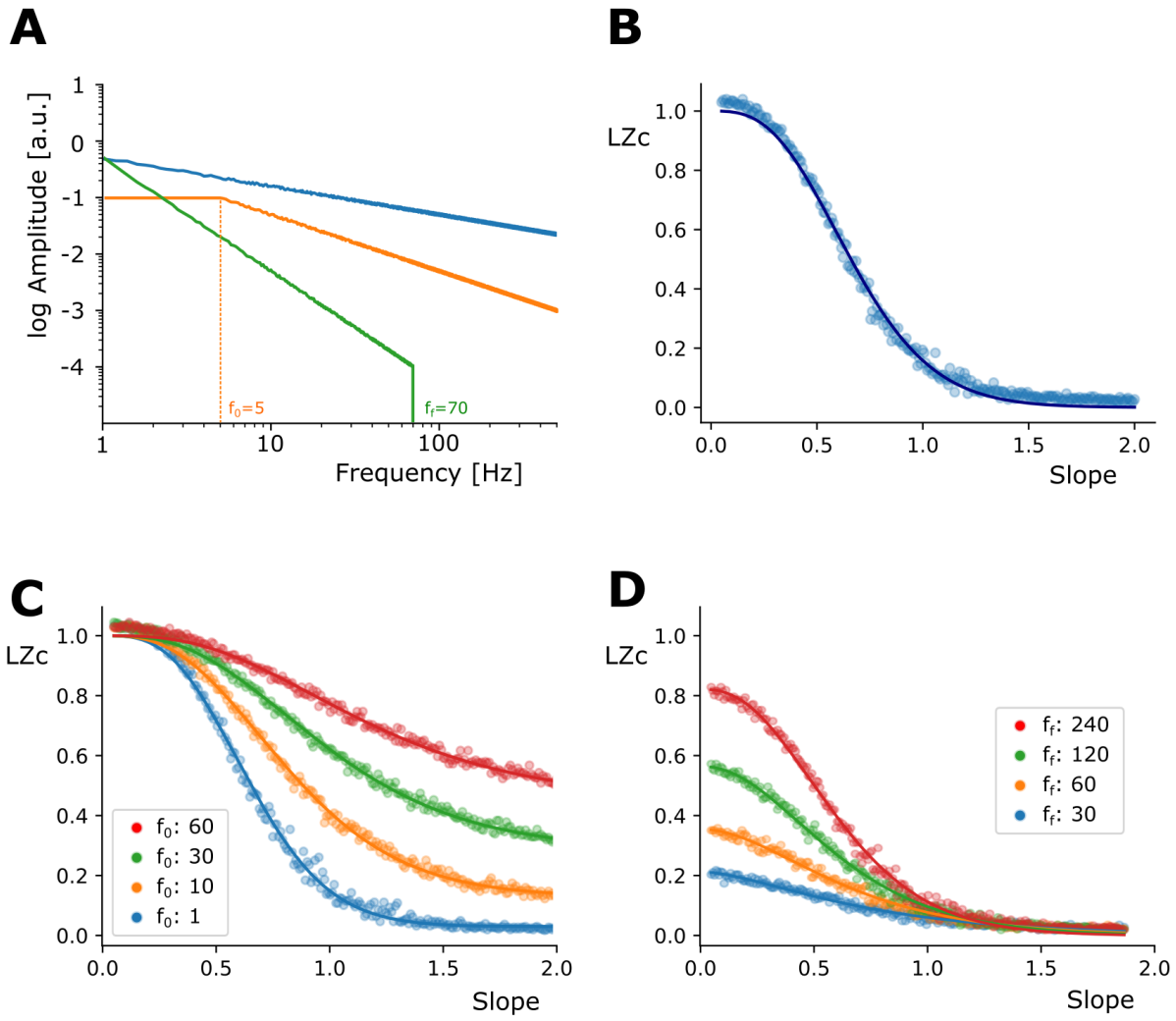

Figure 1.1: iDFT models showcase the inverse relation between LZc and 1/f Slope. ***(A)*** Illustration of the amplitude spectrum in terms of frequency for signals composed using the iDFT model; f0 and ff represent the initial and final frequency of the power law behavior. ***(B)*** Scatter plot of the LZc of 256 signals constructed with different 1/f slopes. Solid line corresponds to the best fit of Equation 3.1. ***(C)*** and ***(D)*** illustrate the effect of including four different f0's and ff's in the construction of signals respectively. Although the curves are scaled in comparison to ***(B)***, an homologous inverse relation is observed.

Electrophysiological field potential signals (e.g. EEG and ECoG) have been shown to present only partial power-law behavior (He, 2014). In other words, only part of their spectrum follows a clear spectral power law distribution. In an attempt to broadly emulate this, we introduced two types of constraints to the spectra of signals: an initial (f0) and a final (ff) 1/f frequency

(see Methods). Both constrains are illustrated in Figure 1.1A (orange trace for f0; green trace for ff). We found that the introduction of greater f0 values (Figure 1.1C) generated signals with greater complexity across all slopes tested. This effect was enhanced for higher slopes compared to lower slopes (Figure 1.1C). Interestingly, the introduction f0 higher than 1Hz reduced the dynamical range of the observed LZc (no longer ranging from 0 to 1). On the other hand, when we included a final frequency ff to the generated signals (a type of low-pass filter), we also found LZc values were reduced, in comparison to the pure power law signals. This effect was more markedly observed in signals with lower slope values. Similarly to f0, we found that ff reduced the dynamical range of possible complexity values, but in a different way: LZc ranged from zero to a value lower than 1. Regardless of these spectral constraints we found that the slope vs. LZc behavior could be modeled with a simple set of related equations (Equations 3.1 and 3.2), with a robust goodness of fit (all $R^2 > 0.98$, see Supplementary Materials).

LFP model

Spectral 1/f power law slope has been suggested as a proxy for the background state (Destexhe et al., 2001) and the balance between excitation and inhibition in cortical circuits (Destexhe et al., 2001; Lombardi et al., 2017; Gao et al., 2017; Trakoshis et al., 2020). In this line, we hypothesised that E/I balance could also be related to the repertoire of cortical activity as indexed by LZc. To test this hypothesis in a more physiologically plausible model, we simulated LFP signals as a linear combination of excitatory and inhibitory currents (see Methods; Destexhe et al., 2001). We conducted simulations with different global firing rates and E/I ratios by parameterizing inhibitory conductances (Fig 2A; see Methods). For each simulated time series, we calculated LZc and the spectral parameters of 1/f slope and offset using the FOOOF toolbox (Donoghue et al., 2020).

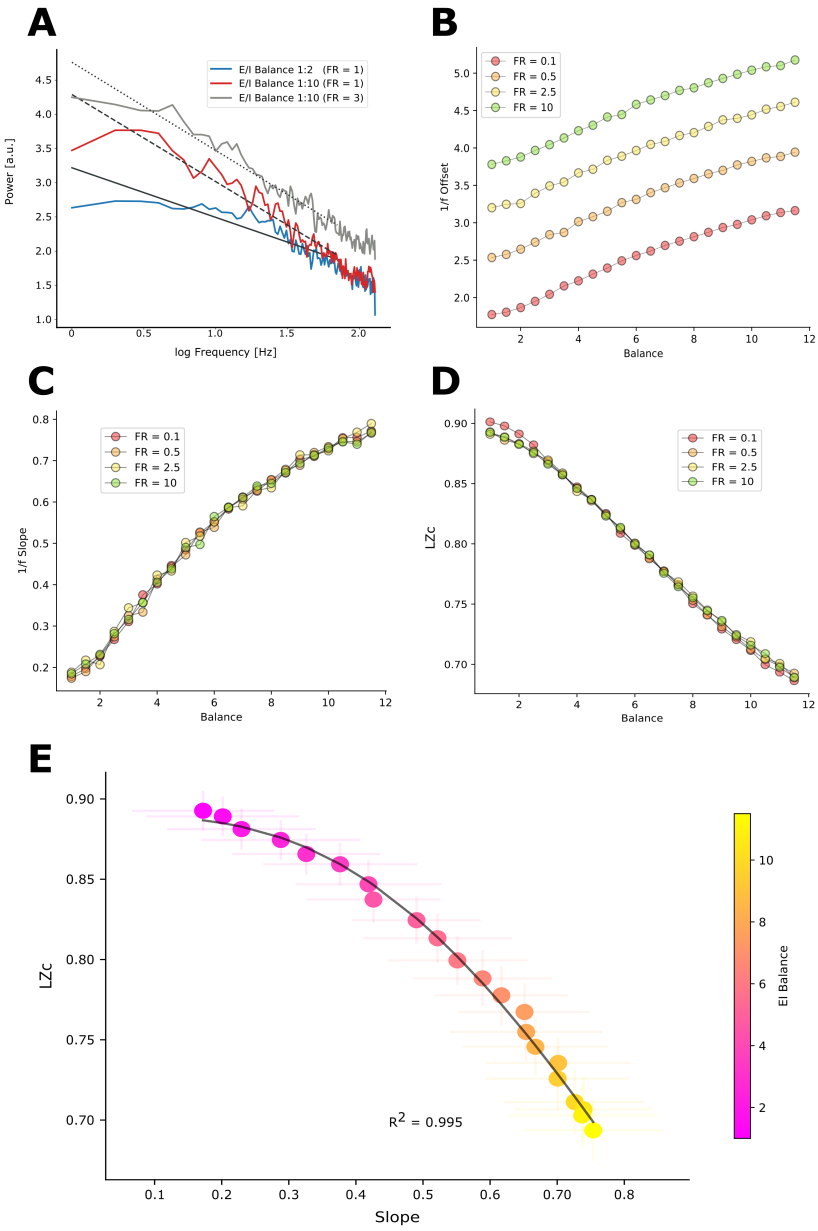

Figure 1.2: LZc and 1/f slope as a function of E/I balance. ***(A)*** Power Spectral Density plots of sample simulated brain signals with different E/I balances and total firing rates constructed using a cortical field potential model. ***(B)*** Plot showing the relation between offset and E/I balance, and its relation to firing rate. ***(C)*** Plots showing the positive relation between 1/f slope and E/I balance, which is independent of firing rate. ***(D)*** Plot showing the inverse relation between LZc and E/I balance. This relation was independent of firing rate. ***(E)*** Color scatter plot showcasing the relation observed between 1/f slope and LZc across a range of E/I balances (color bar) error bars represent the standard deviation across 100 simulations.

Consistent with previous findings using this model (Gao et al., 2017), we found that manipulating E/I balance consistently modulated the offset of the 1/f behavior. However, offset was also strongly modulated by global cortical excitability (firing rate; Figure 1.2B). We found that the 1/f slope was also robustly modulated by E/I balance; however in contrast to offset, the slope was completely independent of global excitability (Figure 1.2C). Interestingly, we found that LZc strongly correlated with E/I balance, with more excitation leading to a smaller repertoire of cortical activity patterns, and more balanced neural population activity presenting higher complexity (Figure 1.2D). Similar to 1/f slope, we found that the effect of changing E/I balance on LZc was independent of the global firing rates of the simulated neural time series.

Given that E/I balance robustly modulated both 1/f slope and LZc, with independence of the firing rate, we next asked whether the relation observed between 1/f slope and LZc seen in our iDFT model could be reproduced in this more plausible cortical model, and if E/I balance tracked this relation. Figure 1.2E depicts the average LZc and 1/f slope for 100 simulations with their corresponding E/I balance values. It illustrates that there is a non-trivial inverse relation between these two measures, as for the iDFT model. As expected, we found that higher E/I balance was associated with flatter slopes and with higher complexity values, while when E/I balance was dominated by inhibition, complexity was reduced and PSD showed steeper slopes. Interestingly, we also found that this behavior could be well adjusted to Equation 3.1. We believe this result proposes a plausible biological mechanism of the observed relation between LZc and the power-law exponent.

Experimental Data

Next, we asked whether the impact of modifying E/I balance on the relationship between 1/f slope and LZc seen in our model could be reproduced in electrophysiological data. We first analyzed two high-density datasets, human EEG and macaque monkey ECoG recordings under propofol anesthesia and eyes-closed resting-state (Chennu et al., 2016); Yanagawa et al., 2013). Propofol is known to directly enhance GABAergic inhibitory activity, and thus reduce E/I balance (Alkire et al., 2008). In accordance with our previous results, we observed markedly increased 1/f slope (conscious state main effect's $F(1) = 1034,\ p < 0.001, \eta^2 = 0.467$; simple

main effects (awake vs anesthesia) for all humans and monkeys showed significant differences, p ¡ 0.001) and reduced LZc with respect to wakefulness in both monkeys and in one human (conscious state main effect F(1) = 442, $p < 0.001, \eta^2 = 0.063$; simple main effects (awake vs anesthesia) for subjects except one human showed significant differences, $p < 0.001$, Supplementary Figure 2). This is illustrated for representative EEG and ECoG datasets in Figure 1.3 A-D).

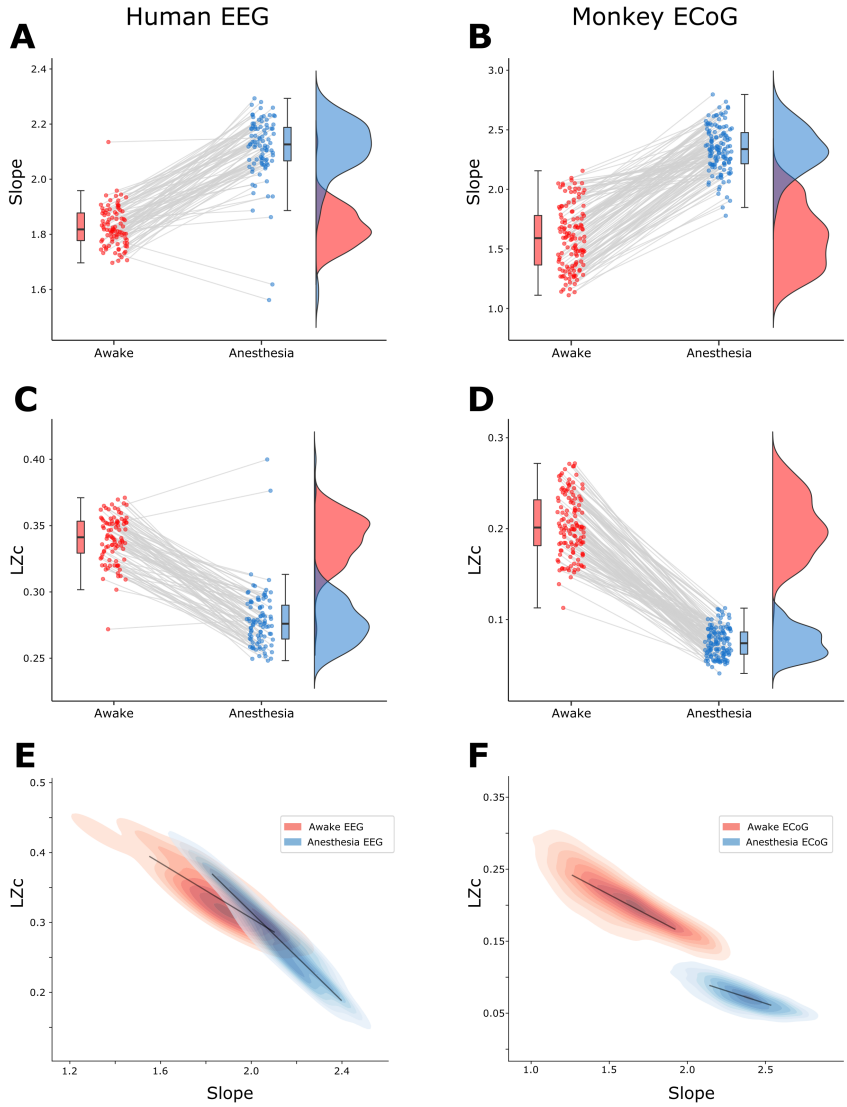

Figure 1.3: Propofol reduces LZc and steepens 1/f slope in human EEG and monkey ECoG data. ***(A)*** Propofol increases 1/f Slope across electrodes in human EEG data of a representative subject. In ***(A)***, ***(B)***, ***(C)*** and ***(D)*** each point depicts the average value (1/f slope or LZc) across time epochs for an electrode. Boxes depict the average value across electrodes, the range that includes 50 % of points and the 2 standard deviations range. Density distributions across electrodes are plotted vertically on the right side of each plot. Blue and Red colors represent Awake and Anesthesia (propofol) respectively for all panels. ***(B)*** Average 1/f slope values for Awake and Anesthesia conditions for a representative monkey's ECoG data. ***(C)*** LZc in the same EEG dataset as ***(A)*** for Awake and Anesthesia conditions. ***(D)*** LZc in the same ECoG data as in ***(B)*** for Awake and Anesthesia. ***(E)*** Depicts a 2D density plot of the LZc vs 1/f slope of all epochs and electrodes for Awake and Anesthesia conditions. Black lines depict the average value, across electrodes, of the slope of the regressions performed between 1/f slope and LZc data (see methods). ***(F)*** Same as ***(E)*** but for ECoG data.

In addition to the individual changes observed to LZc and 1/f slope due to anesthesia, we analyzed the specific relation between these two measures and how it changed due to an increase in inhibitory activity. To this end, we analyzed the correlation, across electrodes, between 1/f slope and LZc. We found a significant and marked inverse relation in both datasets, in accordance with the results of both our models. The correlation between these two measures was consistently found for all datasets analyzed (all $p < 0.05$; see also Supplementary Materials). Interestingly, this correlation was strongly modulated by the propofol-induced reduction in E/I balance. In EEG data we observed an increase in the Pearson product-moment correlation coefficient between 1/f slope and LZc (all simple main effects $p < 0.001$). In contrast ECoG data showed a reduction of this coefficient in response to propofol (all simple main effects $p < 0.001$). We believe this apparent discrepancy (increase in EEG and decrease in ECoG), is due to different baseline levels of LZc and 1/f slope across species (see Discussion).

1.4 Discussion

In this article we explored the possible relation between two apparently dissimilar time series characteristics in the context of brain field potentials. Our results show a robust and inverse relation between LZc and 1/f slope, constitutive of a one-to-one mapping in both synthetic and experimental data. This relation closely followed an x-inverted asymmetric sigmoid function in the whole range of both measures in synthetic data generated by iDFT models. This behavior was, although scaled, present even when the spectral power law behavior only comprised a small portion of all frequencies of the signal (Figure 1.1C, D). This is of particular importance as real electrophysiological signals do not show a 1/f spectral power decay in the whole frequency range (He et al., 2010). In a more neurobiologically plausible model, we observed a similar inverse relation between LZc and 1/f slope, which adjusted to the same mathematical function. Moreover, we show that this relation follows the balance between excitation and inhibition, with greater complexity and flatter 1/f slopes associated with the predominance of excitatory over inhibitory activity. At the same time, although the offset was modulated by E/I balance, the complexity of the signal was completely independent of the offset. We probed this link between E/I balance and LZc by directly contrasting 1/f slope and LZc changes due to a pharmacological

intervention. Propofol, a GABA agonist, produced changes in both measures consistent with what our models predicted: a reduced LZc and increased 1/f slope in both human EEG and monkey ECoG data.

The slope of the spectral power law has been linked to E/I balance (Lombardi et al., 2017), while LZc reflects the vastness of the repertoire of brain activity patterns ((Wenzel et al., 2019)). Although these two measures may seem unrelated at first, we hypothesize that both reflect a specific type of entropy of cortical systems. The entropy of a system can be characterized by the probabilities of each of its possible states (Shannon entropy), but also in terms of the probabilities of the transitions between these states in time, namely its entropy rate (or transition entropy). Low values of 1/f slope represent a flatter power spectrum which is characteristic of irregular desynchronized cortical states while steeper 1/f slopes showcase mainly low frequency periodic behavior (Fazlali et al., 2016; Voytek & Knight, 2015). These two extremes can also be characterized in terms of the transition entropy of their signals: flat 1/f slopes (similar to white noise) have low autocorrelations and thus high entropy rates, while in mainly periodic signals past history strongly constrains future values, thus they present low transition entropies. Interestingly, Amigó et al. (Amigó et al., 2004) have shown for electrophysiological signals that LZc closely reflects the entropy rate of the underlying system. This is particularly useful as direct estimations of entropy rate require much longer data series than LZ76 (Amigó et al., 2004). In our implementation of LZc, because we binarize each signal based on its median value, the number of points in each state (ones and zeros) is equal, which results in a constant Shannon or distribution entropy. In this line, we believe signal's LZc could be reflecting not only the vastness of the repertoire of cortical activity, but also specifically the transition entropy of the system. Thus, the strong relation we observe between LZc and 1/f slope suggests both measures are, at least partially, driven by the transition entropy of the underlying cortical system.

In addition to the 1/f slope, the offset of the PSD has been shown to reflect relevant physiological information (Miller et al., 2014). Changes in the offset have been suggested to be linked to the fMRI BOLD signal, making it a potential bridge between different spatial and temporal scales of brain features (Wen & Liu, 2016). Moreover, computational modeling has shown that broadband spectral shifts reflect changes in total firing rate of local neural populations (Miller et al., 2009; Wen & Liu, 2016). Our results show that quantifying aperiodic activity while manipulating the

E/I balance and firing rates reveals that only the offset is specifically modulated by firing rate (Figure 1.2B) while the slope was only specifically modulated by shifts in E/I the balance (Figure 1.2C). In addition, LZc was not dependent on the firing rate, but was strongly regulated by E/I balance. Although we observe a relation between 1/f offset and LZc, this effect is not specific as the same offset can be the result of many E/I balances and firing rates combinations (Figure 1.2B, Supplementary Figure 1.2). Previous spike model simulations have shown that E/I balance is strongly related to the entropy of the modeled system (Agrawal et al., 2018). In this line, we believe the relation found here between 1/f and LZc suggest that the transition entropy and the E/I balance of cortical systems could be more closely linked than previously thought.

Future work should include the role of oscillations, as recent evidence has suggested that low frequency 1/f slope is dependent on alpha-band activity (Becker et al., 2018). Despite this potential limitation of our simulations, which lacked oscillations, we observe the same general behavior in EEG and ECoG data, which does present oscillatory activity. It should be noted that he exponent of the power-law has been characterized in different frequency ranges across the literature (He et al., 2010; Becker et al., 2018; Lombardi et al., 2017; Miskovic et al., 2019; Zhang et al., 2001; Trakoshis et al., 2020; Schaworonkow & Voytek, 2021). In this line, the frequency ranges that we employed here were based on generating extrapolable interpretations for both local and global measures of field potentials. Moreover, we have shown that changing the initial and cut-off frequency of the power-law decay does not qualitatively affect the relation between 1/f slope and LZc (Fig. 1.1C, D). From this perspective, our results suggest that 1-70 Hz and 1-40 Hz frequency ranges share the characteristic of representing the global state of cortical activity. Further work could include the modeling of tight and loose coupling regimes between excitation and inhibition, which has been suggested as a more plausible mechanism of cortical E/I balance regulation (Dehghani et al., 2016; Denève & Machens, 2016; Trakoshis et al., 2020). These limitations are probably the reason why we also observe a reduced range of both LZc and 1/f slope, in spite of modeling a broad E/I balance range. Despite this limitation, we observe a consistent relation between 1/f slope and LZc across two models and two brain field potential datasets. The E/I balance shapes the computational properties of cortical neurons (Denève & Machens, 2016), and therefore behavior and cognition (Harris & Thiele, 2011). Alterations of this balance have been related to schizophrenia (Uhlhaas & Singer, 2010), autism (Rubenstein

& Merzenich, 2003), and epilepsy (Žiburkus et al., 2013), which suggests it might also play an unexplored role in other neuropsychiatric disorders (Sohal & Rubenstein, 2019). Moreover, E/I balance is not a static property of the cortex. It changes depending on the behavioral state (Waschke et al., 2019), task demands (Pfeffer et al., 2018; Waschke et al., 2019), performance (Sheehan et al., 2018) and depending on circadian rhythms (Bridi et al., 2020), which suggests that this property is under fine dynamic control. It has been proposed that cortical states and neural complexity could be regulated by subcortical cholinergic and noradrenergic activity (D'Andola et al., 2018; Nghiem et al., 2020). Future research could address this topic with a multiscale approach to the underlying cortical states of neuromodulation-related psychiatric disorders (Medel et al., 2019). From this perspective, the readout of E/I balance through brain signal complexity and the power-law of the PSD could be useful for addressing fundamental questions about the modulation of the state dependence of cortical computations. This offers new methods to understand the general mechanisms of cortical states functioning, as well as broadening the diagnostic and therapeutic tools related to neuropsychiatric disorders.

1.5 Supplementary Material

Supplementary Tables

Table S1. Linear fit parameters for iDFT Simulations.

Data		Best Parameters for Eq1 Fit of data						Mode	R2	
Manipulation	Frequency [Hz]	a	std(a)	b	std(b)	c	std (c)			
f0	1	0.0296	0.1016	4.3556	2.8521	1.6211	0.8095	2	0.997	**
f0	10	0.1302	0.1689	2.3486	1.4523	1.5108	0.8666	2	0.997	
f0	30	0.2768	0.3219	1.5176	1.3775	1.5039	1.2066	2	0.996	
f0	60	0.4405	0.5184	1.0644	1.63	1.5809	1.9344	2	0.992	
ff	30	0.2143	0.2933	2.4397	4.2085	0.8963	2.5015	1	0.981	
ff	60	0.3467	0.2549	2.7678	2.6634	1.0516	1.1667	1	0.989	
ff	120	0.5638	0.2447	3.3014	1.9787	1.1513	1.1149	1	0.994	
ff	240	0.8118	0.2283	3.6571	1.6351	1.2773	0.8489	1	0.995	
fc	3	1	0.5827	5.2726	2.532	0.7863	0.6468	1	0.982	
fc	21	0.8712	0.3537	3.1242	1.6342	0.8836	0.6539	1	0.995	
fc	147	0.7875	0.1757	2.4585	1.2555	1.9622	1.4544	1	0.9946	
fc	None	1	0.2224	3.8149	1.7462	1.5253	0.9269	1	0.995	**

Mode	Equation	
1	y = a * exp(-b * (ln(x**c + 1))**2)	where x = slope and y = LZc
2	y = a + (1 - a) * exp(-b * (ln(x**c + 1))**2)	

** Only the mode of the equation (image of the function) changes between these two fits

Table S2. Local field potential model parameters.

Neuron Type	Parameter Name	Value
E & I	Resting Membrane Potential	-65 mV
E	Population Size	8000
E	Population Firing Rate	2 Hz * [0.1, 0.5, 1, 2.5, 10]
E	Reversal Potential	0 mV
E	Conductance Time rise	0.1 ms
E	Conductance Time decay	2 ms
I	Population Size	2000
I	Population Firing Rate	5 Hz * [0.1, 0.5, 1, 2.5, 10]
I	Reversal Potential	-80 mV
I	Conductance Time rise	0.5 ms
I	Conductance Time decay	10 ms

Supplementary Figures

Figure S1. Illustration of LZc algorithm. LZc analyzes a signal step by step quantifying the number of production steps (green lines) required to recreate the original signal. When the signal being analyzed is contained in the previously analyzed segment, only a reproduction is required (black lines). CH(S) indicates the number of production steps already conducted. **Left:** A binary periodic signal can be recreated in just a few steps. The first symbol is always produced (CH(s) = 0), then, as '1' cannot be reproduced from the already analyzed sequence (which only contains '0' at this point), it has to be produced. Then, as '01', with a simple copying procedure, can recreate the rest of the signal, the recreation of S1 is completed within 3 steps. **Right:** For a non-periodic binary signal we also begin by producing the first symbol. Then, as '0' and '00' can be reproduced from the already analyzed '0' we only produce the fourth symbol ('1'). Afterwards, as '1' can be reproduced from '0001', a production process is not required, however, despite the fact that '0' and '1' are present in the already analyzed segment ('00011') the combination '10' is not, thus we need to produce the next '0'. This process continues until the whole signal is recreated. It is noteworthy that the reproduction process does not need to occur from the end of the already analyzed signal, but can take place in the middle (e.g. in step CH(S) = 5). The number of production processes, or equivalent the number of elements in the exhaustive production history of the signal, constitute the base of the LZc measure. LZc corresponds to this value, divided by n/log k(n) where n is the length of the signal and k is the number of possible symbols of the signal (2 for binary signals).

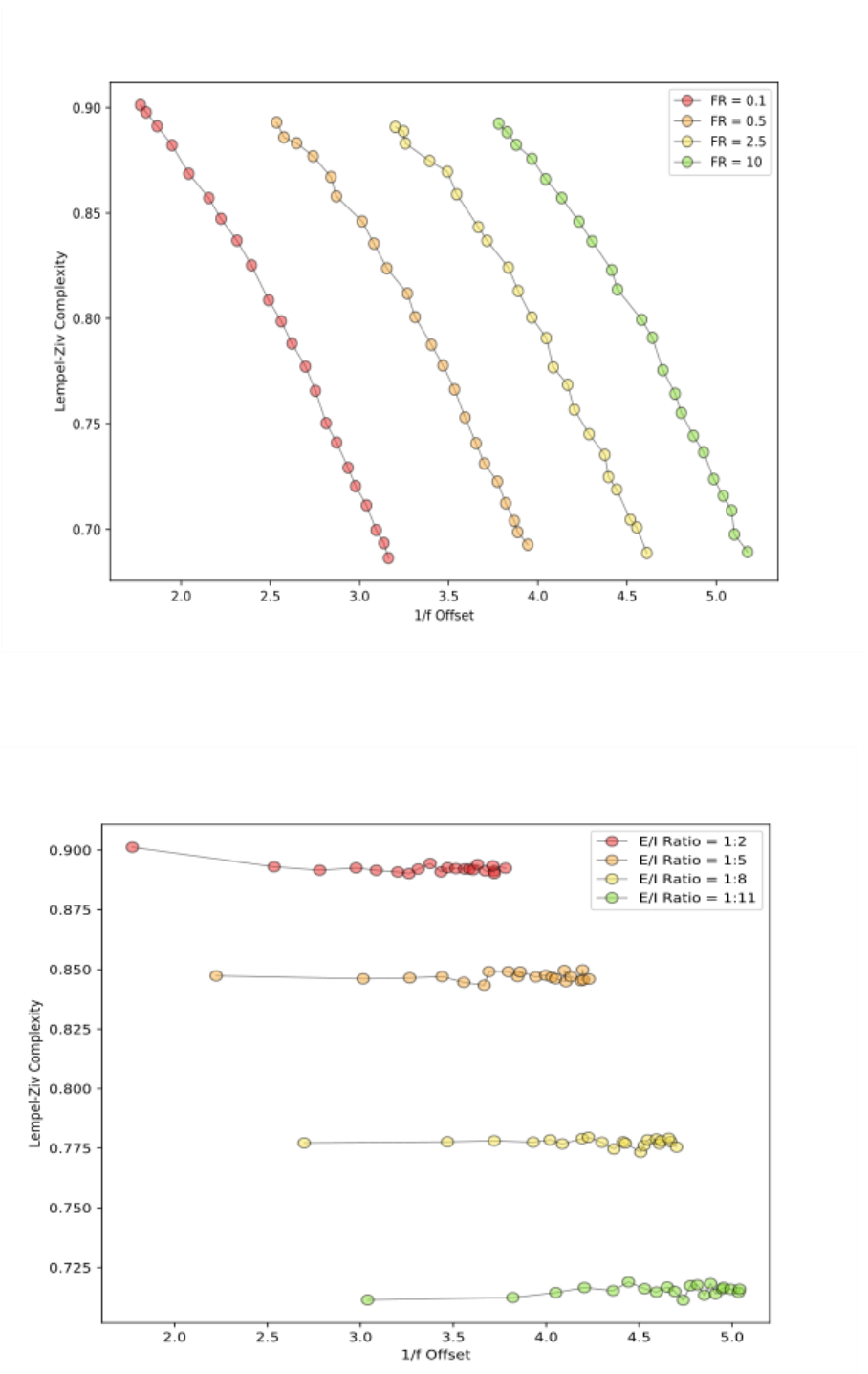

Figure S2. (Top) Color scatter plot showcasing the relation observed between 1/f Offset and Lempel Ziv Complexity for different increasing E/I balances ranging from 1:2 to 1:11 at constant firing rate values.**(Bottom)** Color scatter plot showing the relation between 1/f offset and Lempel Ziv Complexity for increasing firing rates ranging from 0.1-10 at constant E/I ratios.

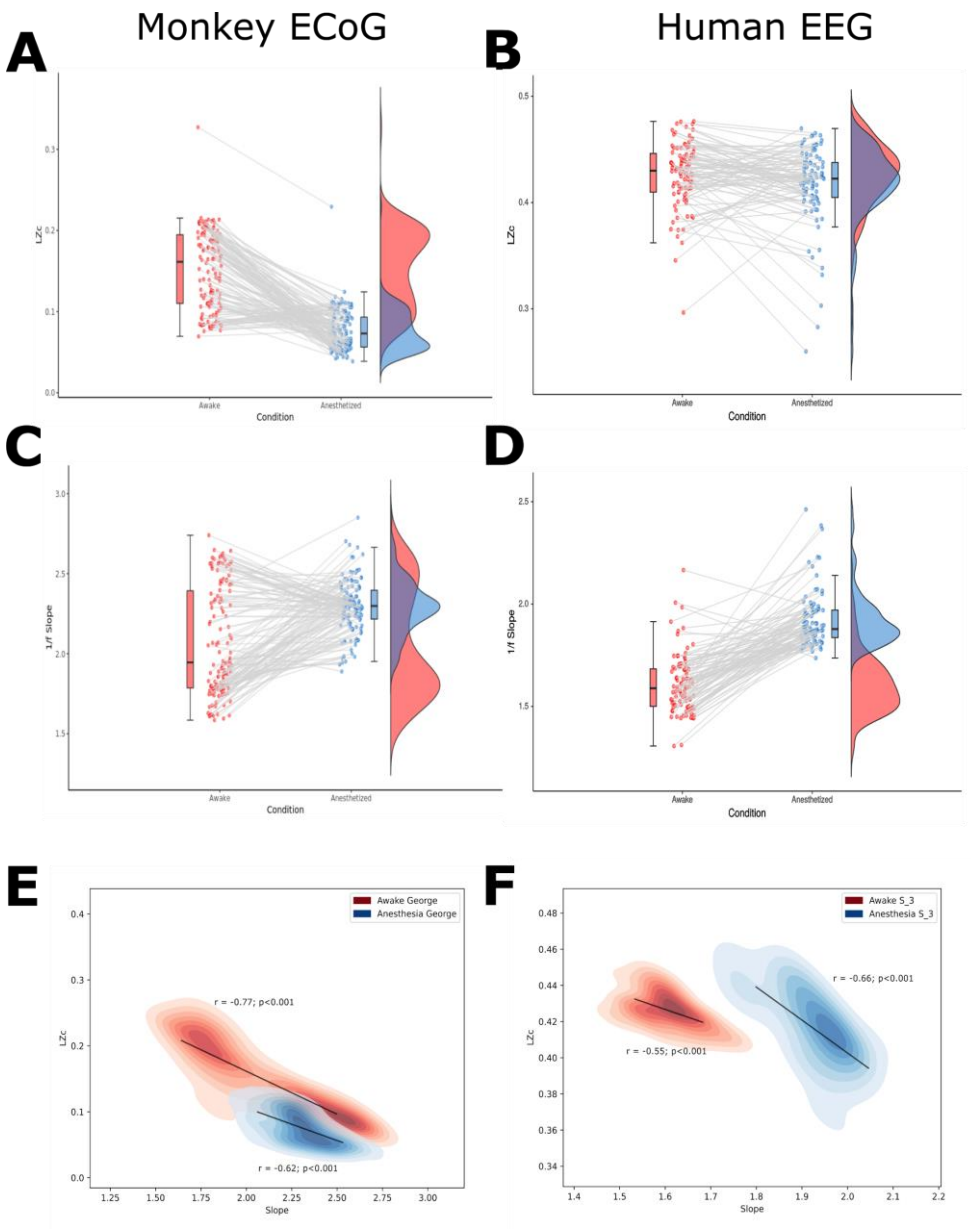

Figure S3. Propofol reduces LZc and increases 1/f slope in human EEG and monkey ECoG data. (A) Propofol increases 1/f Slope across electrodes in monkey ECoG data (George). In (A), (B), (C) and (D) each point depicts the average value (1/f slope or LZc) across time epochs for an electrode. Density distributions across electrodes are plotted vertically on the right side of each plot. Blue and Red colors represent Awake and Anesthesia (propofol) respectively for all panels. **(B)** Average 1/f slope values for Awake and Anesthesia conditions for subject 3 from the human EEG data. **(C)** LZc in the same ECoG dataset as (A) for Awake and Anesthesia conditions. **(D)** LZc in the same EEG data as in (B) for Awake and Anesthesia. **(E)** Depicts a 2D density plot of the LZc vs 1/f slope of all epochs and electrodes for Awake and Anesthesia conditions. Black lines depict the average value, across electrodes, of the slope of the regressions performed between 1/f slope and LZc data (see methods). **(F)** Same as (E) but for human EEG data.

Bibliography

[1] Agrawal, V., Cowley, A. B., Alfaori, Q., Larremore, D. B., Restrepo, J. G., & Shew, W. L. (2018). Robust entropy requires strong and balanced excitatory and inhibitory synapses. Chaos , 28(10), 103115.

[2] Akeju, O., Pavone, K. J., Westover, M. B., Vazquez, R., Prerau, M. J., Harrell, P. G., Hartnack, K. E., Rhee, J., Sampson, A. L., Habeeb, K., Gao, L., Pierce, E. T., Walsh, J. L., Brown, E. N., & Purdon, P. L. (2014). A comparison of propofol- and dexmedetomidine-induced electroencephalogram dynamics using spectral and coherence analysis. Anesthesiology, 121(5), 978–989.

[3] Alkire, M. T., Hudetz, A. G., & Tononi, G. (2008). Consciousness and anesthesia. Science, 322(5903), 876–880.

[4] Allen, M., Poggiali, D., Whitaker, K., Marshall, T. R., & Kievit, R. A. (2019). Raincloud plots: a multi-platform tool for robust data visualization. Wellcome Open Research, 4, 63.

[5] Amigó, J. M., Szczepański, J., Wajnryb, E., & Sanchez-Vives, M. V. (2004). Estimating the entropy rate of spike trains via Lempel-Ziv complexity. Neural Computation, 16(4), 717–736.

[6] Arsiwalla, X. D., & Verschure, P. (2018). Measuring the Complexity of Consciousness. Frontiers in Neuroscience, 12, 424.

[7] Bayne, T., Hohwy, J., & Owen, A. M. (2016). Are There Levels of Consciousness? Trends in Cognitive Sciences, 20(6), 405–413.

[8] Becker, R., Van de Ville, D., & Kleinschmidt, A. (2018). Alpha Oscillations Reduce Temporal Long-Range Dependence in Spontaneous Human Brain Activity. The Journal of Neuroscience: The Official Journal of the Society for Neuroscience, 38(3), 755–764.

[9] Boncompte, G., Villena-González, M., Cosmelli, D., & López, V. (2016). Spontaneous Alpha Power Lateralization Predicts Detection Performance in an Un-Cued Signal Detection Task. PloS One, 11(8), e0160347.

[10] Bridi, M. C. D., Zong, F.-J., Min, X., Luo, N., Tran, T., Qiu, J., Severin, D., Zhang, X.-T., Wang, G., Zhu, Z.-J., He, K.-W., & Kirkwood, A. (2020). Daily Oscillation of the Excitation-Inhibition Balance in Visual Cortical Circuits. Neuron, 105(4), 621–629.e4.

[11] Brunel, N. (2000). Dynamics of networks of randomly connected excitatory and inhibitory spiking neurons. Journal of Physiology, Paris, 94(5-6), 445–463.

[12] Casali, A. G., Gosseries, O., Rosanova, M., Boly, M., Sarasso, S., Casali, K. R., Casarotto, S., Bruno, M.-A., Laureys, S., Tononi, G., & Massimini, M. (2013). A theoretically based index of consciousness independent of sensory processing and behavior. Science Translational Medicine, 5(198), 198ra105.

[13] Chennu, S., O'Connor, S., Adapa, R., Menon, D. K., & Bekinschtein, T. A. (2016). Brain Connectivity Dissociates Responsiveness from Drug Exposure during Propofol-Induced Transitions of Consciousness. PLoS Computational Biology, 12(1), e1004669.

[14] D'Andola, M., Rebollo, B., Casali, A. G., Weinert, J. F., Pigorini, A., Villa, R., Massimini, M., & Sanchez-Vives, M. V. (2018). Bistability, Causality, and Complexity in Cortical Networks: An In Vitro Perturbational Study. Cerebral Cortex , 28(7), 2233–2242.

[15] Deco, G., Ponce-Alvarez, A., Hagmann, P., Romani, G. L., Mantini, D., & Corbetta, M. (2014). How local excitation-inhibition ratio impacts the whole brain dynamics. The Journal of Neuroscience: The Official Journal of the Society for Neuroscience, 34(23), 7886–7898.

[16] Dehghani, N., Peyrache, A., Telenczuk, B., Le Van Quyen, M., Halgren, E., Cash, S. S., Hatsopoulos, N. G., & Destexhe, A. (2016). Dynamic Balance of Excitation and Inhibition in Human and Monkey Neocortex. Scientific Reports, 6, 23176.

[17] Denève, S., & Machens, C. K. (2016). Efficient codes and balanced networks. Nature Neuroscience, 19(3), 375–382.

[18] Destexhe, A., Rudolph, M., Fellous, J. M., & Sejnowski, T. J. (2001). Fluctuating synaptic conductances recreate in vivo-like activity in neocortical neurons. Neuroscience, 107(1), 13–24.

[19] Destexhe, A., Rudolph, M., & Paré, D. (2003). The high-conductance state of neocortical neurons in vivo. Nature Reviews. Neuroscience, 4(9), 739–751.

[20] Fazlali, Z., Ranjbar-Slamloo, Y., Adibi, M., & Arabzadeh, E. (2016). Correlation between Cortical State and Locus Coeruleus Activity: Implications for Sensory Coding in Rat Barrel Cortex. Frontiers in Neural Circuits, 10, 14.

[21] Ferenets, R., Lipping, T., Anier, A., Jäntti, V., Melto, S., & Hovilehto, S. (2006). Comparison of entropy and complexity measures for the assessment of depth of sedation. IEEE Transactions on Bio-Medical Engineering, 53(6), 1067–1077.

[22] Gao, R., Peterson, E. J., & Voytek, B. (2017). Inferring synaptic excitation/inhibition balance from field potentials. In NeuroImage (Vol. 158, pp. 70–78).

[23] Gramfort, A., Luessi, M., Larson, E., Engemann, D. A., Strohmeier, D., Brodbeck, C., Parkkonen, L., & Hämäläinen, M. S. (2014). MNE software for processing MEG and EEG data. NeuroImage, 86, 446–460.

[24] Haider, B., Duque, A., Hasenstaub, A. R., & McCormick, D. A. (2006). Neocortical network activity in vivo is generated through a dynamic balance of excitation and inhibition. The Journal of Neuroscience: The Official Journal of the Society for Neuroscience, 26(17), 4535–4545.

[25] Donoghue, T., Haller, M., Peterson, E. J., Varma, P., Sebastian, P., Gao, R., ... & Voytek, B. (2020). Parameterizing neural power spectra into periodic and aperiodic components. Nature neuroscience, 23(12), 1655-1665.

[26] Harris, K. D., & Thiele, A. (2011). Cortical state and attention. Nature Reviews. Neuroscience, 12(9), 509–523.

[27] He, B. J. (2014). Scale-free brain activity: past, present, and future. Trends in Cognitive Sciences, 18(9), 480–487.

[28] He, B. J., & Raichle, M. E. (2009). The fMRI signal, slow cortical potential and consciousness. Trends in Cognitive Sciences, 13(7), 302–309.

[29] He, B. J., Zempel, J. M., Snyder, A. Z., & Raichle, M. E. (2010). The temporal structures and functional significance of scale-free brain activity. Neuron, 66(3), 353–369.

[30] Huupponen, E., Maksimow, A., Lapinlampi, P., Särkelä, M., Saastamoinen, A., Snapir, A., Scheinin, H., Scheinin, M., Meriläinen, P., Himanen, S.-L., & Jääskeläinen, S. (2008). Electroencephalogram spindle activity during dexmedetomidine sedation and physiological sleep. Acta Anaesthesiologica Scandinavica, 52(2), 289–294.

[31] Iemi, L., Chaumon, M., Crouzet, S. M., & Busch, N. A. (2017). Spontaneous Neural Oscillations Bias Perception by Modulating Baseline Excitability. The Journal of Neuroscience: The Official Journal of the Society for Neuroscience, 37(4), 807–819.

[32] Jas, M., Larson, E., Engemann, D. A., Leppäkangas, J., Taulu, S., Hämäläinen, M., & Gramfort, A. (2018). A Reproducible MEG/EEG Group Study With the MNE Software: Recommendations, Quality Assessments, and Good Practices. Frontiers in Neuroscience, 12, 530.

[33] Klimesch, W., Doppelmayr, M., Russegger, H., Pachinger, T., & Schwaiger, J. (1998). Induced alpha band power changes in the human EEG and attention. Neuroscience Letters, 244(2), 73–76.

[34] Lempel, A., & Ziv, J. (1976). On the Complexity of Finite Sequences. IEEE Transactions on Information Theory / Professional Technical Group on Information Theory, 22(1), 75–81.

[35] Lombardi, F., Herrmann, H. J., & de Arcangelis, L. (2017). Balance of excitation and inhibition determines 1/f power spectrum in neuronal networks. Chaos , 27(4), 047402.

[36] Massimini, M., Ferrarelli, F., Huber, R., Esser, S. K., Singh, H., & Tononi, G. (2005). Breakdown of cortical effective connectivity during sleep. Science, 309(5744), 2228–2232.

[37] Medel, V., Valdés, J., Castro, S., Ossandón, T., & Boncompte, G. (2019). Commentary: Amplification and Suppression of Distinct Brainwide Activity Patterns by Catecholamines [Review of Commentary: Amplification and Suppression of Distinct Brainwide Activity Patterns by Catecholamines]. Frontiers in Behavioral Neuroscience, 13, 217.

[38] Miller, K. J., Honey, C. J., Hermes, D., Rao, R. P. N., denNijs, M., & Ojemann, J. G. (2014). Broadband changes in the cortical surface potential track activation of functionally diverse neuronal populations. NeuroImage, 85 Pt 2, 711–720.

[39] Miller, K. J., Sorensen, L. B., Ojemann, J. G., & den Nijs, M. (2009). Power-law scaling in the brain surface electric potential. PLoS Computational Biology, 5(12), e1000609.

[40] Miskovic, V., MacDonald, K. J., Rhodes, L. J., & Cote, K. A. (2019). Changes in EEG multiscale entropy and power-law frequency scaling during the human sleep cycle. Human Brain Mapping, 40(2), 538–551.

[41] Nghiem, T.-A. E., Tort-Colet, N., Górski, T., Ferrari, U., Moghimyfiroozabad, S., Goldman, J. S., Teleńczuk, B., Capone, C., Bal, T., di Volo, M., & Destexhe, A. (2020). Cholinergic Switch between Two Types of Slow Waves in Cerebral Cortex. Cerebral Cortex , 30(6), 3451–3466.

[42] Pfeffer, T., Avramiea, A.-E., Nolte, G., Engel, A. K., Linkenkaer-Hansen, K., & Donner, T. H. (2018). Catecholamines alter the intrinsic variability of cortical population activity and perception. PLoS Biology, 16(2), e2003453.

[43] Purdon, P. L., & Sampson, A. (2015). Clinical electroencephalography for anesthesiologists part I: background and basic signatures. : The Journal of .... https://anesthesiology.pubs.asahq.org/Article.aspx?articleid=2430415

[44] Reimer, J., Froudarakis, E., Cadwell, C. R., Yatsenko, D., Denfield, G. H., & Tolias, A. S. (2014). Pupil fluctuations track fast switching of cortical states during quiet wakefulness. Neuron, 84(2), 355–362.

[45] Rubenstein, J. L. R., & Merzenich, M. M. (2003). Model of autism: increased ratio of excitation/inhibition in key neural systems. Genes, Brain, and Behavior, 2(5), 255–267.

[46] Rubin, R., Abbott, L. F., & Sompolinsky, H. (2017). Balanced excitation and inhibition are required for high-capacity, noise-robust neuronal selectivity. Proceedings of the National Academy of Sciences of the United States of America, 114(44), E9366–E9375.

[47] Sarasso, S., Rosanova, M., Casali, A. G., Casarotto, S., Fecchio, M., Boly, M., Gosseries, O., Tononi, G., Laureys, S., & Massimini, M. (2014). Quantifying cortical EEG responses to TMS in (un) consciousness. Clinical EEG and Neuroscience: Official Journal of the EEG and Clinical Neuroscience Society , 45(1), 40–49.

[48] Schartner, M., Seth, A., Noirhomme, Q., Boly, M., Bruno, M.-A., Laureys, S., & Barrett, A. (2015). Complexity of Multi-Dimensional Spontaneous EEG Decreases during Propofol Induced General Anaesthesia. PloS One, 10(8), e0133532.

[49] Schaworonkow, N., & Voytek, B. (2020). Longitudinal changes in aperiodic and periodic activity in electrophysiological recordings in the first seven months of life. Developmental cognitive neuroscience, 47, 100895.

[50] Sheehan, T. C., Sreekumar, V., Inati, S. K., & Zaghloul, K. A. (2018). Signal Complexity of Human Intracranial EEG Tracks Successful Associative-Memory Formation across Individuals. The Journal of Neuroscience: The Official Journal of the Society for Neuroscience, 38(7), 1744–1755.

[51] Sohal, V. S., & Rubenstein, J. L. R. (2019). Excitation-inhibition balance as a framework for investigating mechanisms in neuropsychiatric disorders. In Molecular Psychiatry (Vol. 24, Issue 9, pp. 1248–1257). https://doi.org/10.1038/s41380-019-0426-0

[52] Tononi, G., & Edelman, G. M. (1998). Consciousness and complexity. Science, 282(5395), 1846–1851.

[53] Trakoshis, S., Martínez-Cañada, P., Rocchi, F., Canella, C., You, W., Chakrabarti, B., Ruigrok, A. N., Bullmore, E. T., Suckling, J., Markicevic, M., Zerbi, V., MRC AIMS Consortium, Baron-Cohen, S., Gozzi, A., Lai, M.-C., Panzeri, S., & Lombardo, M. V. (2020). Intrinsic excitation-inhibition imbalance affects medial prefrontal cortex differently in autistic men versus women. eLife, 9. https://doi.org/10.7554/eLife.55684

[54] Uhlhaas, P. J., & Singer, W. (2010). Abnormal neural oscillations and synchrony in schizophrenia. Nature Reviews. Neuroscience, 11(2), 100–113.

[55] van Langen, J (2020). Open-visualizations for repeated measures in R. `https://github.com/jorvlan/open-visualizations`.

[56] van Vreeswijk, C., & Sompolinsky, H. (1996). Chaos in neuronal networks with balanced excitatory and inhibitory activity. Science, 274(5293), 1724–1726.

[57] Virtanen, P., Gommers, R., Oliphant, T. E., Haberland, M., Reddy, T., Cournapeau, D., Burovski, E., Peterson, P., Weckesser, W., Bright, J., van der Walt, S. J., Brett, M., Wilson, J., Millman, K. J., Mayorov, N., Nelson, A. R. J., Jones, E., Kern, R., Larson, E., ... SciPy 1.0 Contributors. (2020). SciPy 1.0: fundamental algorithms for scientific computing in Python. Nature Methods, 17(3), 261–272.

[58] Voytek, B., & Knight, R. T. (2015). Dynamic network communication as a unifying neural basis for cognition, development, aging, and disease. Biological Psychiatry, 77(12), 1089–1097.

[59] Waschke, L., Tune, S., & Obleser, J. (2019). Local cortical desynchronization and pupil-linked arousal differentially shape brain states for optimal sensory performance. eLife, 8. https://doi.org/10.7554/eLife.51501

[60] Welch, T. A. (1984). A technique for high-performance data compression. Computer, 6, 8–19.

[61] Wen, H., & Liu, Z. (2016). Broadband Electrophysiological Dynamics Contribute to Global Resting-State fMRI Signal. In The Journal of Neuroscience (Vol. 36, Issue 22, pp. 6030–6040). https://doi.org/10.1523/jneurosci.0187-16.2016

[62] Wenzel, M., Han, S., Smith, E. H., Hoel, E., Greger, B., House, P. A., & Yuste, R. (2019). Reduced Repertoire of Cortical Microstates and Neuronal Ensembles in Medically Induced Loss of Consciousness. Cell Systems, 8(5), 467–474.e4.

[63] Yanagawa, T., Chao, Z. C., Hasegawa, N., & Fujii, N. (2013). Large-scale information flow in conscious and unconscious states: an ECoG study in monkeys. PloS One, 8(11), e80845.

[64] Zhang, X. S., Roy, R. J., & Jensen, E. W. (2001). EEG complexity as a measure of depth of anesthesia for patients. IEEE Transactions on Bio-Medical Engineering, 48(12), 1424–1433.

[65] Žiburkus, J., Cressman, J. R., & Schiff, S. J. (2013). Seizures as imbalanced up states: excitatory and inhibitory conductances during seizure-like events. Journal of Neurophysiology, 109(5), 1296–1306.

Chapter 2

Brain activity complexity has a non-linear relation with the level of propofol sedation

Abstract

Background: Brain activity complexity has risen as a robust correlate of consciousness, showing promise as a possible drug-independent measure to be used to in anaesthesia. Previous studies have mostly compared awake versus deep anaesthesia states, showing higher complexity for the former compared to the latter. However, little attention has been paid to complexity in intermediate states of sedation.

Methods: Here we analysed the Lempel-Ziv Complexity of EEG signals from subjects undergoing moderate propofol sedation, from an open-access database, and related it to behavioral performance as a continuous marker of the level of sedation and to plasma propofol concentrations. We explored its relation to spectral properties, to propofol susceptibility and its topographical distribution.

Results: We found that subjects who retained behavioural performance despite propofol sedation showed increased brain activity complexity compared to baseline

(M = 13.9%, 95% CI = 7.5–20.3). This was not the case for subjects that lost behavioural performance. The increase was most prominent in frontal electrodes, and correlated with behavioural performance and propofol susceptibility. This effect was positively correlated with high-frequency activity. However, abolishing specific frequency ranges (e.g. alpha or gamma) did not reduce the propofol-induced increase in complexity.

Conclusions: Our results show that brain activity complexity can increase in response to propofol, particularly during low-dosage sedation. Propofol-mediated LZc increase was independent of frequency-specific spectral power manipulations, and most prominent in frontal areas. Taken together, these results advance our understanding of brain activity complexity and anaesthetics but also problematise theories of consciousness that propose a direct relation between brain activity complexity and states of consciousness.

Keywords— Complexity, Propofol, Lempel-Ziv Complexity, Sedation, Anaesthesia Monitoring, Brain Oscillations, States of Consiousness, EEG

2.1 Introduction

The search for precise and reliable methods to quantify level of sedation and depth of anaesthesia in clinical settings has drawn increasing attention over the past decades. Current clinically employed anaesthesia monitors, like Bispectral Index (BIS; Aspect Medical Systems, USA) and EntropyTM (Datex-Ohmeda, Finland), are grounded on the quantification of spectral properties of the electroencephalographic (EEG) signal, that is, on the power of specific frequency ranges like those of alpha, delta and gamma bands (Bruhn et al., 2000; Davidson et al., 2004). However, spectral modulations of the EEG signal are known to be strongly dependent on the anaesthetic used (Feshchenko et al., 2004; Warner et al., 2015; Purdon et al., 2015), the patient's age (Zohar et al.,2006; Akeju et al., 2015), among other factors (Kaiser et al., 2020). In contrast, current theories of consciousness, like Integrated Information Theory (Tononi, 2008; Tononi et al., 2016) and Global Neuronal Workspace Theory (Sergent & Dehaene, 2004; Dehaene et al., 2006), em-

phasize information as a key aspect of the neural basis of consciousness. Be it the amount of integrated information in cortical circuits, or the global availability of information, these theories propose that the causal informational relations between neuronal elements, rather than specific oscillations, are the key biological aspect of brain functioning that define states of consciousness like wakefulness or anaesthesia.

Several EEG measures, grounded on Shannon's Information Theory (Shannon, 1948), have been proposed in the last two decades, which aim at quantifying the informational contents and relations of cortical systems. In particular, Lempel-Ziv Complexity (LZc), which computes the number of non-redundant patterns of EEG signals (Lempel & Ziv, 1976), has shown particularly promising results in discriminating global states of consciousness. The pioneer work of Zhang and cols. (2001) showed that, using a simple threshold for the value of LZc, they could discriminate between awake (higher LZc) and deep anaesthesia (lower LZc), using four different anaesthetics with 93% accuracy. More recent work has also found that reverberations of brain activity evoked by transcranial magnetic stimulation are much more complex (LZc) during normal wakefulness than during sleep, or after loss of consciousness (LOC) due to a variety of anaesthetic drugs (Massimini et al., 2005; Sarasso et al., 2015). This results, higher complexity for awake and lower complexity for unconscious cortical states, have been replicated under several contexts, and open the possibility for new anaesthesia monitors based on brain activity complexity, but also in general to better characterize the relation between brain activity complexity and consciousness. However, little attention has been paid to intermediate states like sedation and anaesthesia transitions. One recent study in mice reported that deeper anaesthesia states were related to lower brain activity complexity, as compared to light anaesthesia, suggesting a linear (or monotonic) relation between depth of anaesthesia and brain activity complexity (Dasilva et al., 2020). However, these results have not been replicated in humans. Here we tested whether propofol-induced intermediate states of consciousness, directly quantified by human subject's behavioural performance, showcase intermediate values of brain activity complexity, in between those of wakefulness and deep anaesthesia. We also explored the topological distribution of brain activity complexity during sedation and its possible relation to classical spectral EEG properties like alpha power. The dataset analysed here contained the average performance (number of correct answers) per condition per subject. Additionally, blood samples were obtained during

Low TPC, High TPC and Recovery conditions to quantify plasma propofol concentration. Pre-processing of this database included EEG data filtering (0.5 – 40Hz), segmenting into 10s epochs (approximately 38 clean epochs per subject per condition) and artefact rejection of noisy epochs by visual inspection. Data were re-referenced to the average of all channels.

2.2 Materials and Methods

Data

We analysed an open-access EEG database developed by Chennu and collaborators (2016) . EEG data were acquired from 20 healthy volunteers during closed-eyes resting state for 7 minutes in four consecutive sedation conditions: Baseline, in which no propofol was administered; Mild sedation, in which intravenous target-controlled infusion of propofol was applied, set to a target propofol concentration (TPC) equal to 0.6µg ml^{-1} ; moderate sedation, in which TPC was set to 1.2µg ml^{-1} ; and a Recovery condition, where no further propofol was injected. This was the nomenclature employed in the original work, however, we here decided to refer to Mild and Moderate sedation conditions as Low TPC and High TPC respectively. This is to empathize that these conditions were directly defined by target propofol levels and not its effect, namely the level of sedation or responsiveness. After each condition, a 10 minutes period was allowed to obtain a steady-state propofol plasma concentration. During each condition, subjects also performed an auditory discrimination task in which they were asked to distinguish between a buzz sound or white noise, and to respond accordingly by pressing a button. The

Lempel-Ziv Complexity Algorithm

To apply the LZc algorithm a crucial previous step is required. This algorithm is applicable to signals that contain only few different symbols (typically binary signals), thus we binarized the pre-processed EEG signal, assigning a '1' to each time point with a voltage value above the median of the analysis windows (10 seconds), and a '0' to each time point below the median, following previously employed strategies (Aboy et al., 2006). Then, to each time window, for each condition, each electrode and each subject, we computed the LZc. Detailed descriptions

of the 1976 LZc algorithm can be found in the original article (Lempel & Ziv, 1976) and in Supplementary Material Figure 2.5, which also contains two illustrative step-by-step examples. The script Implementation of this algorithm for Python can also be found in Supplementary Material 2.6 LZc Algorithm Code. Briefly, LZc quantifies the number of non-redundant patterns on a signal, using a step by step strategy. At each time point of the signal, a complexity counter increases if the next symbol of the signal would introduce a pattern never observed before, or one that could not be reproduced from previous segments. On the contrary, if the symbol does not bring strict novelty to what the algorithm has already analysed, the complexity counter does not increase, and the algorithm continues to the next time point. In this line, a constant signal (e.g. '1111111...') will have only two novelties, the one referring to the first symbol ('1') and the second one recreating the rest of the signal. In a signal like '010101...' the complexity counter will reach a value of 3, while more chaotic sequences will increasingly showcase higher values. This complexity counter is then normalized considering both the length of the signal and the number of symbols (2 for binary), finally yielding the LZc value. LZc ranges from 0 for a constant signal ('11111...') to 1 for a completely random signal (Lempel & Ziv, 1976).

Data Analysis

To estimate the complexity level of each subject during each condition, we averaged LZc values across windows, electrodes and subjects for each condition (Figure 2.1A) unless otherwise stated. Statistical analysis were done using Python libraries (NumPy and SciPy (Harris et al., 2020)) and JASP (JASP Team 2019). Significant results were considered as such for tests with p ¡ 0.05 unless otherwise stated. T-test were employed as Post hoc tests in ANOVAs. Python MNE library (Gramfort et al., 2013) was used for topological plots and analyses.

To initially explore the possible effect that TCP conditions had on LZc we conducted a Friedman's test (non-parametric analogous to 1-way ANOVA) on average LZc values per subject across conditions. Separation of participants into Low and High performance groups was conducted by applying a one dimension k-means clustering algorithm (Scipy Python library (Harris et al., 2020)) to the behavioural performance of participants during High TPC condition. K-means algorithm is an iterative process that attempts to find centroids (performance values, 2 in

our case) that minimize the sum of squares of the distance between each centroid and the data points closer to it (than to the other centroid). Once the algorithm converges, the data points closer to each centroid constitute each cluster.

After the separation of participants into Low performance and High performance, we analysed the apparent interaction between condition and performance (Figure 2.1E) via a mixed factor ANOVA with TCP condition (Baseline, Low/High TCP, Recovery) as the within subject factor and performance (High/Low performance) as the between subjects factor. Mann-Whitney test (non-parametric analogous to t-test) was used to compare plasma propofol concentrations between High performance and Low performance groups during the High TPC condition.

After group analyses, we conducted single-subject level analyses of the data within the High TCP condition. A multiple regression was employed to test whether subject's LZc could be predicted by their behavioural performance and/or by their plasma propofol concentrations. To support the robustness of this multiple regression, we conducted an Intraclass Correlational analysis. This strategy allows to compare the within subject variance from between-subjects variance. Within-subjects variance in this design corresponds the difference in LZc between time epochs for each subject, and thus corresponds to variations due to measurement errors and stochastic/random variations in each subject's cortical state. On the other side, between-subject's variance should reflect the differences in LZc given by natural differences that could be explained by our predictors, performance and plasma propofol levels.

Spectral power of particular oscillatory bands was obtained by applying the Fast Fourier Transform to the pre-processed signal (hanning tapper), squaring and median-filtering (1 Hz) (Cole et al., 2019) the result for each frequency range (delta: 0.3 – 3 Hz; theta: 3 – 7 Hz; alpha: 7 – 13 Hz; low beta: 13 – 20Hz; high beta: 20 – 30 Hz; gamma 30 – 40 Hz). The notch filters employed to analyse the possible dependency of LZc with specific frequency bands (Figure 2.2A, C) were IIR, Butterworth of order 4, with a transition bandwidth of 0.2 Hz. Illustrative power spectral density plots of the effects of each notch-filter can be found in Supplementary Material 3 Figure 2.6.

ROI classification of electrodes was defined based on cortical lobes into four bilateral areas: frontal, temporal, parietal and occipital (Figure 2.4). An illustration depicting the specific electrodes used for each ROI can be found in Supplementary Material 4 Figure 2.7.

2.3 Results

LZc, behavioural responsiveness and plasma concentration across sedation conditions

To evaluate the relation between brain activity complexity and level of sedation, we computed the grand average LZc across subjects for each condition. We found that even the low propofol concentrations used here had a significant effect on LZc across conditions (Friedman's $Q = 11.58$, $p = 0.0089$). To our surprise, we found a tendency towards higher LZc during sedation conditions (Low and High TPC) compared to Baseline (Fig. 2.1A). This is opposed to the decrease in measures similar to LZc due to propofol reported in the literature (Schartner et al,, 2015) . It is important to note that neither behavioural performance, plasma propofol concentration nor LZc were homogeneous within each TPC condition, especially during the High TPC condition (Fig. 2.1B, C, D). To account for this variability, we employed two complementary strategies, group comparisons and analyses at the single-subject level.

Group Analysis

We separated subjects using a clustering algorithm (1-D k-means, see Methods), according to performance during High TPC, into High performance ($N = 13$) and Low performance groups ($N = 7$). Using a different statistical strategy, the same grouping of subjects was achieved in the original analysis of this dataset (Chennu et al. 2016). Interestingly, statistical comparisons revealed that subjects that increased their LZc due to propofol almost exclusively belonged to the High performance group (Fig. 2.1E). This group showed a significant increase in LZc compared to their baseline (mixed factor ANOVA, condition*performance $F = 15.81$, $p < 0.001$; Post hoc test: High performance, High TPC vs. Baseline: $t = -4.9$, $p < 0.001$). On the contrary, Low performance subjects did not show a significant LZc modulation by propofol (Low performance, High TPC vs. Baseline: $t = 1.34$, $p = 0.59$) but did show a tendency towards decreasing LZc during High TPC (6 out of 7 showed a lower LZc value in High TPC than in Baseline). It is noteworthy that this difference in LZc for High and Low performance groups was not present during Baseline condition ($t = 0.15$, $p > 0.88$). Although every subject had the same target

propofol concentration, the differences seen here may be nonetheless due to differential dosage. To control for this possibility, we compared their plasma propofol concentrations during the High TPC condition (see Fig. 2.1C). We observed no significant difference when comparing High vs. Low performance groups during High TPC (Mann-Whitney W = 24, p = 0.096).

Single-subject level analyses

To better evaluate the relation between LZc, performance and plasma propofol concentration, we conducted a correlational analysis at the single-subject level. We performed a multiple linear regression on High TPC data using performance (Fig. 2.1F) and propofol concentrations (Fig. 2.1G) as predictors of LZc. We found that, in conjunction, these two predictors significantly explained 51.4% of LZc's variance ($F = 11.1$, $p < 0.001$, adjusted $R\ 2 = 0.514$). This effect was mainly driven by performance, (performance β: $t = 4.48$, $p < 0.001$), which is illustrated by the fact that the regression coefficient associated with propofol concentration was not significantly different from zero (Fig. 2.1G; propofol concentration β: $t = 1.48$, $p = 0.156$). Moreover, when this variable was removed from the model, only a reduction of 3.2% of explained variance was observed (adjusted $R\ 2 = 0.482$, Fig. 2.1F, G). This result indicates that brain activity complexity is a robust predictor of performance during intermediate sedation states, and thus of the level of sedation, more so than plasma propofol concentration. To test whether the observed differences between subjects, analysed in this multiple linear regression, were due to random variations or truly reflected each subject's brain activity complexity, we conducted an Intraclass Correlation analysis. This allows to compare the between-subjects LZc variance with the within-subject (across epochs) variance. We found that between subject's variance accounted for 58.6% of the total variance of the dataset, while epochs (stochastic variations in LZc in time) only accounted for 14%. This indicates that regardless of the low number of subjects in this dataset, inter subject differences in LZc are much more important than noise-related variations.

Five subjects presented very distinct behavioural performances during Low TPC (close to 100%) and High TPC conditions (lower than 70%; see Figure 2.1B). This allowed us to explore LZc dynamics between two conditions with different (not null) propofol dosages in a within-subject manner. As an exploratory analysis we plotted the LZc values of those 5 subjects, relative

to baseline, versus the plasmatic propofol concentration they presented during Low and High TPC conditions (Figure 2.1H). Although no statistical analyses of this data would be feasible due to the small sample (n = 5), this analysis showed that three out of five subjects from this subset showed considerably greater LZc during Low TPC than during baseline, and that all five showcased a reduced brain activity complexity when comparing Low versus High TPC.

Susceptibility

The results presented above suggest that increases in LZc could be used as a possible differentiating characteristic between subjects that are highly susceptible to propofol (Low performance) from those that require a higher dose to reach deeper sedation (High performance). Also, although propofol concentration did not predict LZc by itself (Fig. 2.1G), we hypothesized that its relationship with performance could be informative in this regard. To assess this possibility, we constructed a susceptibility-to-propofol index that accounts for both the amount of behavioural performance lost during sedation and plasma propofol concentration. Susceptibility was defined as the amount of performance lost in High TPC (normalized to range between 0 and 1) divided by the normalized propofol concentration during High TPC (relative to all subjects, also from 0 to 1). We found a robust linear correlation between propofol-induced LZc change and our susceptibility-to-propofol index (Fig. 2.1H; R 2 = 0.52, $p < 0.001$). This suggests that subjects that are more susceptible to propofol sedation are more prone to showcase a decrease in brain activity complexity, while those less susceptible are likely to showcase increases in LZc during propofol sedation.

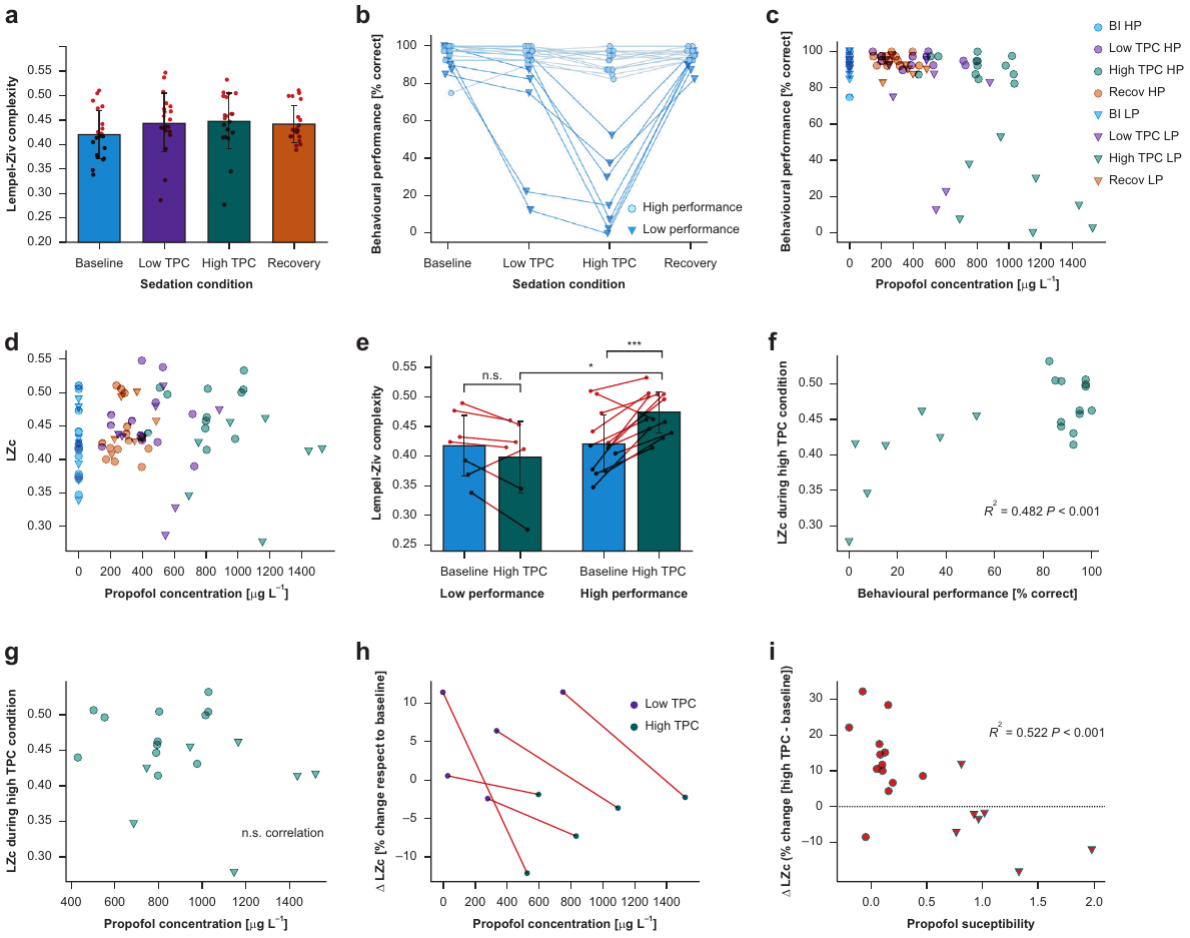

Figure 2.1: Relation between LZc, behaviour and plasma propofol concentration. **A**: Grand average LZc for each condition. Each dot represents each subject's average. **B**: Behavioural performance in the sound discrimination task for each sedation condition. Light circles indicate High performance subjects and dark triangles represent Low performance subjects, as separated by performance during High TPC (k-means). **C**: Scatter plot depicting behavioural performance versus propofol concentration levels for all subjects and conditions. HP and LP represent High and Low performance respectively. **D**: Scatter plot depicting average LZc versus propofol concentration for each subject and condition. Colours and markers' shapes represent the same as in C. **E**: LZc during Baseline and High TPC separated by performance groups. Error bars represent standard deviation. Asterisks represent significance under 2-way mixed effect ANOVA. **F**: Scatter plot showing the linear correlation between LZc and behavioural performance during High TPC. **G**: Scatter plot showing the lack of correlation between LZc and propofol levels during High TPC ($p > 0.05$). **H**: Scatter plot showing LZc values relative to baseline for Low (orange markers) and High (red markers) TPC conditions of 5 subjects that showcased marked differences of behavioural performance between these two sedation conditions (see main text). Same-subject data is represented by markers connected by a grey line. **I**: Scatter plot showing the significant correlation (Pearson) between the percentage change of LZc from Baseline to High TPC condition versus susceptibility at the single-subject level. Note that a positive ΔLZc indicates increase in brain activity complexity due to propofol sedation.

Complexity and Spectral Power

The neural signatures of propofol anaesthesia have been classically studied with spectral analysis, which have robustly shown that sedation and LOC are closely linked to an increase and frontalization of alpha-band activity, among other spectral signatures (Feshchenko et al., 2004) . With this in mind, we wanted to assess whether our results showcasing the relation between performance and LZc were dependent on alpha power. To do this, we performed a notch filter to the EEG signal, effectively eliminating the power in the alpha-band range (7 – 13 Hz), before computing LZc on the EEG signal. We then calculated the difference in LZc due to propofol for each subject (ΔLZc: High TPC – Baseline). We conducted a mixed factors ANOVA with ΔLZc as the dependent variable, performance (low / high) as a between subject factor and filter (No Filter / No Alpha) as a within subject factor. This analysis showed no effect for the filter condition ($F = 0.133$, $p = 0.72$) and a strong effect of performance ($F = 18.38$, $p < 0.001$; Fig. 2.2A). Post hoc analyses confirmed that ΔLZc only differed between pairs of groups with different performance (all $p < 0.05$), but not between groups that differed on the filter treatment (all $p > 0.92$). In addition to this filtering strategy, we wanted to test whether natural variations of alpha power could predict the level of brain activity complexity. We found no significant correlation between LZc and alpha power during the High TPC condition (linear regression, R 2 = 0.039, p = 0.41, Fig. 2.2B). These results suggests that LZc is not dependent on the amplitude of alpha activity.

To further assess the relation between LZc with spectral characteristics of the EEG signal, we subdivided the whole frequency range into six frequency bands (ranging from 0.5 to 40Hz, see methods), quantified their powers and correlated them with LZc for all subjects and conditions (See Supplementary Material 5, Figure 2.8). We found, as suggested by previous simulation results 20 , that in general LZc has a negative correlation with the power of low-frequency activity (e.g. LZc vs delta: $R = -0.42$, $p < 0.001$) and a positive correlation with the power of high frequency activity (e.g. LZc vs gamma: $R = 0.63$, $p < 0.001$). This could imply that the observed increase in LZc due to propofol sedation in High performance subjects is directly caused by changes of the spectral power of low and high frequency bands. To directly test this hypothesis, we conducted a causal analysis in which we separately filtered each of the 6 frequency

bands prior to calculating LZc and assessed the % change in LZc between Baseline and High TPC conditions. Figure 2.2C illustrates these results, which show that the increase in LZc in High performance subjects was not altered by filtering out any specific frequency band. Statistical analysis of this was assessed by means of Bonferroni corrected (12 comparisons) paired t-tests comparing the % change in LZc from filtered signals against zero (Delta p = 0.024; Theta p = 0.0078; Alpha p = 0.018; Low Beta p = 0.0098; High beta p = 0.0098; Gamma p = 0.0028) and comparing the % change in LZc from filtered vs unfiltered signals (all p ¿ 0.05). The comparison of LZc % change from unfiltered signals vs High beta-filtered yielded a marginally significant difference (p = 0.067). These results illustrate that the propofol-induced increase in LZc in High performance subjects (positive % change in LZc) was present regardless of filtering out any frequency band. Thus, although in general LZc correlates with the spectral power of low and high frequency bands, the sedation-induced LZc increase does not appear to depend on the power within any specific frequency range.

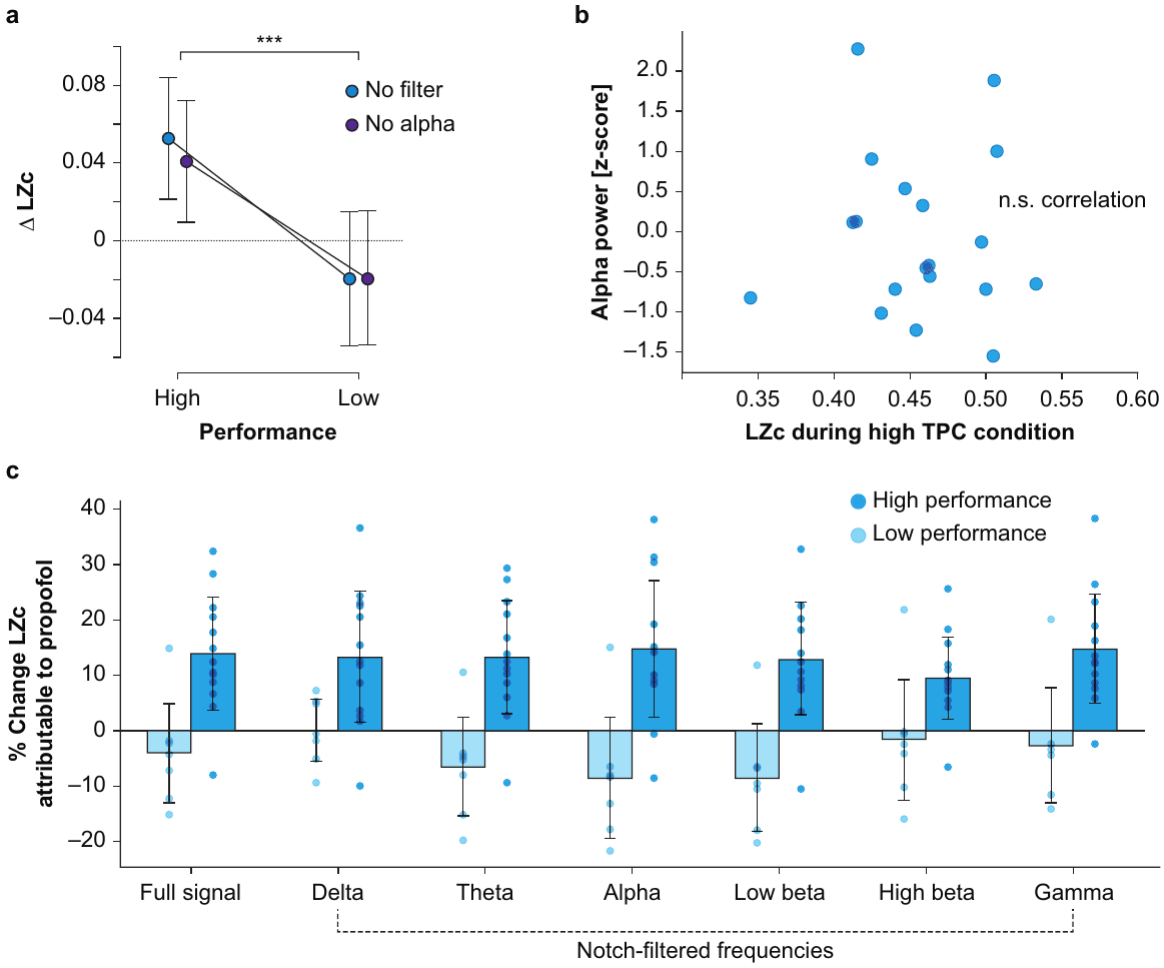

Figure 2.2: Relation between brain activity complexity and spectral power. **A**: Difference in LZc (High TPC minus Baseline) for High and Low performance subjects. Empty circles indicate no extra treatment to the signal before calculating LZc and filled circles indicate filtering out alpha-band power before calculating LZc (see Methods). **B**: Scatter plot relating the spontaneous power of alpha-band and the LZc during High TPC for each subject. No significant correlation was found. **C**: Shows the percentage change of LZc due to propofol sedation (High TPC minus Baseline) in average (bar plots, error bars show standard deviation), and for each subject (markers). This analysis was done for the full EEG signal and for frequency band-specific notch-filtered signals. Light grey indicates Low performance subjects and Dark grey indicates High performance subjects. High performance group consistently showed positive values, indicating that the increase in LZc is mostly independence of single-frequency band power modulations

LZc topological distribution across sedation stages

The interpretations of EEG oscillatory activity, and of most brain activity patterns, are strongly dependent on scalp localization. However, evidence regarding the topographical distribution of brain activity complexity is still sparse. It has been observed, using variations of the original 1976 LZc algorithm, that complexity peaks at frontal electrodes and does not drastically changes topographical distribution in response to anaesthesia (e.g. Lempel-Ziv-Welch (Schartner et al., 2015); Permutation Lempel-Ziv Complexity (Shumbayawonda et al., 2018)). Here, we wanted to assess the distribution of LZc during Baseline and the possible differences in topography given by propofol sedation. Figure 2.3A shows the LZc distribution in each sedation condition. In contrast to what has been reported with other complexity algorithms, we found a relatively low complexity in frontal electrodes during Baseline in comparison, for example, to parietal areas, which showcase two bilateral complexity peaks. Visual inspection of grand average topographic complexity distributions showed no drastic changes due to propofol, beside a general magnitude increase. To better assess this we compared, for each electrode, LZc within TPC conditions (Fig. 2.3B, High performance vs. low performance) and between TPC conditions (Fig. 2.3C, Baseline vs. High TPC). Figure 2.3B (right side) shows the topographical map of t-values of the comparisons between High and Low performance subjects during High TPC. A wide centro-parietal area showed significant differences in this comparison (white markers indicate significance after false discovery rate (FDR TSBKY) (Yoav et al., 2006) correction with $\alpha = 0.01$). Similarly, High performance subjects had significantly greater LZc in centro-parietal electrodes during High TPC in comparison to Baseline (Fig. 2.3C right side). The opposite effect in low performance subjects did not reach statistical significance.

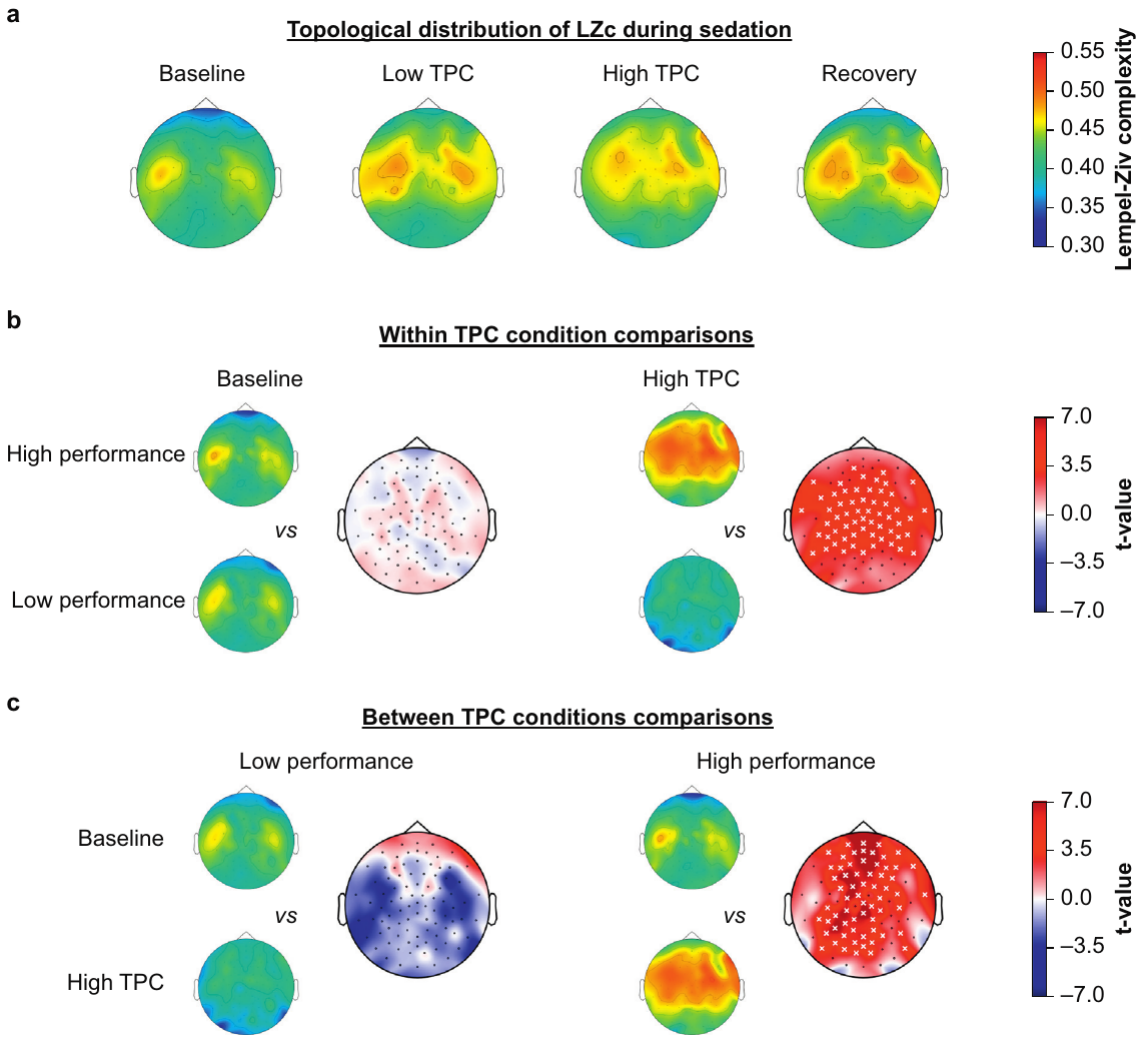

Figure 2.3: Topographical distribution of LZc during propofol sedation and its modulations by performance. **A**: Grand average topographical distribution of LZc during each sedation condition. Two bilateral parietal maxima can be seen for all conditions, and a lower LZc in frontal electrodes in the Baseline condition. **B**: Within sedation condition comparisons: For Baseline (left side) and High TPC (right side) we compared (independent t-test), for each electrode, the LZc values of High performance subjects versus Low performance subjects. Only High TPC showed significant differences between performance groups. **C**: Comparisons made between TPC conditions: For each performance group (Low performance, left side; High performance, right side), and for each electrode we tested the LZc values of Baseline versus High TPC conditions (paired t-tests). Only High performance subjects showed a significant difference between their Baseline and High TPC conditions. For A colour indicates LZc values. For comparisons in B and C subplots colours indicate t-values of statistical comparisons and white markers indicate significant differences after TSBKY FDR correction.

Finally, to further assess these topographical differences, we grouped electrodes into 4 regions of interest (ROI, see Methods) and calculated the averaged LZc for each one. We conducted a 3-way mixed factors ANOVA with ROI and TPC condition as within subject factors and performance as a between subject factor. We found significant main effects of condition, ROI, condition*ROI and condition*performance ($F = 6.10$, $p = 0.024$; $F = 22.83$ $p < 0.001$, $F = 14.53$, $p < 0.001$; $F = 5.37$, $p = 0.032$; respectively). Post hoc analyses showed that the increase in complexity of High performance subjects was primarily driven by frontal electrodes (Fig. 2.4A, $t = 5.79$, $p < 0.001$) and in a lesser degree by parietal ones ($t = 4.12$, $p = 0.035$). No difference was found for occipital electrodes in High performance subjects, nor for any ROI in Low performance subjects (Fig. 2.4B). Thus, our results indicate that, even though frontal regions do not show a particularly distinct complexity during Baseline, they are more responsive to propofol sedation (in High performance subjects) than any other brain area.

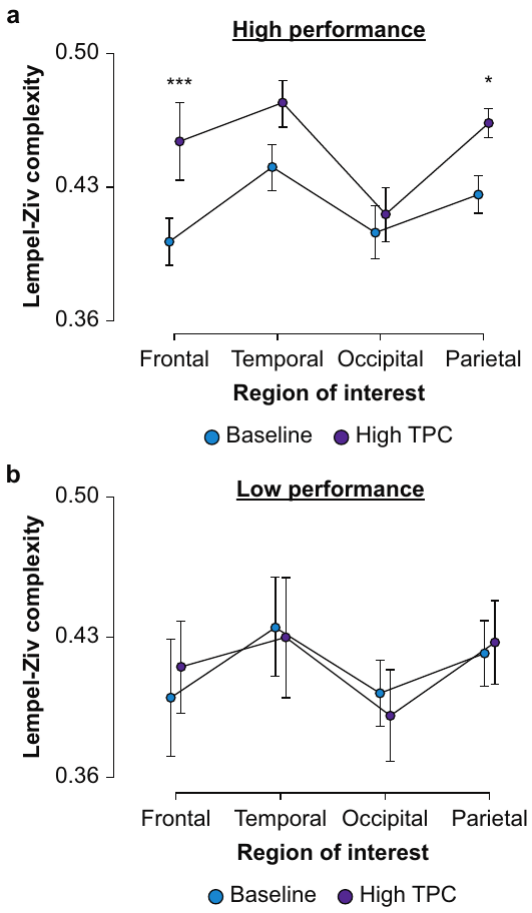

Figure 2.4: Region-specific reactivity of LZc to propofol sedation. **A**: LZc of High performance subjects for each ROI (see Methods and Supplementary Material 3 Fig. 2.6) during Baseline and during High TPC condition. The frontal ROI showed the greater differences between conditions. The parietal ROI also showed a significant increase of LZc due to propofol sedation. **B**: Low performance subjects did not show significant divergences of LZc values.

2.4 Discussion

In the present article we show that the complexity of brain activity, measured as the LZc of resting state EEG signals, can increase during propofol sedation. This increase was only observed in partially sedated subjects, i.e. those that maintained their performance, but not on those that significantly decreased their behavioural performance in a simple discrimination task. The raise in LZc during High TPC (1.2µg ml^{-1}) was not directly correlated with plasma propofol concentration (Fig. 2.1G), but with subject-specific propofol susceptibility (amount of

performance lost per unit of anaesthetic; Fig. 2.1H). As expected, LZc was in general correlated with the spectral power of specific frequency bands (negative correlation for low frequencies and positive for high frequencies). Interestingly, we found that eliminating the spectral power within any frequency band had no significant effect on the increase in LZc shown by High Performance subjects. We also observed topographical differences of this effect, being more marked for frontal and parietal areas, and absent in occipital cortices.

Previous research has repeatedly shown that LZc (or similar measures) decrease after LOC during sleep (Massimini et al., 2005) and during propofol (Zhang et al., 2001; Schartner et al., 2015) or xenon (Sarasso et al., 2015) anaesthesia. This has been stated as support for the Entropic Brain Hypothesis (Carhart-Harris et al., 2014) , which proposes that the complexity (entropy) of brain activity should directly reflect the complexity of states of consciousness (experience). This is consistent with reports of increased brain activity complexity during psychedelics (Timmermann et al., 2019) or ketamine (Sarasso et al., 2015) administrations. However, our results show that brain activity complexity increases, compared to normal wakefulness, without (clear) psychedelic or hallucinatory effects (Purdon et al., 2015), calling into question the proposed direct link between brain activity complexity and the complexity of states of consciousness or experience.

Interestingly, although we observed lower LZc values in frontal regions compared to other brain areas, frontal electrodes showed the most robust propofol-induced complexity increase in High performance subjects (Fig. 2.4A). In opposition, LZc in occipital (visual) cortices was not significantly modulated by propofol. This result fits in line with theories of consciousness like Global Neuronal Workspace Theory, which propose that the neural correlates of consciousness should be located in fronto-parietal associative cortices (Dehaene et al., 1998) . However, further evidence is required to reach a conclusion in this topic. The lack of effect over visual cortices seen here could also be related to the poor visual experiences of participants (eyes closed).

The general correlations between LZc and the spectral power of particular frequencies are to be expected based on simulations and experimental reports (Aboy et al., 2006; Bola et al., 2019; Schartner et al., 2017). However, here we show that the increase in EEG complexity for High performance subjects is not the mere reflection of an increase (or decrease) of power within any particular frequency range (Fig. 2.2C). Instead, we propose it is based on a modulation of

the broad temporal dynamics of different brain processes. One possible avenue of exploration, consistent with LZc showing both a negative correlation with low frequencies and a positive correlation with high frequencies (Supplementary Material 5 Figure 2.8), could be that brain activity complexity is related to 1/f modulations of broad ranges of the frequency spectrum in EEG signals (Medel et al., 2020; Colombo et al., 2019).

Non-linear relations between brain activity measures and anaesthesia have been previously reported. For example, Kuizenga and colleagues (2001) describe that delta and alpha-beta bands show biphasic changes in amplitude during anaesthesia induced by 4 out of the 5 drugs tested (including propofol), robustly increasing just before LOC, and only then decreasing. Propofol, and other anaesthetics, are known to produce what has been called paradoxical excitation at low doses, increasing neuronal activity in high frequencies (Ishizawa et al., 2016) . The term paradoxical is used given the fact that propofol is known to enhance inhibitory GABA A currents in cortical circuits. Mechanistic explanations for this have been proposed, suggesting that propofol would, via interactions with slow K + currents (M-currents), switch the state of interneurons from a synchronized to a more desynchronized state (McCarthy et al., 2008) . This is consistent with the increase in complexity or neural diversity observed in our results. In this line, we believe our results open several possible clinical applications of LZc, as an aid towards titrating sedative and anaesthetic doses, but also as a possible tool to quantify paradoxical excitation.

Limitations of the current study include the small sample size, and the lack of continuous measurement of EEG during transitions between full wakefulness and LOC. However, we believe the results presented here, in the context of others reported in the literature, robustly show that brain activity complexity does not always show a direct or simple relation towards subjects' behavioural performance (i.e. level of sedation; always diminishing in response to anaesthetics); namely because LZc can initially increase with respect to baseline during propofol infusion. Our results also suggest that LZc reflects broad modulations of brain activity, not simply related to frequency-specific spectral power modulations. We believe further research in this topic is required to better understand the relation between different markers of brain activity, states of consciousness and their behaviours during anaesthesia.

2.5 Supplementary Material

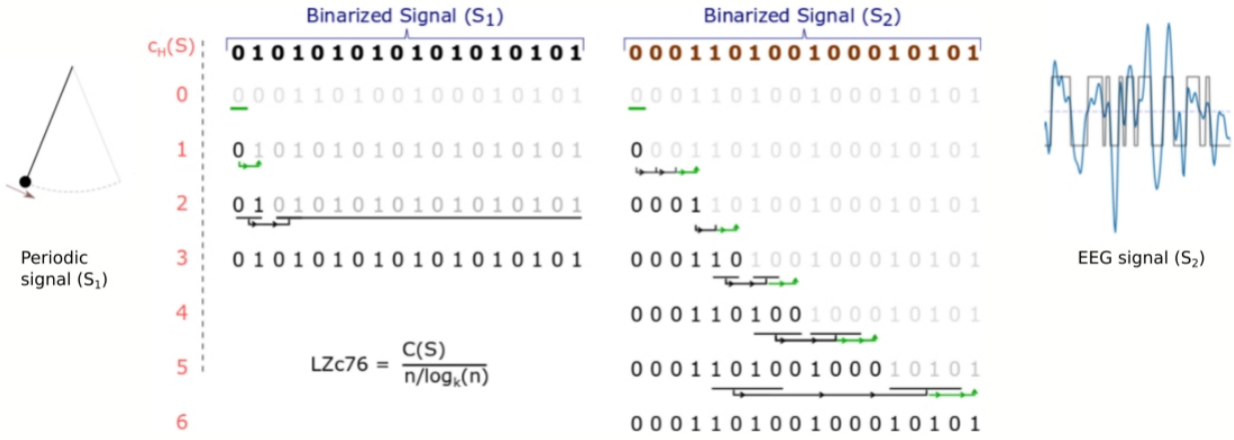

Figure 2.5: Illustration of LZc algorithm. LZc analyses as signal, step by step, by quantifying the number of production steps (green lines) required to recreate the original signal. When the signal being analysed is contained in (reproducible from) the previously analysed segment, no noverlty is found so only a reproduction required. Otherwise, a full production process is conducted. **Left**: A binary periodic signal can be recreated in just a few steps. The first symbol is always produced (CH is increased from zero to one). In the second step, the algorithm read '1' and as '1' cannot be reproduced (obtained) from '0' (the previously analysed sequence to that moment), it has to be produced (CH is increased from 1 to 2). Then, as '01', with a simple copying procedure can recreate the whole rest of the signal, (with a pointer = 2 and length = 16) the recreation of S1 is completed with 3 steps. **Right**: For a binary non-periodic signal we also begin by producing the first symbol. Then, as '0' and '00' can be reproduced from the previously observed part of S2. This symbol is '1', thus only then CH increases (CH = 2). Afterwards, as '1' can be reproduced from '0001', a process continues until the whole signal is recreated (analysed). It is noteworthy that the reproduction process does not need to occur from the end of the already analysed signal, but can take place from the middle (see row 6, CH(S2) = 5). The number of production processes, or equivalently the number of elements in the exhaustive production history of the signal, constitute the base of the LZc measure. LZc corresponds to this value, divided by n/logk(n) where n is the length of the signal and k is the number of possible symbols of the signal (2 for binary signals).

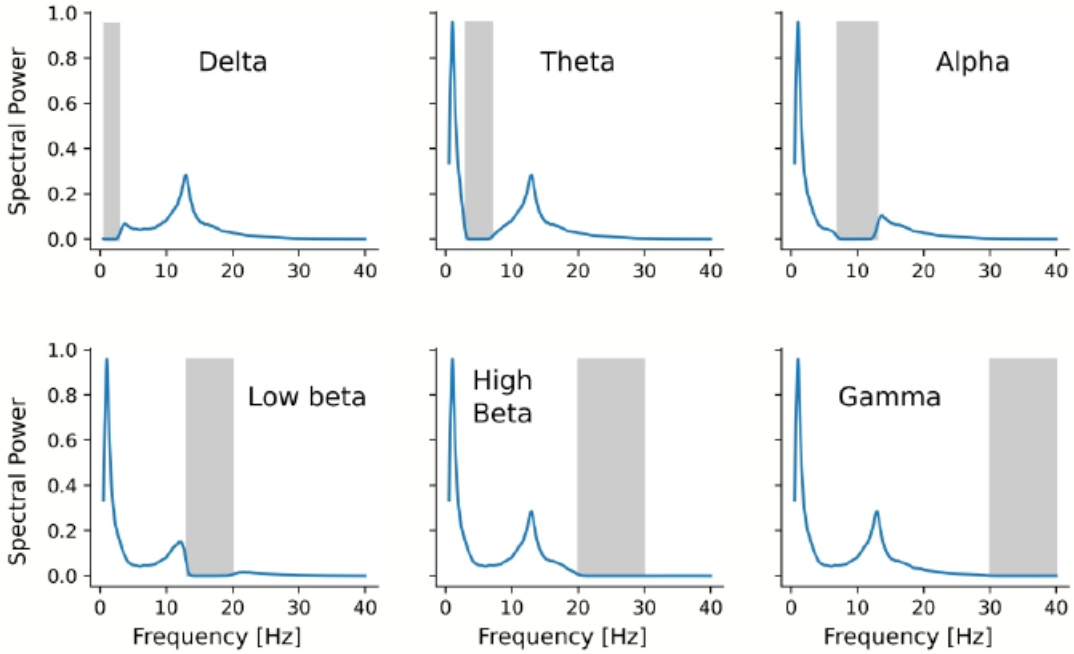

Figure 2.6: Illustration of Notch filters. Each panel depicts the Power Spectral Density plot after eliminating, via notch filter, the spectral power within specific frequency ranges. The frequency range is represented by gray rectangles. Lines correspond to the average normalized spectral power across all subjects, conditions, epochs and electrodes.

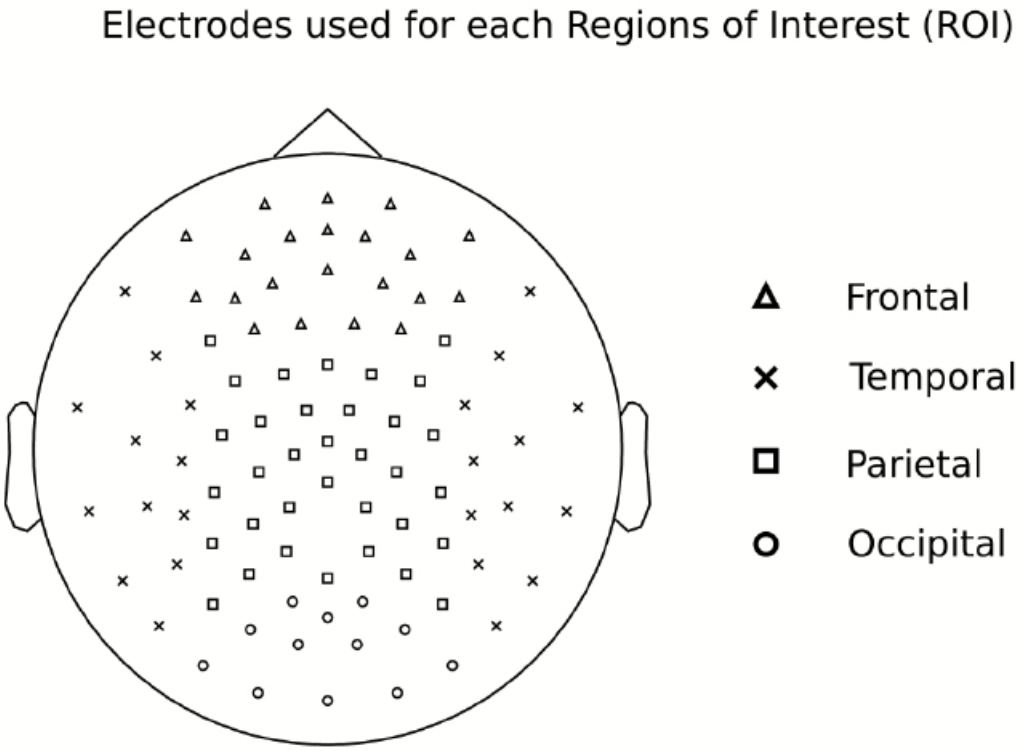
Electrodes used for each Regions of Interest (ROI)
Frontal
Temporal
Parietal
Occipital

Figure 2.7

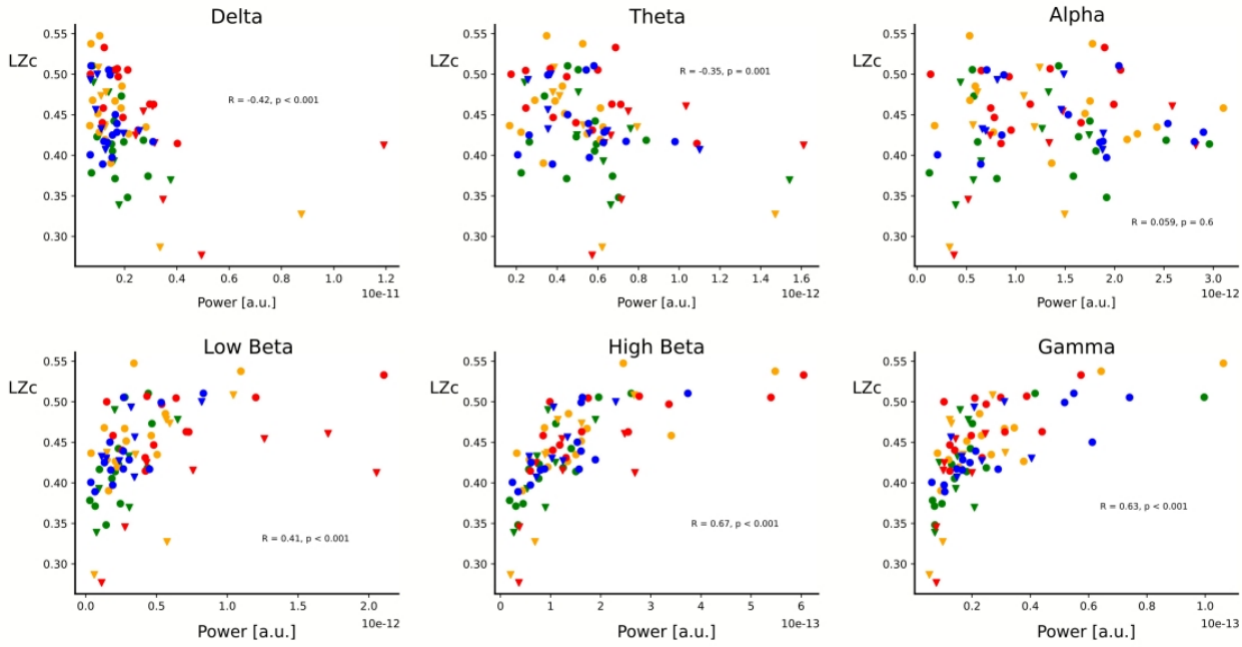

Figure 2.8: Lempel-Ziv Complexity vs Spectral Power per frequency band. Scatter plots showcasing the dependency of LZc with the spectral power of different frequency bands. Each data point depicts the average value for each subject and TPC condition.Circles indicate High performance subjects; Triangles indicate Low performance subjects. Colours indicate conditions: Green = Baseline, Orange = Low TPC, Red = High TPC, Blue = Recovery. Each plot also shows the results of a Pearson correlation. It can be broadly seen that LZc is negatively correlated with the power of low-frequency activity ($R < 0$), while it is positively correlated with the spectral power of high-frequency activity ($R > 0$).

Bibliography

[1] Bruhn J, Bouillon TW, Shafer SL. Bispectral index (BIS) and burst suppression: Revealing a part of the BIS algorithm. J Clin Monit Comput 2000; 16: 593–6

[2] Davidson AJ, Kim MJ, Sangolt GK. Entropy and bispectral index during anaesthesia in children. Anaesth Intensive Care 2004; 32: 485–93

[3] Feshchenko VA, Veselis RA, Reinsel RA. Propofol-induced alpha rhythm. Neuropsychobiology 2004; 50: 257–66

[4] Warner DS, Purdon PL, Sampson A, Pavone KJ, Brown EN. The Electroencephalogram and Brain Monitoring under General Anesthesia Clinical Electroencephalography for Anesthesiologists Part I: Background and Basic Signatures. Anesthesiology 2015; 123: 937–60

[5] Purdon PL, Sampson A, Pavone KJ, Brown EN. Clinical Electroencephalography for Anesthesiologists: Part I: Background and Basic Signatures. Anesthesiology 2015; 123: 937–60

[6] Zohar E, Luban I, White PF, Ramati E, Shabat S, Fredman B. Bispectral index monitoring does not improve early Recovery of geriatric outpatients undergoing brief surgical procedures. Can J Anesth 2006; 53: 20–5

[7] Akeju O, Pavone KJ, Thum JA, et al. Age-dependency of sevoflurane-induced electroencephalogram dynamics in children. Br J Anaesth 2015; 115: i66–i76

[8] Kaiser HA, Hirschi T, Sleigh C, et al. Comorbidity-dependent changes in alpha and broadband electroencephalogram power during general anaesthesia for cardiac surgery. Br J Anaesth 2020; 125: 456–65

[9] Tononi G. Consciousness as integrated information: A provisional manifesto. Biol Bull 2008; 215: 216–42

[10] Tononi G, Boly M, Massimini M, Koch C. Integrated information theory: from consciousness to its physical substrate. Nat Rev Neurosci 2016; 17: 450–61

[11] Sergent C, Dehaene S. Neural processes underlying conscious perception : Experimental findings and a global neuronal workspace framework. J Physiol 2004; 98: 374–84

[12] Dehaene S, Changeux JP, Naccache L, Sackur J, Sergent C. Conscious, preconscious, and subliminal processing: a testable taxonomy. Trends Cogn Sci 2006; 10: 204–11

[13] Shannon CE. A mathematical theory of Communication. Bell Syst Tech J 1948; 27: 379–423

[14] Lempel A, Ziv J. On the Complexity of Finite Sequences. IEEE Trans Inf Theory 1976; 22: 75–81

[15] Zhang XS, Roy R j., Jensen EW. EEG Complexity as a Measure of Depth of Anesthesia for Patients. IEEE Trans Biomed Eng 2001; 48: 1424–33

[16] Massimini M, Ferrarelli F, Huber R, Esser SK, Singh H, Tononi G. Breakdown of Cortical Effective Connectivity during Sleep. Science 2005; 309: 2228–32

[17] Sarasso S, Boly M, Napolitani M, et al. Consciousness and complexity during unresponsiveness induced by propofol, xenon, and ketamine. Curr Biol 2015; 25: 3099–105

[18] Dasilva M, Camassa A, Navarro-Guzman A, et al. Modulation of cortical slow oscillations and complexity across anesthesia levels. Neuroimage 2020; 224: 117415

[19] Chennu S, O'Connor S, Adapa R, Menon DK, Bekinschtein TA. Brain Connectivity Dissociates Responsiveness from Drug Exposure during Propofol-Induced Transitions of Consciousness. PLoS Comput Biol 2016; 12: 1–17

[20] Aboy M, Hornero R, Abásolo D. Interpretation of the Lempel-Ziv Complexity Measure in the Context of Biomedical Signal Analysis. IEEE. Trans. Biomed. Eng. 2006; 53: 2282–8

[21] Harris CR, Millman KJ, van der Walt SJ, et al. Array programming with NumPy. Nature 2020; 585: 357–62

[22] Gramfort A, Luessi M, Larson E, et al. MEG and EEG data analysis with MNE-Python. Front Neurosci 2013; 7: 267

[23] Cole S, Donoghue T, Gao R, Voytek B. NeuroDSP: A package for neural digital signal processing. J Open Source Software 2019; 4: 1272

[24] Schartner M, Seth A, Noirhomme Q, et al. Complexity of multi-dimensional spontaneous EEG decreases during propofol induced general anaesthesia. PLoS One 2015; 10: 1–5

[25] Shumbayawonda E, Tosun PD, Fernández A, Hughes MP, Abásolo D. Complexity changes in brain activity in healthy ageing: A permutation Lempel-Ziv complexity study of Magnetoencephalograms. Entropy 2018; 20: 1–16

[26] Yoav B, Krieger AM, Yekutieli D. Adaptive linear step-up procedures that control the false discovery rate. Biometrika 2006; 93: 491–507

[27] Carhart-Harris RL, Leech R, Hellyer PJ, et al. The entropic brain: A theory of conscious states informed by neuroimaging research with psychedelic drugs. Front Hum Neurosci 2014; 8: 1–22

[28] Timmermann C, Roseman L, Schartner M, et al. Neural correlates of the DMT experience assessed with multivariate EEG. Sci Rep 2019; 9: 1–13

[29] Dehaene S, Kerszberg M, Changeux JP. A neuronal model of a global workspace in effortful cognitive tasks. Proc Natl Acad Sci USA 1998; 95: 14529–34

[30] Bola M, Owlowski P, Plomecka M, Marchewka A. EEG signal diversity during propofol sedation: an increase in sedated but responsive, a decrease in sedated and unresponsive subjects. bioRxvi 2019

[31] Schartner MM, Pigorini A, Gibbs SA, et al. Global and local complexity of intracranial EEG decreases during NREM sleep. Neurosci Conscious 2017

[32] Medel V, Irani M, Ossandon T, Boncompte G. Complexity and 1/f slope jointly reflect cortical states across different E/I balances. BioRxiv 2020; 298497

[33] Colombo MA, Napolitani N, Boly M, et al. The spectral exponent of the resting EEG indexes the presence of consciousness during unresponsiveness induced by propofol, xenon, and ketamine. NeuroImage; 2019, 189: 631-644.

[34] Kuizenga K, Wierda JMKH, Kalkman CJ. Biphasic EEG changes in relation to loss of consciousness during induction with thiopental, propofol, etomidate, midazolam or sevoflurane. Br J Anaesth 2001; 86: 354–60

[35] Ishizawa Y, Ahmed OJ, Patel SR, et al. Dynamics of propofol-induced loss of consciousness across primate neocortex. J Neurosci 2016; 36: 7718–26

[36] McCarthy MM, Brown EN, Kopell N. Potential network mechanisms mediating electroencephalographic beta rhythm changes during propofol-induced paradoxical excitation. J Neurosci 2008; 28: 13488–504

[37] Welch TA. A technique for high-performance data compression. Computer 1984; 17: 8–19

Chapter 3

Interpreting the neuromodulation of 1/f aperiodic activity through the switch of adaptation currents

Abstract

Brain activity can switch between a variety of states that each have different effects on perception, cognition and behavior. Fluctuations in arousal and neural desynchronization are related to changes from innatentive to vigilant states. However, their relation and the underlying mechanisms relating them are unclear. Here, using in-silico modeling we show that changes in desynchronization -as indexed by 1/f slope- and arousal can be adressed by changing activity-dependent adaptation, which diminishes K+ channels. Predictions from the model are validated in three published data from two species (Macacque and human). We find that pharmacological decrease of noradrenergic modulation -which increases baseline activity-dependent adaptation- steepens the 1/f slope in invasive recordings. In contrast, pharmacological increase of arousal-related modulation increases neural desynchronization, as adressed by 1/f slope of the power spectrum. These results suggest that neural desynchronization is achieved by shifts in activity-dependent adaptation currents which can be modulated by arousal-related neuromodulation.

3.1 Introduction

To actively engage in ever changing environmental demands, animals dynamically switch between a variety of behavioral states that differentially affect neural responsiveness and the ability to optimally process information. Variations in these so-called "cortical states" have been studied at different timescales, ranging from slow changes occurring in the sleep-wake cycle (Lee and Dan, 2012), and at faster timescales during wakefulness where rapid switches from inattentive to vigilant state is required (McGinley et al., 2015). These switches are supported by a tightly controlled activity in brainstem neurons that diffusely release neuromodulators at their cortical target sites, shaping the neural activity at both meso (McCormick et al., 2020) and the macro scale (Shine, 2019).

Decades of research have characterized global electrophysiological patterns that depend on the cortical state of the animal. Classic electroencephalographic (EEG) studies have shown that the EEG has fast low-amplitude fluctuations when the animals are awake, and as the animal transits to sleep, the EEG starts to show increasing high-amplitude slow patterns (Harris and Thiele, 2011). Multi-scale approaches have revealed that high-amplitude slow EEG activity reflects synchronous cortical states, in which silent and highly active periods are alternated slowly (Steriade et al., 1993) while fast low-amplitude fluctuation corresponds to irregular firing and desynchronized EEG (Lee and Dan, 2012).

Computational approaches have shown that the range of firing patterns from synchronized to desynchronized, can be achieved by simulating a network of neurons with balanced excitatory and inhibitory synaptic activity (van Vreeswijk and Sompolinsky 1996; Brunel, 2000) modulated by activity-dependent adaptation on excitatory cells which dynamically close K+ channels (Nghiem et al., 2020; Goldman et al., 2020b; Zerlaut et al., 2018). From this perspective, in order to shape the so-called "default activity pattern" of cortical activity (Sanchez-Vives et al., 2017) and transition the cerebral cortex from a synchronized to desynchronized state, the brain depends on global variables, such as relative levels of excitation and inhibition (Haider et al. 2006) and the level of activity-dependent adaptation on excitatory populations (Goldman et al., 2020a; Zerlaut et al., 2017; Sanchez-Vives et al., 2017; D'Andola et al., 2018). Interestingly, there is strong evidence showing that extracellular application of common neuromodulators, such

as noradrenaline or acetylcholine, eliminates the activity-dependent adaptation seen by the injection of a depolarizing current. This evidence suggests that diminishing adaptation through neuromodulation could facilitate E/I balance (Nghiem et al., 2020) and suggests a mechanistic role of ascending arousal system in regulating E/I balance and cortical state.

A sensitive means for quantifying cortical state involves the background activity of the spectral power of brain field potentials. Specifically, models have shown that the background 1/f slope of the power spectral density (PSD) is well explained by the sum of stochastic excitatory and inhibitory currents (Sheehan et al. 2018; Destexhe et al. 2001; Gao et al., 2017). Moreover, by parameterizing the 1/f shape of the PSD, E/I balance can be directly inferred from background field potential activity (Gao et al., 2017; Trakoshis et al. 2020; Waschke et al., 2021; Colombo et al., 2019; Medel et al., 2020). These lines of evidence suggest a tractable hypothesis: that neuromodulatory tone should shape E/I balance, and hence, alter the 1/f slope of the PSD of field potentials.

To test this hypothesis we use both computational and empirical approaches to demonstrate the close relationship between activity-dependent adaptation and the 1/f slope of electrophysiological field potentials. First, we extend previous simulation approaches (Destexhe et al., 2001; Gao et al., 2017; Medel et al., 2020) by adding an activity-dependent adaptation parameter over inter-spike interval distributions and show that changing adaptation shapes the 1/f slope. Next, we test our computational predictions on two open datasets. The first dataset contains a Monkey (Macaca mulatta) local field potential (LFP) signal under dexmedetomidine (Ballesteros et al., 2020), a well known α_2-agonist that strongly decreases noradrenergic transmission by inhibiting locus coeruleus neurons (Nacif-Coelho et al., 1994; Jorm and Stamford, 1993; Chiu et al., 1995) and show that diminishing noradrenaline steepens the 1/f slope, putatively increasing adaptation. Next, we analyze human EEG data (Albrecht et al., 2016) of eyes-closed resting-state EEG with pharmacological manipulation of both dopaminergic and noradrenergic systems and show that increasing neuromodulation flattens the 1/f slope, putatively eliminating adaptation. These results suggest that arousal-related neuromodulators shape activity-dependent adaptation currents in the cerebral cortex shaping E/I balance.

3.2 Materials and Methods

Local Field Potential Simulations

We simulated cortical Local Field Potential (LFP) time series as a sum of excitatory and inhibitory point-conductances (Destexhe et al., 2001; Gao et al., 2017). Briefly, we obtained different inter-spike intervals (ISI) from independent Poisson processes with specified average rates and number of neurons for GABA-A and AMPA neurons and generated binary time series. The ISI distribution is described by white noise (Schwalger et al., 2010) which can capture ISI density (Schwalger et al., 2010) and satisfies the Poisson property that mean equals variance:

$$\mu = (FR * N_i) \tag{3.1}$$

$$\sigma^2 = \mu \tag{3.2}$$

$$ISI\ N(\mu, \sigma^2) \tag{3.3}$$

where μ, σ^2 are the mean and variance of the Poisson distribution, FR is the firing rate of the simulated population, and N is the number of simulated neurons. Sampled values with ISI ¡ 0 were set as 0. Each spike time s_k was then computed as the cumulative sum of the ISI vector of length K:

$$S_k = \sum_{i=1}^{k} ISI_i, for\ k = 1, 2, ..., K \tag{3.4}$$

These signals describe the firing rate of all simulated neurons. We discretized the spike train vector to obtain the firing rate at each time bin, defined as 1ms. To obtain synaptic signals we convoluted the discretized spike time series with empirically defined rise and decay time-constant conductance kernels for GABA-A and AMPA synapses (Gao et al., 2017; Destexhe et al., 2001; Supplementary Figure 3.4). The conductances of each neural population was obtained by convolving the discretized spike train vector B with a kernel resembling the synaptic conductance

function g:

$$G = (B * g(t)) \tag{3.5}$$

where the synaptic conductance function g that spans the time t is defined as

$$g(t) = -e^t/\tau_{rise} + e^t/\tau_{decay} \tag{3.6}$$

Finally, the LFP was computed as the sum of each synaptic current (Mazzoni et al., 2015; Destexhe et al., 2001), which were obtained by multiplying each conductance by the difference between the resting potential V_E and the typical reversal potential for GABA-A and AMPA receptors (see Supplementary Table 3.1) V_r.

$$LFP = I_E + I_I \tag{3.7}$$

$$LFP = G_E(V_E - V_r) + G_I(V_I - Vr) \tag{3.8}$$

The detailed parameters used in the LFP simulations can be found in Supplementary Table 3.1. Each simulated LFP time series consisted of 10 seconds with timesteps of 1 millisecond. We employed this modeling strategy due to the fact that it has been shown to capture amplitude and spectral characteristics of synaptic conductances observed in vivo (Destexhe et al., 2001), and has been previously validated as a tool to infer the E/I balance of cortical tissues (Gao et al., 2017).

Simulating Adaptation in Inter-Spike Interval distributions

We manipulated adaptation by shaping the ISI distributions drawn from the independent Poisson processes. Previous modelling and characterization work have shown that adaptation lowers the mean while increases the variance of the probability density function of the ISI (Ladenbauer et al., 2014). To simulate adaptation, we shaped the ISI distribution by using a modulated Poisson signal (See Methods), similar to known modulations of variance seen at in vivo conditions (Goris et al., 2010; Munn et al., 2020). We added adaptation to the ISI by modulating the

variance of the distribution:

$$\sigma^2 = \mu + \alpha \tag{3.9}$$

where μ, σ^2 are the mean and variance of the Poisson distribution, and α is the additive gain modulation term. Based on previous work (Ladenbauer et al., 2014; Nghiem et al., 2020; Barranca et al., 2018; Pozzorini et al., 2013), we applied adaptation effect only in excitatory and not inhibitory neurons, maintaining inhibitory neurons in the canonical relation of poisson-point processes where the mean equals the variance of the distribution.

Power Spectral Density and Aperiodic 1/f Analysis

We calculated the Power Spectral Density (PSD) using Welch's method of the Fourier Transform as implemented in the MNE toolbox (Gramfort et al., 2014; Jas et al., 2018). We parameterized periodic and aperiodic components of the PSD using the *"Fitting Oscillations& One Over f"* (FOOOF) toolbox (Donoghue et al., 2020). The FOOOF algorithm decomposes the log PSD into a summation of narrowband Gaussian periodic (oscillations) and aperiodic (1/f offset and slope) components for the whole frequency range. The algorithm estimates periodic and aperiodic components, removes the periodic ones and estimates again until only the aperiodic components of the signal remain. This allows for estimation of offset and power-law slope with considerable independence from oscillatory behavior, which is particularly important for empirical signal analysis (Donoghue et al., 2020; Voytek & Knight, 2015). FOOOF toolbox also contains a "knee" parameter, which was not considered as it corresponds to changes in the 1/f slope at higher frequencies that were not analyzed in this study. We set the algorithm with peak width limits: [1-8], maximum number of peaks: 6; peak threshold 1.5; and 'fixed' aperiodic mode. Power spectra were parameterized across the frequency range 20 to 70 Hz in simulated data, 10 to 50 Hz in LFP and 20 to 40 Hz in EEG.

LFP Data

We analyzed an open dataset of one monkey with extracellular microelectrode arrays (Ballesteros et al., 2020) implanted in the primary somatosensory cortex (S1) and the ventral premotor

area (PMv). Each array contained 16 (S1) or 13 (PMv) platinum-iridium recording microelectrodes separated by 400 μm and had a total size of 1.95 $\times$ 2.5 mm. Analog data were amplified, band-pass filtered between 0.5 Hz and 8 kHz and sampled at 40 kHz. LFPs were filtered with a low-pass filtering at 200 Hz and down-sampled at 1 kHz.

Dexmedetomidine was infused for a total 60 min at 18 μg/kg/h for the first 10 min. The infusion rate of dexmedetomidine was determined to induce loss of consciousness (LOC) in approximately 10 min. A behavioral task was used to monitor the animal's arousal. LOC was defined as the time at which the probability of task engagement was decreased to less than 0.3 (Mukamel et al., 2014). The monkey had 3 sessions of dexmedetomidine infusion. In Figure 3.2 we report average result of all sessions, and each session's results can be found in Supplementary Figure 3.5.

The original paper (Ballesteros et al., 2020) was focused on the relation between task performance and the transition between loss of consciousness (LOC), return of consciousness (ROC) and the abrupt wakefulness induced by the α^2 antagonist. As the periods of consciousness of the original dataset are based on behavior alone and not on plasma concentration of dexmedetomidine, and as we are mainly interested in the acute effect of decreased noradrenaline transmission, in this work we only focus on Awake and LOC periods.

EEG Data

We analyzed an open dataset of human resting-state EEG (Albrecht et al., 2016). The data consisted in twenty-eight healthy participants (14 male and 14 female) with mean age of 25 years. Participants were administered either dexamphetamine or placebo in a counterbalanced order: 14 participants received placebo on first the week and dexamphetamine in the second week, while 14 participants received dexamphetamine first and placebo second. With a dose of 0.45 mg/kg and a mean participant weight of 71 kg, the average dexamphetamine per person was 32 mg which was orally administered. Participants came to the centre for two testing sessions, 1 week apart. The resting state procedure testing began at 200 min post dose, shortly after the reference peak dexamphetamine concentration for oral administration of 25 mg (Asghar et al., 2003). This is also close to the peak time of the autonomic effects of dexamphetamine (Albrecht

et al. 2011).

The EEG was recorded at 1 kHz with a Neuroscan 32-channel system according to the extended 10–20 system using an Ag/AgCl electrode cap that included vertical and horizontal electrooculograms. Data was segmented into 2 s non-overlapping epochs and baseline-corrected using the entire epoch. The average number of epochs used after artifact rejection for the dexamphetamine and placebo conditions respectively, were 57 (dexamphetamine) and 59 (placebo) epochs per person. We used eyes-closed resting-state data, where participants were instructed to relax as much as possible (to reduce muscle artefacts) and limit eye movements during 4 minutes. For repeated-measure analysis at the subjects level, we selected ROIs based on electrode comparison (Figure 3.3C) and literature (Arnsten, 1998). The selected ROIs were frontal electrodes corresponding to FP1, FP2, F3, F4, F7, F8, FZ, FCZ, FC3, FC4, FT7, FT8. Further preprocessing and experimental details can be found in the original paper (Albrecht et al., 2016).

Statistical Analysis

Experimental data was visualized using a python implementation of raincloud plots (Allen et al., 2021; van Langen, 2020) and topoplot from open-source python package MNE (Gramfort et al., 2014; Jas et al., 2018). The relation between 1/f slope and adaptation was calculated using nonparametric Spearman rank-order correlation coefficient (Figure 3.1D). Aperiodic 1/f slope differences between awake and dexmedetomidine were assessed by repeated measures ANOVA using the mean values of each electrode across sessions (Figure 3.2C, D). Topographic differences among groups in 1/f slope (Figure 3.3C) were assessed using Wilcoxon signed-rank test, which is a non-parametric version of the paired T-test. Differences among groups in 1/f Slope in the region-of-interest (ROI) across subjects (Figure 3.3D) were assessed by repeated measures ANOVA, Group (Placebo, Dexamphetamine) and Session (First, Second) where used as levels. All reported p-values were corrected by multiple comparison.

3.3 Results

To explore the role of adaptation in 1/f slope of field potentials, we used a previously validated simulation of synaptic background activity of LFP based on independent excitatory and

inhibitory point-conductances (Destexhe et al., 2001; Gao et al., 2017; Medel et al., 2020; See Methods). As it has been shown previously with these models we observe that the log-log of the PSD follows a decaying 1/f power law for frequencies past 20 Hz (Figure 3.1C) which directly results from the addition of the different rise and decay time constant profiles of AMPA and GABA-A currents (Gao et al., 2017; Destexhe and Rudolph, 2004). It has been shown with the same model that artificially disrupting the excitation and inhibition balance changes the 1/f slope of the power law (Gao et al., 2017).

We next added an adaptation parameter that replicated the effects of adaptation over the variance of the ISI distribution (Schwalger et al., 2010; Ostojic, 2011; Ladenbauer et al., 2014) we used an additive gain modulation α over the Poisson-like white noise that constructed the ISI distribution (Figure 3.1A; See Methods). We generated 30 LFP time series with different α (Figure 3.1B) ranging from 0 to 0.3 with 50 repetitions each. Next, we calculated the power spectral density of each signal and calculated the spectral parameter of 1/f slope (Donoghue et al., 2020).

Consistent with the unaltered model (Destexhe et al., 2001; Gao et al., 2017; Trakoshis et al., 2020), we found that manipulating α did not change global structure of the PSD. However, we found a robust modulation of the 1/f slope towards higher values (steeper slope) as α increased (Figure 3.1C). Next, we averaged the aperiodic values of the 50 repetitions in each α gain level and found that both signals were highly correlated (rho = 0.993, $p<0.001$; Figure 3.1D). Our result shows that adding variance to the ISI distribution -our proxy to adaptation- steepens the 1/f slope. This showcases the relation between excitatory synaptic adaptation and 1/f slope in silico.

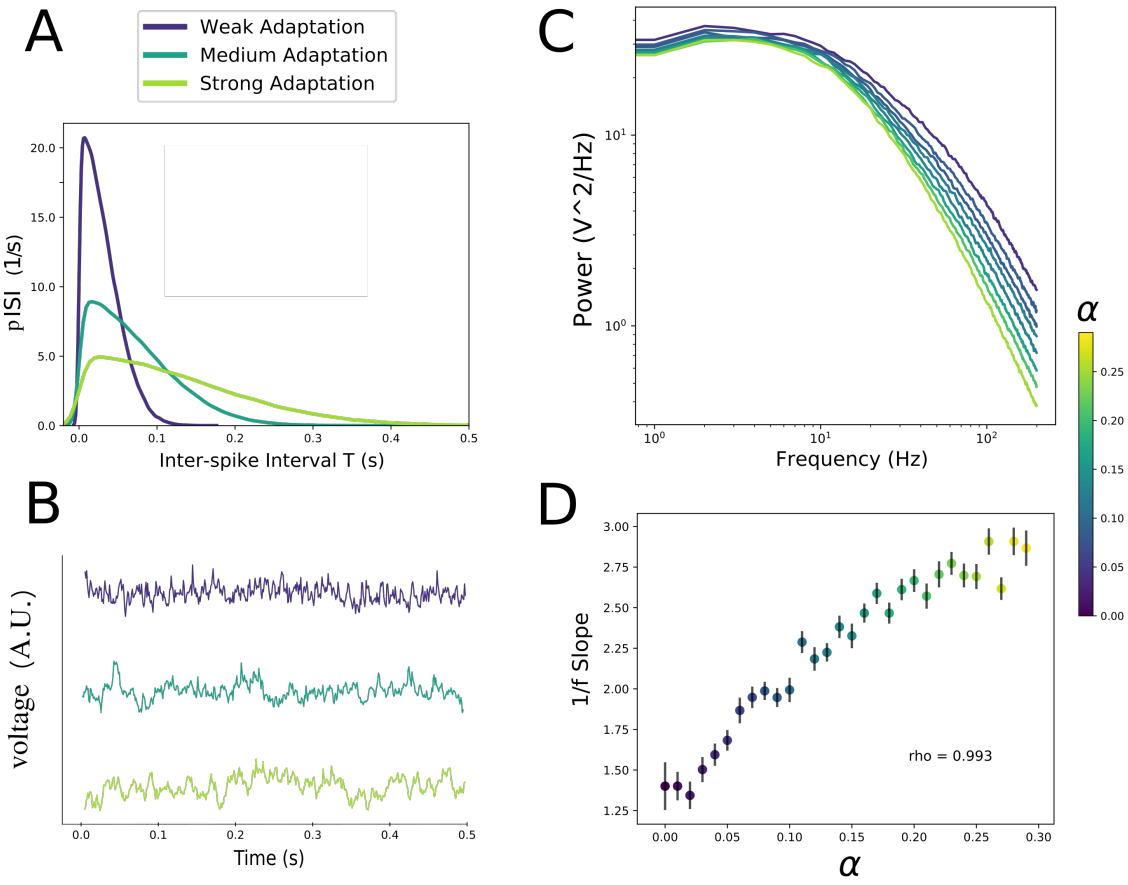

Figure 3.1: LFP simulation shows a tight relation between adaptation (α) and 1/f Slope. ***(A)*** Inter-spike Interval distribution for different adaptation α . Replicated from Ladenbauer and cols. (2014). ***(B)*** Voltage traces of 0.5 seconds of simulated signals with different α. Colors are the same as for panel A. ***(C)*** Power spectral density of the simulated signals with different α, denoted by the colorbar. ***(D)*** Scatter plot of the 30 α values averaged across the 50 simulation repetitions. Lines denotes the standard error of the mean and color the level of α. The inner panel shows the Spearman rank-order correlation coefficient.

Next, we asked whether the steepening of the 1/f slope due to the increase of adaptation seen in our model could be reproduced in electrophysiological data by decreasing the neuromodulation of the ascending arousal system. To test this hypothesis, we analyzed an open dataset (Ballesteros et al., 2020) of monkey LFP under dexmedetomidine anesthesia with two microelectrode arrays implanted in the primary somatosensory cortex (S1) and the ventral premotor area (PMv) (Figure 3.2A). Dexmedetomidine differs from common anesthetics many of which

act by increasing inhibitory postsynaptic currents through GABA receptor targeting (Nelson et al., 2002). Instead, it selectively targets α_2a adrenergic receptors altering the level of arousal by reducing the firing rate of the locus coeruleus, thus diminishing noradrenergic tone in the cortex (Correa-Sales et al., 1992; Jorm and Stamford, 1993; Chiu et al., 1995), possibly due to selectively targeting postsynaptic α_2a receptors on noradrenergic neurons (Gilsbach et al., 2009; Hu et al., 2012).

Consistent with well-known effects of dexmedetomidine over extracellular potentials, we found that decreasing noradrenergic neuromodulation shifted LFP signals towards a highly synchronized signal (Figure 3.2B), with a clear slow oscillation similar to N2 sleep stage (Akeju et al., 2016). Next we calculated the PSD of awake and dexmedetomidine conditions across the 3 sessions of sedation and found that both PMv and S1 showed a clear increase in low-frequency and decrease in high-frequency power (Figure 3.3C, D left panel). We then calculated the 1/f slope by parameterizing the power spectra (see Methods) in each session and electrode. As predicted, 1/f slope becomes significantly steeper for S1(for mean sessions, $F = 346.572$, $p < 0.001$ Bonferroni Corrected, $\eta_2 = 0.959$) as well as in PMv (for mean sessions, $F = 165.443$, $p < 0.001$ Bonferroni Corrected, $\eta_2 = 0.932$) when decreasing noradrenergic transmission (Figure 3.3C, D right panel), which suggests that increased adaptation due to a decrease of noradrenergic neuromodulation steepens the 1/f slope.

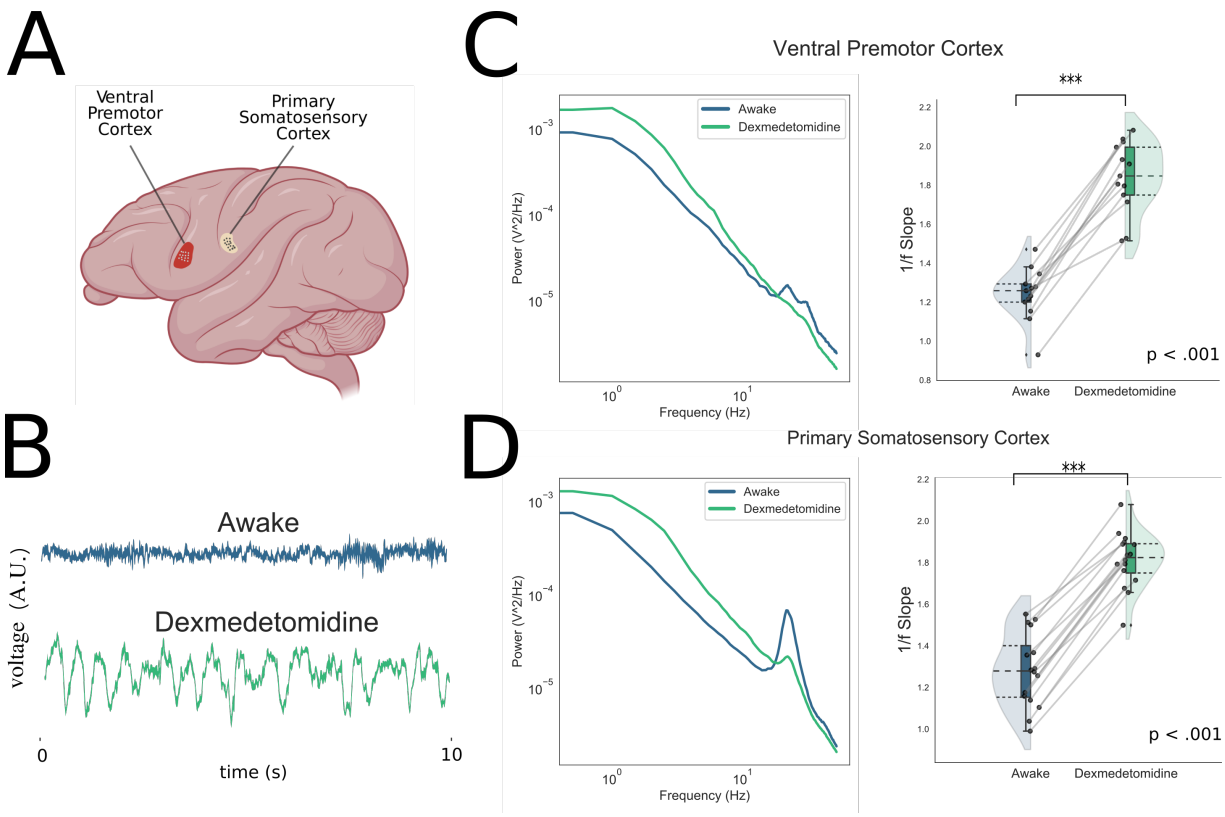

Figure 3.2: Decrease in noradrenergic neuromodulation by dexmedetomidine steepens 1/f Slope in intracortical Monkey LFP. ***(A)*** Location of the microelectrode implantation sites. Analyzed neural recording was performed in the Ventral Premotor Cortex (PMv, red) and the Primary Somatosensory Cortex (S1, beige). ***(B)*** Example voltage of 10 seconds traces from S1 under awake (blue) and dexmedetomidine (green) conditions. (***C***, ***D***) Left panel show the PSD of a representative electrode in PMv ***(C)*** and S1 ***(D)*** in awake and dexmedetomidine conditions. In the right panel, repeated-measure raincloud plot of the 1/f average across sessions depicting the differences between electrodes in awake and dexmedetomidine conditions. See Supplementary Figure 3.4 for dissagregated results by session.

Transitions from synchronized to desynchronized state are likely supported by an increase in arousal-related neuromodulation which would diminish adaptation and, thus, tighten E/I balance (Harris and Thiele, 2011; Lee and Dan, 2012; Waschke et al., 2021). Intermediate levels of arousal -such as spontaneous awake resting state- would recruit only baseline levels of neuromodulation and thus have intermediate levels of adaptation, which might be decreased by increasing arousal or pharmacologically increasing arousal-related neuromodulation. This decrease of adaptation should conclude in a flatter 1/f slope as compared to resting-state baseline conditions. We test this hypothesis by analyzing an open dataset of human resting-state EEG (Albrecht et al., 2016)

with dexamphetamine, a monoaminergic agonist which inhibits the monoaminergic transporters, mainly noradrenergic and dopaminergic transporters (Rizzo and Gulisano, 2013), thus increasing noradrenergic and dopaminergic neurotransmission.

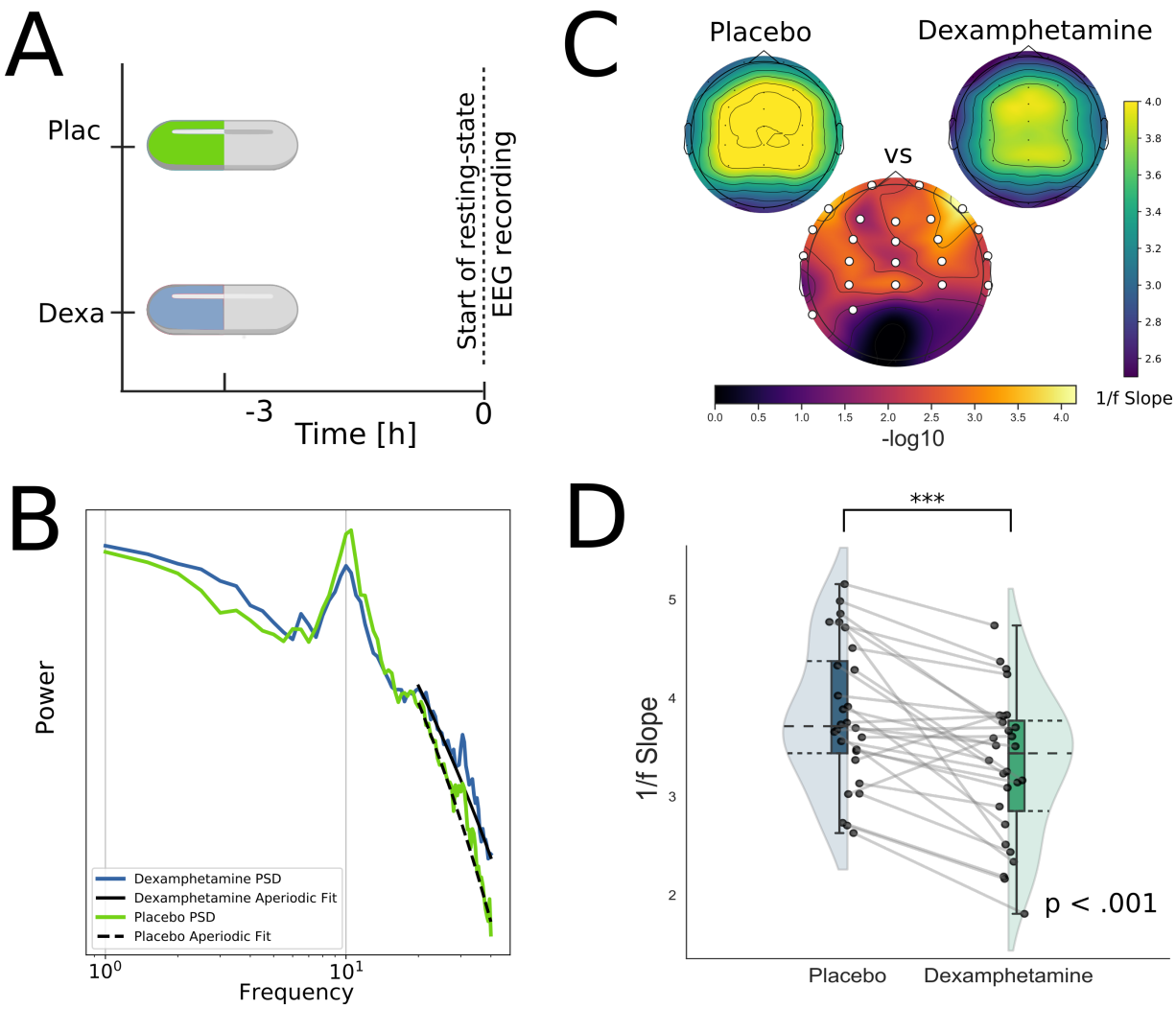

Figure 3.3: Increase in noradrenergic and dopaminergic neuromodulation by dexamphetamine flattens the 1/f Slope in Humans eyes-closed resting-state EEG. ***(A)*** Types and time course of the experimental session. Each subject participated in two sessions, involving the administration of placebo (green) and dexamphetamine (blue) (1 week apart, counterbalanced order). ***(B)*** Example of single-subject power spectral density from FZ electrode. In light green placebo conditions, and blue depicts dexamphetamine. Solid black line shows the 1/f aperiodic fit for dexamphetamine, while the dashed black line shows placebo aperiodic fit. ***(C)*** Upper topoplots show the grand average topological distribution of 1/f slope during placebo (left) and dexamphetamine (right). Central maxima can be seen for both conditions. Bottom topoplot represents Wilcoxon signed-rank test for each electrode in -log10 p-values for better visualization. White dots represent statistically significant values after FDR multiple comparison correction ($p<0.05$). ***(D)*** Average on frontal ROIs (see Methods) with repeated-measure raincloud plot of the 1/f average across subjects ($p<0.001$, Bonferroni corrected). Each dot represents a subject and the gray line connects the same subject in the different conditions.

The resting state procedure testing began at 200 min post dose (Figure 3.3A), shortly after the reference peak dexamphetamine concentration for oral administration of 25 mg (Asghar et al., 2003). This is also close to the peak time of the autonomic effects of dexamphetamine (Albrecht et al. 2011). We transformed the signal to the frequency domain and analyzed the PSD of the subjects. Notably, we found that at higher frequencies (>20) there was a clear 1/f power law decay (Figure 3.3B). Next, we compared topographic distribution of the 1/f slope in the high-range (see Methods) from placebo and dexamphetamine group and found a topographical distribution with the highest values (steeper slope) in central electrodes, while lesser values (flatter slope) in frontal and occipital areas (Figure 3.3C, upper panels). Although the differences in 1/f slope were distributed across the scalp, the main differences between conditions (Wilcoxon signed-rank test for each electrode, FDR corrected $p<0.05$) were in frontal and central areas (Figure 3.3C, lower panel). This is consistent with previous evidence showing the acute effect of dexamphetamine on frontal and central areas (Arnsten, 1998). In order to explore the robustness of change across subjects, we selected a broad region-of-interest including frontal and central electrodes (See Methods) and average them to obtain a mean value per participant in both conditions. We found that dexamphetamine flattened the 1/f slope (Figure 3.3D) independent of session order (Condition effect $F = 19.398$, $p < 0.001$ Bonferroni Corrected, $\eta_2 = 0.160$; Session effect $F = 0.4$, $p = 0.448$, $\eta_2 = 0.03$, Condition*Session effect $F = 8.758e\text{-}5$, $p = 0.993$, $\eta_2 = 3.664e\text{-}6$) which suggests that decreased adaptation due to an increase of arousal-related neuromodulation flattens the 1/f slope.

3.4 Discussion

In the current work, we tested the hypothesis that the ascending neuromodulatory system shapes the aperiodic 1/f slope of field potentials from the cerebral cortex of both monkey and human participations. Within our framework, adaptation is diminished by monoaminergic neuromodulation and thus prevents the endogenous closure of K+ ion channels (McCormick and Williamson, 1989). This mechanism thus putatively maintains E/I balance (Nghiem et al., 2020). We first tested this mechanism by developing a simple modelling strategy of background LFP signals with E/I balance based on ISI distribution with an adaptation parameter on excitatory

neurons which adds variance to the ISI histogram (Figure 3.1A; See Methods). When calculating the aperiodic activity of the simulated signals, we found that increasing adaptation robustly steepened the 1/f slope of the PSD. We next showed that the steepening of the 1/f slope due to the increase of adaptation seen in our model was reproduced in in vivo intracranial LFP data (Ballesteros et al., 2020). Specifically, the aperiodic 1/f slope was decreased by the administration of dexmedetomidine (Figure 3.2), which decreased noradrenergic signaling by inhibiting the spiking activity within the locus coeruleus (Nacif-Coelho et al., 1994; Jorm et al., 1993; Chiu et al., 1995). Finally, we show that pharmacologically increasing arousal-related neuromodulation with dexamphetamine induced a flatter 1/f slope (Figure 3.3) in human scalp EEG data (Albrecht et al., 2016). Our results suggest a mechanistic role of ascending neuromodulatory arousal system in shaping aperiodic signal and neural variability through the switch of activity-dependent adaptation currents.

Activity-dependent adaptation can be related to several biophysical mechanisms (Benda and Herz, 2003). Recent work has shown that spike-triggered and subthreshold adaptation have different effects on threshold, gain and spike train statistics (Ladenbauer et al., 2014). However, the reported biophysical mechanisms and types of adaptation all include a form of slow negative feedback to the excitability of the cell. Moreover, it has been shown that increasing spike-triggered or subthreshold adaptation both lead to activity-dependent adaptation as shown by the gradual increase of the ISI, represented by an increase in the variance of the ISI distribution (Liu et al., 2001; Schwalger et al., 2010; Ladenbauer et al., 2012; Ladenbauer et al., 2014). From this perspective, our approximation is a simple yet well supported strategy to simulate adaptation as ISI distributions on point-conductance based signals (Destexhe et al., 2001).

It has been proposed that adaptation is a key element supporting the"default activity pattern" of cortical activity (Sanchez-Vives et al., 2017). The bistable dynamics that emerge at high levels of adaptation have been suggested as the mechanism that triggers the transition from Up to Down states in the synchronized state (Sanchez-Vives et al., 2017; Zerlaut et al., 2017). Recent evidence has proposed that two types of synchronized activity can be seen as a function of adaptation, which switch from high adaptation anesthesia-like to sleep-like slow waves with lower adaptation due to endogenous neuromodulatory control (Nghiem et al., 2020). Moreover, the authors show that the highly regular synchronized state can be transitioned to a more sleep-

like synchronized state by adding arousal-related neuromodulation (Nghiem et al., 2020). This is consistent with recent evidence showing that adding arousal-related neuromodulation in cortical slices in vitro increases increases the complexity of the signal as compared to spontaneous slow oscillation and the high-excitability state with kainate (D'Andola et al., 2018). Moreover, computational evidence showing that the effect of adaptation on adaptive exponential integrate-and-fire neurons as well as in more realistic Hodgkin-Huxley-based neurons show an increase in global synchronization and neural coupling (Ladenbauer et al., 2012), and also promotes periodic signals facilitating network-based oscillations (Augustin et al., 2013).

There are several studies indicating that dexmedetomidine-induced sedation depends on the inhibition of locus coeruleus neurons (Nacif-Coelho et al., 1994; Jorm et al., 1993; Chiu et al., 1995). Interestingly, recent evidence has shown locus coeruleus exhibited an increased functional connectivity to the brainstem while a decreased connectivity to the cortex in dexmedetomidine condition (Song et al., 2017). This is complementary with results from the same group reporting a decreased metabolic response accompanied with a decreased thalamic functional connectivity with posterior cingulate cortex (Akeju et al., 2014). Consistent with these findings, increasing arousal-related neuromodulation through dexamphetamine can induce reanimation from general anesthesia (Kenny et al., 2015). Increasing arousal-related neuromodulation also shapes large-scale correlations (reviewed in van den Brink et al., 2019) which has topological dynamics sensitive to cognitive demands (Shine et al., 2018). Similarly, evidence has shown that the effect of acute dexamphetamine can reduce the connectivity in the default-mode network (Schrantee et al., 2016), while amphetamine can increase brain signal variability in BOLD fMRI during a working memory task (Garret et al., 2015).

When interpreting the role of neural variability in optimal behavioral state (McGinley et al., 2015), it should be considered that background noise fluctuations can serve as gain modulators of information in the cortex where the addition of noise can enhance neural responsiveness (Chance et al., 2002; Zerlaut et al., 2017; Destexhe et al., 2003). Moreover, it has been shown that synaptic background activity controls information transfer from thalamus to cortex (Wolfart et al., 2005). Interestingly, activity-dependent adaptation represents a cellular mechanism of the modulation of response gain associated with selective attention (McAdams and Maunsell, 1999). Moreover, arousal-related neuromodulators contribute substantially to attentional upregulation

of neural excitability (Herrero et al., 2009) which is likely produced via downregulation of activity-dependent adaptation which decreases K+ currents (Madison et al., 1987; McCormick, 1992; Sripati and Johnson, 2006).

Neuromodulation is known to play a key role in cortical plasticity (Sara and Segal, 1991), which in turn has been proposed to affect E/I balance (Murphy and Miller, 2003; Froemke, 2015) by suppressing ongoing inhibitory inputs to pyramidal cells (Martins and Froemke, 2015). This framework has been used to develop whole-brain modelling with local changes of E/I balance induced by increased neuromodulation (Pfeffer et al., 2020). Our work could be understood as complementary to this perspective, as it points out an alternative approach which considers that the decrease in excitation due to activity-dependent adaptation can increase inhibitory gain (Nghiem et al., 2020), thus shaping E/I balance. This is funded in the well-known experimental observation that pyramidal neurons are typically more likely to undergo adaptation than inhibitory neurons, where the latter appear to have absent adaptation response (La Camera et al., 2006; Augustin et al., 2013; Barranca et al., 2019). Our approach also differs from previous theoretical evidence suggesting that spike-frequency adaptation exhibits a necessary attenuation over excitatory neurons in order to maintain balanced dynamics (Barranca et al., 2019). We here have a different theoretical focus, as we wanted to study effect on neural variability and aperiodic 1/f signal in balanced activity as the initial condition, where the number of excitatory neurons was higher than inhibitory, but inhibition was faster (See Methods; Supplementary Table 3.1).

The slope of the spectral power law has been extensively related to E/I balance (Lombardi et al., 2017; Gao et al., 2017; Colombo et al., 2019; Trakoshis et al., 2020; Medel et al., 2020; Washcke et al., 2021). It is important to note that the 1/f parametrization (Donoghue et al., 2020) can model other two parameters that were not explored in this work: the 'knee' which is related to the timescale of the signal (Gao et al., 2020); and the 'offset' which is the intercept of the 1/f function, and represents the broadband signal (Manning et al., 2009; Ossandón et al., 2011). Although ISI distributions and the autocorrelation function have been shown to be analytically related (Gerstner and Kistler, 2002) they can present qualitatively different features in each different explored regime (Ostojic, 2011) which suggest a more complex relation that has to be further explored and are beyond the scope of this work. We recently showed that E/I balance is tracked specifically by 1/f slope and not offset, and that the aperiodic slope

was intimately related with Lempel-Ziv complexity (Lempel and Ziv, 1976; Medel et al., 2020) which is an information-based measure calculated in the time domain and reflects the vastness of repertoire of brain activity patterns (Wenzel et al., 2019). Other measures have reported similar relations with 1/f aperiodic signal and E/I balance, namely entropy-based measures (Waschke et al., 2019) and memory-based signals such as Hurst exponent (Trakoshis et al., 2020). Considering the robustness of the spectral parameterization in separating oscillatory from aperiodic signal in the frequency domain, further work should explore how each of these similar measures in the temporal domain relate in a broad parameter space and conditions.

Animals interact with the dynamic nature of the world with a high temporal resolution that is supported by a tightly controlled ascending neuromodulation. Our results could be interpreted as a possible mechanism where selective top-down allocation of attentional resources recruit ascending neuromodulation, which may rapidly eliminate adaptation thus providing a tighter E/I balance and the necessary desynchronized cortical state to process high-level information. Note that this hypothesis can be understood as complementary with recent proposed neural mechanisms controlling attention-related shifts in neural variability (Harris and Thiele, 2011; Washke et al., 2021). Placing our findings into the perspective of cognition, it appears as highly relevant to characterize the dynamic shaping of 1/f aperiodic activity by ascending neuromodulators on a finer temporal scale. In fact, recently it was shown that a single dose atomoxetine -a selective noradrenergic agonist- shapes a neural variability measure during perception of ambiguous visual stimuli (Pfeffer et al., 2018). This is consistent with evidence that show aperiodic measures implicated in neuromodulator-related psychiatric disorders such as ADHD (Robertson et al., 2019; Pertermann et al., 2019; Ostlund et al., 2021) and ASD (Trakoshis et al., 2020; Bruining et al., 2020). as the level of background neural activity (Voytek and Knight, 2015) as physiological markers of network dynamics. Even though pharmacological interventions are ideal to elucidate the acute effect of arousal-related neuromodulation on cortical states, they fail to describe its dynamic nature. Given the well-established role of the locus coeruleus in driving cortical states and pupil diameter (Aston-Jones and Cohen, 2005; Joshi et al., 2016; Yüzgeç et al., 2018), the analysis of the pupil appears as an excellent candidate to relate endogenous time-varying neuromodulation levels with brain states (Vinck et al., 2015; Reimer et al., 2016; Wainstein et al., 2017; Medel et al., 2019). Extending our results using non-invasive measures of arousal-related

neuromodulation such as pupillometry would give a broader understanding of how neuromodulators temporally interact with brain state fluctuations and cognition. This could potentiate future research to further understand the mechanisms underlying switches in cortical state (McGinley et al., 2015) and understand the functional dynamics underlying several neuromodulator-related psychiatric disorders, as well as to pave the path to design targeted therapeutic strategies.

3.5 Supplementary Material

Neuron Type	Parameter Name	Value
E & I	Resting Membrane Potential	-65 mV
E	Population Size	8000
E	Population Firing Rate	2 Hz
E	Reversal Potential	0 mV
E	Conductance Time Rise	0.1 ms
E	Conductance Time Decay	2 ms
E	Adaptation α	varies
I	Population Size	2000
I	Population Firing Rate	5 Hz
I	Reversal Potential	-80 mV
I	Conductance Time Rise	0.5 ms
I	Conductance Time Decay	10 ms

Table 3.1: Local Field Potential model Parameters

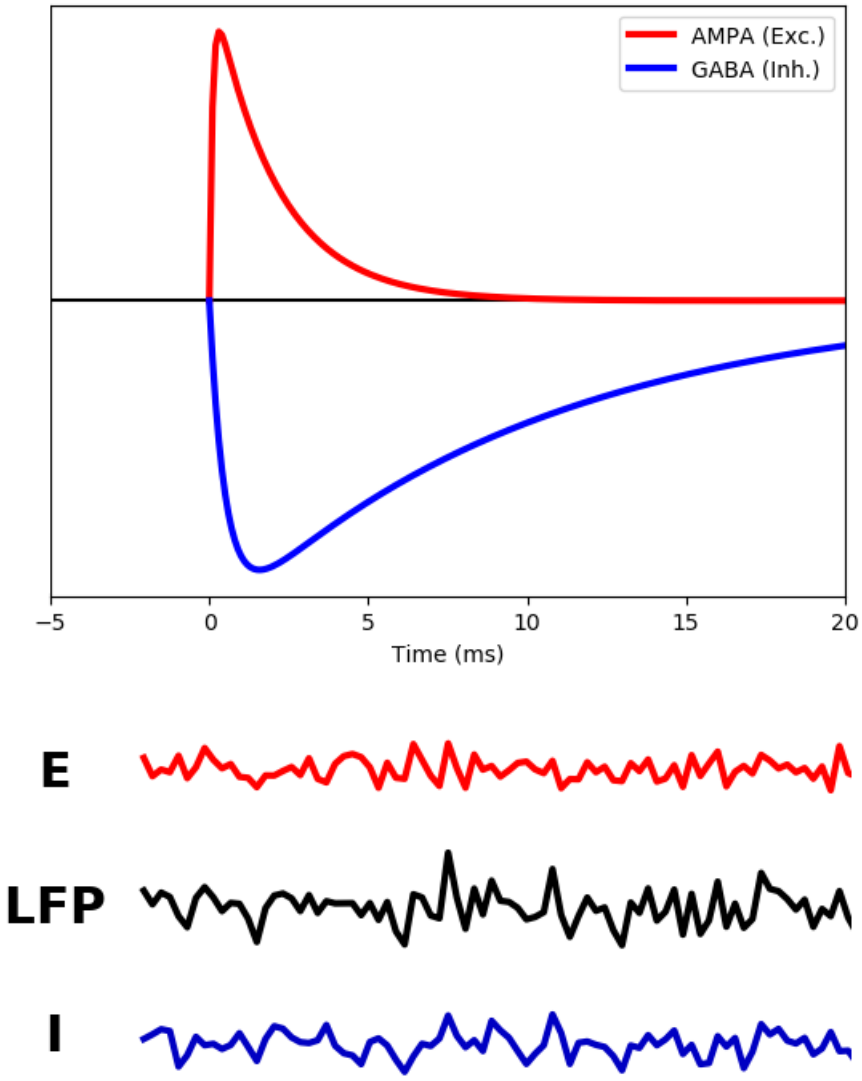

Figure 3.4: Top shows the AMPA and GABA conductance profiles drawn from the double-exponential defined by the decay and rise time-constant kernels that convoluted the discretized spike time series. Bottom shows excitatory (red), inhibitory (blue) currents, and in the middle the linear sum (Mazzoni et al., 2015) which represents the LFP.

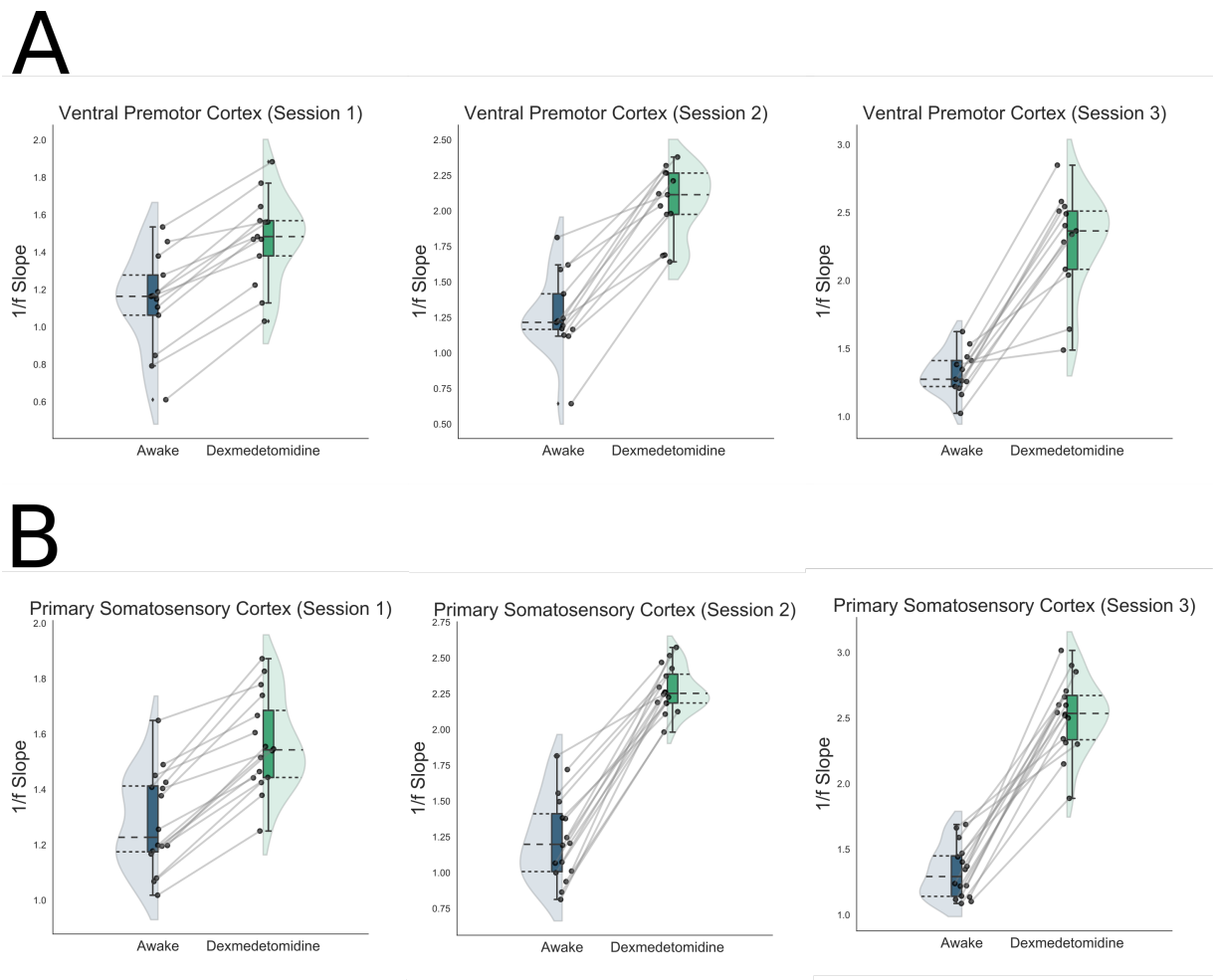

Figure 3.5: Effect of decreasing noradrenergic neuromodulation by acute Dexmedetomidine in Monkey LFP across sessions in ***(A)*** Ventral Premotor Cortex micro Electrodes and ***(B)*** Primary Somatosensory Cortex micro electrodes.

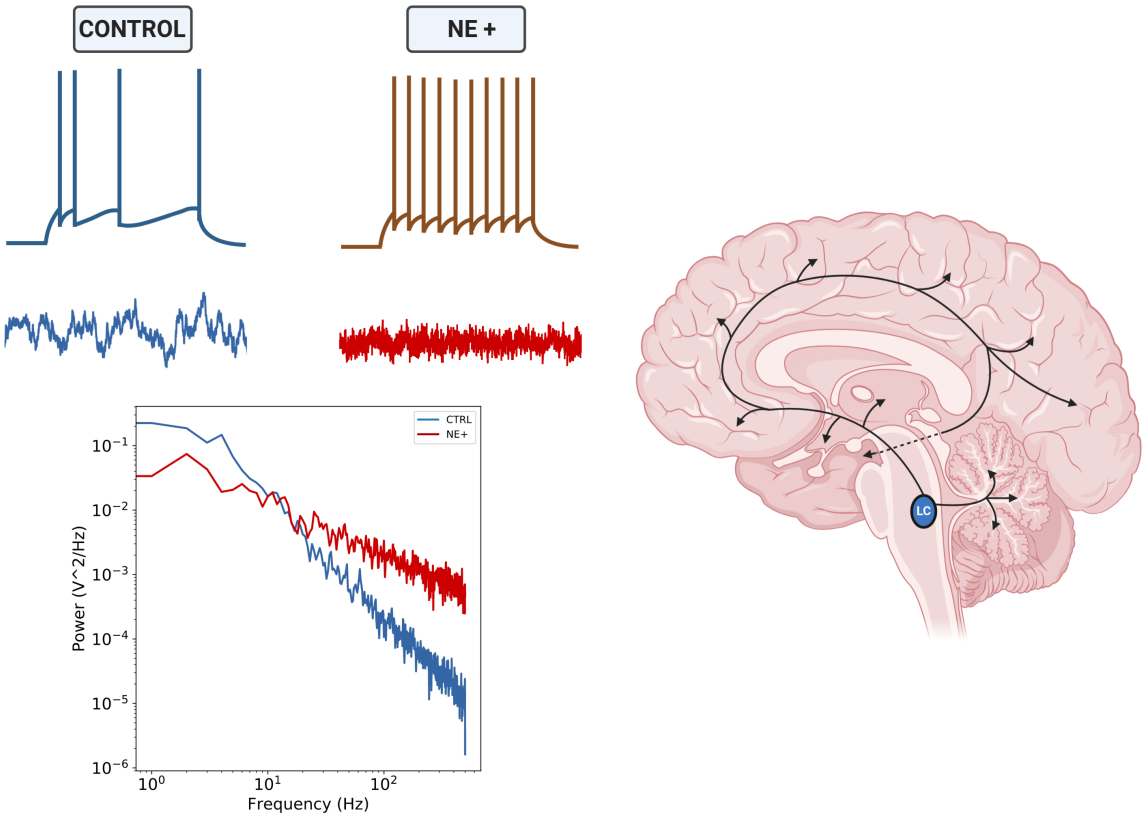

Figure 3.6: Summary of proposed interpretation of arousal-related neuromodulation in eliminating activity-dependent adaptation and shaping 1/f slope.

Bibliography

[1] Akeju, O., Kim, S. E., Vazquez, R., Rhee, J., Pavone, K. J., Hobbs, L. E., ...& Brown, E. N. (2016). Spatiotemporal dynamics of dexmedetomidine-induced electroencephalogram oscillations. PloS one, 11(10), e0163431.

[2] Albrecht, M. A., Martin-Iverson, M. T., Price, G., Lee, J., Iyyalol, R.,& Waters, F. (2011). Dexamphetamine effects on separate constructs in the rubber hand illusion test. Psychopharmacology, 217(1), 39-50.

[3] Albrecht, M. A., Roberts, G., Price, G., Lee, J., Iyyalol, R.,& Martin-Iverson, M. T. (2016). The effects of dexamphetamine on the resting-state electroencephalogram and functional connectivity. Human brain mapping, 37(2), 570-588.

[4] Allen, M., Poggiali, D., Whitaker, K., Marshall, T. R., van Langen, J.,& Kievit, R. A. (2021). Raincloud plots: a multi-platform tool for robust data visualization [version 2; peer review: 2 approved].

[5] Arnsten, A. F. (1998). Catecholamine modulation of prefrontal cortical cognitive function. Trends in cognitive sciences, 2(11), 436-447.

[6] Asghar, S. J., Tanay, V. A., Baker, G. B., Greenshaw, A.,& Silverstone, P. H. (2003). Relationship of plasma amphetamine levels to physiological, subjective, cognitive and biochemical measures in healthy volunteers. Human Psychopharmacology: Clinical and Experimental, 18(4), 291-299.

[7] Aston-Jones, G.,& Cohen, J. D. (2005). An integrative theory of locus coeruleus nore-

pinephrine function: adaptive gain and optimal performance. Annu. Rev. Neurosci., 28, 403-450.

[8] Augustin, M., Ladenbauer, J.,& Obermayer, K. (2013). How adaptation shapes spike rate oscillations in recurrent neuronal networks. Frontiers in computational neuroscience, 7, 9.

[9] Ballesteros, J. J., Briscoe, J. B.,& Ishizawa, Y. (2020). Neural signatures of α_2-Adrenergic agonist-induced unconsciousness and awakening by antagonist. Elife, 9, e57670.

[10] Barranca, V. J., Huang, H.,& Li, S. (2019). The impact of spike-frequency adaptation on balanced network dynamics. Cognitive neurodynamics, 13(1), 105-120.

[11] Benda, J.,& Herz, A. V. (2003). A universal model for spike-frequency adaptation. Neural computation, 15(11), 2523-2564.

[12] Bhatia, A., Moza, S.,& Bhalla, U. S. (2019). Precise excitation-inhibition balance controls gain and timing in the hippocampus. Elife, 8, e43415.

[13] Bruining, H., Hardstone, R., Juarez-Martinez, E. L., Sprengers, J., Avramiea, A. E., Simpraga, S., ...& Linkenkaer-Hansen, K. (2020). Measurement of excitation-inhibition ratio in autism spectrum disorder using critical brain dynamics. Scientific reports, 10(1), 1-15.

[14] Brunel, N. (2000). Dynamics of sparsely connected networks of excitatory and inhibitory spiking neurons. Journal of computational neuroscience, 8(3), 183-208.

[15] Chance, F. S., Abbott, L. F.,& Reyes, A. D. (2002). Gain modulation from background synaptic input. Neuron, 35(4), 773-782.

[16] Chiu, T. H., Chen, M. J., Yang, Y. R., Yang, J. J.,& Tang, F. I. (1995). Action of dexmedetomidine on rat locus coeruleus neurons: intracellular recording in vitro. European journal of pharmacology, 285(3), 261-268.

[17] Colombo, M. A., Napolitani, M., Boly, M., Gosseries, O., Casarotto, S., Rosanova, M., ...& Sarasso, S. (2019). The spectral exponent of the resting EEG indexes the presence of consciousness during unresponsiveness induced by propofol, xenon, and ketamine. NeuroImage, 189, 631-644.

[18] Correa-Sales, C., Rabin, B. C.,& Maze, M. (1992). A hypnotic response to dexmedetomidine, an α_2 agonist, is mediated in the locus coerüleus in rats. The Journal of the American Society of Anesthesiologists, 76(6), 948-952.

[19] D'Andola, M., Rebollo, B., Casali, A. G., Weinert, J. F., Pigorini, A., Villa, R., ...& Sanchez-Vives, M. V. (2018). Bistability, causality, and complexity in cortical networks: an in vitro perturbational study. Cerebral cortex, 28(7), 2233-2242.

[20] Destexhe, A.,& Rudolph, M. (2004). Extracting information from the power spectrum of synaptic noise. Journal of computational neuroscience, 17(3), 327-345.

[21] Destexhe, A., Rudolph, M.,& Paré, D. (2003). The high-conductance state of neocortical neurons in vivo. Nature reviews neuroscience, 4(9), 739-751.

[22] Destexhe, A., Rudolph, M., Fellous, J. M.,& Sejnowski, T. J. (2001). Fluctuating synaptic conductances recreate in vivo-like activity in neocortical neurons. Neuroscience, 107(1), 13-24.

[23] Donoghue, T., Haller, M., Peterson, E. J., Varma, P., Sebastian, P., Gao, R., ...& Voytek, B. (2020). Parameterizing neural power spectra into periodic and aperiodic components. Nature neuroscience, 23(12), 1655-1665.

[24] Froemke, R. C. (2015). Plasticity of cortical excitatory-inhibitory balance. Annual review of neuroscience, 38, 195-219.

[25] Funai, Y., Pickering, A. E., Uta, D., Nishikawa, K., Mori, T., Asada, A., ...& Furue, H. (2014). Systemic dexmedetomidine augments inhibitory synaptic transmission in the superficial dorsal horn through activation of descending noradrenergic control: an in vivo patch-clamp analysis of analgesic mechanisms. PAIN®, 155(3), 617-628.

[26] Gao, R., Peterson, E. J.,& Voytek, B. (2017). Inferring synaptic excitation/inhibition balance from field potentials. Neuroimage, 158, 70-78.

[27] Garrett, D. D., Nagel, I. E., Preuschhof, C., Burzynska, A. Z., Marchner, J., Wiegert, S., ...& Lindenberger, U. (2015). Amphetamine modulates brain signal variability and work-

ing memory in younger and older adults. Proceedings of the National Academy of Sciences, 112(24), 7593-7598.

[28] Gerstner, W.,& Kistler, W. M. (2002). Spiking neuron models: Single neurons, populations, plasticity. Cambridge university press.

[29] Gilsbach, R., Röser, C., Beetz, N., Brede, M., Hadamek, K., Haubold, M., ...& Hein, L. (2009). Genetic dissection of α_2-adrenoceptor functions in adrenergic versus noradrenergic cells. Molecular pharmacology, 75(5), 1160-1170.

[30] Goldman, J. S., Tort-Colet, N., Di Volo, M., Susin, E., Bouté, J., Dali, M., ...& Destexhe, A. (2019). Bridging single neuron dynamics to global brain states. Frontiers in systems neuroscience, 13, 75.

[31] Goldman, J., Kusch, L., Hazalyalcinkaya, B., Depannemaecker, D., Nghiem, T. A., Jirsa, V.,& Destexhe, A. (2020). Brain-scale emergence of slow-wave synchrony and highly responsive asynchronous states based on biologically realistic population models simulated in The Virtual Brain. BioRxiv.

[32] Goris, R. L., Movshon, J. A.,& Simoncelli, E. P. (2014). Partitioning neuronal variability. Nature neuroscience, 17(6), 858-865.

[33] Gramfort, A., Luessi, M., Larson, E., Engemann, D. A., Strohmeier, D., Brodbeck, C., ...& Hämäläinen, M. S. (2014). MNE software for processing MEG and EEG data. Neuroimage, 86, 446-460.

[34] Haider, B., Duque, A., Hasenstaub, A. R.,& McCormick, D. A. (2006). Neocortical network activity in vivo is generated through a dynamic balance of excitation and inhibition. Journal of Neuroscience, 26(17), 4535-4545.

[35] Harris, K. D.,& Thiele, A. (2011). Cortical state and attention. Nature reviews neuroscience, 12(9), 509-523.

[36] Herrero, J. L., Roberts, M. J., Delicato, L. S., Gieselmann, M. A., Dayan, P.,& Thiele, A. (2008). Acetylcholine contributes through muscarinic receptors to attentional modulation in V1. Nature, 454(7208), 1110-1114.

[37] Hu, F. Y., Hanna, G. M., Han, W., Mardini, F., Thomas, S. A., Wyner, A. J.,& Kelz, M. B. (2012). Hypnotic hypersensitivity to volatile anesthetics and dexmedetomidine in dopamine β-hydroxylase knockout mice. The Journal of the American Society of Anesthesiologists, 117(5), 1006-1017.

[38] J. van Langen. (2020). Open-visualizations in R and Python (Version v.1.0.4). Zenodo. https://zenodo.org/record/3715576

[39] Jas, M., Larson, E., Engemann, D. A., Leppäkangas, J., Taulu, S., Hämäläinen, M.,& Gramfort, A. (2018). A reproducible MEG/EEG group study with the MNE software: recommendations, quality assessments, and good practices. Frontiers in neuroscience, 12, 530.

[40] Jorm, C. M.,& Stamford, J. A. (1993). Actions of the hypnotic anaesthetic, dexmedetomidine, on noradrenaline release and cell firing in rat locus coeruleus slices. BJA: British Journal of Anaesthesia, 71(3), 447-449.

[41] Joshi, S., Li, Y., Kalwani, R. M.,& Gold, J. I. (2016). Relationships between pupil diameter and neuronal activity in the locus coeruleus, colliculi, and cingulate cortex. Neuron, 89(1), 221-234.

[42] Kalmbach, A.,& Waters, J. (2014). Modulation of high-and low-frequency components of the cortical local field potential via nicotinic and muscarinic acetylcholine receptors in anesthetized mice. Journal of neurophysiology, 111(2), 258-272.

[43] Kenny, J. D., Taylor, N. E., Brown, E. N.,& Solt, K. (2015). Dextroamphetamine (but not atomoxetine) induces reanimation from general anesthesia: implications for the roles of dopamine and norepinephrine in active emergence. PLoS One, 10(7), e0131914.

[44] La Camera, G., Rauch, A., Thurbon, D., Luscher, H. R., Senn, W.,& Fusi, S. (2006). Multiple time scales of temporal response in pyramidal and fast spiking cortical neurons. Journal of neurophysiology, 96(6), 3448-3464.

[45] Ladenbauer, J., Augustin, M.,& Obermayer, K. (2014). How adaptation currents change threshold, gain, and variability of neuronal spiking. Journal of Neurophysiology, 111(5), 939-953.

[46] Ladenbauer, J., Augustin, M., Shiau, L.,& Obermayer, K. (2012). Impact of adaptation currents on synchronization of coupled exponential integrate-and-fire neurons. PLoS Comput Biol, 8(4), e1002478.

[47] Lee, S. H.,& Dan, Y. (2012). Neuromodulation of brain states. Neuron, 76(1), 209-222.

[48] Lempel, A.,& Ziv, J. (1976). On the complexity of finite sequences. IEEE Transactions on information theory, 22(1), 75-81.

[49] Liu, Y., Cui, L., Schwarz, M. K., Dong, Y.,& Schlüter, O. M. (2017). Adrenergic gate release for spike timing-dependent synaptic potentiation. Neuron, 93(2), 394-408.

[50] Lombardi, F., Herrmann, H. J.,& de Arcangelis, L. (2017). Balance of excitation and inhibition determines 1/f power spectrum in neuronal networks. Chaos: An Interdisciplinary Journal of Nonlinear Science, 27(4), 047402.

[51] Madison, D. V., Lancaster, B.,& Nicoll, R. A. (1987). Voltage clamp analysis of cholinergic action in the hippocampus. Journal of Neuroscience, 7(3), 733-741.

[52] Manning, J. R., Jacobs, J., Fried, I.,& Kahana, M. J. (2009). Broadband shifts in local field potential power spectra are correlated with single-neuron spiking in humans. Journal of Neuroscience, 29(43), 13613-13620.

[53] Martins, A. R. O.,& Froemke, R. C. (2015). Coordinated forms of noradrenergic plasticity in the locus coeruleus and primary auditory cortex. Nature neuroscience, 18(10), 1483-1492.

[54] Mazzoni, A., Lindén, H., Cuntz, H., Lansner, A., Panzeri, S.,& Einevoll, G. T. (2015). Computing the local field potential (LFP) from integrate-and-fire network models. PLoS computational biology, 11(12), e1004584.

[55] McAdams, C. J.,& Maunsell, J. H. (1999). Effects of attention on the reliability of individual neurons in monkey visual cortex. Neuron, 23(4), 765-773.

[56] McCormick, D. A. (1992). Neurotransmitter actions in the thalamus and cerebral cortex and their role in neuromodulation of thalamocortical activity. Progress in neurobiology, 39(4), 337-388.

[57] McCormick, D. A.,& Williamson, A. (1989). Convergence and divergence of neurotransmitter action in human cerebral cortex. Proceedings of the National Academy of Sciences, 86(20), 8098-8102.

[58] McCormick, D. A., Nestvogel, D. B.,& He, B. J. (2020). Neuromodulation of brain state and behavior. Annual review of neuroscience, 43, 391-415.

[59] McGinley, M. J., David, S. V.,& McCormick, D. A. (2015). Cortical membrane potential signature of optimal states for sensory signal detection. Neuron, 87(1), 179-192.

[60] Medel, V., Irani, M., Ossandon, T.,& Boncompte, G. (2020). Complexity and 1/f slope jointly reflect cortical states across different E/I balances. BioRxiv.

[61] Medel, V., Valdés, J., Castro, S., Ossandón, T.,& Boncompte, G. (2019). Commentary: Amplification and Suppression of Distinct Brainwide Activity Patterns by Catecholamines. Frontiers in behavioral neuroscience, 13, 217.

[62] Munk, M. H., Roelfsema, P. R., König, P., Engel, A. K.,& Singer, W. (1996). Role of reticular activation in the modulation of intracortical synchronization. Science, 272(5259), 271-274.

[63] Munn, B., Zeater, N., Pietersen, A. N., Solomon, S. G., Cheong, S. K., Martin, P. R.,& Gong, P. (2020). Fractal spike dynamics and neuronal coupling in the primate visual system. The Journal of physiology, 598(8), 1551-1571.

[64] Murphy, B. K.,& Miller, K. D. (2003). Multiplicative gain changes are induced by excitation or inhibition alone. Journal of Neuroscience, 23(31), 10040-10051.

[65] Nacif-Coelho, C., Correa-Sales, C., Chang, L. L.,& Maze, M. (1994). Perturbation of ion channel conductance alters the hypnotic response to the α_2-adrenergic agonist dexmedetomi-

dine in the locus coeruleus of the rat. In The Journal of the American Society of Anesthesiologists (Vol. 81, No. 6, pp. 1527-1534). The American Society of Anesthesiologists.

[66] Nelson, L. E., Guo, T. Z., Lu, J., Saper, C. B., Franks, N. P.,& Maze, M. (2002). The sedative component of anesthesia is mediated by GABA A receptors in an endogenous sleep pathway. Nature neuroscience, 5(10), 979-984.

[67] Nelson, L. E., Lu, J., Guo, T., Saper, C. B., Franks, N. P.,& Maze, M. (2003). The α_2-adrenoceptor agonist dexmedetomidine converges on an endogenous sleep-promoting pathway to exert its sedative effects. The Journal of the American Society of Anesthesiologists, 98(2), 428-436.

[68] Nghiem, T.-A. E., Tort-Colet, N., Górski, T., Ferrari, U., Moghimyfiroozabad, S., Goldman, J. S., Teleńczuk, B., Capone, C., Bal, T., di Volo, M., & Destexhe, A. (2020). Cholinergic Switch between Two Types of Slow Waves in Cerebral Cortex. Cerebral Cortex , 30(6), 3451–3466.

[69] Ossandón, T., Jerbi, K., Vidal, J. R., Bayle, D. J., Henaff, M. A., Jung, J., ...& Lachaux, J. P. (2011). Transient suppression of broadband gamma power in the default-mode network is correlated with task complexity and subject performance. Journal of Neuroscience, 31(41), 14521-14530.

[70] Ostlund, B. D., Alperin, B. R., Drew, T.,& Karalunas, S. L. (2021). Behavioral and cognitive correlates of the aperiodic (1/f-like) exponent of the EEG power spectrum in adolescents with and without ADHD. Developmental cognitive neuroscience, 100931.

[71] Ostojic, S. (2011). Interspike interval distributions of spiking neurons driven by fluctuating inputs. Journal of neurophysiology, 106(1), 361-373.

[72] Pertermann, M., Mückschel, M., Adelhöfer, N., Ziemssen, T.,& Beste, C. (2019). On the interrelation of 1/f neural noise and norepinephrine system activity during motor response inhibition. Journal of neurophysiology, 121(5), 1633-1643.

[73] Pfeffer, T., Avramiea, A. E., Nolte, G., Engel, A. K., Linkenkaer-Hansen, K.,& Donner, T. H. (2018). Catecholamines alter the intrinsic variability of cortical population activity and perception. PLoS biology, 16(2), e2003453.

[74] Pfeffer, T., Ponce-Alvarez, A., Meindertsma, T., Gahnström, C., van den Brink, R. L., Nolte, G., ...& Donner, T. H. (2020). Circuit mechanisms for chemical modulation of cortex-wide network interactions and exploration behavior. BioRxiv.

[75] Pozzorini, C., Naud, R., Mensi, S.,& Gerstner, W. (2013). Temporal whitening by power-law adaptation in neocortical neurons. Nature neuroscience, 16(7), 942-948.

[76] Reimer, J., McGinley, M. J., Liu, Y., Rodenkirch, C., Wang, Q., McCormick, D. A.,& Tolias, A. S. (2016). Pupil fluctuations track rapid changes in adrenergic and cholinergic activity in cortex. Nature communications, 7(1), 1-7.

[77] Rizzo, R.,& Gulisano, M. (2013). Clinical pharmacology of comorbid attention deficit hyperactivity disorder in Tourette syndrome. International review of neurobiology, 112, 415-444.

[78] Robertson, M. M., Furlong, S., Voytek, B., Donoghue, T., Boettiger, C. A.,& Sheridan, M. A. (2019). EEG power spectral slope differs by ADHD status and stimulant medication exposure in early childhood. Journal of neurophysiology, 122(6), 2427-2437.

[79] Sanchez-Vives, M. V., Massimini, M.,& Mattia, M. (2017). Shaping the default activity pattern of the cortical network. Neuron, 94(5), 993-1001.

[80] Sara, S. J.,& Segal, M. (1991). Plasticity of sensory responses of locus coeruleus neurons in the behaving rat: implications for cognition. Progress in brain research, 88, 571-585.

[81] Schwalger, T., Fisch, K., Benda, J.,& Lindner, B. (2010). How noisy adaptation of neurons shapes interspike interval histograms and correlations. PLoS Comput Biol, 6(12), e1001026.

[82] Selimbeyoglu, A., Kim, C. K., Inoue, M., Lee, S. Y., Hong, A. S., Kauvar, I., ...& Deisseroth, K. (2017). Modulation of prefrontal cortex excitation/inhibition balance rescues social behavior in CNTNAP2-deficient mice. Science translational medicine, 9(401).

[83] Sheehan, T. C., Sreekumar, V., Inati, S. K.,& Zaghloul, K. A. (2018). Signal complexity of human intracranial EEG tracks successful associative-memory formation across individuals. Journal of Neuroscience, 38(7), 1744-1755.

[84] Shine, J. M. (2019). Neuromodulatory influences on integration and segregation in the brain. Trends in cognitive sciences, 23(7), 572-583.

[85] Shine, J. M., van den Brink, R. L., Hernaus, D., Nieuwenhuis, S.,& Poldrack, R. A. (2018). Catecholaminergic manipulation alters dynamic network topology across cognitive states. Network Neuroscience, 2(3), 381-396.

[86] Song, A. H., Kucyi, A., Napadow, V., Brown, E. N., Loggia, M. L.,& Akeju, O. (2017). Pharmacological modulation of noradrenergic arousal circuitry disrupts functional connectivity of the locus coeruleus in humans. Journal of Neuroscience, 37(29), 6938-6945.

[87] Spencer, R. C., Devilbiss, D. M.,& Berridge, C. W. (2015). The cognition-enhancing effects of psychostimulants involve direct action in the prefrontal cortex. Biological psychiatry, 77(11), 940-950.

[88] Sripati, A. P., Yoshioka, T., Denchev, P., Hsiao, S. S.,& Johnson, K. O. (2006). Spatiotemporal receptive fields of peripheral afferents and cortical area 3b and 1 neurons in the primate somatosensory system. Journal of Neuroscience, 26(7), 2101-2114.

[89] Steriade, M., Nunez, A.,& Amzica, F. (1993). A novel slow (¡ 1 Hz) oscillation of neocortical neurons in vivo: depolarizing and hyperpolarizing components. Journal of neuroscience, 13(8), 3252-3265.

[90] Stiefel, K. M., Gutkin, B. S.,& Sejnowski, T. J. (2009). The effects of cholinergic neuromodulation on neuronal phase-response curves of modeled cortical neurons. Journal of computational neuroscience, 26(2), 289-301.

[91] Trakoshis, S., Rocchi, F., Canella, C., You, W., Chakrabarti, B., Ruigrok, A. N., ...& MRC AIMS Consortium. (2020). Intrinsic excitation-inhibition imbalance affects medial prefrontal cortex differently in autistic men versus women. Elife, 9, e55684.

[92] van den Brink, R. L., Pfeffer, T.,& Donner, T. H. (2019). Brainstem modulation of large-scale intrinsic cortical activity correlations. Frontiers in human neuroscience, 13, 340.

[93] Van Vreeswijk, C.,& Sompolinsky, H. (1996). Chaos in neuronal networks with balanced excitatory and inhibitory activity. Science, 274(5293), 1724-1726.

[94] Vinck, M., Batista-Brito, R., Knoblich, U.,& Cardin, J. A. (2015). Arousal and locomotion make distinct contributions to cortical activity patterns and visual encoding. Neuron, 86(3), 740-754

[95] Voytek, B.,& Knight, R. T. (2015). Dynamic network communication as a unifying neural basis for cognition, development, aging, and disease. Biological psychiatry, 77(12), 1089-1097.

[96] Wainstein, G., Rojas-Líbano, D., Crossley, N. A., Carrasco, X., Aboitiz, F.,& Ossandón, T. (2017). Pupil size tracks attentional performance in attention-deficit/hyperactivity disorder. Scientific reports, 7(1), 1-9.

[97] Wang, X. J. (2010). Neurophysiological and computational principles of cortical rhythms in cognition. Physiological reviews, 90(3), 1195-1268.

[98] Waschke, L., Donoghue, T., Fiedler, L., Smith, S., Garrett, D. D., Voytek, B.,& Obleser, J. (2021). Modality-specific tracking of attention and sensory statistics in the human electrophysiological spectral exponent. BioRxiv.

[99] Waschke, L., Tune, S.,& Obleser, J. (2019). Local cortical desynchronization and pupil-linked arousal differentially shape brain states for optimal sensory performance. Elife, 8, e51501.

[100] Wenzel, M., Han, S., Smith, E. H., Hoel, E., Greger, B., House, P. A.,& Yuste, R. (2019). Reduced repertoire of cortical microstates and neuronal ensembles in medically induced loss of consciousness. Cell systems, 8(5), 467-474.

[101] Wolfart, J., Debay, D., Le Masson, G., Destexhe, A.,& Bal, T. (2005). Synaptic background activity controls spike transfer from thalamus to cortex. Nature neuroscience, 8(12), 1760-1767.

[102] Yüzgeç, Ö., Prsa, M., Zimmermann, R.,& Huber, D. (2018). Pupil size coupling to cortical states protects the stability of deep sleep via parasympathetic modulation. Current Biology, 28(3), 392-400.

[103] Zerlaut, Y.,& Destexhe, A. (2017). Enhanced responsiveness and low-level awareness in stochastic network states. Neuron, 94(5), 1002-1009.

[104] Zerlaut, Y., Chemla, S., Chavane, F.,& Destexhe, A. (2018). Modeling mesoscopic cortical dynamics using a mean-field model of conductance-based networks of adaptive exponential integrate-and-fire neurons. Journal of computational neuroscience, 44(1), 45-61.

Chapter 4

Attentional rapid state shift is related to transient 1/f aperiodic activity and phasic Arousal in human iEEG and scalp EEG

Abstract

Brain states dynamically couple to environmental and cognitive demands. Evidence suggest that these brain state shifts are the result of a close interrelation between the degree of desynchronization and the activity of arousal-related neuromodulation such as the locus-coeruleus noradrenergic (LC-NE) system. We examine this nexus in humans during a visuospatial working memory task with invasive and non-invasive electrophysiological recordings with simultaneous pupil data as an indirect index of arousal-related LC-NE system activity. We show that the temporal fluctuation of neural desynchronization -as adressed by time-resolved 1/f aperiodic activity- is flattest at the highest attentional demand, suggesting a transient attentional recruitment of neural desynchronization. These 1/f rapid attentional shifts can be represented as a low-dimensional signal which strongly correlates with pupil

diameter at both intracranial and scalp EEG scales. Our results speak to mechanistic models linking neural desynchronization and arousal-related neuromodulation at behaviorally-relevant timescales.

4.1 Introduction

In this chapter, we present evidence supporting the integration of the observations from the previous chapters -aperiodic activity, E/I balance, neuromodulation, and behavior-. In the previous chapters, we introduced the 1/f slope of the field potential's PSD as a proxy of E/I balance (Gao et al., 2017; Colombo et al., 2019; Trakoshis et al., 2020; Medel et al., 2020) and study its effect in behavior (Boncompte et al., 2021; Chapter 2). We also presented computational and experimental evidence that supports that 1/f slope -our proxy of E/I balance- is related to LC-NE system and arousal-related neuromodulation through the effect of eliminating spike-frequency adaptation currents (Medel et al., In Prep; Chapter 3). Here we propose that the relation between LC-NE system tracks the temporal dynamics of E/I balance -as adressed by quantifying time-resolved 1/f slope- and that this fluctuation will be coupled to the attentional demand of the subjects.

To examine the nexus between E/I balance and phasic arousal-related neuromodulation during attentional information processing, the 1/f aperiodic activity can be integrated (correlated) with pupil diameter data while participants perform a task. Pupil diameter is an established indirect index of Locus-Coeruleus noradrenergic (LC-NE) system activity (Chmielewski et al. 2017; Costa and Rudebeck 2016; Joshi et al. 2016), although acetylcholinergic (ACh) system have also been reported to modulate pupil diameter (Fotiou et al. 2009; Naicker et al. 2016; Reimer et al., 2016). Larger pupil diameters reflect higher arousal-related neuromodulation concentrations (Phillips et al. 2000) and are related to an increase in the firing rate of NE neurons (Costa and Rudebeck 2016; Joshi et al. 2016; Varazzani et al. 2015). In contrast to acute activation of arousal-related neuromodulatory system as seen in electrical stimulation (Liu et al., 2017) or pharmacological intervention (Phillips et al., 2000), the integration of electrophysiological parameters with pupillometry provides more ecological and time-resolved information on the interaction between arousal-related neuromodulation, brain, and the dynamics of behaviorally

relevant state switches (Schwalm & Jubal, 2017). With this structure, we can observe the behaviorally relevant time points at which neural aperiodic activity is modulated by arousal-related neuromodulation.

In awake attentive state, animals are in a dynamic state of cortical activity which is characterized by fast switching from inattentive awake to high attentional state, which is related to environmental and cognitive demands (McGinley et al., 2015a; McGinley et al., 2015b). This fast switching behavior has been related to intrinsic top-down modulation of cortical activity related to attentional recruitment (McCormick et al., 2020) and it has been intimately linked to pupil diameter, (Reimer et al., 2016) a proxy of noradrenergic neuromodulation (Vinck et al., 2016; Aston-Jones and Cohen, 2005). Although these results have been widely studied in animal models with invasive electrophysiology of membrane potential recordings, here we seek to understand these phenomena from a multi-scale approach grounded in theoretical considerations of neural activity and cognition. Using a bottom-up strategy, starting with field-potential simulations showing that E/I balance is related to 1/f slope and high complexity, to the interpretation of changes in 1/f slope as a result of neuromodulatory action over adaptation currents (Medel et al., In Prep; Chapter 3), we have shown that 1/f and complexity are intimately related to behavior (Boncompte et al., 2021). In this line, we propose that attentional fast cortical state switching occurs as a result of the interaction between ascending arousal neuromodulation which shapes E/I balance.

In this chapter, we present evidence that supports 1/f aperiodic activity as a multiscale global signal that is grounded on theoretical considerations and fluctuates according to behavioral demand. We explore 1/f principal component analysis at intracranial EEG and scalp EEG scales, and show that both scales have similar characteristics and are highly correlated with pupil diameter -our proxy of arousal-related neuromodulation (Aston-Jones and Cohen, 2005)-.

4.2 Materials and Methods

Subjects

For the iEEG group, four patients with drug-resistant epilepsy participated in this study. The participants were stereotactically implanted with multisite EEG depth electrodes at the Epilepsy Department of the Grenoble Neurological Hospital (Grenoble, France). In collaboration with the medical staff, and based on visual inspection, electrodes presenting pathological waveforms were discarded from the present study. All participants had normal vision without corrective glasses. All participants provided written informed consent, and the experimental procedures were approved by the local Ethical Committee (CPP Sud-Est V n 09-CHU-12). For the EEG group, subjects were 18 typically developing children ranging from 10 to 13 yo (mean = 11.8, SD = 0.85, 15 male).

Visuospatial Working Memory Task

Subjects performed a Sternberg-type delayed visuospatial working memory task. The memoranda were 1- or 2-dot arrays, with the dots located variably in any of the sixteen spaces of a 4×4 grid (Figure 4.1A).

On each trial, subjects were instructed to start by fixating on the center of the empty grid. After 1.5 seconds, the dot array presentation commenced. Three different dot arrays were presented on each trial. Each array was presented for 1 second, with a 0.5 seconds inter-stimulus interval delay between arrays, during which the empty grid was presented (Figure 4.1A). After the last delay period, a distractor image was presented for 1 second. After the distractor, a 'probe' dot was presented for 2 seconds. This was a dot within the grid, and subjects had to answer 'yes' if the probe dot had been presented in one of the trial's previous arrays, or 'no' if it had not. Immediately after probe offset, we provided a feedback image for 1.5 seconds, indicating if the subject response was correct or incorrect. The participants were instructed to respond as fast as possible.

We used three distractors: (1) A fixation cross; (2) a neutral face; and (3) an emotional face. Distractors were constructed and modified from Karolinska Directed Emotional Faces database

(Calvo & Lundqvist, 2008). Distractor types were presented randomly. There were two trial types, according to cognitive load: in low-load trials, only one dot was presented on each image, whereas in high-load trials, two dots were presented on each image. Therefore, in low-load trials subjects had to retain the location of three dots (one per image) and in high-load trials, they had to retain the location of six dots (two per image).

A total of 80 trials were presented in each session, separated in 4 blocks of 20 trials. Sessions usually lasted 30 minutes. Stimuli were presented using Presentation® software (Neurobehavioral Systems, Inc.) and subjects delivered their responses using a keypad.

Intracranial EEG

Each participant was implanted with SEEG electrodes (diameter of 0.8 mm). Depending on the implanted structure, electrodes were composed of 10 to 15 contacts that were 2-mm wide and 1.5-mm apart (DIXI Medical Instrument, Besancon, France). Intracranial neural recordings were conducted using an audio–video-EEG monitoring system (Micromed, Treviso, Italy), which allowed simultaneous recording of up to 210 depth-EEG channels sampled at 1024 Hz. Intracranial EEG signals were recorded from a total of 773 intracerebral sites across all participants (between 162 and 210 sites per participant). The coordinates of each electrode contact were given following these references: origin (anterior commissure), anteroposterior axis (anterior commissure–posterior commissure), and vertical axis (interhemispheric plane). The electrodes were then localized in each individual participant using Talairach coordinates, which were then transformed to MNI coordinate system using standard procedures (i.e., tal2mni.m MATLAB function). We then automatically assigned electrodes to brain regions based on 2 distinct atlases: Brodmann areas and Schaeffer atlas (Schaeffer et al., 2018).

Data from iEEG recordings were preprocessed using a pipeline consistent with previous work (Kucyi et al., 2018; Kucyi et al., 2020). Notch filtering was performed to attenuate power-line noise (zero-phase, third order, Butterworth filter with band-stop between 47–53, 97–103, and 147–153 Hz for data. We then re-referenced the signal from each channel to the common average signal across all channels, with the following channel types excluded from the common average: those that (a) showed pathological activity during clinical monitoring (as noted by a neurolo-

gist); (b) were manually labeled as clear outliers on power spectra plots of all channels; (c) had a variance greater or lesser than five times the median variance across all channels; or (d) had greater than three times the median number of spikes across all channels, with spikes defined as 100 µV changes between successive samples.

Scalp EEG

The EEG data were recorded using a 10-5 34 channel Neuroscan EEG system at a sampling rate of 1000 Hz. All the pre-processing of EEG data was conducted in MATLAB using the EEGLAB 13.6.5b toolbox. First, the data were resampled to 500 Hz, referenced to mastoids, filtered between 0.5 and 42 Hz, and epoched leaving us with an 8 s trial. Then we visually inspected the complete recordings and spherically interpolated channels which were extremely deviated, without taking into consideration eye blink artifacts, as these were removed later using independent component analysis (ICA). Then, we rejected epochs using a threshold of -150 to +150 uV, without considering eye blink artifacts as well. Each recording was again visually inspected to check whether it was needed to interpolate more channels, reject more trials or too many trials were rejected leaving the recording unusable. Until this step the data was thus resampled, filtered, epoched, and semi-cleaned up, ready to be further cleared from eye movement and blink artifacts using ICA implemented in EEGLAB. Only independent components with clear and specific patterns of eye movement and blink artifacts were rejected from the data.

Pupil data acquisition, preprocessing and analysis

Pupil diameter data were acquired with Eyelink 1000 (SR Research Ltd., Mississauga, Ontario, Canada), with a 1kHz sampling frequency. Subjects sat in front of a table containing the computer screen for image presentation and the eye tracker device. For the EEG group, the subjects kept their head in a forehead/chin rest (SR Research Ltd.). Subjects were placed at a viewing distance of 30 cm from the display monitor.

Pupil diameter data preprocessing was performed using Matlab software with in-house functions consistent with previous preprocessing strategies (Wainstein et al., 2017). Periods of blinks in which no pupil diameter information was available were detected by the Eyelink software. Pupil

data surrounding blinks were removed from the time series used in the analyses and were interpolated using a cubic spline, implemented through Matlab function spline. To obtain the pupil diameter average profile (Figure 4.4A), the data of each participant were filtered by a bandpass Butterworth filter between 0.025 Hz and 4 Hz. This strategy extracted the high-frequency noise and eliminated the basal slow drift of the pupil diameter across trials. All trials with more than 50% of missing data (due to blinks or outliers) were not considered in the analysis. Data analysis was restricted to the 12-s trial period (Figure 4.1A). Finally, the pupil time-series was normalized by means of a z-score, separately for each trial.

Spectral Analyses

We conducted two analysis techniques to assess spectral activity from neural recordings. First, we computed a time-frequency analysis (Figure 4.2) using the multitaper method (8 tapers, frequency range 0.5 to 150 Hz with a scaling number of cycles depending on frequency bin) implemented in MNE python toolbox (Gramfort et al., 2014; Jas et al., 2018). The Time-frequency signal was normalized by using z-score of the complete trial. Second, we separated the spectrum in several standard-frequency bands defined as follows: theta (θ) [4–8 Hz], alpha (α) [8–15 Hz], beta (β) [16–30 Hz]. This was achieved by first filtering the raw EEG signals using a finite impulse response filtering (FIR, order = 3) and then computing the Hilbert transform over the complete trial. Additionally, we calculated broadband gamma [50–150 Hz] using 10 Hz frequency bands (e.g., 10 bands, beginning with 50-60 Hz up to 140-150 Hz) and for each bandpass filtered signal, we computed the envelope using Hilbert transform. To account for the 1/f decay, we normalized by means of z-score the signal of each 10 Hz step band-pass envelope and averaged together, to provide one single time-series of broadband gamma across the entire session.

Time-resolved aperiodic 1/f activity

To obtain a time-resolved measure of aperiodic 1/f activity, the squared magnitude of the Hamming-windowed Fourier Transform (window size of 1 s, 0.05 s step) was used. We parameterized the PSD using the "Fitting Oscillations & One Over f" (FOOOF) toolbox (Donoghue

et al., 2020). The FOOOF algorithm decomposes the log PSD into a summation of narrowband Gaussian periodic (oscillations) and aperiodic (1/f offset and slope) components for the whole frequency range. The algorithm estimates periodic and aperiodic components, removes the periodic ones, and estimates again until only the aperiodic components of the signal remain. This allows for the estimation of offset and power-law slope with considerable independence from oscillatory behavior, which is particularly important for empirical signal analysis (Donoghue et al., 2020; Voytek Knight, 2015). FOOOF toolbox also contains a "knee" parameter, which was not considered as it corresponds to changes in the autocorrelation function (Gao et al., 2020) which is related to lower frequencies power (Fallon et al., 2020), and is beyond the scope of this study. We set the algorithm with peak width limits: [1-8], the maximum number of peaks: 6; peak threshold 1.5; and 'fixed' aperiodic mode. Due to the differential distribution of basal 1/f signals across the cortex (Mahjoory et al., 2020), we normalized the time-resolved signal by means of z-score using the whole trial. Power spectra were parameterized across the frequency range 1 to 40 Hz and 40 to 80 Hz in iEEG, while for scalp EEG the range of 10 to 40 Hz was used.

Principal Component Analysis

We used linear dimensionality reduction of the data temporal 1/f signal using principal component analysis (PCA) to project it to a lower-dimensional space. For the iEEG dataset, data from each trial were concatenated to form a single-trial time series per subject and a temporal PCA was performed on the resultant data. Principal axes in feature space, representing the spatial directions of maximum variance in the data, were used to consider the spatial contributions of each electrode to the tPC. Data were segmented to obtain the single-trial tPC and were averaged to obtain the mean tPC across trials. For the EEG dataset, we concatenated each subject's 1/f trial average signal to form a single time series for all subjects. Data were segmented to obtain the single-subject tPC and then averaged to obtain the mean tPC. The algorithm was implemented with sklearn.decomposition.PCA function from scikit-learn python toolbox (Pedregosa et al., 2011).

Statistical Analysis

Data were visualized using a python implementation of raincloud plots (Allen et al., 2021; van Langen, 2020). Single-trial, time-frequency, and topoplot from open-source python package MNE (Gramfort et al., 2014; Jas et al., 2018). Scatter plots from Seaborn (Waskom et al., 2020). Glass brains were visualized using python pysurfer toolbox. Cross-correlation was obtained with scipy function scipy.signal.correlate and then the value of each correlation value in each temporal lag was normalized to obtain the maximum value of correlation as value 1. Correlation between tPC1 and band-limited amplitude was obtained by resampling each band-pass signal to the number of samples of tPC1, and then calculating the Pearson correlation coefficient using scipy.stats.pearsonr function.

We constructed null distributions to test the significance of the correlation between pupil diameter and tPC1 of the 1/f signal. In order to preserve temporal dependence in time-series data, bootstrap algorithms sample from the original data in blocks rather than sampling single observations. We used a data-driven block length selection algorithm based on Politis and White (2004) with corrections by Patton, Politis, and White (2007). Based on the notion of spectral estimation via the flat-top lag windows (Politis and Romano, 1995) the algorithm produces optimal block-lengths for the circular block bootstrap preserving canonic temporal properties of time series (Politis and White, 2004). We implemented this algorithm with recombinator python repository (`https://github.com/InvestmentSystems/recombinator`). We generated 10000 new time-series by resampling using a circular-block bootstrap and calculated the correlation value between each null pupil signal and the tPC1 1/f, thus generating a null distribution of correlation values. The significance of the original value can be tested if the value is lesser than the 2.5th percentile or greater than the 97.5th percentile of the distribution (Supplementary Figure 4.9).

4.3 Results

Four participants performed a visuospatial working memory task (Figure 4.1A) while electrophysiological data were recorded from multilead EEG depth electrodes (Figure 1B). In each trial, participants were instructed to answer whether a target dot (Probe) in a spatial grid was

present or absent in the previously shown dots (Load; Figure 4.1A). The participants were instructed to respond as fast as possible. The working memory recall condition of the probe is intimately related to attentional recruitment and ascending system activation (Wainstein et al., 2017). Although the task has two load conditions (see Material and Methods), we did not find performance nor reaction time differences between conditions. For this reason, further analysis is done in both conditions indistinctly.

We analyzed the spatially heterogeneous electrodes (Figure 4.1B; n=773). These intracranial recordings provided a means to assess data with minimal contamination from non-neural sources. We develop a novel pipeline analysis that obtains the time-varying aperiodic component of the signal by applying sliding-window analysis and computing the fitting of the 1/f slope in each PSD (Figure 4.1C; see Material and Methods). Due to a clear "knee" at 40 Hz (Figure 4.1C, Figure 4.3A) we, therefore, split the spectrum in two equally spanning sub-ranges, obtaining low-range (1-40 Hz) and high range (40-80 Hz) fits (Figure 4.1C). Note that both of these ranges have been extensively used in previous reports (Gao et al., 2017, Medel et al., 2020; Trakoshis et al., 2020; Colombo et al., 2019).

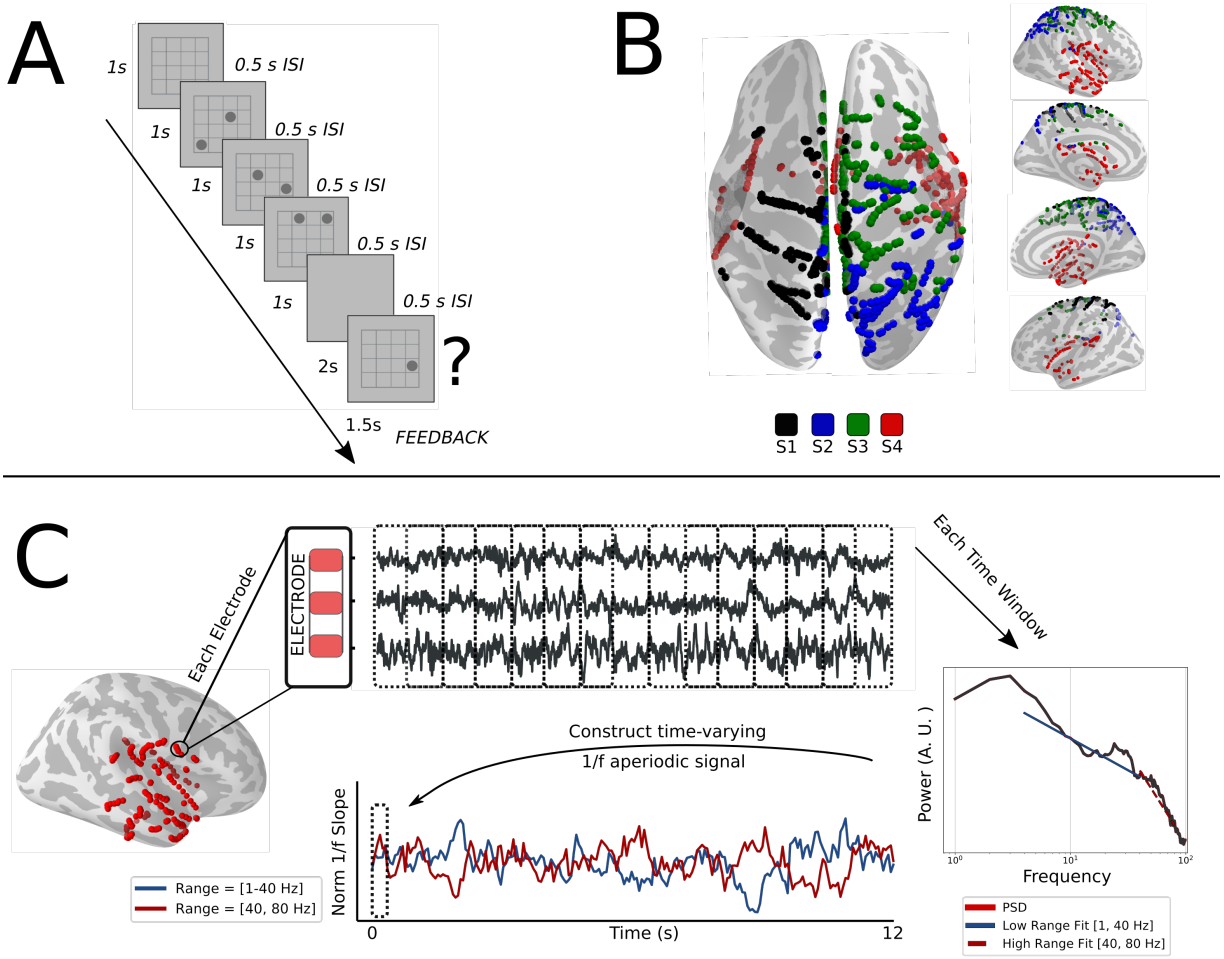

Figure 4.1: Experimental design, distribution of intracranial electrode contacts across participants, and analysis pipeline. (**A**) Experimental design of the visuospatial working memory task. For each trial, participants were instructed to respond whether the presented dot appeared in the three previously presented grids. (**B**) Depth-electrode recording sites across subjects, projected on inflated fsaverage brain. Left: dorsal; Right: lateral (top/bottom) and medial (middle) views. Each color represents a participant. (**C**) Analysis pipeline. At the single-subject level, we segment the data into trials in each electrode. Next, we apply a sliding-window analysis with temporal overlap to obtain time-resolved PSD. To each PSD in each time window, we fit the 1/f slope to low (1-40 Hz) and high (40-80 Hz) frequency ranges. Finally, for every time window, we obtain an estimate of the 1/f slope of each frequency range to construct a time-resolved aperiodic activity.

Spectrograms showing power amplitude for frequencies ranging from 0.5 to 150 Hz revealed heterogeneous spectral signatures across electrodes. As is to be expected, some electrodes showed specific sensitivity to the attentional recruitment, manifesting a transient increase in broad-band

gamma (50-150 Hz; Figure 4.2A, B) while others did not appear to be specifically responsive to the probe. Related to broad-band activations, we found that the high-range 1/f slope also changed transiently before probe onset (Figure 4.2A, B, top), where attentional recruitment had an acute effect in flattening the 1/f slope. We analyzed the single-trial resolution of this effect and found that the flattening of the 1/f slope had a single-trial resolution which was coupled to the onset of the probe and decreased once the subject pressed the button of response (Figure 4.2A, B, middle). Thus, 1/f slope temporal dynamics are consistent with attentional recruitment at the visuospatial working-memory task, which suggest a rapid top-down modulation of desynchronization (See Supplementary Figure 4.7).

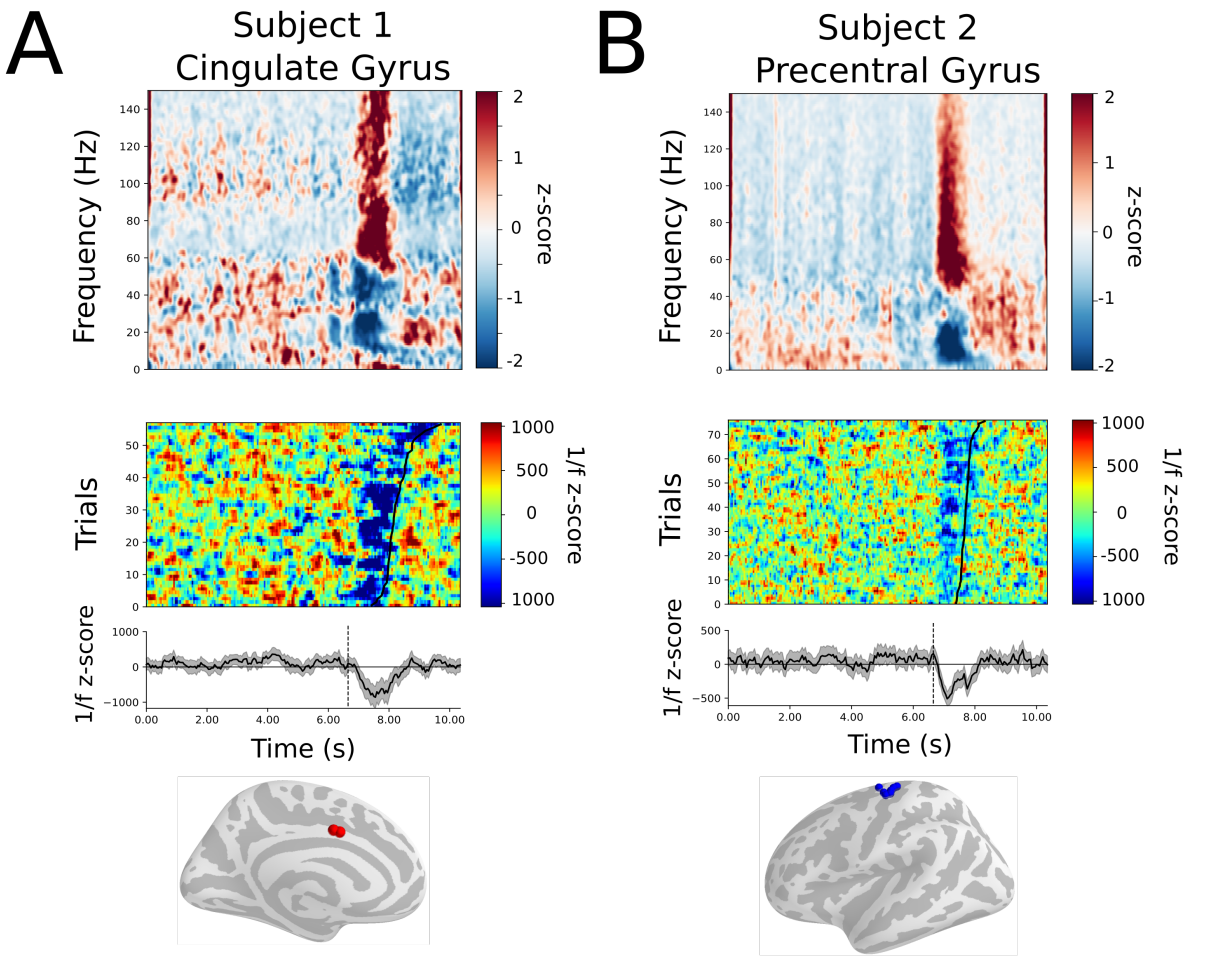

Figure 4.2: Illustrative time-frequency maps and single-trial 1/f aperiodic activity in example areas. (**A**) and (**B**) shows one brain area of each of the two illustrative participants. At the top, morlet-wavelet time-frequency maps are presented for the range between 0.5 to 150 Hz. Note the broad-band gamma activation at probe onset. At the middle-top, a single-trial 1/f slope of the high-range is presented. Colors represent 1/f z-score, where positive values represent a steepening of the slope, while more negative values depict a flattening. Trials are sorted according to reaction-time latencies (black line). The middle-bottom shows the median across trials of 1/f z-score fluctuation at high-range. The dashed line represents the onset of the attentional probe. At the bottom, the recording sites of the brain area represented, corresponding to (A) Cingulate Gyrus, and (B) Precentral Gyrus.

We noted -as it has been previously reported (Miller et al., 2007)- that activations of broad-band gamma were accompanied by an increase in low-frequency power (delta) and a decrease in

intermediate frequencies such as theta, alpha, and beta bands, which is consistent with the dual shape of the PSD seen in Figure 4.1. Previous reports have shown that the 1/f slope at a high range (between 30 and 80 Hz approximately) is correlated with the balance between excitation and inhibition. Interestingly, further reports have found consistent results in different ranges (Waschke et al., 2021; Medel et al., 2020; Trakoshis et al., 2020; Colombo et al., 2019).

As mentioned above, we explored two ranges of 1/f slope due to a prominent "knee" in the PSD. Interestingly, we found that the knee only appeared at baseline, at 40 Hz (Figure 4.3A). Moreover, this shape changed in the attentional recruitment at the probe, transitioning to a single 1/f slope across from 1 to 80 Hz. We next tested whether these signals presented temporal correlations. To have a general signal that can be extrapolated to the whole brain state, we obtained a low-dimensional aperiodic activity by means of principal component analysis (See Material and Methods). We obtained the first temporal principal component (tPC1) of the 1/f signal, which represented more than 30% of the variance of the electrodes. We found that both 1/f ranges presented a high anti-correlated structure (Figure 4.3B). This result is consistent with the time-frequency chart displayed in Figure 4.2, considering that an increase in delta and a decrease in middle frequencies are accompanied by an increase in broadband gamma. To further explore this relation, we calculated the cross-correlation of both tPC1. We found that tPC1 at the high range fit (which is canonically related to balance between E/I) has its highest correlation when it lags -500ms before tPC1 of the low fit (Figure 4.3C). This show that changes in the high-range desynchronization (tPC1) shape low-range desynchronization (tPC2), suggesting that local E/I balance could be shaping the aperiodic activity at lower frequencies.

We next explored the relation between tPC1 of both ranges with canonical band-limited power by means of Hilbert Transform. As expected, the tPC1 of the low range correlated significantly with the lower frequencies of the spectrum in a relatively proportional manner (Figure 4.3D), which suggests that common band-limited filtering of the signal may capture part of the aperiodic signal contained at the lower range. On the other hand, tPC1 of the high range correlated significantly with higher band-limited power fluctuations, suggesting that these signals may also contain part of the 1/f signal activity (Figure 4.3D).

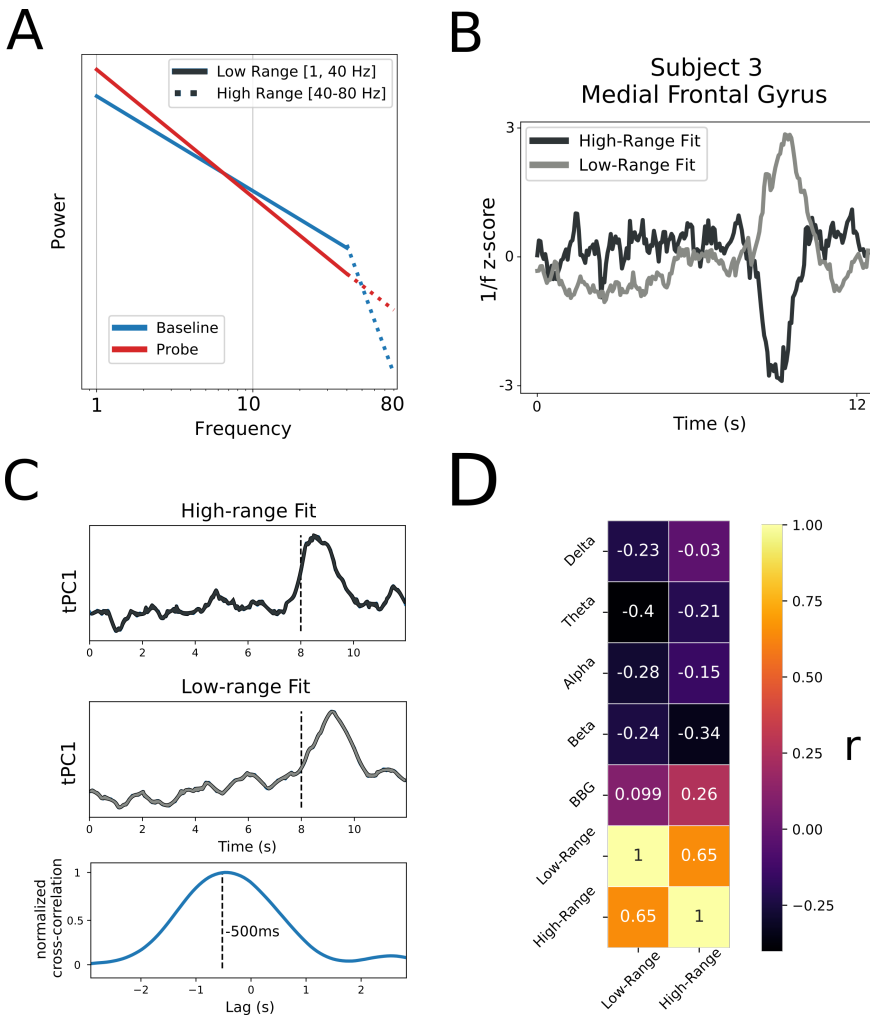

Figure 4.3: Low-dimensional 1/f fluctuation across the cortex and frequency ranges. (**A**) Illustrative 1/f fit at two frequency ranges shows different characteristics depending on the attentional state. The blue line represents the baseline, while the red line depicts the attentional probe segment. The solid line shows the low-range fit and the dashed line represents the high-range fit. (**B**) shows a subject and electrode example of the antagonist temporal dynamics between high and low range fits during VSWM. (**C**) Illustration of dimensionality reduction (n=4) of 1/f fluctuation in each range by means of temporal Principal Component Analysis (tPC). At the bottom, the low-dimensional aperiodic activity cross-correlation in each range has its maximum correlation when the high-range tPC1 precedes by 500 ms the low-range tPC1. (**D**) shows a correlation matrix of each averaged activity of band-limited power with low and high-range tPC1, depicting the spectral contributions are relatively homogenous, suggesting that each band-limited power contains some portion of variance explained by low-dimensional aperiodic activity.

Pupil diameter is a well-known proxy of ascending arousal system activation, which has been shown to be coupled to behaviorally relevant fast switching of cortical states (McGinley et al.,

2015a). We hypothesize that transient flattening of 1/f slope of high range, and steepening at the low range is temporally coupled to arousal-related neuromodulation as observed by pupil diameter fluctuations. We analyzed the simultaneous recording of pupil diameter in three subjects that performed the VWM task. We found that each subject presented a fluctuation of their pupil diameter according to the task (Figure 4.4A). Moreover, we found that attentional recruitment at the probe had a significant effect in widening pupil diameter, as compared to baseline, at a single-trial basis (Figure 4.4B).

Next, we explored the relation between pupil diameter and tPC1 of both ranges. We generated 10000 null pupil signals with a bootstrap block-resampling method (See Materials and Methods) and correlated each null signal with tPC1. We found that each real correlation was significant. To further explore this relation, we calculated the correlation value of the pupil diameter with each electrode, obtaining a distribution of correlation coefficients. We then correlated this distribution with the tPC1 weight of each electrode and found that the higher the correlation of the electrode with the pupil diameter, the higher was its participation in tPC1 (Figure 4.4C). Interestingly, the electrodes that were most significant at their relation with pupil diameter, and had their highest weights in the tPC1, were mostly distributed in the frontoparietal network (Figure 4.4D). These results suggest that the shape of the spectrum (1/f slope) is a general property of electrophysiological signals that fluctuates in a low-dimensional structure and is coupled to arousal-related neuromodulation, as observed by its correlation with pupil diameter.

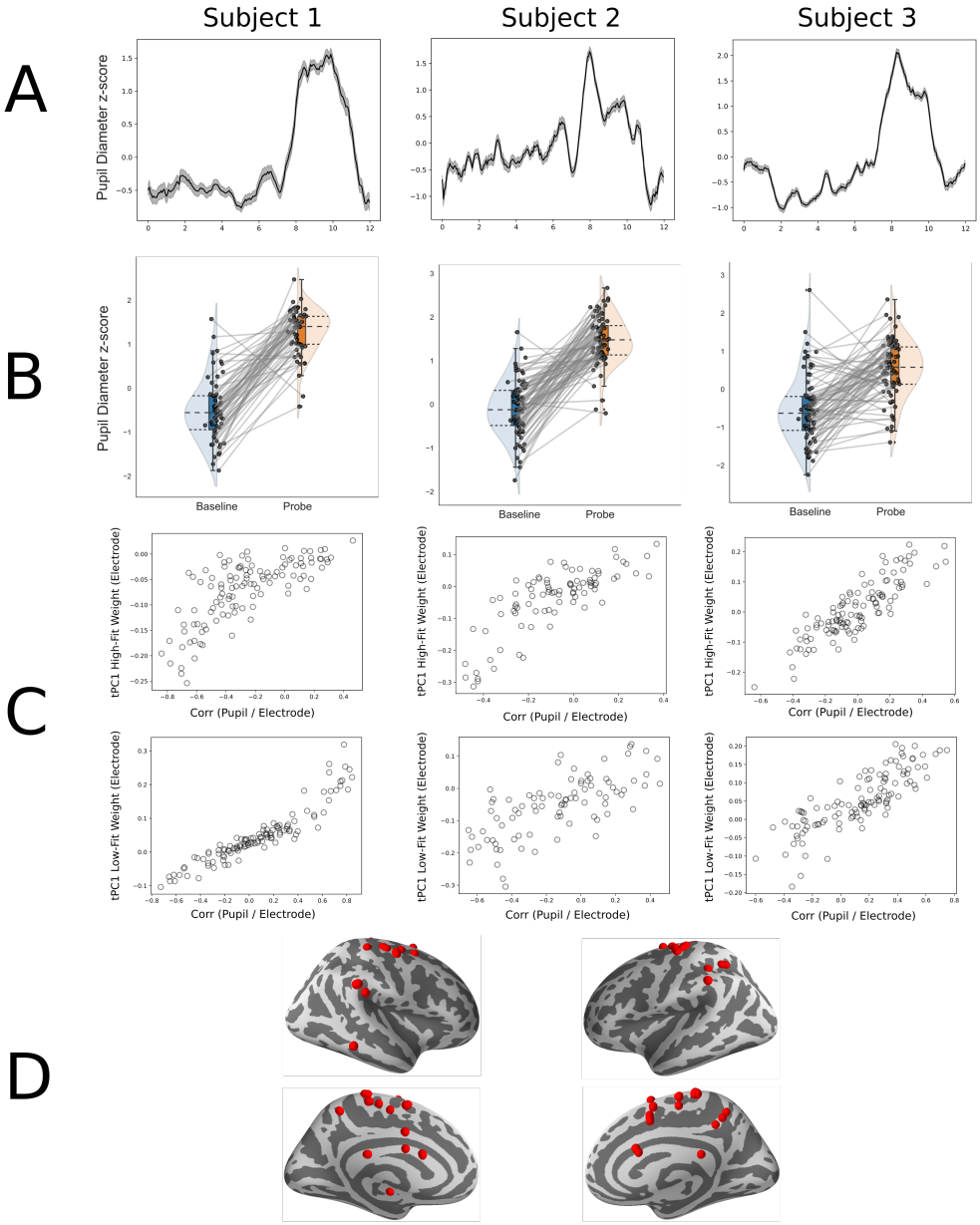

Figure 4.4: Temporal Coupling between tPC1 in the low and high range of 1/f activity with phasic pupil dilation. (**A**) Each panel shows averaged pupil diameter fluctuation for each subject, in the VSWM task. Shaded lines show the standard error of the mean. Note the phasic increase of pupil diameter at the attentional probe (8s). (**B**) Single-trial change in phasic pupil diameter shows an increase at the attentional probe as compared to the baseline state. (**C**) The distribution of correlation values between each iEEG electrode and pupil diameter is correlated with the tPC1 weight in each subject, suggesting that tPC1 captures a low-dimensional aperiodic spatial component that corresponds to pupil fluctuations. (**D**) shows the electrodes with the highest correlation with pupil and highest tPC1 weight.

The low-dimensional structure of the 1/f aperiodic activity consists -as we have shown- of two aperiodic ranges inversely correlated that are both consistently related to arousal-related neuromodulation, as seen by its relation with pupil diameter signal (Figure 4.4). We hypothesize that the low-dimensional structure of this relation is scalable to mesoscale signals as the EEG. Considering that EEG recordings are considered to have important artifacts in frequencies higher than 40 Hz, the low-dimensional aperiodic activity that is consistent with that range is the low range. Thus, we hypothesize that the tPC1 of low-range at EEG is correlated with pupil diameter in attention.

To test this, we explored the tPC1 of the 1/f slope in scalp-EEG in healthy children. The pupil diameter data of this experimental group has been already published elsewhere (Wainstein et al. 2017; Rojas-Líbano et al. 2019). Similar to the task done by the iEEG group, in this experimental paradigm subjects performed an almost exact version which only differed by the total time duration of the stimuli, being this version faster and longer in trials (See Wainstein et al., 2017; Rojas-Líbano et al., 2019; Supplementary Figure 4.10). We analyzed data from 18 subjects using the same methodological approach described in Figure 4.1, with the exception that due to the high signal-to-noise ratio we calculated the time-varying 1/f slope over the mean trial of each subject instead of the single-trial version reported in the iEEG group. To avoid event-related potentials which are known to have an effect over broad frequency ranges in scalp EEG, we subtracted evoked activity to each trial before averaging thus obtaining induced activity, and then calculated the 1/f slope at low-range (1-40 Hz) for each electrode and subject. Next, we calculated the tPC1 for each subject by concatenating each subject's signal (See Materials and Methods).

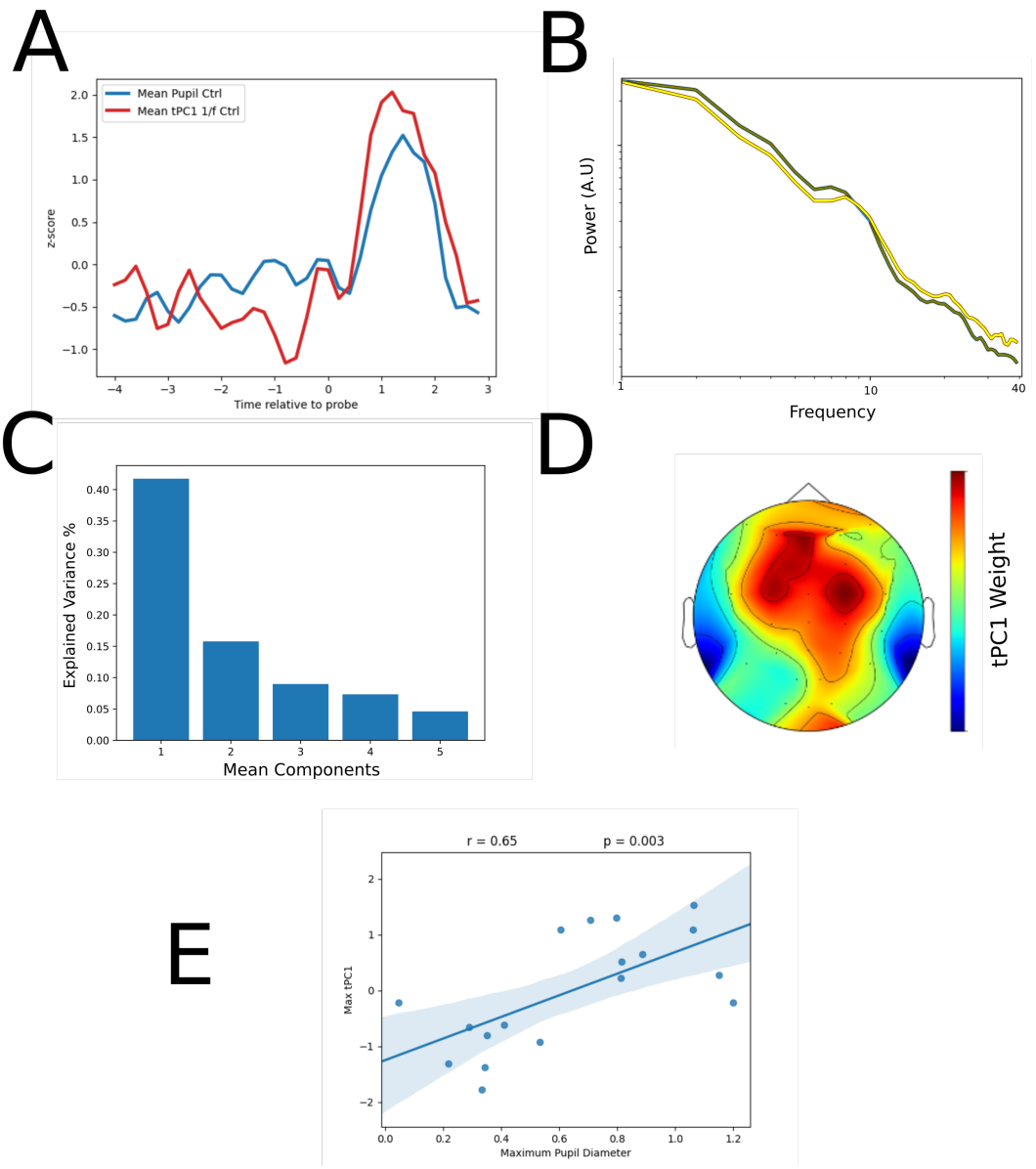

Figure 4.5: Temporal Coupling of Low range tPC1 of 1/f across control subjects in scalp EEG and pupil dilation. (**A**) shows the averaged pupil diameter (blue) and averaged tPC1 (red) across subjects, where phasic pupil diameter is coupled with tPC1 of low-frequency range 1/f fit, mainly at the attentional probe. Note that the tPC1 signal was normalized to fit in a similar range as the pupil diameter. (**B**) Illustrative power spectral density of baseline (yellow) and probe (gray), showing a similar tendency as seen in Figure 4.3 in the steepening of the 1/f slope at lower frequencies when attentional recruitment occurred. (**C**) Mean explained variance of each principal component across subjects. Average tPC1 explained more than 40% of the variance. (**D**) shows the spatial topography of the tPC1 weights, distributing mainly at midline electrodes, with its peak at the mid-frontal area. (**E**) Subject relation between maximum pupil diameter and maximum value of tPC1 shows a positive correlation (Pearson r = 0.65, p-value ¡ 0.005).

We found that mean tPC1 of 1/f slope in scalp EEG -which explained more than 40% of the variance (Figure 4.5C)- had a temporal fluctuation in accordance with the task design, having its maximum peak value at the attentional recruitment in the probe (Figure 4.5A), which represents a steeper 1/f slope at probe as compared to baseline state (Figure 4.5B). The spatial weight of the tPC1 which depicts the individual contribution of each electrode to the tPC1 had maximum in midline electrodes, particularly in mid-frontal electrodes (Figure 4.5C). To test the correlation between tPC1 of the aperiodic signal and the pupil diameter, we correlated the mean maximum pupil dilation with their maximum tPC1 at the subject's level. We found that both measures were significantly correlated (Pearson R = 0.65, p ¡ 0.005; Figure 4.5E).

We thus show that the low-dimensional fluctuation of 1/f slope transiently changes in close relation to attentional recruitment, and this signal is also highly correlated to phasic pupil dilation across spatial and temporal scales.

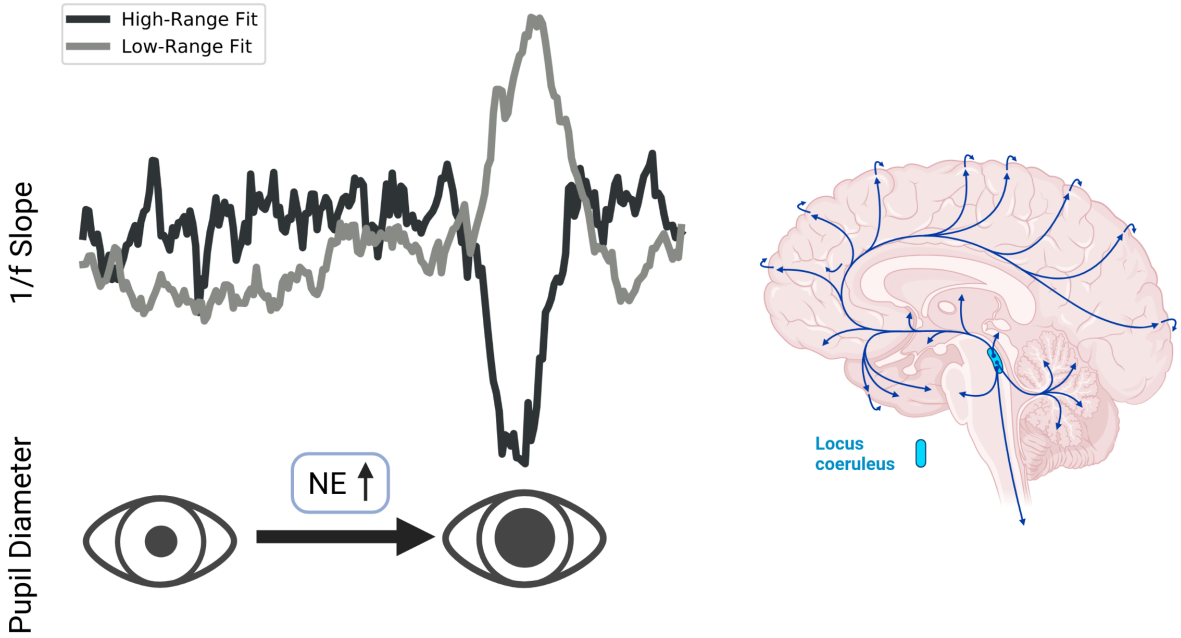

Figure 4.6: Summary figure. Attentional rapid state shift is related to an increase in noradrenergic signaling as represented by the dilation of pupil diameter and is coupled to 1/f aperiodic signal fluctuation.

4.4 Discussion

This chapter presents evidence that attentional rapid state switch is related to transient low-dimensional 1/f aperiodic activity and phasic pupil diameter increase in human iEEG and scalp EEG. First, we show that the spectral periodic and aperiodic features showed strong task responsiveness (Figure 4.2; Supplementary Figure 4.7). To capture the global cortical state, we calculated the temporal low-dimensional aperiodic activity through temporal PCA (Supplementary Figure 4.8; see Materials and Methods) and found two antagonistic frequency ranges of aperiodic activity, where both responded transiently to attentional recruitment (Figure 4.3). Particular band contributions to 1/f aperiodic tPC1 were relatively proportional, suggesting that each band activity is composed of both aperiodic and periodic components (Figure 4.3D). Next, we show that pupil diameter had phasic dilation at the probe's onset (Figure 4A, 4B), which suggests that attentional shifts are coupled to higher arousal-related neuromodulation. We found that tPC1 was intimately related to pupil diameter (Figure 4.4C), and both time series had significant correlation values (Supplementary Figure 4.9). Finally, we show the low-dimensional aperiodic activity can be extrapolated to a broader electrophysiological scale with EEG data at the low-frequency range. As expected, we found that pupil diameter was highly coupled with tPC1 (Figure 4.5).

Recently, it has been proposed that the action of neuromodulatory systems like LC-NE system over cognition occurs in a low-dimensional manifold (McCormick et al., 2020; Shine et al. 2019). For example, Shine et al. (2019) performed a temporal principal component analysis (PCA) over fMRI-BOLD activity, which is known to have a less complex spectrum of frequencies as compared to electrophysiology. This suggests that the dimensionality reduction of BOLD is capturing the main fluctuating property of this signal. However, electrophysiological signals are known to have multiple sources interacting, such as ultra-slow oscillations (He and Raichle 2009), cross-frequency coupling, local oscillatory power, and background activity (He and Raichle 2009; Voytek and Knight 2015). From this perspective, to perform a similar dimensionality reduction as the one done by Shine et al. (2019), it is necessary to filter the desired signal hypothesized under neuromodulatory control, representing the global cortical state. We here show that by performing a similar dimensionality reduction approach as Shine et al. (2019) over our selected

signal (1/f slope), we were able to identify a low-dimensional signal that was heavily task-related and highly correlated with pupil diameter.

Our results are consistent with recent findings suggesting the aperiodic exponent as a neural correlate of information processing in children and adolescents (Ostlund et al., 2021) and can serve as a proxy of neuromodulatory ascending-system integrity (Robertson et al., 2019; Pertermann et al., 2019). Our work highlights the usage of temporal resolution of 1/f aperiodic activity and suggests that dynamic transition between cortical states is highly related to noradrenergic signaling as observed by the relation between 1/f slope and pupil diameter. Although recent work had studied 1/f exponent in the EEG across the cognitive task and its relation with event-related potential (Dave et al., 2018), we here discard evoked activity and analyzed aperiodic signal in a time-resolved fashion.

When interpreting the role of neural background activity in rapid attentional recruitment, it should be considered that its fluctuations can serve as fast modulators of information (Harris and Thiele, 2011), where a state with higher noise can enhance neural information and responsiveness (Chance et al., 2002; Zerlaut et al., 2017; Destexhe et al., 2003). Moreover, LC-NE system and arousal-related neuromodulators contribute substantially to attentional upregulation of neural excitability (Herrero et al., 2009), which is likely produced via downregulation of activity-dependent adaptation, decreasing K+ currents (Madison et al., 1987; McCormick, 1992; Sripati and Johnson, 2006; Medel et al., In Prep).

The spectral power-law slope has been extensively related to E/I balance (Lombardi et al., 2017; Gao et al., 2017; Colombo et al., 2019; Trakoshis et al., 2020; Medel et al., 2020; Washcke et al., 2021). It is important to note that the 1/f parametrization (Donoghue et al., 2020) can model other two parameters that were not explored in this work: the 'knee', which is related to the timescale of the signal (Gao et al., 2020); and the 'offset' which is the intercept of the 1/f function, and represents the broadband signal (Manning et al., 2009; Ossandón et al., 2011). We recently showed that E/I balance is tracked precisely by 1/f slope and not offset and that the aperiodic slope was intimately related with Lempel-Ziv complexity (Lempel and Ziv, 1976; Medel et al., 2020), which is an information-based measure calculated in the time domain and reflects the vastness of repertoire of brain activity patterns (Wenzel et al., 2019). Other measures have reported similar relations with 1/f aperiodic signal and E/I balance, namely entropy-based

measures (Waschke et al., 2019) and memory-based signals such as Hurst exponent (Trakoshis et al., 2020). Considering the robustness of the spectral parameterization in separating oscillatory from the aperiodic signal in the frequency domain, further work should explore how each of these similar measures in the temporal domain relates to broad parameter space and conditions.

Consistent with our biological framework, clinical and animal models of ADHD and ASD have shown altered GABAergic and glutamatergic activity (Edden et al., 2012; Hammerness et al., 2012; Zimmerman et al., 2015), suggesting that arousal-related neuromodulation affects multi-scale activity by disrupting the balance between excitation and inhibition (Morello et al., 2020; Lee et al., 2017; Sohal Rubenstein, 2019). Coherent with this, evidence has shown that static aperiodic measures implicated in neuromodulator-related psychiatric disorders, such as ADHD (Robertson et al., 2019; Pertermann et al., 2019; Ostlund et al., 2021) and ASD (Trakoshis et al., 2020; Bruining et al., 2020), both of which have previously been related with pupil diameter alterations (Wainstein et al., 2017; DiCriscio et al., 2017). It has recently been argued that clinically relevant measures, such as band ratio, can be conflated by aperiodic activity (Donoghue et al., 2020b). We contribute to this literature by showing that dynamic aperiodic shifts can give a more refined analysis of the possible brain mechanisms involved in arousal-related neuromodulation and its effect on attention. Studies that simultaneously consider periodic and aperiodic changes from a time-resolved perspective will be critical for clarifying these impairments' neural mechanisms and their relation with LC-NE system and arousal-related neuromodulation.

Placing our findings into the perspective of cognition, our novel results shed light on the temporal resolution of the dynamic shaping of cortical states putatively by ascending neuromodulators on a fine temporal scale relevant for attentive behavior.

4.5 Supplementary Material

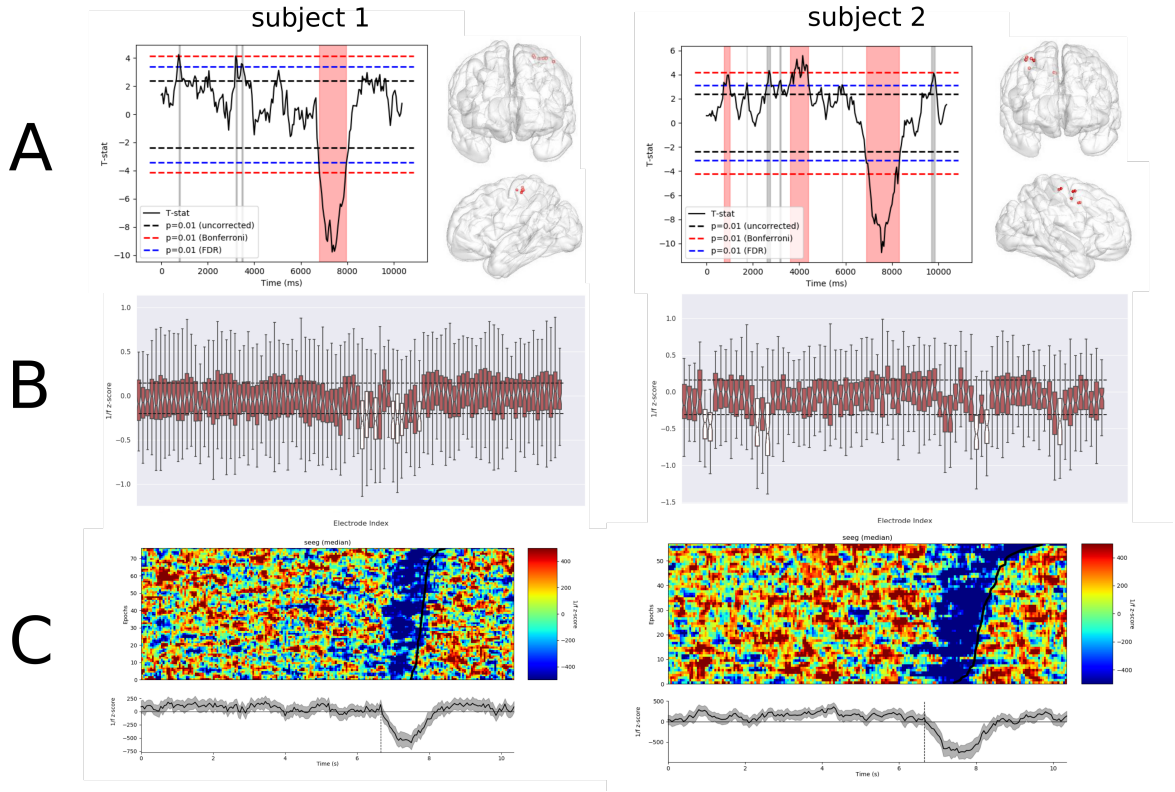

Figure 4.7: Complementary approach to show task-responsive electrodes. We used the z-score normalized 1/f signal and selected the probe temporal samples. Next, we selected the electrodes that had +3 or -3 standard deviation. (**A**) shows the t-statistics comparing the signal with null hypothesis that the mean was equal to 0. Dashed lines show multiple comparison threshold of significance. Vertical red blocks show significant clusters (p¡0.05). (**B**) shows the selected electrodes, and horizontal dashed lines represent the SD criteria. Selected electrodes are shown in the glass-brain. (**C**) Top shows single-trial time-resolved 1/f aperiodic activity of the median of the selected electrodes. Bottom shows the median across selected electrodes and trials of 1/f z-score activity. (Glass-brain from LAN toolbox; `http://neurocics.udd.cl/LANtoolbox.html`).

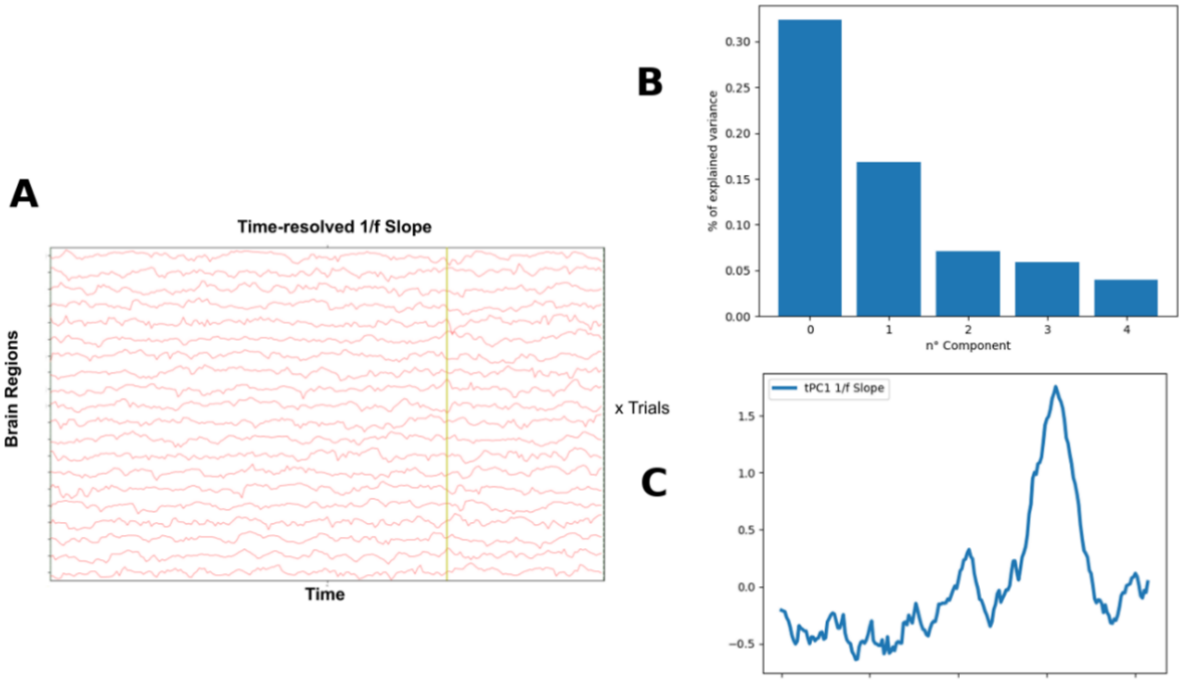

Figure 4.8: Illustration of temporal principal component analysis (tPC). (**A**) shows the single-trial signal of 1/f activity. To obtain tPC we concatenated each trial to obtain a single time-serie containing all trials across electrodes. Next, we calculated tPC and reduced the spatial dimension to 5 components that together explained near 40% of the variance (**B**). We then segmented the tPC to recover single-trial resolution. (**C**) shows the mean tPC1 in an example subject at the low 1/f frequency range.

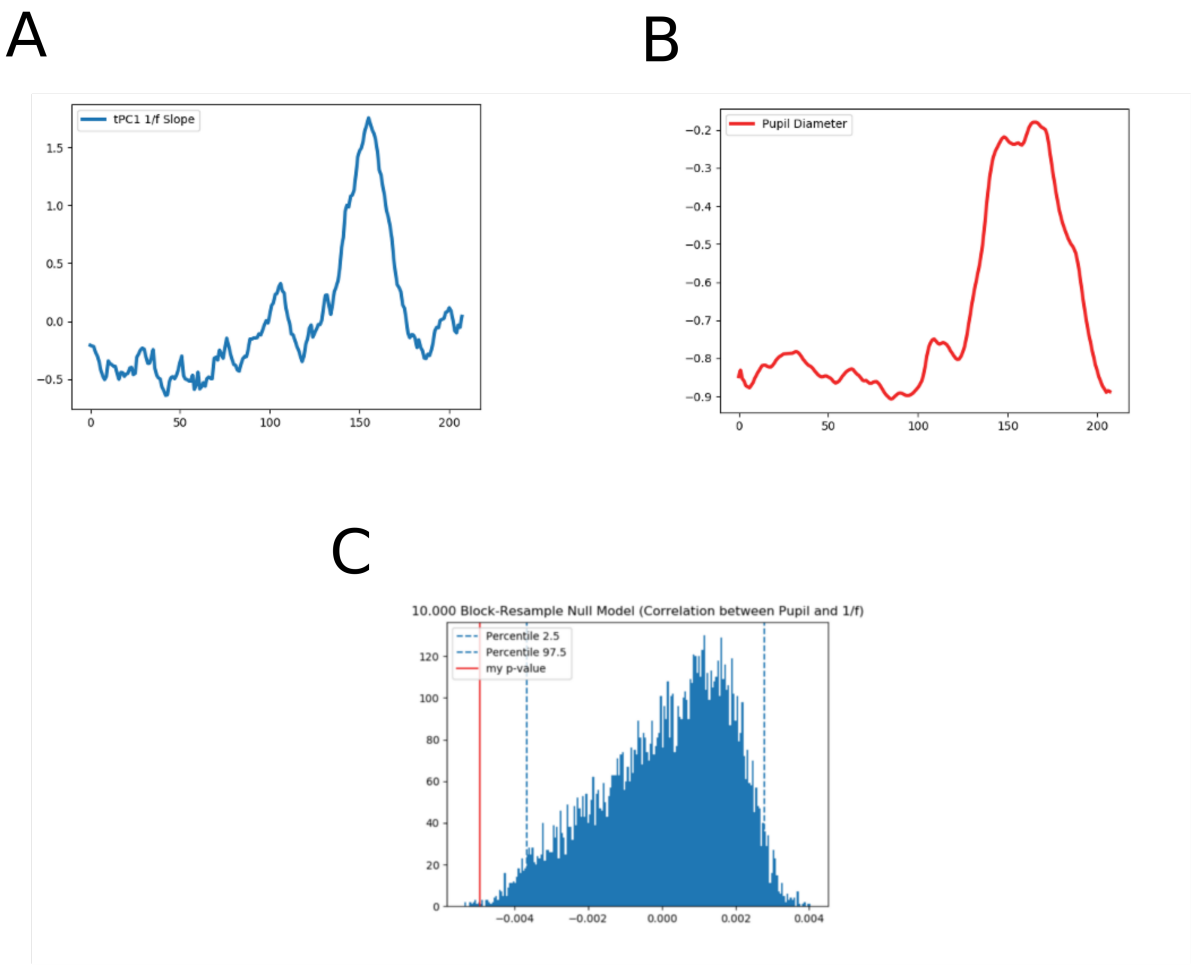

Figure 4.9: Pipeline of correlation between pupil diameter and tPC1. (**A**) shows illustrative mean tPC1 for low-range 1/f fit. (**B**) shows illustrative mean pupil diameter. Both signals depicted in (A) and (B) are correlated. Next, we built null signals of pupil diameter implementing block-resampling with 10.000 permutations, and to each null pupil signal we calculated the Pearson correlation with tPC1. (**C**) shows the null distribution of p-values for each correlation. Dashed lines represent the 2.5 and 97.5 percentiles, while the red line shows the p-value of the original correlation.

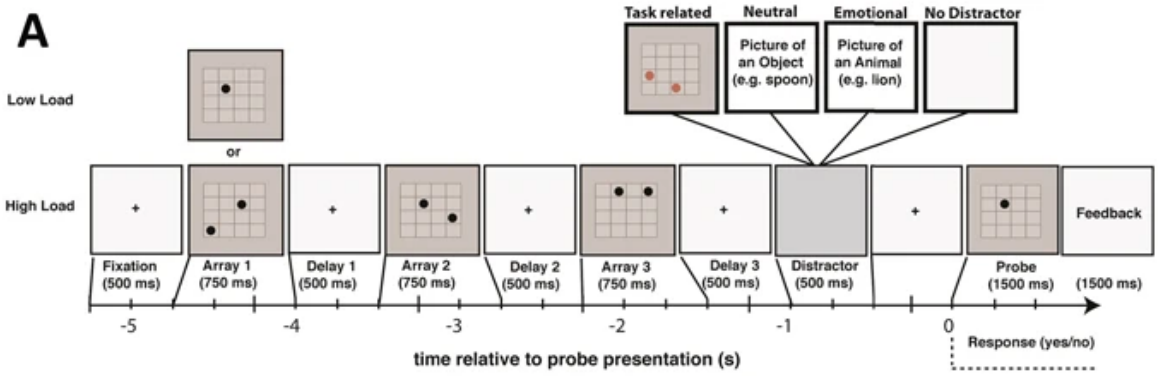

Figure 4.10: Experimental design of VSWM task (obtained from Wainstein et al., 2017).

Bibliography

[1] Gao, R., Peterson, E. J., Voytek, B. (2017). Inferring synaptic excitation/inhibition balance from field potentials. Neuroimage, 158, 70-78.

[2] Colombo, M. A., Napolitani, M., Boly, M., Gosseries, O., Casarotto, S., Rosanova, M., ... Sarasso, S. (2019). The spectral exponent of the resting EEG indexes the presence of consciousness during unresponsiveness induced by propofol, xenon, and ketamine. NeuroImage, 189, 631-644.

[3] Trakoshis, S., Rocchi, F., Canella, C., You, W., Chakrabarti, B., Ruigrok, A. N., ... MRC AIMS Consortium. (2020). Intrinsic excitation-inhibition imbalance affects medial prefrontal cortex differently in autistic men versus women. Elife, 9, e55684.

[4] Medel, V., Irani, M., Ossandon, T., Boncompte, G. (2020). Complexity and 1/f slope jointly reflect cortical states across different E/I balances. bioRxiv.

[5] Boncompte, G., Medel, V., Cortínez, L. I., Ossandón, T. (2021). Brain activity complexity has a non-linear relation to the level of propofol sedation. British Journal of Anaesthesia.

[6] Chmielewski, W. X., Mückschel, M., Ziemssen, T., Beste, C. (2017). The norepinephrine system affects specific neurophysiological subprocesses in the modulation of inhibitory control by working memory demands. Human Brain Mapping, 38(1), 68-81.

[7] Costa, V. D., Rudebeck, P. H. (2016). More than meets the eye: the relationship between pupil size and locus coeruleus activity. Neuron, 89(1), 8-10.

[8] Joshi, S., Li, Y., Kalwani, R. M., Gold, J. I. (2016). Relationships between pupil diameter and neuronal activity in the locus coeruleus, colliculi, and cingulate cortex. Neuron, 89(1), 221-234.

[9] Fotiou, D. F., Stergiou, V., Tsiptsios, D., Lithari, C., Nakou, M., Karlovasitou, A. (2009). Cholinergic deficiency in Alzheimer's and Parkinson's disease: evaluation with pupillometry. International Journal of Psychophysiology, 73(2), 143-149.

[10] Naicker, P., Anoopkumar-Dukie, S., Grant, G. D., Neumann, D. L., Kavanagh, J. J. (2016). Central cholinergic pathway involvement in the regulation of pupil diameter, blink rate and cognitive function. Neuroscience, 334, 180-190.

[11] Reimer, J., McGinley, M. J., Liu, Y., Rodenkirch, C., Wang, Q., McCormick, D. A., Tolias, A. S. (2016). Pupil fluctuations track rapid changes in adrenergic and cholinergic activity in cortex. Nature communications, 7(1), 1-7.

[12] Phillips, M. A., Szabadi, E., Bradshaw, C. M. (2000). Comparison of the effects of clonidine and yohimbine on spontaneous pupillary fluctuations in healthy human volunteers. Psychopharmacology, 150(1), 85-89.

[13] Varazzani, C., San-Galli, A., Gilardeau, S., Bouret, S. (2015). Noradrenaline and dopamine neurons in the reward/effort trade-off: a direct electrophysiological comparison in behaving monkeys. Journal of Neuroscience, 35(20), 7866-7877.

[14] Liu, Y., Rodenkirch, C., Moskowitz, N., Schriver, B., Wang, Q. (2017). Dynamic lateralization of pupil dilation evoked by locus coeruleus activation results from sympathetic, not parasympathetic, contributions. Cell reports, 20(13), 3099-3112.

[15] Schwalm, M., Jubal, E. R. (2017). Back to pupillometry: How cortical network state fluctuations tracked by pupil dynamics could explain neural signal variability in human cognitive neuroscience. Eneuro, 4(6).

[16] McGinley, M. J., Vinck, M., Reimer, J., Batista-Brito, R., Zagha, E., Cadwell, C. R., ... McCormick, D. A. (2015a). Waking state: rapid variations modulate neural and behavioral responses. Neuron, 87(6), 1143-1161.

[17] McGinley, M. J., David, S. V., McCormick, D. A. (2015b). Cortical membrane potential signature of optimal states for sensory signal detection. Neuron, 87(1), 179-192.

[18] McCormick, D. A., Nestvogel, D. B., He, B. J. (2020). Neuromodulation of brain state and behavior. Annual review of neuroscience, 43, 391-415.

[19] Aston-Jones, G., Cohen, J. D. (2005). An integrative theory of locus coeruleus-norepinephrine function: adaptive gain and optimal performance. Annu. Rev. Neurosci., 28, 403-450.

[20] Calvo, M. G., Lundqvist, D. (2008). Facial expressions of emotion (KDEF): Identification under different display-duration conditions. Behavior research methods, 40(1), 109-115.

[21] Schaefer, A., Kong, R., Gordon, E. M., Laumann, T. O., Zuo, X. N., Holmes, A. J., ... Yeo, B. T. (2018). Local-global parcellation of the human cerebral cortex from intrinsic functional connectivity MRI. Cerebral cortex, 28(9), 3095-3114.

[22] Kucyi, A., Schrouff, J., Bickel, S., Foster, B. L., Shine, J. M., Parvizi, J. (2018). Intracranial electrophysiology reveals reproducible intrinsic functional connectivity within human brain networks. Journal of Neuroscience, 38(17), 4230-4242.

[23] Kucyi, A., Daitch, A., Raccah, O., Zhao, B., Zhang, C., Esterman, M., ... Parvizi, J. (2020). Electrophysiological dynamics of antagonistic brain networks reflect attentional fluctuations. Nature communications, 11(1), 1-14.

[24] Gramfort, A., Luessi, M., Larson, E., Engemann, D. A., Strohmeier, D., Brodbeck, C., ... Hämäläinen, M. S. (2014). MNE software for processing MEG and EEG data. Neuroimage, 86, 446-460.

[25] Jas, M., Larson, E., Engemann, D. A., Leppäkangas, J., Taulu, S., Hämäläinen, M., Gramfort, A. (2018). A reproducible MEG/EEG group study with the MNE software: recommendations, quality assessments, and good practices. Frontiers in neuroscience, 12, 530.

[26] Donoghue, T., Haller, M., Peterson, E. J., Varma, P., Sebastian, P., Gao, R., ... Voytek, B. (2020). Parameterizing neural power spectra into periodic and aperiodic components. Nature neuroscience, 23(12), 1655-1665.

[27] Voytek, B., Knight, R. T. (2015). Dynamic network communication as a unifying neural basis for cognition, development, aging, and disease. Biological psychiatry, 77(12), 1089-1097.

[28] Gao, R., van den Brink, R. L., Pfeffer, T., Voytek, B. (2020). Neuronal timescales are functionally dynamic and shaped by cortical microarchitecture. Elife, 9, e61277.

[29] Fallon, J., Ward, P. G., Parkes, L., Oldham, S., Arnatkevičiūtė, A., Fornito, A., Fulcher, B. D. (2020). Timescales of spontaneous fMRI fluctuations relate to structural connectivity in the brain. Network Neuroscience, 4(3), 788-806.

[30] Mahjoory, K., Schoffelen, J. M., Keitel, A., Gross, J. (2020). The frequency gradient of human resting-state brain oscillations follows cortical hierarchies. Elife, 9, e53715.

[31] Pedregosa, F., Varoquaux, G., Gramfort, A., Michel, V., Thirion, B., Grisel, O., ... Duchesnay, E. (2011). Scikit-learn: Machine learning in Python. the Journal of machine Learning research, 12, 2825-2830.

[32] Waskom, M. L. (2021). Seaborn: statistical data visualization. Journal of Open Source Software, 6(60), 3021.

[33] Politis, D. N., White, H. (2004). Automatic block-length selection for the dependent bootstrap. Econometric reviews, 23(1), 53-70.

[34] Politis, D., White, H., Patton, A., Politis, D. N., White, H. (2009). Correction to "Automatic Block-Length Selection for the Dependent Bootstrap" by. In Econometric Reviews.

[35] Politis, D. N., Romano, J. P. (1995). Bias-corrected nonparametric spectral estimation. Journal of time series analysis, 16(1), 67-103.

[36] Wainstein, G., Rojas-Líbano, D., Crossley, N. A., Carrasco, X., Aboitiz, F., Ossandón, T. (2017). Pupil size tracks attentional performance in attention-deficit/hyperactivity disorder. Scientific reports, 7(1), 1-9.

[37] Miller, K. J., Leuthardt, E. C., Schalk, G., Rao, R. P., Anderson, N. R., Moran, D. W., ... Ojemann, J. G. (2007). Spectral changes in cortical surface potentials during motor movement. Journal of Neuroscience, 27(9), 2424-2432.

[38] Waschke, L., Donoghue, T., Fiedler, L., Smith, S., Garrett, D. D., Voytek, B., Obleser, J. (2021). Modality-specific tracking of attention and sensory statistics in the human electrophysiological spectral exponent. bioRxiv.

[39] Rojas-Líbano, D., Wainstein, G., Carrasco, X., Aboitiz, F., Crossley, N., Ossandón, T. (2019). A pupil size, eye-tracking and neuropsychological dataset from ADHD children during a cognitive task. Scientific data, 6(1), 1-6.

[40] Shine, J. M., Breakspear, M., Bell, P. T., Martens, K. A. E., Shine, R., Koyejo, O., ... Poldrack, R. A. (2019). Human cognition involves the dynamic integration of neural activity and neuromodulatory systems. Nature neuroscience, 22(2), 289-296.

[41] He, B. J., Raichle, M. E. (2009). The fMRI signal, slow cortical potential and consciousness. Trends in cognitive sciences, 13(7), 302-309.

[42] Ostlund, B. D., Alperin, B. R., Drew, T., Karalunas, S. L. (2021). Behavioral and cognitive correlates of the aperiodic (1/f-like) exponent of the EEG power spectrum in adolescents with and without ADHD. Developmental cognitive neuroscience, 48, 100931.

[43] Robertson, M. M., Furlong, S., Voytek, B., Donoghue, T., Boettiger, C. A., Sheridan, M. A. (2019). EEG power spectral slope differs by ADHD status and stimulant medication exposure in early childhood. Journal of neurophysiology, 122(6), 2427-2437.

[44] Pertermann, M., Bluschke, A., Roessner, V., Beste, C. (2019). The modulation of neural noise underlies the effectiveness of methylphenidate treatment in attention-deficit/hyperactivity disorder. Biological Psychiatry: Cognitive Neuroscience and Neuroimaging, 4(8), 743-750.

[45] Dave, S., Brothers, T. A., Swaab, T. Y. (2018). 1/f neural noise and electrophysiological indices of contextual prediction in aging. Brain research, 1691, 34-43.

[46] Harris, K. D., Thiele, A. (2011). Cortical state and attention. Nature reviews neuroscience, 12(9), 509-523.

[47] Chance, F. S., Abbott, L. F., Reyes, A. D. (2002). Gain modulation from background synaptic input. Neuron, 35(4), 773-782.

[48] Zerlaut, Y., Destexhe, A. (2017). Enhanced responsiveness and low-level awareness in stochastic network states. Neuron, 94(5), 1002-1009.

[49] Destexhe, A., Rudolph, M., Paré, D. (2003). The high-conductance state of neocortical neurons in vivo. Nature reviews neuroscience, 4(9), 739-751.

[50] Herrero, J. L., Roberts, M. J., Delicato, L. S., Gieselmann, M. A., Dayan, P.,& Thiele, A. (2008). Acetylcholine contributes through muscarinic receptors to attentional modulation in V1. Nature, 454(7208), 1110-1114.

[51] Madison, D. V., Lancaster, B.,& Nicoll, R. A. (1987). Voltage clamp analysis of cholinergic action in the hippocampus. Journal of Neuroscience, 7(3), 733-741.

[52] McCormick, D. A. (1992). Neurotransmitter actions in the thalamus and cerebral cortex and their role in neuromodulation of thalamocortical activity. Progress in neurobiology, 39(4), 337-388.

[53] Lombardi, F., Herrmann, H. J., de Arcangelis, L. (2017). Balance of excitation and inhibition determines 1/f power spectrum in neuronal networks. Chaos: An Interdisciplinary Journal of Nonlinear Science, 27(4), 047402.

[54] Manning, J. R., Jacobs, J., Fried, I., Kahana, M. J. (2009). Broadband shifts in local field potential power spectra are correlated with single-neuron spiking in humans. Journal of Neuroscience, 29(43), 13613-13620.

[55] Ossandón, T., Jerbi, K., Vidal, J. R., Bayle, D. J., Henaff, M. A., Jung, J., ... Lachaux, J. P. (2011). Transient suppression of broadband gamma power in the default-mode network is correlated with task complexity and subject performance. Journal of Neuroscience, 31(41), 14521-14530.

[56] Wenzel, M., Han, S., Smith, E. H., Hoel, E., Greger, B., House, P. A., Yuste, R. (2019). Reduced repertoire of cortical microstates and neuronal ensembles in medically induced loss of consciousness. Cell systems, 8(5), 467-474.

[57] Waschke, L., Tune, S., Obleser, J. (2019). Local cortical desynchronization and pupil-linked arousal differentially shape brain states for optimal sensory performance. Elife, 8, e51501.

[58] Edden, R. A., Crocetti, D., Zhu, H., Gilbert, D. L., Mostofsky, S. H. (2012). Reduced GABA concentration in attention-deficit/hyperactivity disorder. Archives of general psychiatry, 69(7), 750-753.

[59] Zimmermann, A. M., Jene, T., Wolf, M., Görlich, A., Gurniak, C. B., Sassoè-Pognetto, M., ... Rust, M. B. (2015). Attention-deficit/hyperactivity disorder–like phenotype in a mouse model with impaired actin dynamics. Biological psychiatry, 78(2), 95-106.

[60] Hammerness, P., Biederman, J., Petty, C., Henin, A., Moore, C. M. (2012). Brain biochemical effects of methylphenidate treatment using proton magnetic spectroscopy in youth with attention-deficit hyperactivity disorder: A controlled pilot study. CNS neuroscience therapeutics, 18(1), 34-40.

[61] Morello, F., Voikar, V., Parkkinen, P., Panhelainen, A., Rosenholm, M., Makkonen, A., ... Partanen, J. (2020). ADHD-like behaviors caused by inactivation of a transcription factor controlling the balance of inhibitory and excitatory neuron development in the mouse anterior brainstem. Translational psychiatry, 10(1), 1-15.

[62] Sohal, V. S., Rubenstein, J. L. (2019). Excitation-inhibition balance as a framework for investigating mechanisms in neuropsychiatric disorders. Molecular psychiatry, 24(9), 1248-1257.

[63] Bruining, H., Hardstone, R., Juarez-Martinez, E. L., Sprengers, J., Avramiea, A. E., Simpraga, S., ... Linkenkaer-Hansen, K. (2020). Measurement of excitation-inhibition ratio in autism spectrum disorder using critical brain dynamics. Scientific reports, 10(1), 1-15.

[64] DiCriscio, A. S., Troiani, V. (2017). Pupil adaptation corresponds to quantitative measures of autism traits in children. Scientific reports, 7(1), 1-9.

[65] Donoghue, T., Dominguez, J., Voytek, B. (2020). Electrophysiological frequency band ratio measures conflate periodic and aperiodic neural activity. Eneuro, 7(6).

Chapter 5

Conclusions

This dissertation combines computational neuroscience by simulating brain activity as well as modelling-driven analysis of electrophysiological data to infer mesoscale neural dynamics. With this strategy the selected signals -aperiodic and complexity- are beyond mere correlates of cognition and allow the possibility to serve as proxies of low-level biological mechanisms underlying attention.

The main hypothesis of this dissertation was that cortical states, balance between E/I, LC-NE neuromodulation and cognitive processes such as attention, are tightly intertwined. This junction and the brain mechanisms supporting this junction was explored. Our evidence shows that this relation is supported by LC-NE neuromodulatory mechanism which would change E/I balance shaping mesoscale signals. We presented our results, in a two step hypothesis procedure to incorporate computational modelling with experimental data analysis.

Our *Objective 1* was explored in **Chapter 1**, where we make use of neural modelling and simulation to relate two apparently diverse field potential signals (Lempel-Ziv Complexity and 1/f slope of the power spectrum) as reflecting the cortical state, and thus the balance between excitation and inhibition. With this model-driven analytical tool, we extend the analysis towards cognition to explore *Objective 2*. In **Chapter 2**, we make use of an open dataset to show that changes in our proxy of balance between excitation and inhibition can track the state of sedation and behavioral performance of subjects with pharmacologically increased inhibition. The modulation of the balance between excitation and inhibition does not occur by itself, though.

Changes in the balance may occur by direct pharmacological intervention (as in Chapter 1 and 2), or it can be regulated by a dynamical top-down controlled system, which is what we proposed to explore in *Objective 3*. In **Chapter 3** we show that changes in our proxy of balance between excitation and inhibition can also occur by manipulating spike-frequency adaptation, a mechanism known to depend on K+ channels which regulate the burstiness of neural activity. The dynamic elimination of spike-frequency adaptation by arousal-related neuromodulation diminishes K+ and increases the burstiness of neural population activity, making the system enter in a highly non-linear state. Although the balance between excitation and inhibition can be regulated by arousal-related neuromodulation, this mechanism is known to be under important top-down control with strong temporal resolution depending on the behavioral context. We explored *Objective 4* in **Chapter 4** where we show how our proxy of excitation and inhibition changes in a visuospatial working memory task. Furthermore, we characterize the temporal dynamics of this fluctuation according to the attentional demand, and show that the balance between excitation and inhibition is maximal in the highest attentional demand, suggesting that this mechanism is under fine top-down control. Indeed, our proxy of excitation and inhibition balance strongly correlates with arousal-related neuromodulation as addressed by pupil diameter signal. As predicted, the balance between excitation and inhibition reflects a multiscale parameter of cortical state which can be observed as a low-dimensional signal across the brain. This low-dimensional signal tracks attentional loading, as well as arousal-related neuromodulation in both invasive and non-invasive electrophysiological recordings, evidencing the scalability of the proposed modeling-driven measure.

Neuroscience is quickly moving towards big data. In the case of cognitive neuroscience, where space and time are of essence, the high-dimensionality of brain signals makes as an important task in the field, to provide meaningful description of the mechanisms underlying each latent process that compose the whole complex signal. With this established, insightful questions and hypotheses can be formulated to search for the biological underpinnings of cognition.

Adaptive cognitive flexibility is thought to arise from coordinated mesoscopic circuit dynamics which organize in macroscopic brain networks. The ascending arousal system innervates heterogeneously to different areas, modulating diverse aspects of cortical brain dynamics. A major challenge to step further this dissertation is to integrate macroscale brain connectivity,

such as large-scale functional network topology, and explore brain activity and its multiple configurations linking dynamics to biology in order to step closer to a mechanistic understanding of cognition.

Appendices

Appendix A

frontiers in Behavioral Neuroscience

GENERAL COMMENTARY
published: 18 September 2019
doi: 10.3389/fnbeh.2019.00217

Commentary: Amplification and Suppression of Distinct Brainwide Activity Patterns by Catecholamines

Vicente Medel[1,2]*, *Joaquín Valdés*[1,2], *Samy Castro*[3,4], *Tomás Ossandón*[2] and *Gonzalo Boncompte*[2]

[1] Centro Interdisciplinario de Neurociencias, Pontificia Universidad Católica de Chile, Santiago, Chile, [2] Neurodynamics of Cognition Laboratory, Departamento de Psiquiatría, Facultad de Medicina, Pontificia Universidad Católica de Chile, Santiago, Chile, [3] Neural Dynamics Laboratory, Centro Interdisciplinario de Neurociencia de Valparaíso, Universidad de Valparaíso, Valparaíso, Chile, [4] Programa de Doctorado en Ciencias, Mención Neurociencia, Universidad de Valparaíso, Valparaíso, Chile

Keywords: locus coeruleus (LC), norepinephrine (NE), catecholaminergic receptors, atomoxetine (ATX), fMRI, iEEG, pupil diameter

A Commentary on

Amplification and Suppression of Distinct Brainwide Activity Patterns by Catecholamines
by van den Brink, R. L., Nieuwenhuis, S., and Donner, T. H. (2018). J. Neurosci. 38:7476–7491. doi: 10.1523/JNEUROSCI.0514-18.2018

OPEN ACCESS

Edited by:
Iris Manor,
Geha Mental Health Center, Israel

Reviewed by:
Alexander Thiele,
Newcastle University, United Kingdom

***Correspondence:**
Vicente Medel
vimedel@uc.cl

Specialty section:
This article was submitted to Learning and Memory, a section of the journal Frontiers in Behavioral Neuroscience

Received: *05 February 2019*
Accepted: *02 September 2019*
Published: *18 September 2019*

Citation:
Medel V, Valdés J, Castro S, Ossandón T and Boncompte G (2019) Commentary: Amplification and Suppression of Distinct Brainwide Activity Patterns by Catecholamines. Front. Behav. Neurosci. 13:217. doi: 10.3389/fnbeh.2019.00217

Brain states like sleep and vigilance, as well as fluctuating levels of arousal and attention, are characterized by diverse patterns of brain activity. These global dynamics are strongly driven by the activity of catecholaminergic neuromodulatory systems (Sara and Bouret, 2012; Reimer et al., 2014; van den Brink et al., 2016). Specifically, norepinephrine (NE) levels have been shown to be coupled to brain states (Eschenko et al., 2011; McGinley et al., 2015). The cortical influence of NE comes from neurons originating in the locus coeruleus (LC) which has widespread projections to the forebrain and has been assumed to have a uniform impact on brain activity. However, neuromodulatory effects vary in part because of the heterogeneous cortical distribution of NE synaptic receptors (Zilles and Amunts, 2009) which suggests that cortical modulation of NE is more complex than previously thought (Totah et al., 2018).

Using fMRI and pharmacological intervention, van den Brink et al. (2018) sought to determine whether NE modulation on brainwide interactions occurred in a spatially distributed manner depending on receptor genes. For this, they analyze resting-state fMRI functional connectivity (FC) in healthy subjects under both placebo condition and a pharmacological increase of NE levels by a single dose of atomoxetine (ATX), an inhibitor of the NE transporter. They use a previously proposed approach (Donner et al., 2013) to decompose the FC matrices into spatial modes of brain organization that capture the heterogeneous atomoxetine-induced effects over intrinsic brain variations.

To compare the spatial modes with well-known brain characteristics, the authors correlate these spatial modes with canonical resting-state FC networks (Smith et al., 2009). Interestingly, the ATX spatial mode correlates with the right frontoparietal network (FPN) while the placebo spatial mode correlates with the left FPN and the default-mode network, which has important roles in cognition. This is of special interest, considering that these networks are obtained from the resting-state, which suggests that slow spontaneous fluctuations are modulated by NE even in the absence of task. Indeed, the authors interpret that ATX might induce a shift toward a goal-oriented stimulus processing brain state. Considering the computational evidence that resting-state fluctuations may arise from slow fluctuation of ionic concentrations (Krishnan et al., 2018), van den Brink et al. (2018) results experimentally supports the understanding of catecholaminergic modulation as a

spatially heterogeneous gain function of biophysical dynamics (Shine et al., 2018).

If the above were true, a strong coupling between the spatial modes and the localization of NE receptors would be expected. Indeed, using the receptor's transcriptional maps from the Allen Brain Institute (Hawrylycz et al., 2015), the authors show that the heterogeneous spatial modes are partially explained by the spatial heterogeneity of NE receptors. Specifically, the distribution of the spatial modes significantly correlates with the localization of β NE receptors and with α1 NE receptors, but not with α2 NE receptors or NMDA receptors. This is of special interest because α2 shows higher affinity to NE than α1 receptors (Berridge and Spencer, 2016). Both of these receptors are known to be cognitively important but in different ways. α2 activation has been linked to enhanced working memory capacity, while α1 is related to high arousal situations and impaired working memory while promoting attention flexibility (Berridge and Spencer, 2016). This is in line with the adaptive gain theory proposed by Aston-Jones and Cohen (2005), which links LC-NE activity with cognitive performance. Interestingly, as the authors note, there is a significant expression of NE receptors in subcortical areas, including α2 NE autoreceptors in the LC, which should be taken into account to describe these complex phenomena. However, and perhaps more importantly, recent evidence has shown that ATX has opposite effects in network integration in resting state compared to cognitive tasks, which supports a state-dependent modulation of brain connectivity by catecholamines (Shine et al., 2019).

Humans interact with the dynamic nature of the world with a high temporal resolution. Placing van den Brink et al. (2018) findings into the perspective of spontaneous fluctuations in cognition, it appears as highly relevant to characterize the dynamic shaping of brain activity by neuromodulators on a finer temporal scale using electrophysiology (e.g., McGinley et al., 2015). In this line, Pfeffer et al. (2018) found that a single dose of ATX shapes an aperiodic measure of the field potential during perception of ambiguous visual stimuli. This is consistent with evidence that proposes aperiodic measures such as the level of background neural activity (Voytek and Knight, 2015) as physiological markers of network dynamics. Interestingly, the aperiodic activity has been shown to highly correlate with spiking activity (Manning et al., 2009), and is a good electrophysiological correlate of the BOLD signal (Wen and Liu, 2016), emerging as a candidate to link micro and macro scale in the study of neuromodulation of brain activity. Thus, it is tempting to test if the spatial modes revealed by fMRI are spatially coincident with electrophysiological field potential patterns, such as aperiodic broadband, as previous studies have done (Ossandón et al., 2011).

The results presented by van den Brink et al. (2018) extend our understanding of the fine-grained spatial architecture of brain activity and its reshaping by ATX. Although pharmacological interventions studies contribute to elucidate the catecholaminergic effects on cortical states, they fail to describe its naturally dynamic fluctuations. Given the well-established role of the LC in driving cortical states and pupil diameter (Aston-Jones and Cohen, 2005; Yüzgeç et al., 2018), pupillometry appears as an excellent candidate to relate endogenous time-varying NE levels with brain states (Reimer et al., 2014; Wainstein et al., 2017).

van den Brink et al. (2018) contribute to the challenge of linking macro scale brain organization with low-level characteristics of neurotransmitter receptors. Extending these important results using higher temporal resolution methods, as intracranial EEG, and adding in parallel pupillometry would give a broader understanding of how neuromodulators spatially interact with brain state fluctuations and cognition. This could potentiate future research to understand the multiscale functional dynamics underlying several neuromodulator-related psychiatric disorders as well as to pave the path to design targeted therapeutic strategies.

AUTHOR CONTRIBUTIONS

All authors listed have made a substantial, direct and intellectual contribution to the work, and approved it for publication.

FUNDING

This work was supported by FONDECYT project 1180932 and CONICYT fellowships to VM (21180871), JV (21180599), and SC (21140603).

ACKNOWLEDGMENTS

We thank Martín Irani, Jimena Sierralta, Patricio Orio, and Nicolás Crossley for their valuable comments on earlier versions of the manuscript.

REFERENCES

Aston-Jones, G., and Cohen, J. D. (2005). An integrative theory of locus coeruleus-norepinephrine function: adaptive gain and optimal performance. *Annu. Rev. Neurosci.* 28, 403–450. doi: 10.1146/annurev.neuro.28.061604.135709

Berridge, C. W., and Spencer, R. C. (2016). Differential cognitive actions of norepinephrine a2 and a1 receptor signaling in the prefrontal cortex. *Brain Res.* 1641, 189–196. doi: 10.1016/j.brainres.2015.11.024

Donner, T. H., Sagi, D., Bonneh, Y. S., and Heeger, D. J. (2013). Retinotopic patterns of correlated fluctuations in visual cortex reflect the dynamics of spontaneous perceptual suppression. *J. Neurosci.* 33, 2188–2198. doi: 10.1523/JNEUROSCI.3388-12.2013

Eschenko, O., Magri, C., Panzeri, S., and Sara, S. J. (2011). Noradrenergic neurons of the locus coeruleus are phase locked to cortical up-down states during sleep. *Cereb. Cortex* 22, 426–435. doi: 10.1093/cercor/bhr121

Hawrylycz, M., Miller, J. A., Menon, V., Feng, D., Dolbeare, T., Guillozet-Bongaarts, A., et al. (2015). Canonical genetic signatures of the adult human brain. *Nat. Neurosci.* 18, 1832–1844. doi: 10.1038/nn.4171

Krishnan, G. P., González, O. C., and Bazhenov, M. (2018). Origin of slow spontaneous resting-state neuronal fluctuations in brain networks. *Proc. Natl. Acad. Sci. U.S.A.* 115, 6858–6863. doi: 10.1073/pnas.1715841115

Manning, J. R., Jacobs, J., Fried, I., and Kahana, M. J. (2009). Broadband shifts in local field potential power spectra are correlated with single-neuron spiking in humans. *J. Neurosci.* 29, 13613–13620. doi: 10.1523/JNEUROSCI.2041-09.2009

McGinley, M. J., David, S. V., and McCormick, D. A. (2015). Cortical membrane potential signature of optimal states for sensory signal detection. *Neuron* 87, 179–192. doi: 10.1016/j.neuron.2015.05.038

Ossandón, T., Jerbi, K., Vidal, J. R., Bayle, D. J., Henaff, M.-A., Jung, J., et al. (2011). Transient suppression of broadband gamma power in the default-mode network is correlated with task complexity and subject performance. *J. Neurosci.* 31, 14521–14530. doi: 10.1523/JNEUROSCI.2483-11.2011

Pfeffer, T., Avramiea, A. E., Nolte, G., Engel, A. K., Linkenkaer-Hansen, K., and Donner, T. H. (2018). Catecholamines alter the intrinsic variability of cortical population activity and perception. *PLoS Biol.* 16:e2003453. doi: 10.1371/journal.pbio.2003453

Reimer, J., Froudarakis, E., Cadwell, C. R., Yatsenko, D., Denfield, G. H., and Tolias, A. S. (2014). Pupil fluctuations track fast switching of cortical states during quiet wakefulness. *Neuron* 84, 355–362. doi: 10.1016/j.neuron.2014.09.033

Sara, S. J., and Bouret, S. (2012). Orienting and reorienting: the locus coeruleus mediates cognition through arousal. *Neuron* 76, 130–141. doi: 10.1016/j.neuron.2012.09.011

Shine, J. M., Aburn, M. J., Breakspear, M., and Poldrack, R. A. (2018). The modulation of neural gain facilitates a transition between functional segregation and integration in the brain. *eLife* 7:e31130. doi: 10.7554/eLife.31130

Shine, J. M., Breakspear, M., Bell, P. T., Martens, K. E., Shine, R., Koyejo, O., et al. (2019). Human cognition involves the dynamic integration of neural activity and neuromodulatory systems. *Nat. Neurosci.* 22, 289–296. doi: 10.1038/s41593-018-0312-0

Smith, S. M., Fox, P. T., Miller, K. L., Glahn, D. C., Fox, P. M., Mackay, C. E., et al. (2009). Correspondence of the brain's functional architecture during activation and rest. *Proc. Natl. Acad. Sci. U.S.A.* 106, 13040–13045. doi: 10.1073/pnas.0905267106

Totah, N. K., Neves, R. M., Panzeri, S., Logothetis, N. K., and Eschenko, O. (2018). The locus coeruleus is a complex and differentiated neuromodulatory system. *Neuron* 99, 1055–1068. doi: 10.1016/j.neuron.2018.07.037

van den Brink, R. L., Nieuwenhuis, S., and Donner, T. H. (2018). Amplification and suppression of distinctbrainwide activity patterns by catecholamines. *J. Neurosci.* 38, 7476–7491. doi: 10.1523/JNEUROSCI.0514-18.2018

van den Brink, R. L., Pfeffer, T., Warren, C. M., Murphy, P. R., Tona, K. D., van der Wee, N. J., et al. (2016). Catecholaminergic neuromodulation shapes intrinsic MRI functional connectivity in the human brain. *J. Neurosci.* 36, 7865–7876. doi: 10.1523/JNEUROSCI.0744-16.2016

Voytek, B., and Knight, R. T. (2015). Dynamic network communication as a unifying neural basis for cognition, development, aging, and disease. *Biol. Psychiatry* 77, 1089–1097. doi: 10.1016/j.biopsych.2015.04.016

Wainstein, G., Rojas-Líbano, D., Crossley, N. A., Carrasco, X., Aboitiz, F., and Ossandón, T. (2017). Pupil size tracks attentional performance in attention-deficit/hyperactivity disorder. *Sci. Rep.* 7, 1–9. doi: 10.1038/s41598-017-08246-w

Wen, H., and Liu, Z. (2016). Broadband electrophysiological dynamics contribute to global resting-state fMRI signal. *J. Neurosci.* 36, 6030–6040. doi: 10.1523/JNEUROSCI.0187-16.2016

Yüzgeç, Ö., Prsa, M., Zimmermann, R., and Huber, D. (2018). Pupil size coupling to cortical states protects the stability of deep sleep via parasympathetic modulation. *Curr. Biol.* 28, 392–400.e3. doi: 10.1016/j.cub.2017.12.049

Zilles, K., and Amunts, K. (2009). Receptor mapping: architecture of the human cerebral cortex. *Curr. Opin. Neurol.* 22, 331–339. doi: 10.1097/WCO.0b013e32832d95db

Conflict of Interest Statement: The authors declare that the research was conducted in the absence of any commercial or financial relationships that could be construed as a potential conflict of interest.

Appendix B

NeuroImage 219 (2020) 117027

Contents lists available at ScienceDirect

NeuroImage

journal homepage: www.elsevier.com/locate/neuroimage

Transitions between human functional brain networks reveal complex, cost-efficient and behaviorally-relevant temporal paths

Juan P. Ramirez-Mahaluf [a], Vicente Medel [b], Ángeles Tepper [a], Luz Maria Alliende [a], Joao R. Sato [c], Tomas Ossandon [a,b], Nicolas A. Crossley [a,b,d,e,f,*]

[a] Department of Psychiatry, School of Medicine, Pontificia Universidad Católica de Chile, Santiago, Chile
[b] Center for Integrative Neuroscience, School of Medicine, Pontificia Universidad Católica de Chile, Santiago, Chile
[c] Center for Mathematics, Computing and Cognition, Universidade Federal do ABC - Santo André, São Paulo, Brazil
[d] Biomedical Imaging Center, Pontificia Universidad Católica de Chile, Chile
[e] Millennium Nucleus for Cardiovascular Magnetic Resonance, Chile
[f] Institute of Psychiatry, Psychology and Neuroscience, King's College London, London, UK

ARTICLE INFO

Keywords:
Dynamic connectivity
Cognition
Motor
Resting state
Brain networks

ABSTRACT

Resting-state functional MRI activity is organized as a complex network. However, this coordinated brain activity changes with time, raising questions about its evolving temporal arrangement. Does the brain visit different configurations through time in a random or ordered way? Advances in this area depend on developing novel paradigms that would allow us to shed light on these issues. We here propose to study the temporal changes in the functional connectome by looking at transition graphs of network activity. Nodes of these graphs correspond to brief whole-brain connectivity patterns (or meta-states), and directed links to the temporal transition between consecutive meta-states. We applied this method to two datasets of healthy subjects (160 subjects and a replication sample of 54), and found that transition networks had several non-trivial properties, such as a heavy-tailed degree distribution, high clustering, and a modular organization. This organization was implemented at a low biological cost with a high cost-efficiency of the dynamics. Furthermore, characteristics of the subjects' transition graphs, including global efficiency, local efficiency and their transition cost, were correlated with cognition and motor functioning. All these results were replicated in both datasets. We conclude that time-varying functional connectivity patterns of the brain in health progress in time in a highly organized and complex order, which is related to behavior.

1. Introduction

The brain uses a large amount of energy in organizing its spontaneous intrinsic activity into a complex network (Achard and Bullmore, 2007; Bullmore and Sporns, 2012, 2009; Raichle and Mintun, 2006). This organization is specific to the individual (Amico and Goñi, 2018; Finn et al., 2015), and its changes have been associated with development (Dosenbach et al., 2010; Sato et al., 2015), cognition (Crossley et al., 2013; van den Heuvel et al., 2009), emotion (Ramirez-Mahaluf et al., 2018), and the presence of disease (Crossley et al., 2017; Fornito et al., 2015).

Several functional MRI studies have also suggested that the brain's slow oscillatory activity and interactions between regions change over time (Chang and Glover, 2010; Hutchison et al., 2013; Smith et al., 2012). These fluctuations present stable periods or meta-states with a distinct organization (Betzel et al., 2016; Shine et al., 2016; Vidaurre et al., 2017). Using different approaches, recent studies have proposed that the time the brain dwells in specific meta-states is of biological importance. For example, the amount of time brain dynamics remain in meta-states dominated by connections between areas usually related to higher-order cognitive traits (such as the default-mode network, language and prefrontal areas) has been associated with the individual's cognitive skills (Vidaurre et al., 2017). Failure to engage brain dynamics in meta-states involving long-range connections has been observed in pathological brain states such as schizophrenia (Damaraju et al., 2014). Similarly, cognitive impairment associated with brain ageing has been linked to brain dynamics remaining shorter periods in states characterized by strong global connectivity (Cabral et al., 2017). A natural focus of studies examining these dynamic changes has been on describing the

* Corresponding author. Diagonal Paraguay 362, Santiago, Chile.
E-mail address: ncrossley@uc.cl (N.A. Crossley).

https://doi.org/10.1016/j.neuroimage.2020.117027
Received 4 May 2020; Received in revised form 2 June 2020; Accepted 4 June 2020
Available online 6 June 2020

interactions between regions in specific meta-states, and the time spent in each state. Less has been centered on examining the temporal dimension of these phenomena, exploring the way the brain visits these meta-states. In other words, it is yet unclear whether the temporal progression of these changes follows a specific order, or whether the brain transits through these different meta-states in a random way. The previously mentioned study on ageing (Cabral et al., 2017) not only highlighted that cognitive decline was associated with less time spent in globally connected brain states, but also with a higher rate of change between different meta-states. Examining more in detail the temporal organization of how meta-states are visited could provide further clues of brain functioning in health and disease.

Unpacking the temporal dynamics of brain functional networks requires new insights and tools to examine them (Sizemore and Bassett, 2018). In order to explore the complex temporal organization of brain networks, we developed further the idea of considering the order in which the brain visits different meta-states as a path (Miller et al., 2016; Vidaurre et al., 2017). We extended this insight by considering the trajectory through meta-states during the whole registering period as a directed graph. Nodes in these graphs represent whole-brain connectivity states (meta-states) and links represent the temporal transition between them. Analyzing these graphs allowed us to explore whether meta-states were visited in a non-random sequence. We used this approach to examine resting-state functional MRI data from 160 healthy subjects from the Human Connectome Project, and a second replication sample from 54 healthy subjects. We explored whether these transition networks of brain functioning had several non-trivial properties, and their relationship to cognition and behavior.

2. Methods

2.1. Subjects

We included in our analyses two datasests of resting-state fMRI data. The first included 160 healthy, unrelated adult participants (age: 22–35 years) from the Human Connectome Project (HCP) (Van Essen et al., 2012). All subjects underwent a neuropsychological assessment, and none had a prior history of psychiatric or neurological illnesses (Van Essen et al., 2012). A second cohort of healthy subjects included 54 participants (age: 22.9 $\pm$ 3.6 years, mean $\pm$ standard deviation; 34 males) without any psychiatric, neurological or medical illness who were recruited at our center in Santiago, Chile. The study was carried out in accordance with ethical guidelines criteria established by the Pontificia Universidad Católica de Chile as approved by its Ethics Committee (Ref: 15–297) and written informed consent was obtained from all participants.

2.2. Data acquisition and preprocessing

HCP data comprised 1200 frames of multiband, gradient-echo planar imaging acquired during a period of 14 min and 33 s with the following parameters: TR 720 ms; TE 33.1 ms; flip angle, 52°; field of view, 280 $\times$ 180 mm; matrix, 140 $\times$ 90; and voxel dimensions, 2 mm isotropic. Individuals fixated on a projected bright crosshair on a dark background during data acquisition. Two runs acquired for each individual were concatenated and analyzed in our study. Resting-state fMRI data were preprocessed with the HCP functional pipeline, including fMRIVolume and fMRISurface pipeline outputs and motion parameters (Glasser et al., 2013).

Our second cohort of subjects were scanned in a Philips Ingenia 3T MRI with a 16-channel coil. Resting-state images were acquired during 8.33 min while subjects had their eyes opened using an EPI acquisition with a TR of 2.5s, TE 32 ms, and a flip angle of 82°. Forty slides with a continuous descending order were acquired, using a field of view of 220 $\times$ 220mm, and an isotropic voxel size of 2.75 mm. A structural T1-weighted image with a voxel size of 1.0 mm^3 isotropic, a minimum TI delay of 965.2, TE 3.5, TR 7.7 and flip angle of 8° was also acquired. Preprocessing of the functional images followed previously published pipelines (Parkes et al., 2018). Briefly, this included slice-time correction, realignment, normalization, spatial smoothing with a 6 mm FHWM kernel and temporal filtering between 0.008 and 0.08 Hz. Management of residual movement was performed using an automated-ICA method (Pruim et al., 2015).

3. Data analysis

3.1. Temporal meta-states

All data analyses were done with MATLAB (Mathoworks®). We used a whole-brain template with similarly-sized regions (638 nodes) (Crossley et al., 2013), to explore functional connectivity between every pair of regions in the resting state sessions from each individual. Multiplication of temporal derivatives (MTD) (Shine et al., 2015), a method with a high sensitivity to changes in functional connectivity and robust to noise introduced by head movement, was used as our metric of functional connectivity within time windows of length of 7 vol (5040 ms) for our HCP dataset. The size of this time window was selected since it has been described as the most effective trade-off between sensitivity and specificity (Shine et al., 2015). Considering the longer TR used in the acquisition of the data in our second cohort, we used a similar window length of 5000 ms, but which consisted of 2 volumes. The differences in the temporal resolution between datasets allowed us to test the reliability of our analyses. The full connectivity matrix of the time window (638 $\times$ 638) was defined as a brain state.

3.2. Brain state transitions network construction

We then estimated the similarity between all brain states within a subject using correlations, and clusterized the brain states according to their similarity using k-means (Peer et al., 2017). This procedure allowed us to assign each brain state a brain state cluster or meta-state. For each subject, we explored a range between 35 and 55 numbers of clusters. While previous studies have suggested that brain dynamics organize into fewer number of meta-states, clustering is likely to be influenced by the amount of data analyzed. On the other hand, graph analytic methods provide interesting insights into complex networks, which consist of a large number of interacting components. We therefore capitalized on the high temporal resolution and longer period of recording of the HCP data to extract between 35 and 55 meta-states, which would suit our analysis.

3.3. Construction of the transition network between meta-states

We then built a network of meta-state transitions in time, where each meta-state was a node and the transitions between meta-states were the directed edges. A weight was assigned to each edge according to the number of times the brain transitioned between the connected meta-states, in the direction of the edge. Fig. 1 summarizes the construction of this directed and weighted network.

Several parameters were measured from the resulting directed and weighted graph, including widely-used graph-analytic measures such as the weighted degree distribution (Achard et al., 2006; Rubinov and Sporns, 2010), modularity (Newman, 2006), and local and global efficiency (Latora and Marchiori, 2001). We also measured parameters trying to provide insights into the biological cost of the network, including:

- *Transition cost*: This is a global parameter of the transition network. It is defined as the distance between one meta-state and the next one (1 – correlation coefficient of their connectivity matrices), possibly reflecting the metabolic cost associated with switching from one pattern of connectivity to another. This cost was composed of two parameters, which we describe as the immobility of the network

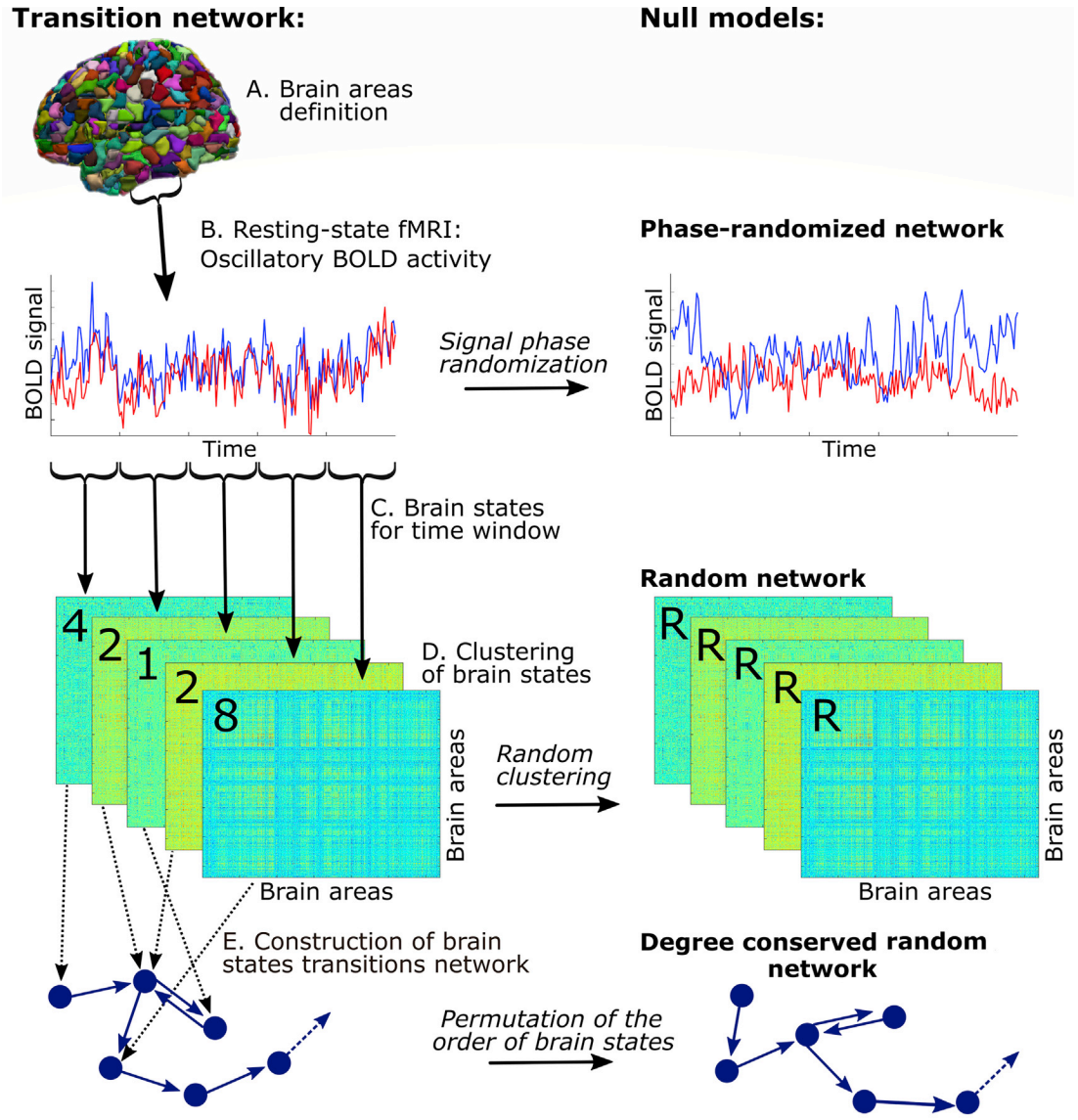

Fig. 1. Construction of transition networks and null models used.
Brain areas are defined using a template (**A**), and their average time course is extracted (**B**). A measure of functional connectivity, namely multiplication time derivatives, is measured between all pairs of regions for each non-overlapping time window of approximately 5 s (7 or 2 vol, depending on each dataset). Functional connectivity across regions within the window defines a brain state (**C**), which are clustered to allocate them to specific meta-states (**D**). Finally, the directed graph of the trajectory taken by the brain through each meta-state is calculated (**E**). Note that connections between two nodes A to B and B to A in the resulting directed graph are not equivalent. Three null-models are used at different stages of the analysis.

(number of times the brain dynamics remained in the same meta-state between two consecutive windows), and the leap size (the transition cost without considering the immobility periods).

- *Static cost*: This is a cost parameter previously used in the literature (Fornito et al., 2011) that applies to each specific meta-state. It is defined as the sum of all products generated by the multiplication of the connectivity between two regions with the Euclidean distance between the centroids of them.
- *Cost-efficiency:* Following previous studies (Fornito et al., 2011), we also examined the global efficiency of the transition network accounting for its cost (in this case, the transition cost).

3.4. Null models

We compared the observed transition-network parameters described above with 3 different null models (Fig. 1):

a) *Random null model,* where the probability of the transition from one meta-state to another one was completely random, generating a random network (10,000 iterations) (Bullmore and Sporns, 2012).
b) *Degree conserved null model,* where the rewiring of the network was performed in such a way that the distribution of the number of connections to nodes, or the degree distribution of the network, was maintained (10,000 iterations). This is similar in principle to the popular (Maslov and Sneppen, 2002) algorithm. This was accomplished by scrambling the full path of transitions underwent by brain dynamics (for example, from ABABCABCD to AADBACBCB).
c) *BOLD time-series randomization,* where the phase of the extracted time-series from all regions of interest were scrambled and then time-series were reconstructed (100 iterations) (Zalesky et al., 2012). We used the same scrambling sequence across ROIs in a null model to maintain not only the autocorrelation function and power spectrum, but also the distribution of correlation values.

The graph measures of transition networks were normalized by the respective null model when visually presented (observed metric/null model metric). They were also plotted in a natural logarithmic scale to maintain the symmetry between increases or decreases. Values of 0, highlighted with a dotted line in the graphs, correspond to no differences between the observed metric and null model.

3.5. Behavioral analyses

To explore the biological importance of the non-trivial properties of these graphs, we correlated the graph measures across subjects with behavioral measurements. For the HCP dataset, we examined tests in different domains, including cognition, emotion, motor, personality and sensory. Due to the large number of behavioral tests, we performed a principal component analysis (PCA) for each behavioral category to reduce its dimensionality, and used the two principal components that together explained more than 50% of the variance in the data. Furthermore, we were aware that we would compare these two components with multiple graph-analytic metrics. We therefore corrected for multiple comparisons using false discovery rates independently for each of the 5 behavioral domains measured (2 components x 7 graph metrics = 14 comparisons). Information regarding the domains measured by cognitive and motor assessments can be found on Table S1 and S2 respectively. For our second cohort scanned in Santiago, we used the general intelligence quotient (IQ) value as a measure of global cognitive performance. This value was estimated from 7 subtests of the Chilean version of the WAIS-IV cognitive battery (block design, similarities, vocabulary, matrix reasoning, arithmetic, information and coding).

3.6. Meta-state organization and its relationship with canonical resting-state networks

We also related the meta-states found in discrete windows with the previously-known brain organization into canonical resting-state

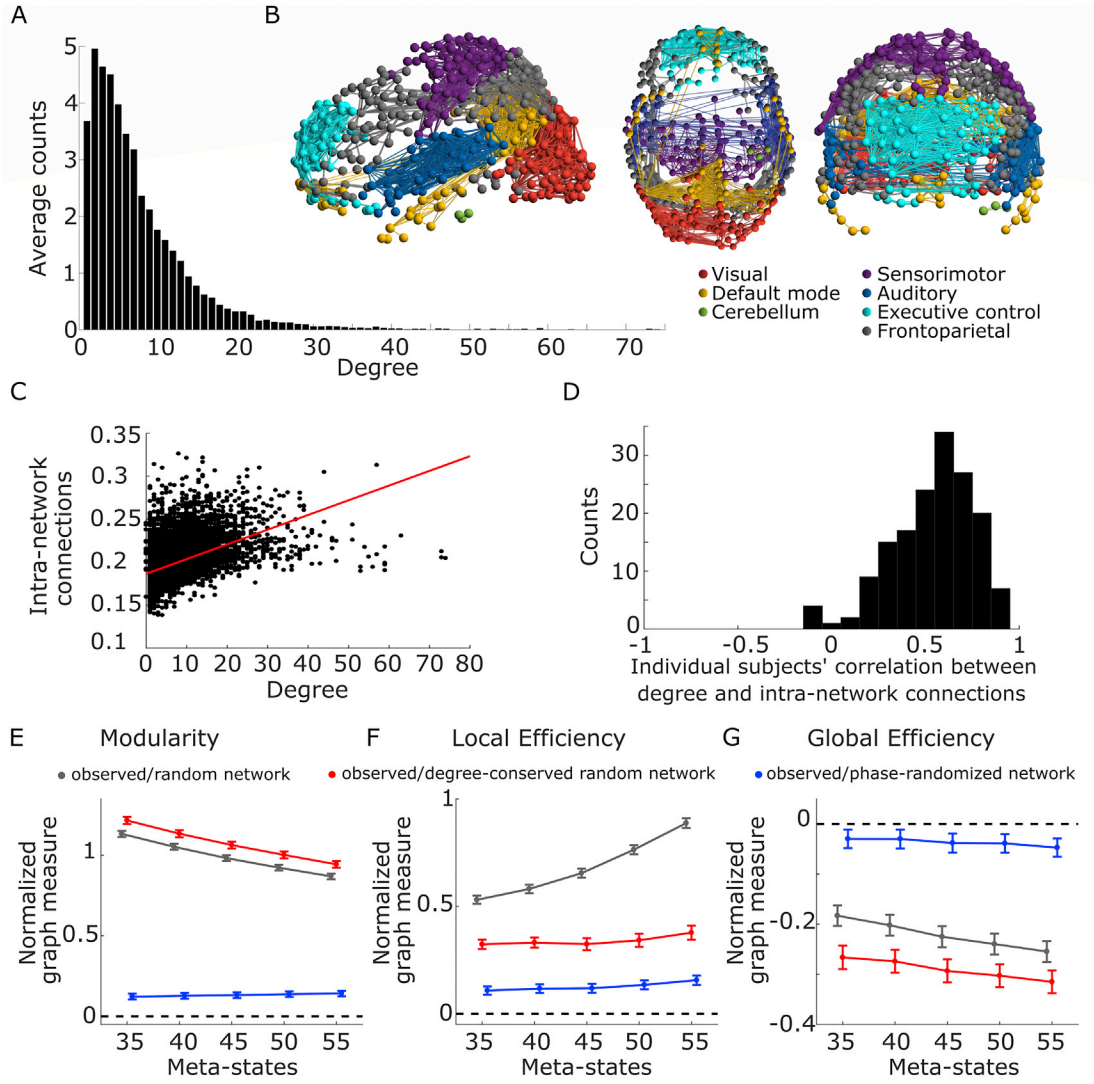

Fig. 2. Topological properties of transition networks.
A. Mean degree distribution histogram across subjects. **B.** Intra-network connections of canonical networks included visual (red), default mode (yellow), cerebellum (green), sensorimotor (magenta), auditory (blue), executive control (cyan) and frontoparietal (gray) networks. Only the strongest connections (0.2%) are displayed for visualization purposes. **C.** Degree and ratio of intra-cannonical network connections for each meta-state were positively correlated (all meta-states from all subjects pooled). **D.** Histogram of correlations between degree and intra-module connections for each subject. **E**, **F**, and **G** describe the ratio between the observed property in the transition graph and different null models for (**E**) modularity (Q value), (**F**) local efficiency and (**G**) global efficiency. The ratios between the transition network and a null model are plotted on a natural logarithmic scale, and plotted alongside its 95% confidence interval of the mean. Dotted lines mark the line of no difference with the null models. Comparisons with random null model networks are plotted in gray, with degree-conserved null network in red, and the randomized time series null model in blue.

functional networks. We used 10 ICA-based rsfMRI maps from previous work (Smith et al., 2009), defining 7 networks corresponding to: visual (including components describing primary and secondary visual cortices), default mode, cerebellum, sensorimotor, auditory, executive control and frontoparietal networks (jointly left and right). We then thresholded the 10% of strongest connections for each meta-state, and calculated the proportion of connections from the total that linked regions within the ICA-described networks. A high index would imply that the strongest connections within a specific meta-state were between regions known to be organized into canonical resting-state networks from previous studies. On the contrary, a low index would suggest that the whole-brain organization within that time window departs greatly from these canonical resting-state networks.

4. Results

4.1. Transition networks of resting-state fMRI meta-states have non-trivial topological properties

We first present the results from our discovery sample from the HCP dataset. Like other complex networks, the degree distribution of the brain transitions network was heavy-tailed across subjects. Following a previous study (Achard et al., 2006), four distributions were compared using Akaike's information criterion: a power law, $P(k) \sim K^{-\alpha}$; an exponential, $P(k) \sim e^{-ak}$; an exponentially truncated power law, $P(k) = K^{\alpha-1} e^{k/kc}$; and a gaussian distribution. The exponentially truncated power law was the best-fitting model for 92% of the subjects (n = 147), while a power law was the best-fitting for the remaining subjects (8%, n = 13) (Fig. 2A). This observed degree distribution among the subjects differed to the degree distribution of their respective null models that did not conserve this characteristic, namely *random networks* and *phase-randomization networks* (Table S3; $\chi^2 = 130.8$, $p < 10^{-29}$ and $\chi^2 = 6.7$, $p = 0.035$, respectively). Post-hoc analyses suggested these differences were driven in both cases by the higher proportion of exponentially-truncated power law fit in the observed networks ($\chi^2 = 111.6$, $p < 10^{-25}$ and $\chi^2 = 6.3$, $p = 0.012$, respectively).

Then, we explored if these hub meta-states were similar to well-known functional canonical resting-state networks, looking at the proportion of strongest connections between regions within the same canonical resting-state network (Fig. 2B). We found a positive correlation between the weighted degree of the meta-state and its ratio of intra-canonical-network connections in the whole group (Fig. 2C, $R = 0.48$, [95% CI 0.46 to 0.50]). This relationship applied within most subjects, who presented a positive correlation between degree and the ratio of the intra-canonical-network connections (Fig. 2D, median correlation of 0.5711, [95% CI 0.5379 to 0.6135]). In other words, the brain spent most time in meta-states that resembled most the canonical-network organization.

Previous work has shown that whole-brain dynamics grouped into different clusters of meta-states with similar characteristics (Shine et al., 2016; Vidaurre et al., 2017). In line with these results, a community detection algorithm (Newman, 2006) showed that the brain transition network could be decomposed into a few clusters, identifying a range between 2 and 7 modules (median = 4) across subjects. Newman's modularity index Q was significantly higher for the brain transition networks than for all 3 null models across all k-values of meta-states (Fig. 2E, see also Table S4).

We then explored the efficiency of the network (Latora and Marchiori, 2001). First, we examined the local efficiency, a concept closely related to the clustering coefficient, which describes how fault-tolerant is the system by measuring the number of connections between neighbors of a node. Local efficiency in the transition networks was significantly higher compared to all 3 null models (Fig. 2F, see also Table S4).

The global efficiency of the transition networks, which is closely related to path length and describes how much resources should travel on average in the network to get from one point to another, was consistently lower than null models (Fig. 2G, see also Table S4). Transition networks were thus not efficient in visiting a brain state from another point in the network, traversing on average too many nodes. Considering the temporal nature of the network, this meant brain networks were significantly slower to visit brain meta-states compared to random networks.

4.2. Transition networks are highly cost-efficient

Our result showing that the dynamics of brain meta-states were significantly slow (low global efficiency) could be explained as a way of keeping biological costs low (Zalesky et al., 2014). We therefore evaluated the cost of transitions, which we conceptualized as how much the brain had to change its connectivity pattern between one meta-state and the other (measured by 1-ρ, where ρ is the Pearson's correlation coefficient of their connectivity matrices). The transition cost was significantly lower compared to all three null models (Fig. 3A, see also Table S5).

As described in the methods, costs in transition networks could be kept low by reducing the size of the leap from one brain-state to the next one, or else by staying in the same meta-state in consecutive time-windows, which we define as immobility. Immobility was significantly higher in the observed data compared to all three null models (Fig. 3B, Table S5). Leap size, the average distance from one brain-state to the next one (excluding the cases when the brain remains in the same meta-state in consecutive windows), was significantly lower compared to all three null models (Fig. 3C, Table S5). Thus, the lower transition cost was driven by a network that remained more frequently within the same meta-state, but also by reducing its leap size, or moving to another meta-state which was not that different from the current one.

Examining costs in functional networks also raised the question about how the system solved the costs of remaining in one meta-state. Previous fMRI studies have inferred this cost from the product of the strength of the functional connectivity and the Euclidean distance between the regions, assuming that interactions at longer distances convey a higher cost. We found that most subjects presented a negative correlation between this "static" cost of the meta-state and the number of times it was visited (Fig. 3D, median correlation = −0.4566, [95% CI −0.4872 to −0.3785]). As such, brain dynamics tend to avoid spending long time in a state which requires a high biological cost to maintain.

We then explored whether transition networks were organized efficiently considering this low running cost (Achard and Bullmore, 2007). Cost-efficiency (global efficiency normalized by the cost) was indeed higher than *random networks* and *randomized time series networks* (Fig. 3E, Table S5). When compared to *degree conserved random networks* it depended on the number of meta-states (k-value): the cost-efficiency was higher for k = 35 and 40 (Fig. 3E; Table S5), it was not statistically different for k = 45 and 50 (Fig. 3E; Table S5) and was lower for k = 55 (Fig. 3E; Table S5). Therefore, the cost-efficiency of the network was partly driven by its heavy-tailed degree distribution.

4.3. The cost of switching between transitions and the network's global efficiency is related to the overall cognitive functioning and motor capacity of the subjects

The large number of subjects scanned in the Human Connectome Project also allowed us to relate individual differences in the dynamics of brain meta-states transitions with cognitive, motor, perceptual, emotional or personality related traits measured in that project (Van Essen et al., 2012).

4.4. Cognition

We found a positive correlation between the cost of the transitions and the first cognitive dimension, which weighed equally across cognitive tasks ($R = 0.2587$, p-FDR = 0.0092; see Table S1 for cognitive-coefficients PCAs). In other words, subjects with better general cognitive function were also more capable of switching between very different

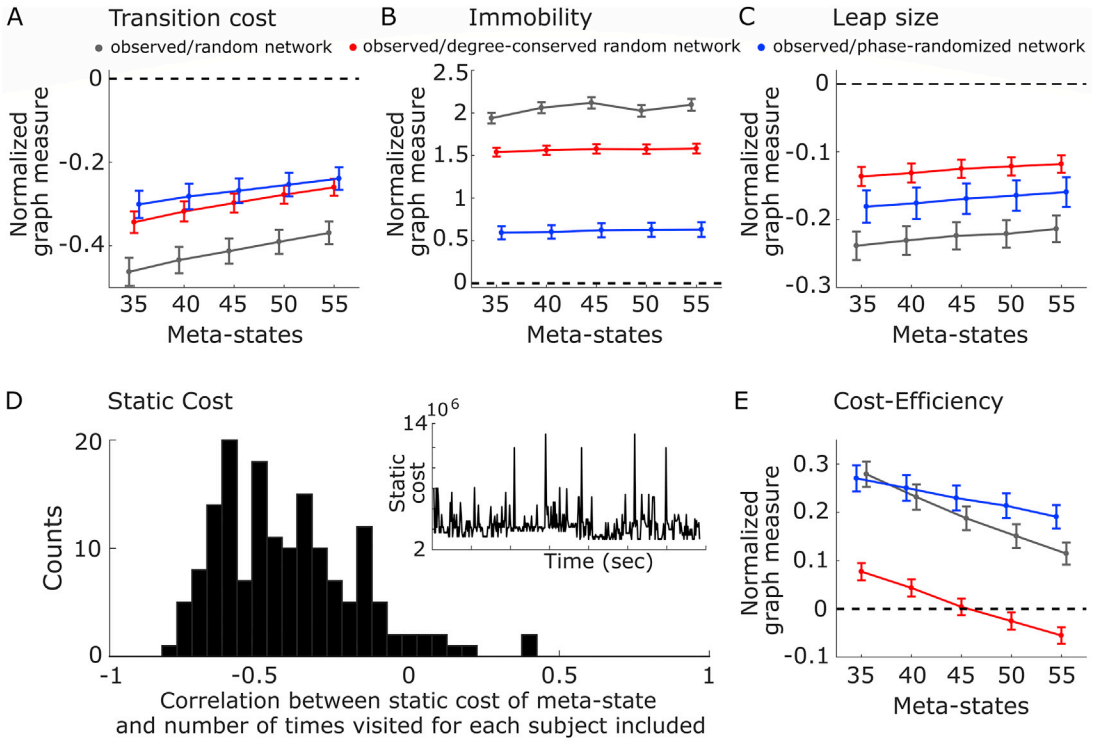

Fig. 3. Economical properties of transition networks.
A. Transition cost, **B.** Immobility **C.** Leap size **D.** Correlations of static cost of meta-states and number of times they are visited across subjects. The inset displays an example of static cost evolution in time from one subject. Note that this subject remains most of the time in meta-states with low static cost, and this property is seen across all subjects **E.** Cost-Efficiency. As in Fig. 2, the ratio between the transition network and a null model is plotted on a natural logarithmic scale, alongside its 95% confidence interval of the mean. Doted lines mark the line of no difference with the null models. Comparisons with random null model in gray, degree conserved null model in red, and randomized time series null model in blue.

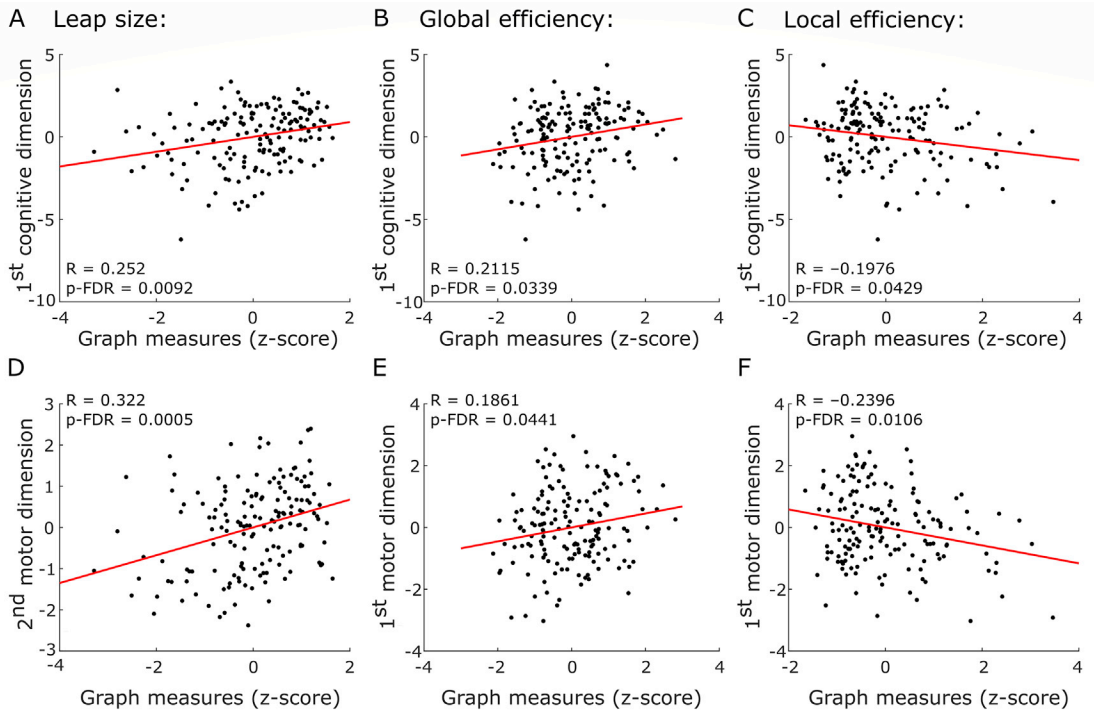

Fig. 4. Transition networks properties are related to cognition and motor capacity.
Scatter plots showing the significant correlations between topological characteristics of the transition networks in subjects and the PCAs of cognitive and motor tasks. Graph measures are displayed using z-scores.

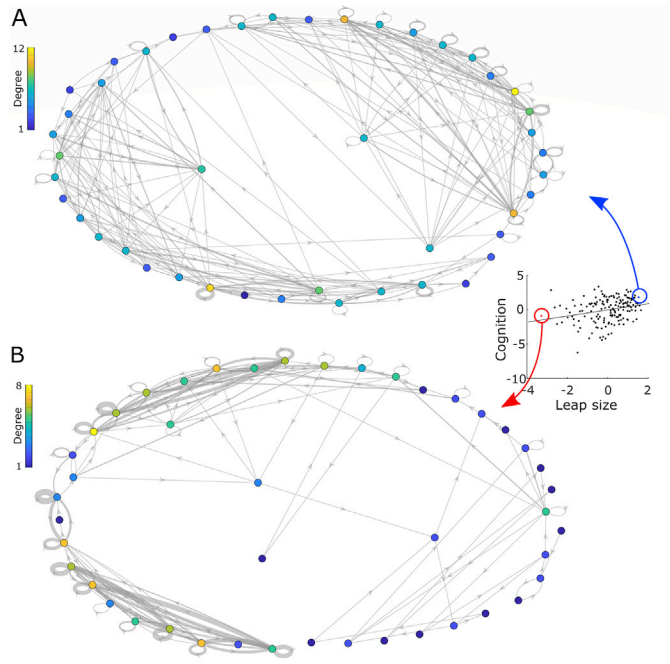

Fig. 5. Example networks of subjects with differing levels of cognition. Transition networks from two subjects who perform among the best and worse in cognitive tests. Layout of the graph is such that the distance between nodes is proportional to their transition cost (1 – correlation of connectivity matrices). The color of nodes denote the degree, the arrow of links represent the direction, and the width of links the number of transition between the connected nodes (weight). Self-connections of the nodes represent consecutive periods (time windows) in which the brain remained in the same meta-state (immobility). The inset shows the scatter plot between leap size and cognitive dimension highlighting both subjects.

brain states that allegedly would incur a high biological cost. When looking at whether the higher cost of transitions depended on a longer leap or a less mobile network, we found that the first cognitive dimension correlated with leap size (Fig. 4A, $R = 0.252$, p-FDR = 0.0092), but not with immobility ($R = –0.1382$, p-uncorrected = 0.0814). Global efficiency and the first cognitive dimension were also positively correlated (Fig. 4B, $R = 0.2115$, p-FDR = 0.0339). Subjects with higher cognitive performance visited more efficiently different meta-states.

A negative correlation between local efficiency and first cognitive dimension was also present (Fig. 4C, $R = -0.1976$, p-FDR = 0.0429). Subjects with a higher cognitive performance presented less redundant trajectories between meta-states.

To illustrate these differences, Fig. 5 displays the transition graphs of two subjects, one scoring among the best and the other the worst in cognitive performance. The layout of nodes is proportional to their transition distance, so the spatial proximity in the figure of the meta-states is proportional to their similarity. As can be seen, the temporal path depicted in the transition graph of the subject scoring highest spans longer distances (larger leap size), reaching rapidly other nodes (higher global efficiency), with an apparent less redundant path (lower local clustering).

4.5. Motor

A significant correlation was also present between both first and second dimensions of motor tasks and transition cost ($R = 0.1855$, p-FDR = 0.0441 and $R = 0.2599$, p-FDR = 0.0063, respectively). As such, subjects who were better in physical endurance, strength, locomotion, and dexterity (Table S2, see for motor-coefficients PCAs), were capable of transiting between very different meta-states. We also found a significant correlation between the second motor dimension and leap size (Fig. 4D, $R = 0.322$, p-FDR = 0.0005), but not immobility ($R = -0.1553$, p-uncorrected = 0.05 and $R = -0.0167$, p-uncorrected = 0.8338, for 1st and 2nd motor dimensions).

A significant correlation between global efficiency and first motor dimension was also found (Fig. 4E, $R = 0.1861$, p-FDR = 0.0441). Subjects who were better in motor performance (endurance, locomotion and strength) used shorter paths to visit different meta-states.

A negative correlation between local efficiency and the first motor dimension was also present (Fig. 4F, $R = -0.2396$, p-FDR = 0.0106). Subjects with a higher motor performance presented less redundant trajectories between meta-states.

We also found a negative correlation between cost-efficiency and the second motor dimension ($R = -0.2192$, p-FDR = 0.0188). This result must be interpreted with care, since this negative association appeared to be driven by the high correlation between transition cost and the second motor dimension.

4.6. Emotion, sensory and personality traits

We did not find any significant association between emotion, sensory and personality domains, with the graph measures of the transition networks.

Subject-specific characteristics are not correlated with analogous topological organization calculated from the static graph (whole-registering period network).

We also explored the relationship between all these cognitive and behavioral metrics with graph metrics from the network built from the whole registration period (the “static” network traditionally explored in fMRI studies). We found no significant correlation between the cognitive, motor, or any other dimension examined and the equivalent graph analytic properties of the static (whole time-series) brain network (Table S6 and S7).

4.7. Transition graphs are reliable for each subject

Since the Human Connectome Project data were acquired in two stages of 15 min, we used this division to explore the reliability of our network metrics. As can be seen in Figure S1, all network metrics measured in the different stages were significantly correlated, with correlations ranging from 0.19 for immobility, to 0.71 for leap size.

4.8. Transition networks measures and their relationship with cognition are replicable

We replicated our analyses of the transition networks using a second dataset of resting-state fMRI data of 54 healthy subjects. Although the acquisition of resting-state data differed greatly, with a shorter acquisition time (8 min) and a lower temporal resolution (TR = 2.5s), the non-trivial graph properties of transition networks were replicated. As Figure S2 shows, transition networks had a heavy-tailed distribution, with high clustering and modularity, with low transition costs, and high cost-efficiency.

We then explored the relation between transition networks metrics and cognition, using the intelligence quotient (IQ). Remarkably, we replicated our findings of a positive correlation between IQ and the cost of the transitions (Fig. 6A, $R = 0.3003$, $p = 0.0274$), leap size (Fig. 6B, $R = 0.3062$, $p = 0.0243$), and global efficiency (Fig. 6C, $R = 0.2764$, $p = 0.0431$). Local efficiency, previously found to correlate negatively with cognition, was negatively correlated with IQ as well (Fig. 6D, $R = -0.2767$, $p = 0.0428$).

5. Discussion

We here showed that functional brain networks have a highly organized temporal structure, where different brain states are visited in a

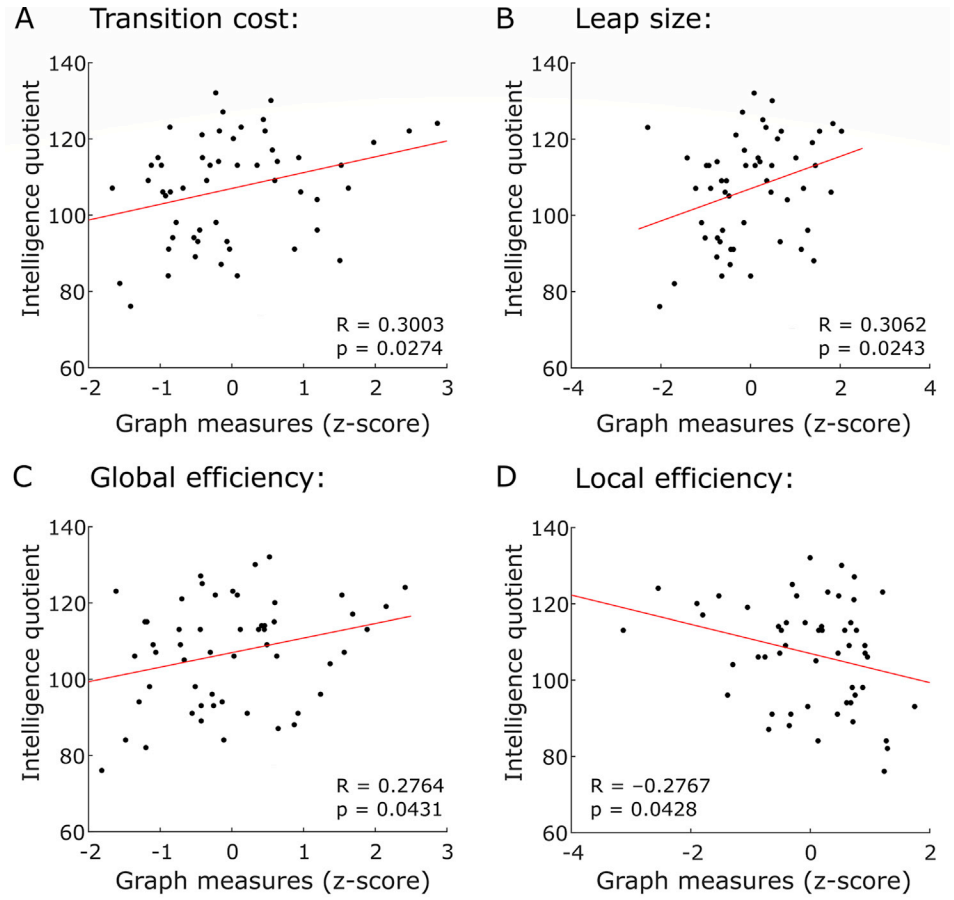

Fig. 6. Transition networks properties are related to IQ value in a second cohort.
Scatter plot shows the significant correlations between graph measures and the IQ value. Graph measures are expressed as z-scores.

cost-effective, locally-clustered, and modular arrangement. Furthermore, the characteristics of these paths are related to the cognitive and behavioral characteristics of the individuals. We replicated our findings in two datasets, providing evidence that our results are consistent across samples and differences in image acquisitions. Brain networks and their progression in time thus behave like a piece of music, for example Beethoven's 5th symphony. Different musicians may play sometimes in a coordinated way, similar to brain areas functionally connected. The overall harmony revolves around a dominant chord (C minor), which one could consider analogous to the information one gets when looking at whole-registering period (static) functional connectivity networks. However, the essence of the musical piece, and we here argue that brain functioning as well, is not grasped until one considers how it temporally progresses from note to note forming harmonized melodies.

Economic constraints have been suggested as one of the main principles ruling how the brain organizes itself (Bullmore and Sporns, 2012). Their modulating effect has also been shown for the dynamic fluctuations observed in functional networks with fMRI, with temporal changes concentrating in the long-range, integrative, but costly brain connections, providing a cost-efficient solution for the brain (Zalesky et al., 2014). Our findings are very much in line with this idea, with the brain path minimizing the biological costs that require switching from one state to the other, and avoiding spending a long time in brain states that require high biological investment for their maintenance.

Transition networks also had other hallmarks of complex systems. Our finding of an exponentially-truncated power-law distribution mirrors other systems with complex organization instantiated in physical systems that limits their organization (Achard et al., 2006). Within this heavy-tailed distribution, there were a few highly visited meta-states, which were similar in their organization to resting-state networks. This is perhaps unsurprising when one considers that resting-state networks are the average connection profiles of a whole recording period in which hub meta-states account for a significant part. Other relevant characteristics of our transition networks were their highly modular organization, which echoes previous findings on resting-state fMRI dynamics (Shine et al., 2016; Vidaurre et al., 2017), as well as their redundant trajectory (high local efficiency). This organization suggests that predicting a future brain-state from a preceding one might be possible to a certain level.

This new approach to brain dynamics provides new insights into brain functioning otherwise missed, as shown in our results relating the paths' organization with the cognitive and behavioral individual characteristics, which were not present in the "static" connectivity analyses. Previous studies had suggested that configurations in structural and functional brain networks with high global efficiency, allowing for proper parallel processing, would facilitate cognition (Li et al., 2009; van den Heuvel et al., 2009). Adding a new level of complexity, we found that trajectories between functional networks with high global efficiency were also related to higher cognition, reflecting that not only is relevant how efficiently connected are the brain networks, but also how efficiently these networks are visited in time. Another interesting insight related to general cognition was that it was correlated with a higher capacity to switch between very different meta-states (longer leap size). This resonates with the suggestion that higher cognition is related to rapid adaptation of different patterns of functional connectivity according to task demands (Cole et al., 2013). Thus, higher cognition is related to efficient planning of how to explore the landscape of possible meta-states, as well as the capacity to jump farther from one point to the other. It is true that our measures of cognition were different in the two

datasets analyzed, namely the principal components explaining most of the variance of a cognitive battery and measured IQ. However, we would argue that both characterize similar cognitive profiles (general cognition), increasing the replicability of our results when changing methodological considerations.

Our network metrics were also correlated with motor skills, including transition cost, which was also related to general cognition. Since we did not measure motor skills in our subjects recruited locally, we could not explore how replicable these results were. However, our results are interesting since they could help us relate cognition with physical activity, particularly considering that there is a large amount of evidence supporting a beneficial effect of physical activity on cognition (Erickson et al., 2011; Hillman et al., 2008). Our results suggest another possible mechanism: physical training helps the brain jump farther to more distant meta-states. From a neurobiological perspective, it is interesting to note that growth factors have been suggested to mediate the brain effects of exercise. Growth factors also modulate synaptic plasticity and functional connectivity (Cotman et al., 2007; Voss et al., 2013), linking our observation of greater changes in the functional connectivity patterns with exercise.

Examining complex systems of interacting components as networks is a simple and useful solution to discover the underlying organizational principles from the large amount of data acquired. This indeed is the case in the brain (Bullmore and Sporns, 2009). The dynamic nature of functional brain networks has increased again the order of data examined, and challenged scientists to come up with new ways of understanding the temporal organization (Sizemore and Bassett, 2018). Our suggestion to consider the paths as a directed graph is a simple yet powerful one, providing several novel insights into brain functioning. It has yet to be seen whether it will also provide new insights into brain dysfunction. It is also a flexible conceptual approach, that can well be applied to other brain signals (such as EEG), or even to other dynamic systems beyond the brain.

Our study has several limitations. Perhaps the most important one is that we used windows of the same length assuming that meta-states last all the same amount of time. This imposed pacing on brain dynamics is unlikely to be correct (Vidaurre et al., 2017). However, a temporal path could stay within the same meta-state in consecutive time windows, and our metric of immobility allowed us to examine what role this possibility had in the organization. One could also question the number of meta-states expected, which we considered to be between 35 and 55 that is higher than the number of previously cited meta-states. Forcing the data to cluster into smaller groups could introduce some organization; however, we do not see that in our null models, including one based on surrogates of fMRI time-series (phase randomization). Differing views on these two methodological decisions (fixed windows, and number of meta-states) are expected since we do not yet know the characteristics and numbers of meta-states in the healthy brain. It is also unclear how similar is the organization across different subjects. To some extent, this problem resonates with the discussion about how to divide the brain into regions. This is undoubtedly important for connectivity analyses (Smith et al., 2011; Zalesky et al., 2010), but does not necessarily prevent network analyses from providing insights into brain functioning (Bullmore and Sporns, 2009). We aimed to show a novel approach to the higher-level analysis of the brain's dynamic organization, that could be used in the future with more precise definitions of dynamic meta-states provided by new research. We also showed significant reliability on metrics measured in different 15-min resting-state periods. However, some of the global metrics such as immobility had relatively low correlation values between sessions. On the one hand, this could suggest that some metrics derived from our method require extended periods of fMRI measurement to provide a full and reliable view of the temporal organization of an individual's brain. Future work will focus on examining the limits of this temporal resolution, and ways to improve its reliability. On the other, one could speculate that a low reliability between sessions would be expected in graph metrics related to intra-individual characteristics that changed significantly during this very short period. As most of us have experienced when volunteering in a neuroimaging study, it is likely that there were changes in the level of arousal of subjects between the two sessions. The extent to which network characteristics such as immobility are related to different levels of arousal is an area we would like to explore further.

Our study also has several strengths. Firstly, we replicated our results in a second cohort. The functional MRI sequence from that second cohort did not share the high temporal resolution of the Human Connectome Project Data, ending with a noisier estimate of the functional connectivity within each time window. The fact that our results were overall similar to the original analysis supports the replicability of our findings. Secondly, we also compared our findings against 3 null models: a random network, a degree-conserved random network (Maslov and Sneppen, 2002), and a BOLD-time series randomization null models (Zalesky et al., 2014). Each null model has its limitations, but jointly provided a robust proof of our findings. These included accounting for the effect of some of the characteristics of the network's organization, such as its degree distribution (degree-conserved random network), or the correlated noise in time-series (BOLD-time series randomization). The latter model allowed us to conclude for example that the observed low transition cost is not simply due to temporal blurring. Furthermore, our results were consistently found along with a range of clustering solutions. Overall, all these analyses performed show that our findings were not restricted to specific acquisition of the data or restricted to certain methodological assumptions in the analyses.

In summary, we conclude that the paths that brain dynamics take are non-trivial and related to differences in cognition and motor skills.

Code availability

All analyses were performed using in-house Matlab scripts; this code is available from the authors upon request.

Declaration of competing interest

The authors declare no competing interests.

CRediT authorship contribution statement

Juan P. Ramirez-Mahaluf: Conceptualization, Methodology, Software, Formal analysis, Data curation, Writing - original draft, Visualization, Funding acquisition. **Vicente Medel:** Software, Formal analysis, Visualization, Writing - review & editing. **Ángeles Tepper:** Software, Data curation, Writing - review & editing. **Luz Maria Alliende:** Investigation, Data curation, Writing - review & editing. **Joao R. Sato:** Conceptualization, Writing - review & editing. **Tomas Ossandon:** Funding acquisition, Writing - review & editing. **Nicolas A. Crossley:** Conceptualization, Methodology, Formal analysis, Investigation, Writing - review & editing.

Acknowledgements

This work was funded by the Agencia Nacional de Investigación y Desarrollo from Chile (ANID), through its programs ANILLO PIA ACT1414 and PIA ACT192064, FONDECYT postdoctorado (Ref: 3190311 to JPRM), and FONDECYT regular (Ref: 1160736 to NAC, and *Ref:* 1180932 to TO). NAC is supported by the Millennium Science Initiative of ANID Chile, grant Nucleus for Cardiovascular Magnetic Resonance. We thank Albert Compte for his insightful comments on the manuscript.

Appendix A. Supplementary data

Supplementary data to this article can be found online at https://doi.org/10.1016/j.neuroimage.2020.117027.

References

Achard, S., Bullmore, E., 2007. Efficiency and cost of economical brain functional networks. PLoS Comput. Biol. 3, 0174–0183.

Achard, S., Salvador, R., Whitcher, B., Suckling, J., Bullmore, E.T., 2006. A resilient, low-frequency, small-world human brain functional network with highly connected association cortical hubs. J. Neurosci. 26, 63–72.

Amico, E., Goñi, J., 2018. The quest for identifiability in human functional connectomes. Sci. Rep. 8, 8254.

Betzel, R.F., Fukushima, M., He, Y., Zuo, X.N., Sporns, O., 2016. Dynamic fluctuations coincide with periods of high and low modularity in resting-state functional brain networks. Neuroimage 127, 287–297.

Bullmore, E., Sporns, O., 2012. The economy of brain network organization. Nat. Rev. Neurosci. 13, 336–349.

Bullmore, E., Sporns, O., 2009. Complex brain networks: graph theoretical analysis of structural and functional systems. Nat. Rev. Neurosci. 10, 186–198.

Cabral, J., Vidaurre, D., Marques, P., Magalhães, R., Silva Moreira, P., Miguel Soares, J., Deco, G., Sousa, N., Kringelbach, M.L., 2017. Cognitive performance in healthy older adults relates to spontaneous switching between states of functional connectivity during rest. Sci. Rep. 7, 5135.

Chang, C., Glover, G.H., 2010. Time-frequency dynamics of resting-state brain connectivity measured with fMRI. Neuroimage 50, 81–98.

Cole, M.W., Reynolds, J.R., Power, J.D., Repovs, G., Anticevic, A., Braver, T.S., 2013. Multi-task connectivity reveals flexible hubs for adaptive task control. Nat. Neurosci. 16, 1348–1355.

Cotman, C.W., Berchtold, N.C., Christie, L.A., 2007. Exercise builds brain health: key roles of growth factor cascades and inflammation. Trends Neurosci. 30, 464–472.

Crossley, N.A., Marques, T.R., Taylor, H., Chaddock, C., Dell'Acqua, F., Reinders, A.A.T.S., Mondelli, V., DiForti, M., Simmons, A., David, A.S., Kapur, S., Pariante, C.M., Murray, R.M., Dazzan, P., 2017. Connectomic correlates of response to treatment in first-episode psychosis. Brain 140, 487–496.

Crossley, N.A., Mechelli, A., Vertes, P.E., Winton-Brown, T.T., Patel, A.X., Ginestet, C.E., McGuire, P., Bullmore, E.T., 2013. Cognitive relevance of the community structure of the human brain functional coactivation network. Proc. Natl. Acad. Sci. 110, 11583–11588.

Damaraju, E., Allen, E.A., Belger, A., Ford, J.M., McEwen, S., Mathalon, D.H., Mueller, B.A., Pearlson, G.D., Potkin, S.G., Preda, A., Turner, J.A., Vaidya, J.G., Van Erp, T.G., Calhoun, V.D., 2014. Dynamic functional connectivity analysis reveals transient states of dysconnectivity in schizophrenia. NeuroImage Clin 5, 298–308.

Dosenbach, N.U.F., Nardos, B., Cohen, A.L., Fair, D.A., Power, J.D., Church, J.A., Nelson, S.M., Wig, G.S., Vogel, A.C., Lessov-Schlaggar, C.N., Barnes, K.A., Dubis, J.W., Feczko, E., Coalson, R.S., Pruett, J.R., Barch, D.M., Petersen, S.E., Schlaggar, B.L., 2010. Prediction of individual brain maturity using fMRI. Science 329, 1358–1361.

Erickson, K.I., Voss, M.W., Prakash, R.S., Basak, C., Szabo, A., Chaddock, L., Kim, J.S., Heo, S., Alves, H., White, S.M., Wojcicki, T.R., Mailey, E., Vieira, V.J., Martin, S.A., Pence, B.D., Woods, J.A., McAuley, E., Kramer, A.F., 2011. Exercise training increases size of hippocampus and improves memory. Proc. Natl. Acad. Sci. 108, 3017–3022.

Finn, E.S., Shen, X., Scheinost, D., Rosenberg, M.D., Huang, J., Chun, M.M., Papademetris, X., Constable, R.T., 2015. Functional connectome fingerprinting: identifying individuals using patterns of brain connectivity. Nat. Neurosci. 18, 1664–1671.

Fornito, A., Zalesky, A., Bassett, D.S., Meunier, D., Ellison-Wright, I., Yücel, M., Wood, S.J., Shaw, K., O'Connor, J., Nertney, D., Mowry, B.J., Pantelis, C., Bullmore, E.T., 2011. Genetic influences on cost-efficient organization of human cortical functional networks. J. Neurosci. 31, 3261–3270.

Fornito, A., Zalesky, A., Breakspear, M., 2015. The connectomics of brain disorders. Nat. Rev. Neurosci. 16, 159–172.

Glasser, M.F., Sotiropoulos, S.N., Wilson, J.A., Coalson, T.S., Fischl, B., Andersson, J.L., Xu, J., Jbabdi, S., Webster, M., Polimeni, J.R., Van Essen, D.C., Jenkinson, M., 2013. The minimal preprocessing pipelines for the Human Connectome Project. Neuroimage 80, 105–124.

Hillman, C.H., Erickson, K.I., Kramer, A.F., 2008. Be smart, exercise your heart: exercise effects on brain and cognition. Nat. Rev. Neurosci. 9, 58–65.

Hutchison, R.M., Womelsdorf, T., Allen, E.A., Bandettini, P.A., Calhoun, V.D., Corbetta, M., Della Penna, S., Duyn, J.H., Glover, G.H., Gonzalez-Castillo, J., Handwerker, D.A., Keilholz, S., Kiviniemi, V., Leopold, D.A., de Pasquale, F., Sporns, O., Walter, M., Chang, C., 2013. Dynamic functional connectivity: promise, issues, and interpretations. Neuroimage 80, 360–378.

Latora, V., Marchiori, M., 2001. Efficient behavior of small-world networks. Phys. Rev. Lett. 87, 198701.

Li, Y., Liu, Y., Li, J., Qin, W., Li, K., Yu, C., Jiang, T., 2009. Brain anatomical network and intelligence. PLoS Comput. Biol. 5.

Maslov, S., Sneppen, K., 2002. Specificity and stability in topology of protein networks. Science 296, 910–913.

Miller, R.L., Yaesoubi, M., Turner, J.A., Mathalon, D., Preda, A., Pearlson, G., Adali, T., Calhoun, V.D., 2016. Higher dimensional meta-state analysis reveals reduced resting fMRI connectivity dynamism in schizophrenia patients. PloS One 11, e0149849.

Newman, M.E.J., 2006. Modularity and community structure in networks. Proc. Natl. Acad. Sci. 103, 8577–8582.

Parkes, L., Fulcher, B., Yücel, M., Fornito, A., 2018. An evaluation of the efficacy, reliability, and sensitivity of motion correction strategies for resting-state functional MRI. Neuroimage 171, 415–436.

Peer, M., Prüss, H., Ben-Dayan, I., Paul, F., Arzy, S., Finke, C., 2017. Functional connectivity of large-scale brain networks in patients with anti-NMDA receptor encephalitis: an observational study. The Lancet Psychiatry 4, 768–774.

Pruim, R.H.R., Mennes, M., van Rooij, D., Llera, A., Buitelaar, J.K., Beckmann, C.F., 2015. ICA-AROMA: a robust ICA-based strategy for removing motion artifacts from fMRI data. Neuroimage 112, 267–277.

Raichle, M.E., Mintun, M.A., 2006. Brain work and brain imaging. Annu. Rev. Neurosci. 29, 449–476.

Ramirez-Mahaluf, J.P., Perramon, J., Otal, B., Villoslada, P., Compte, A., 2018. Subgenual anterior cingulate cortex controls sadness-induced modulations of cognitive and emotional network hubs. Sci. Rep. 8, 8566.

Rubinov, M., Sporns, O., 2010. Complex network measures of brain connectivity: uses and interpretations. Neuroimage 52, 1059–1069.

Sato, J.R., Salum, G.A., Gadelha, A., Vieira, G., Zugman, A., Picon, F.A., Pan, P.M., Hoexter, M.Q., Anés, M., Moura, L.M., Del'Aquilla, M.A.G., Crossley, N., Amaro, E., Mcguire, P., Lacerda, A.L.T., Rohde, L.A., Miguel, E.C., Jackowski, A.P., Bressan, R.A., 2015. Decreased centrality of subcortical regions during the transition to adolescence: a functional connectivity study. Neuroimage 104, 44–51.

Shine, J.M., Koyejo, O., Bell, P.T., Gorgolewski, K.J., Gilat, M., Poldrack, R.A., 2015. Estimation of dynamic functional connectivity using Multiplication of Temporal Derivatives. Neuroimage 122, 399–407.

Shine, J.M., Koyejo, O., Poldrack, R.A., 2016. Temporal metastates are associated with differential patterns of time-resolved connectivity, network topology, and attention. Proc. Natl. Acad. Sci. 113, 9888–9891.

Sizemore, A.E., Bassett, D.S., 2018. Dynamic graph metrics: tutorial, toolbox, and tale. Neuroimage 180, 417–427.

Smith, S.M., Fox, P.T., Miller, K.L., Glahn, D.C., Fox, P.M., Mackay, C.E., Filippini, N., Watkins, K.E., Toro, R., Laird, A.R., Beckmann, C.F., 2009. Correspondence of the brain's functional architecture during activation and rest. Proc. Natl. Acad. Sci. 106, 13040–13045.

Smith, S.M., Miller, K.L., Moeller, S., Xu, J., Auerbach, E.J., Woolrich, M.W., Beckmann, C.F., Jenkinson, M., Andersson, J., Glasser, M.F., Van Essen, D.C., Feinberg, D.A., Yacoubb, E.S., Ugurbil, K., 2012. Temporally-independent functional modes of spontaneous brain activity. Proc. Natl. Acad. Sci. U.S.A. 109, 3131–3136.

Smith, S.M., Miller, K.L., Salimi-Khorshidi, G., Webster, M., Beckmann, C.F., Nichols, T.E., Ramsey, J.D., Woolrich, M.W., 2011. Network modelling methods for FMRI. Neuroimage 54, 875–891.

van den Heuvel, M.P., Stam, C.J., Kahn, R.S., Hulshoff Pol, H.E., 2009. Efficiency of functional brain networks and intellectual performance. J. Neurosci. 29, 7619–7624.

Van Essen, D.C., Ugurbil, K., Auerbach, E., Barch, D., Behrens, T.E.J., Bucholz, R., Chang, A., Chen, L., Corbetta, M., Curtiss, S.W., Della Penna, S., Feinberg, D., Glasser, M.F., Harel, N., Heath, A.C., Larson-Prior, L., Marcus, D., Michalareas, G., Moeller, S., Oostenveld, R., Petersen, S.E., Prior, F., Schlaggar, B.L., Smith, S.M., Snyder, A.Z., Xu, J., Yacoub, E., 2012. The Human Connectome Project: a data acquisition perspective. Neuroimage, Connectivity 62, 2222–2231.

Vidaurre, D., Smith, S.M., Woolrich, M.W., 2017. Brain network dynamics are hierarchically organized in time. Proc. Natl. Acad. Sci. 114, 12827–12832.

Voss, M.W., Erickson, K.I., Prakash, R.S., Chaddock, L., Kim, J.S., Alves, H., Szabo, A., Phillips, S.M., Wójcicki, T.R., Mailey, E.L., Olson, E.A., Gothe, N., Vieira-Potter, V.J., Martin, S.A., Pence, B.D., Cook, M.D., Woods, J.A., McAuley, E., Kramer, A.F., 2013. Neurobiological markers of exercise-related brain plasticity in older adults. Brain Behav. Immun. 28, 90–99.

Zalesky, A., Fornito, A., Bullmore, E., 2012. On the use of correlation as a measure of network connectivity. Neuroimage 60, 2096–2106.

Zalesky, A., Fornito, A., Cocchi, L., Gollo, L.L., Breakspear, M., 2014. Time-resolved resting-state brain networks. Proc. Natl. Acad. Sci. 111, 10341–10346.

Zalesky, A., Fornito, A., Harding, I.H., Cocchi, L., Yücel, M., Pantelis, C., Bullmore, E.T., 2010. Whole-brain anatomical networks: does the choice of nodes matter? Neuroimage 50, 970–983.

Appendix C

The ascending arousal system promotes optimal performance through meso-scale network integration in a visuospatial attentional task

Authors

Gabriel Wainstein[1], Daniel Rojas-Libano[2], Vicente Medel[1,9], Dag Alnæs[3,4], Knut K. Kolskår[3, 5,6], Tor Endestad[5,7,8], Bruno Laeng[5,7], Tomas Ossandon[9,10], Nicolás Crossley[9], Elie Matar[1] and James M. Shine[1,11*]

Affiliations

1 Brain and Mind Centre, The University of Sydney, Sydney, NSW, Australia
2 Centro de Neurociencia Humana y Neuropsicología, Facultad de Psicología, Universidad Diego Portales, Santiago, Chile
3 NORMENT, Division of Mental Health and Addiction, University of Oslo, and Oslo University Hospital, Oslo, Norway
4 Bjørknes University College, Oslo, Norway
5 Department of Psychology, University of Oslo, Oslo, Norway
6 Sunnaas Rehabilitation Hospital HT, Nesodden, Norway
7 RITMO Centre for Interdisciplinary Studies in Rhythm, Time and Motion, University of Oslo, Norway
8 Helgelandssykehuset Mosjøen, Helse Nord, Norway
9 Department of Psychiatry, School of Medicine, Pontificia Universidad Católica de Chile, Santiago, Chile
10 Institute for Biological and Medical Engineering, Schools of Engineering, Medicine and Biological Sciences, Pontificia Universidad Católica de Chile, Chile
11 Centre for Complexity, The University of Sydney, Sydney, NSW, Australia

Corresponding author

* James M. Shine – mac.shine@sydney.edu.au

Abstract

Previous research has shown that the autonomic nervous system provides essential constraints over ongoing cognitive function. However, there is currently a relative lack of direct empirical evidence for how this interaction manifests in the brain at the macro-scale level. Here, we examine the role of ascending arousal and attentional load on large-scale network dynamics by combining pupillometry, functional MRI and graph theoretical analysis to analyze data from a visual motion-tracking task with a parametric load manipulation. We found that attentional load effects were observable in measures of pupil diameter and in a set of brain regions that parametrically modulated their BOLD activity and meso-scale network-level integration. In addition, the regional patterns of network reconfiguration were correlated with the spatial distribution of the α2a adrenergic receptor. Our results further solidify the relationship between ascending noradrenergic activity, large-scale network integration, and cognitive task performance.

Author Summary

In our daily lives, it is usual to encounter highly demanding cognitive tasks. They have been traditionally regarded as challenges that are solved mainly through cerebral activity, specifically via information-processing steps carried by neurons in the cerebral cortex. Activity in cortical networks thus constitutes a key factor for improving our understanding cognitive processes. However, recent evidence has shown that evolutionary older players in the central nervous system, such as brainstem's ascending modulatory systems, might play an equally important role in diverse cognitive mechanisms. Our article examines the role of the ascending arousal system on large-scale network dynamics by combining pupillometry, functional MRI and graph theoretical analysis.

Introduction

Cognitive processes emerge from the dynamic interplay between diverse mesoscopic brain systems [1,2]. Thus, the neural activity supporting cognition does not exist in a vacuum, but instead is deeply embedded within the ongoing dynamics of the physiological networks of the body[3]. In particular, the neural processes underlying cognition are shaped and constrained by the ascending arousal system, whose activity acts to facilitate the integration between internal states and external contingencies[4]. Timely and selective interactions between the ascending arousal system and the network-level configuration of the brain are thus likely to represent crucial constraints on cognitive and attentional processes. Yet, despite these links, we currently have a relatively poor understanding of how the ascending arousal system helps the brain as a whole to functionally reconfigure during cognitive processes, such as attention, in order to facilitate effective cognitive performance.

Recent evidence has linked higher-order cognitive functions in the brain to the intersection between whole-brain functional network architecture and the autonomic arousal system[2,5–8]. Central to these relationships is the unique neuroanatomy of the ascending noradrenergic system. For instance, the pontine locus coeruleus, which is a major hub of the ascending arousal system, sends widespread projections to the rest of the brain[9]. Upon contact, adrenergic axons release noradrenaline, which acts as a ligand on three types of post- and pre-synaptic adrenergic receptors (i.e., α1, α2 and β). The functional effects of each of these receptors depend on their differential sensitivities to noradrenaline (affinities for the ligand differ across receptors: $\alpha2 > \alpha1 > \beta$) and intracellular cascades, as well as their neuronal and regional distributions[9–14]. By modulating the excitability of targeted regions, the locus coeruleus can effectively coordinate neural dynamics across large portions of the cerebral cortex[15,16]. However, it is challenging to non-invasively track the engagement of the locus coeruleus during whole-brain neuroimaging and cognitive task performance.

Fortunately, it has been widely shown that the pupil diameter directly responds to changes in the activity of the locus coeruleus, and thus serves as an indirect, non-invasive measure of the noradrenergic system[17,18].Specifically pupil diameter has been shown to indirectly monitor the neuromodulatory influences of the ascending arousal system on a variety of different brain regions[5,11,19–21] . Moreover, noradrenergic-mediated dilations in pupil diameter have been shown to effectively track the allocation of attentional resources[22–24], in addition to both physical and mentally effortful processes[25,26] . Fast, phasic changes in pupil diameter have also been shown

to directly relate to changes in the activity of the locus coeruleus[18,27,28]. While there is some evidence that pupil diameter covaries with other subcortical systems, such as the cholinergic[29] and serotoninergic system[30], the physiological mechanism for these effects is more opaque, and there is also clear causal evidence linking stimulation of the locus coeruleus to dilation of the pupil[19,31]. Despite these insights, several questions remain unanswered regarding how these processes are related to the complex architecture of the brain[32]. For instance, the processes by which the ascending arousal system modulates the functional dynamics of brain networks to facilitate attention, decision making and optimal behavioural performance have only begun to be explored[31,33–35].

To examine these relationships in more detail, participants performed a motion-tracking task (top panel of Figure 1A) involving four levels of increasing attentional load, which was modulated by manipulating the number of items required to covertly attend to over an 11s tracking period. Specifically, subjects were instructed to covertly track the movement of several pre-identified targets (two to five) in a field of non-target stimuli (ten in total, including targets; see Figure 1). To investigate the network topological signatures of performing this task, we collected concurrent BOLD fMRI and pupillometry data. We hypothesized that, if increasing mental effort led to the reconfiguration of large-scale network architecture via the ascending arousal system, then the number of items required to be tracked over time (i.e., the attentional load) should relate to: i) increased pupil diameter; ii) heightened BOLD activity within attentional networks; and iii) augmented topological integration. Also, we predicted that individual differences in pupil diameter should track individual differences in effective attentional performance and decision processes[35–37]. Finally, we tested if the regional patterns of network configuration were predicted by the distribution of a predefined adrenergic receptor density atlas[31,34,38,39]. Our results confirm these predictions, and hence provide a mechanistic link between network topology, ascending noradrenergic arousal and attentional load.

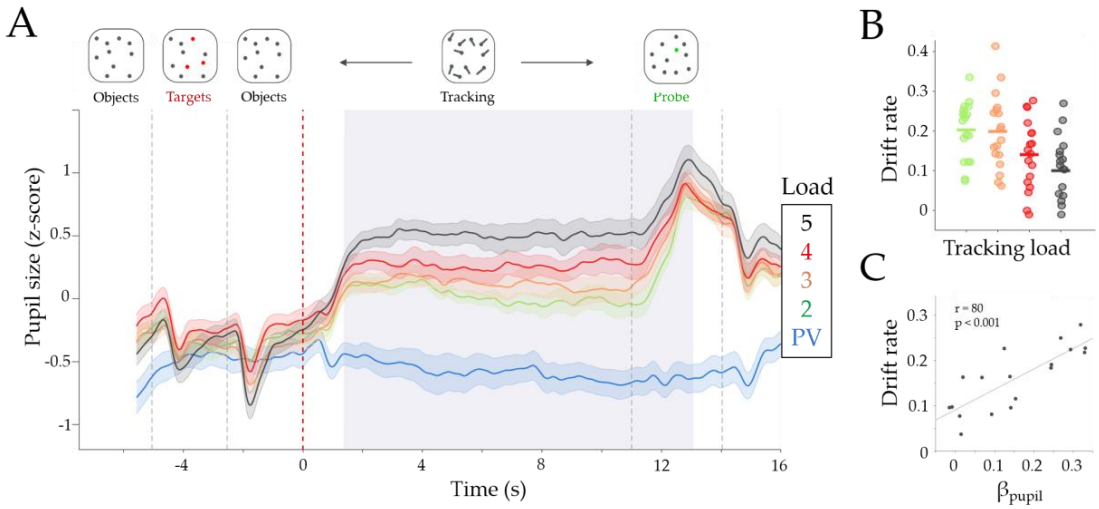

Figure 1: Effect of task difficulty on pupil diameter. A) Group average (z-score) pupil diameter time series for each Load condition. Colors represent passive viewing (PV) in blue, and Loads 2 to 5 in green, orange, red and black, respectively. The shaded area represents the standard error of the mean. We observed an average increase in pupil diameter, during tracking, with each Load condition. The light grey area represents timepoints with significant parametric effect ($\beta_{pupil} > 0$; FDR corrected at $p < 0.01$). Dotted lines represent the onset of each trial event (showed in the top part of the Figure). The red dotted line (Time = 0) is the tracking onset period when the dots began to move; B) Drift rate in each load condition. Each dot is the drift rate for each subject and load (mean $\beta_{Drift} = -0.03$, $t_{(17)} = -7.43$, $p = 9.7x10^{-7}$); C) Pearson correlation between the pupil parametric effect of Load (β_{pupil}) with the average drift rate across subjects ($r_{drift} = 0.8$, $p = 1.0x10^{-4}$). The x-axis is the mean beta estimate of the pupillary load effect of the significative time window (β_{pupil}) and the y-axis represents the mean drift rate across Loads.

Results

The Relationship Between Sympathetic Tone and Attentional Processing

Consistent with previous work[5], our two level analysis - linear regression within each subject, and a two-tailed *t*-test between subjects - found that task performance (i.e., correct responses) decreased with attentional load (mean $\beta_{Acc} = -6.66$; $t_{(17)} = -5.19$, $p = 7.2x10^{-5}$; Figure S1B) while RT increased with attentional load (mean $\beta_{RT} = 0.06$, $t_{(17)} = 5.10$, $p = 8.8x10^{-5}$). We expanded on this result by translating performance into EZ-diffusion model parameters. Roughly, this approach uses the accuracy and reaction time distribution to estimate three latent parameters[40]: drift rate, a marker of the accumulation of decision evidence (Eq. 1); boundary criteria, the amount of evidence required to make a decision (Eq. 2); and non-decision time, the epoch spent processing the tasks perceptually (Eq. 3). The advantages of using this model are twofold: firstly, there are well-known links between the parameters to decision making processes[41,42], pupil diameter[27,43] and network reconfiguration[2]; secondly, drift rate accounts for the accuracy-reaction time trade off, as it takes into consideration both accuracy and the

variability in reaction time into its calculation. In this way, our approach offers a better approximation of the ongoing computational processing during the task than accuracy and RT[44,45]. Using this approach, we observed a decrease in both the boundary criteria (β_{Bound} = -0.01, $t_{(17)}$ = -2.70, p = 0.015) and drift rate (mean β_{Drift} = -0.03, $t_{(17)}$ = -7.43, p = 9.7x10^{-7}; Figure 1B), and an increase in the non decision time (mean β_{nd} = 0.07, $t_{(17)}$ = 5.32, p = 5.5x10^{-5}) with increasing attentional load.

By calculating the linear effect of load on pupil size across a moving average window of 160ms (see Methods), we observed a main effect of increased pupil diameter across both the tracking and probe epochs ($\beta_{pupil} > 0$, $p_{FDR} < 0.01$; light grey in Figure 1A depict significant epochs of time during the task; and in Figure S1A show the group average β_{pupil} time series). We also observed a positive correlation between mean β_{pupil} during the significant period (for simplicity we will refer to this value as βpupil) to the mean drift rate, mean boundary criteria and accuracy across all loads (Pearson's r_{drift} = 0.8, p = 1.0x10^{-4}; Figure 1C; r_{acc} = 0.68, p = 1.5x10^{-3}, Figure S1C; r_{α} = 0.71, p = 9x10^{-4}). The same relationships were not observed with non-decision time (Pearson's r_{nd} = -0.31, p = 0.19). Additionally, we analysed whether this effect was present both within and between subjects in a trial-by-trial manner. To this end, we created a logistic linear mixed model (Eq. 6) to test whether pupil diameter was a predictor of performance (i.e., correct or incorrect response), as we would expect that incorrect responses should relate to decreased pupil diameter in difficult trials. We used the average pupil diameter within each trial of Load 4 and 5 (to account for the ceiling effect of Load 2 and 3) as regressors and subject as a grouping variable. We found a statistically significant fixed effect of pupil diameter on performance within each trial (β = 0.0127 ± 5x10^{-4}; $t_{(286)}$= 2.48; p = 0.013). Furthermore, we analyzed the random effect coefficients, which are the dispersion of the regressor across the grouping variable from the fixed regressor (in this case there is one value per subject), to assess the role of average across task performance. We found that the random effect covaried with the average performance and drift rate of each subject (Accuracy: Pearson's r = 0.73, p = 8x10^{-5} ; Drift: Pearson's r = 0.73, p = 5x10^{-5}) suggesting that trial by trial pupil diameter was a better predictor of performance (i.e., correct or incorrect) on subjects with higher average performance in comparison to subjects with lower performance across the task. In conclusion, these results suggest that attentional load manipulation and pupil dilation covaried with performance on this attentionally demanding task both within and between subjects.

Network Integration Increases as a Function of Attentional Load

Based on previous studies, we hypothesized that an increase in attentional load should recruit a distributed functional network architecture[5], heightening network integration[2,12,34]. To test this hypothesis, we implemented a hierarchical topological network analysis[46–48] on the average time-resolved functional connectivity matrix calculated across the tracking period of the task. Our analysis identified a subnetwork of tightly inter-connected regions that were part of attentional, somatomotor, and cerebellar network (red in Figure 2) that increased its BOLD activity after the tracking onset (Figure 2F). The tightly integrated regions were diversely connected to a separate frontoparietal sub-module (blue in Figure 2) that was less active during the trial. Two remaining sub-modules (yellow and green in Figure 2) showed a negative BOLD response during the tracking period and were part of a diverse set of networks. Interestingly, 81% of the Frontoparietal network (FPN) and all the Default Mode Network (DMN) were found to be within this less active group (see Supplementary Table S2 for the complete list of regions and sub-module assignments).

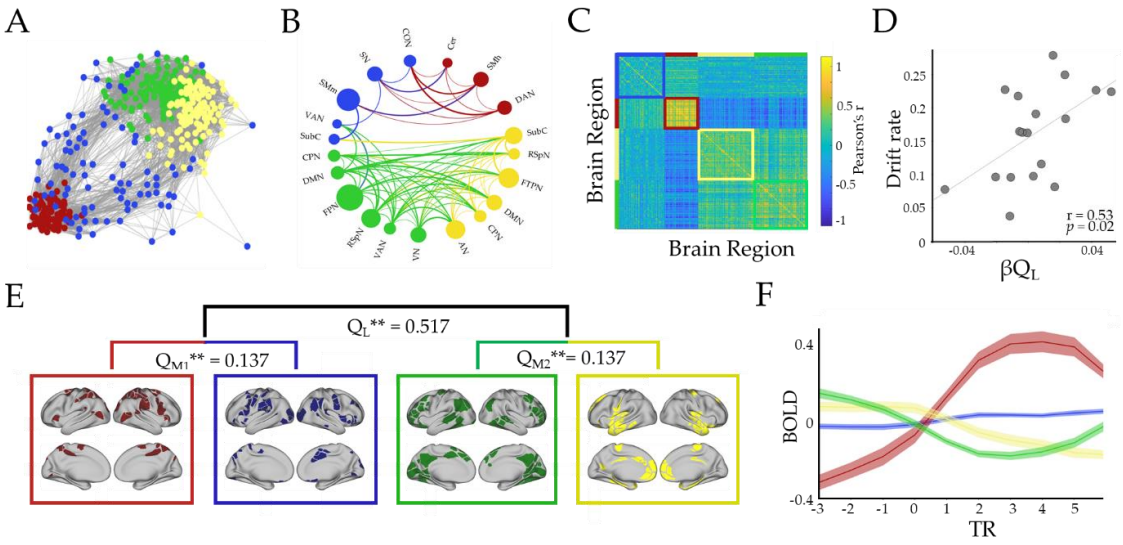

Figure 2: Hierarchical functional topology analysis of the brain during tracking across all loads. We observed two large-scale modules, and two meso-scale modules within each larger module (Module one [M1, red/blue] and Module two [M2, green/yellow], respectively): M1 corresponded to predominantly attentional and somatomotor network, and M2 to Frontoparietal (FPN) and Default Mode Network (DMN) among others (B and E). A) Forced directed plot representation of the average cluster across subjects. Edges higher than 0.15 are shown. Each color represents a unique sub module; B) A circle plot representing the resting state regions that were included within each sub module, with networks with > 30% of regions in each submodule shown in the plot. The diameter of the circles corresponds to the percentage of network regions that participated in that cluster. Connection width relates to average positive connection strength (functional connectivity), however only connections with r > 0.1 are shown; C) Connectivity matrix (Pearson's r) between all pair of regions ordered by

module assignments – note the strong anti-correlation between the red and green/yellow sub-modules; D) Correlation between parametric load effect on large scale modularity (β_Q value), and drift rate (Pearson's r = 0.53; p = 0.022); E) Hierarchical analysis representation: Q_L, Q_{M1} and Q_{M2} represent the modularity value for each level (Q_L large scale, and $Q_{M1\text{-}M2}$ meso-scale level) and ** represents the probability of finding this value when running a null model (p = 0 for all three modularity values). The brain maps correspond to the cortical regions associated with each sub module; F) BOLD mean effect for each sub-cluster, each line represents the group average, and shaded areas are the standard error of the mean, x-axis is Repetition Time (TR) centered around tracking onset (TR = 0). DAN, dorsal attention; VN, visual; FPN, frontoparietal; SN, salience; CO, cingulo-opercular; VAN, ventral attention; SMm, somatomotor mouth; SMh, somatomotor hand; RSpN, retrosplenial; FTP, frontotemporal; DMN, default mode; AN, auditory; CPN, cinguloparietal; SubC, subcortex; Cer, Cerebellar.

Contrary to expectations, we did not observe significant parametric topological change (i.e., modularity, Q) at the macroscopic level as a function of attentional load ($p > 0.05$ for all TRs, Figure S2A). However, when analysing the correlation between modularity and performance measures (i.e., accuracy, drift rate and pupil diameter), we observed that an increase in the large-scale modularity load effect (i.e., higher modularity with load, β_{QL}) positively correlated with higher mean drift rate (Pearson's r = 0.53; p = 0.022; Figure 2D), mean accuracy (Pearson's r = 0.61; p = 0.007; Supplementary Figure S3A), but was independent from βpupil (Pearson's r = 0.43; p = 0.073). These results suggested that the system reconfigured during tracking towards increasing modularity, which in turn affected the efficient encoding of the ongoing task during tracking and hence, the decision-making process during the task probe.

Upon closer inspection of the data (Figure 2C), we observed a substantial number of nodes that were playing an integrative role during task performance, albeit at a finer resolution than the initial analysis suggested. We performed the modularity assignment within each large-scale module. The hierarchical analysis resulted in two pairs of sub-modules at the meso-scale level with a significant modularity (compared to 100 random graphs with preserved signed degree distribution; Q_{M1} = 0.137, p = 0; Q_{M2} = 0.137, p = 0; Figure 2E). Specifically, the red sub-module was found to selectively increase its participation coefficient (PC) at the meso-scale level (i.e., by increasing the connection weights to the blue submodule in comparison to intramodular connections; Eq. 5) as a function of increasing attentional load ($\beta_{PC} = 2.4\text{x}10^{-3}$, $t_{(17)} = 3.57$; p = 0.002; Figure 3A). Additionally, the extent of integration in the red sub-module was positively correlated across subjects with βpupil(Pearson r = 0.62, p = 0.006; Figure 3B), drift rate (Pearson's r = 0.66, p = 0.002; Figure 3C) and accuracy (r = 0.57, p = 0.012, Figure S3B). Importantly, these relationships were found to be specific to the red sub-module (Blue: Pearson's r = -0.02, p = 0.936; Yellow: Pearson's r = -0.011, p = 0.965;

Green: Pearson's r = -0.12, $p = 0.617$).

Based on these results, we implemented a linear mixed model (Eq. 7), using the subjects' average pupil response within each Load as a regressor and the average participation of the red sub module as the dependent variable, with grouping by subject. Using this approach, we observed a significant fixed effect of pupil diameter on PC ($\beta = 7.6\text{x}10^{-3} \pm 3\text{x}10^{-3}$, $t_{(70)} = 2.60$, $p = 0.011$). Furthermore, the random effect coefficients (i.e., the between subject variation of the regressor value) correlated positively with accuracy (Pearson's r = 0.47, $p = 0.048$) and drift rate (Pearson's r = 0.62, $p = 0.005$), suggesting that subjects with a strong relationship between red module integration and pupil diameter have better behavioural outcomes. We then correlated the red βPC to the load effect on large scale modularity (βQ_L, Fig. 2D) and observed a significant positive correlation (Pearson's r = 0.59, $p = 0.009$). Finally, given that both of the topological parameters were correlated to drift rate and also with each other, we performed a partial correlation between drift rate and βPC controlling by βQ_L (r = 0.51, $p = 0.034$), and the partial correlation between drift rate and βQ_L controlling by βPC (r = 0.36, $p = 0.145$). This suggests that drift rate is correlated to the mesoscale integration of the red sub-module, but less so with increases in large scale modularity. Thus, although the macroscale network did not demonstrate increased integration *per se*, the relative amount of meso-scale integration within the red community was associated with increased performance (i.e., drift rate) and sympathetic arousal (i.e., pupil diameter), both between and within subjects. In this way, these results provide a direct relationship between the effect of attention load on pupillometry, drift rate, and a trade-off between large-scale segregation and meso-scale network integration.

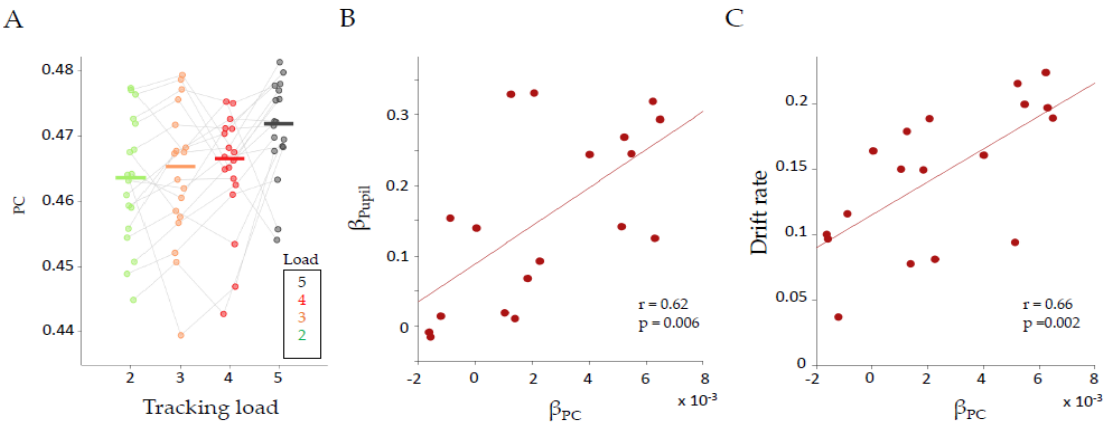

Figure 3: Relationships between load effect on participation, drift rate and pupil load effect. A) Average participation coefficient (PC) for each load, for the red module, during tracking. Each color represents the corresponding tracking load (from 2 to 5). Grey lines correspond to each subject; B-C) A

regression parameter (β_{PC}) was calculated for each subject and then correlated to β_{pupil} (B; r = 0.62; p = 0.006) and Drift rate (C; r = 0.66; p = 2.4x10^{-3}). Each circle corresponds to the mean value per subject.

Network meso-scale integration and adrenergic receptor density

Given the relationship between mental effort, noradrenergic tone and pupil dilation[5,18,26,49,50], the results of our analyses strongly suggested that the adrenergic system is involved in the meso-scale network reconfiguration observed during attentional tracking. The locus coeruleus can impact the cortical system in multiple ways, both through direct release of noradrenaline onto cortical neurons, and through the modulation of subcortical regions (such as the thalamic nuclei) with concurrent impact on the cortical dynamic. Importantly, in either case, the modulation is dependent on the noradrenergic receptors subtypes, which have different sensitivities to noradrenaline[13,51], variable expression in the cerebral cortex[52,537,58] and also belong to distinct classes (i.e., α1, α2, and β receptors). In particular, the α2a has been previously associated with working memory, adaptive gain and effective attention[13,51,54]. To gain a deeper insight into the role of α2a receptors in mesoscale integration during attentional tracking, we extracted the regional expression of the ADRA2A gene (which codes for α2a adrenoceptors) from the Allen Human Brain Atlas repository[55,56], and compared the cortical regional expression of this gene with the brain activity patterns identified in our network analysis (Figure 2E).

Based on the relationships between pupil diameter (Figure 1), topological signatures (Figure 2) and task performance (Figure 3), and the known link between these variables and engagement of the noradrenergic system, we hypothesized that the different modules and sub-modules that we observed should have different densities of neuromodulatory receptors to account for the differential patterns across the network. To test this hypothesis, we conducted a two-tailed t-test in each hierarchical level comparing the density of the ADRA2A expression between modules. To account for spatial autocorrelation, we generated 5,000 surrogates maps with the same spatial autocorrelation of the ADRA2A map, calculated a t-statistic for each surrogate and the evaluated the probability of finding the observed t-statistic against the null distribution[57,58]. We indeed observed significant differences between modules at the meso-scale level. Specifically, we found significant differences between the blue and yellow sub-modules ($t_{(194)}$ = 3.82, p = 2x10^{-4}, p_{SA} = 0.02) and the differences between green and yellow sub-modules ($t_{(177)}$ = -4.47, p = 1.3x10^{-5}, p_{SA} = 0.004), while the other differences did not survive the spatial autocorrelation test (green-red: $t_{(152)}$ = 0.47; p = 0.635, p_{SA} = 0.590; yellow-red: $t_{(156)}$ = -3.02, p = 0.003, p_{SA} = 0.121; green-blue: $t_{(173)}$ = -0.68,

p = 0.496, p_{SA} = 0.324; red-blue: $t_{(135)}$ = -1.30, p = 0.195 , p_{SA} = 0.237; Figure S5A).

The modulatory effects of noradrenaline have been argued to depend directly on ongoing glutamatergic activity in target regions[59,60]. Moreover, it has been shown that the main source of the BOLD activity is the neurovascular response caused by pyramidal neurons containing Cyclo-oxygenase-2[61]. Importantly, this evoked response following noradrenergic activation is dependent on the ongoing activity of the pyramidal neurons[62]. Thus, the role of noradrenaline on brain dynamics and BOLD response depends critically on ongoing glutamatergic activity, which putatively represents pooled neural spiking activity[63]. Given the differential task-related BOLD activity of the different sub-modules (i.e., Figure 2F, Figure S4and Figure 4A), and the observed regional variability and specificity of integration across the network, we hypothesized that network-level integration would be explained by the combined effect of ongoing BOLD activity and the distribution of the adrenergic receptor expression. Finally, we predicted that the role of the α2a receptor atlas in shaping brain activity and topology should be dependent of the subjects' pupil diameter, such that higher βpupil should rely on a stronger relationship between network topology and α2a receptor expression.

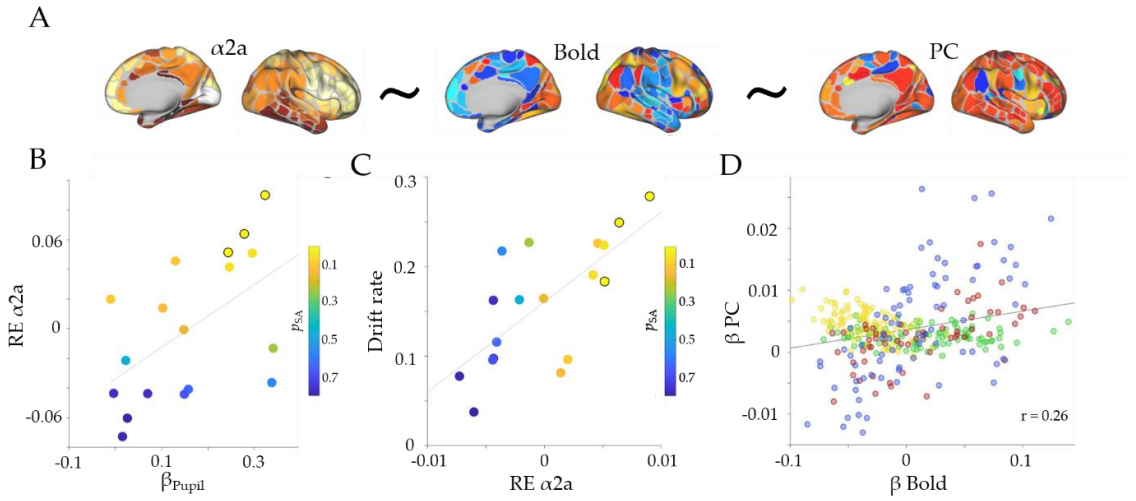

Figure 4: Receptor density analysis. A) Spatial maps of α2a density (left), BOLD parametric effect (middle) and Participation Coefficient parametric effect (right); '~' represents the linear model tested in the analysis; B) Scatter plot depicting the relationship between β_{Pupil} and the random effect of α2a (RE α2a; r = 0.54, p = 0.02); C) Scatter plot depicting the relationship between the random effect of α2a and drift rate (r = 0.70, p = 0.001) – the colors of the dots represent the p_{SA} value from the linear effect of α2a on βBOLD within each subject and the marked circles correspond to subjects with $p_{SA} < 0.05$; D) Pearson correlation of the group average BOLD parametric effect (β_{BOLD}) and participation coefficient (β_{PC}; r = 0.26, $p = 17 \times 10^{-7}$). Colors represent each module assignment as in Figure 2.

To evaluate between these different hypotheses, we created three linear mixed models in order to better disentangle the different plausible interactions between the variables (see Methods), while still controlling for between subject's variability as grouping variable. Additionally, to control for spatial autocorrelation, we used 5,000 surrogate maps that maintained the spatial autocorrelation of the α2a while permuting the density values. In the first model (Eq. 8), we tested the hypothesis that the parametric BOLD effect (i.e., βBOLD, Figure S4) is shaped by the distribution of α2a receptors. We found significant evidence for a positive fixed effect of α2a on βBOLD activity, however this effect did not survive correction for spatial autocorrelation ($\beta_{\alpha 2a} = 0.037 \pm 0.016$; $t_{(5992)} = 2.29$; $p = 0.022$; $p_{SA} = 0.106$; Table S2). Furthermore, we correlated the random effect coefficients (from the original and the surrogate maps) to both βPC and βpupil, and observed a significant positive correlation between the participation coefficient and both pupils (Pearson's r = 0.54, $p = 0.02$, $p_{SA} = 0.036$; Figure 4B) and mean drift rate (Pearson's r = 0.70, $p = 0.001$, $p_{SA} = 0.001$; Figure 4C). This result shows the manner in which pupil diameter linearly shapes βBOLD cortical map through the engagement of the α2a receptor expression map. Importantly, although the fixed effect of α2a on βBOLD didn't survive the spatial autocorrelation correction, the linear correlation of this effect with both βpupil and drift rate (between subjects) did survive the correction.

To further analyze the between subject differences in the role of α2a receptor atlas in shaping the βBOLD map, we ran a separate linear model within each subject with α2a as a regressor and βBOLD of each region as the dependent variable (while also correcting for spatial autocorrelation using 5,000 surrogate maps). As can be seen in Figure 4B-C, we observed a dependency between the p_{SA} value, βpupil and drift rate, in which the βpupil and drift rate subject effects survived the spatial autocorrelation correction ($p_{SA} < 0.05$; marked circles in Fig. 4B-C). Despite these results, there was no significant effect of α2a on βPC (Eq. 9; $\beta_{\alpha 2a} = 0.001 \pm 0.003$; $t_{(5992)} = -0.51$; $p = 0.6$), and no significant Pearson's correlation were found between the random effects and both β_{pupil} or drift rate (r = -0.24, $p = 0.33$ and r = -0.23, $p = 0.341$, respectively). However, we did find a significant effect of βBOLD on βPC (Eq. 10; $\beta = 0.0259 \pm 0.006$; $t_{(5992)} = 3.96$; $p = 7.55 \times 10^{-5}$). Together these results propose a closer link between pupil diameter, ascending neuromodulation and the cortical neuromodulation dependent on α2a receptor density.

Finally, we observed a differential relationship between βPC and βBOLD depending on the large-scale module to which the regions were assigned (Figure 4D). We expanded the former result by measuring, within each subject, the Pearson correlation between the β_{BOLD} and β_{PC} separately in each module (M1 being the modules assigned as red and blue, and M2 assigned as yellow and green; Figure 2). The results demonstrated a significant difference between modules, meaning that the M1has a higher correlation with βPC, in comparison to M2 ($t_{(17)} = -12.99$, $p = 2.93 \times 10^{-10}$). These results provided evidence that the adrenergic receptor distribution of α2a shapes the βBOLD activation map in proportion to the subject's pupil diameter. Additionally, βBOLD activation map modulates (i.e., was related to) meso-scale integration, and meso-scale integration is related to pupil diameter. Based on these results, we hypothesise that the adrenergic system shapes the BOLD activity, which in turns shapes the topology of the network towards integration. However, future work is required in order to test this hypothesis more directly, for instance by combining optogenetic approaches with neuronal recordings in awake animals.

Discussion

Here, we leveraged a unique dataset to simultaneously track pupil diameter and network topology during an attentional demanding task with increasing attentional load. Our results provide integrative evidence that links the ascending arousal system to the mesoscale topological signature of the functional brain network during the processing of an attentionally demanding cognitive task. Pupil diameter tracked with attentional load (Figure 1A) and was related to the speed of information accumulation as estimated by a drift diffusion model (Figure 1B-C). Additionally, we observed concurrent pupil dilations and adaptive mesoscale parametric topological changes as a function of task demands (Figures 2 and 3). Finally, we found evidence that topological reconfiguration was dependent on the regional activity and the genetic expression of the adrenergic receptors in the brain (Figure 4). Together, these results provide evidence for the manner in which the ascending arousal noradrenergic system reconfigures brain network topology so as to promote attentional performance according to task demands.

The relationship between performance and pupil diameter is consistent with the predictions of Adaptive Gain Theory[17]. Within this framework, the locus coeruleus is proposed to adaptively alter its activity according to the demands imposed on the system. More specifically, the theory proposes that performance follows an inverted U-shaped relationship with arousal, such that maximal operational flexibility in the

noradrenergic system is associated with optimal task performance[13,54]. We observed that load-related increases in pupil diameter, presumably due to increased activity in the ascending arousal system[17,18,64], relates closely with the activity and topology of the broader brain network (Figure 2), in a manner that is reflective of effective task performance (Figure 3). Similar effects have been described in animal models after a chemogenetic activation of the locus coeruleus, which strongly alters the large-scale network structure towards large-scale integration, specifically in regions with heightened adrenergic receptor expression[31]. How these changes, which are likely related to the modulation of the neural gain that mediates effective connections between distributed regions of the brain[15,33], are traded-off against requirements for specificity and flexibility remains an important open question for future research.

The addition of attentional load was found to alter the integration of meso-scale sub-modules, but not the higher-level modular organization. This topological result is somewhat more targeted than those described in previous work[2,34,65]. While these differences may be related to disparities in the way that the data were analyzed, the results of our study do demonstrate that alterations in the cerebral network topology at a relatively local (i.e., sub-modular) level are crucial for effective task performance[66]. Additionally, our results replicate and expand upon a previous study[67], in which the authors found that short term practice on an attentional task was related to increased coupling between attentional networks and segregation among task-negative (DMN) and frontoparietal network (FPN). Our study replicates the graph theoretical results of that study, while also directly relating the findings to the architecture of the ascending neuromodulatory system. One potential explanation for these results comes from animal studies, in which rapid changes in pupil diameter have been compared to changes in neural population activity at the microscale[18,49,50]. These studies suggest that the ascending arousal system may be able to alter the topology of the network in a hierarchical manner that is commensurate with the spatiotemporal scale of the arousal systems' capacity [2]. Future work that integrates results across spatiotemporal scales is required to appropriately adjudicate the implications of this hypothesis.

Importantly, our approach is not without limitations. For one, the participation measures used in our linear mixed model were estimated at the meso-scale level, and hence derived from different modular partitions. Furthermore, the specificity of the pupillary response as a correlate of LC activity is currently under active debate. For instance, in addition to the strong empirical links between the noradrenergic system

and pupil dilation, there is also evidence that the pupil is dilated in concert with activity in the basal forebrain cholinergic system[68], however it bears mention that both peripheral[69] and central cholinergic tone[21] is associated with pupillary constriction. There are more plausible physiological routes for the serotonergic system to dilate the pupil (via the excitation of the intermediolateral cell column), and in keeping with this, there is evidence that the serotonergic system is linked with pupil dilation[30]. Nevertheless, it is important to take into account that the neuromodulatory arousal system is replete with complex interconnections[70–73]. In addition, based on the current lack of a specific mechanism involving pupillary changes through the cholinergic system, it is highly probable that those correlations are due to indirect modulation of pupillary responses (e.g., via indirect neuromodulation mediated by the LC system). On another hand, we acknowledge the limitations of the atlas receptor analysis and the linear model used in our study. More specific neurobiological properties of the receptor distributions are needed to make better inferences, and hence provide more accurate answers of their role in brain dynamics. For instance, it would be ideal to compare receptor distributions that incorporated layer-specific expression, as there are well-known cellular and circuit differences across layers in the cerebral cortex[74,75]. Importantly, taking into consideration the strong correlation between different genetic expression maps[76], it is possible that the current correlation between ADRA2A expression and brain activity is a false positive caused by another neuroanatomical gradient strongly correlated to the ADRA2A. Therefore, future work studying the interaction between genetic expression of the neuromodulatory receptors, pupil diameter and brain activity is needed. In spite of this limitation, we believe in the importance of integrating pupil diameter and receptor distribution in the analysis as the relationships between noradrenergic tone, brain activity and network topology will help us to disentangle the mechanistic steps connecting the locus coeruleus system to both pupil diameter and brain dynamics.

In summary, we provide evidence linking mesoscale topological network integration, hierarchical organization and BOLD dynamics in the human brain that increases in attentional load, thus providing further mechanistic clarity over the processes that underpin the Adaptive Gain Model of noradrenergic function in the central nervous system.

Methods

Participants

18 right-handed individuals (age 19–26 years; 5 male) were included in this study. Exclusion criteria included: standard contraindications for MRI; neurological disorders; mental disorders or drug abuse. All participants gave written informed consent before the experiment.

Parametric Motion Tracking Task

Each trial of the task involved the same basic pattern (Figure 1A): the task begins with a display presenting the objects (i.e., blue colored disks); after a 2.5 s delay, a subset of the disks turns red for another 2.5 seconds; all of the disks then return to blue (2.5 seconds) before they started moving randomly inside the tracking area. The participants' job is to track the 'target' dots on the screen while visually fixating at the cross located at the center of the screen. After a tracking period of ~11 seconds, one of the disks is highlighted in green (a 'probe') and the subject is then asked to respond, as quickly as possible, as to whether the green probe object was one of the original target objects. The number of objects that subjects were required to attend to across the tracking period varied across trials. There were five trial types: passive viewing (PV), in which no target is assigned; and four load conditions, in which two to five targets were assigned for tracking. We operationalized attentional load as the linear effect of increasing task difficulty (i.e., the number of targets to be tracked).

The experiment was conducted using a blocked design, in which each block included: instruction (1s); fixation (0.3s, present throughout the rest of trial); object presentation (all objects were blue; 2.5s); target assignment (i.e., the targets changed color from blue to red; 2.5s); object representation (objects back to the original blue color; 2.5s); object movement/attentional tracking (moving blue dots; 11s); object movement cessation (0.5s); and a final probe (color change to green and response; 2.5 s). The total duration of each trial was 22.8s. Each condition was repeated 4 times in one fMRI-run, which also included 4 separate fixation periods of 11s each between five consecutive trials. All participants completed 4 separate runs of the experiment, each of which comprised 267 volumes. The order of the conditions was pseudo-random, such that the different conditions were grouped in sub-runs of triplets: PV, pseudo-random blocks of Loads 2 through 5 and a fixation trial. All objects were identical during the tracking interval and standard object colors were isoluminant (to minimize incidental pupillary responses during the task).

Behavior and EZ-Diffusion Model

The EZ-diffusion model was used to interpret the performance measures from the task[45,77]. This model considers the mean RT of correct trials, SD-RT across correct trials, and mean accuracy across the task and computes from these a value for drift rate (v, equation 1), boundary separation (a, equation 2) , and non-decision time (equation 3) – the three main parameters for the drift-diffusion model[77,78].

$$v = sign\left(P - \frac{1}{2}\right) \cdot 0.1 \cdot \sqrt[4]{\frac{log\left(\frac{P}{1-P}\right) \cdot \left[P^2 \cdot log\left(\frac{P}{1-P}\right) - P \cdot log\left(\frac{P}{1-P}\right) + P - \frac{1}{2}\right]}{VRT}} \quad (1)$$

$$a = 0.01 \cdot \frac{log\left(\frac{P}{1-P}\right)}{v} \quad (2)$$

$$Ter = MRT - \frac{a}{2 \times v} \times \frac{(1 - e^{-100 \cdot v \cdot a})}{(1 + e^{-100 \cdot v \cdot a})} \quad (3)$$

In which P is the average performance (range between 0 to 1); sign is an operator that will be -1 if $P < 0.5$ or +1 if $P > 0.5$; VRT is the standard deviation of reaction time (in seconds); and MRT is the mean reaction time (in seconds).

Pupillometry

Fluctuations in pupil diameter of the left eye were collected using an MR-compatible coil-mounted infrared EyeTracking system (NNL EyeTracking camera, NordicNeuroLab, Bergen, Norway), at a sampling rate of 60 Hz and recorded using the iView X Software (SensoMotoric Instruments, SMI GmbH, Germany). Blinks, artifacts and outliers were removed and linearly interpolated[79]. High frequency noise was smoothed using a 2nd order 2.5 Hz low-pass Butterworth filter. To obtain the pupil diameter average profile for each level of attentional load (Fig. 1B), data from each participant was normalized across each task block (corresponding to the five consecutive trials between fixations). This allowed us to correct for low frequency baseline changes without eliminating the load effect and baseline differences due to load manipulations[80,81]. Following this, a linear regression was performed in each time point using the task load as regressor and resulting in a 'load effect' time series for each subject.

MRI Data

Imaging data were collected on a Philips Achieva 3 Tesla MR-scanner, equipped with an 8-channel Philips SENSE head coil (Philips Medical Systems, Best, Netherlands) at the Interventional Centre, Oslo University Hospital, Norway. Functional data were

collected using a BOLD-sensitive T2* weighted echo-planar imaging sequence (36 slices, no gap; repetition time (TR), 2,2s; echo time (TE), 30 ms; flip-angle, 80°; voxel size, 3x3x3; field of view (FOV), 240x240 mm; interleaved acquisition). Anatomical T1-weighted images consisting of 180 sagittal oriented slices were obtained using a turbo field echo pulse sequence (TR, 6.7 ms; TE, 3.1 ms; flip angle 8°; voxel size 1x1.2x1.2 mm; FOV, 256x256 mm).

fMRI Data Preprocessing

After realignment (using FSL's MCFLIRT), we used FEAT to unwarp the EPI images in the y-direction with a 10% signal loss threshold and an effective echo spacing of 0.333. Following noise-cleaning with FIX (custom training set for scanner, threshold 20, included regression of estimated motion parameters), the un-warped EPI images were then smoothed at 6 mm FWHM, and non-linearly co-registered with the anatomical T1 to 2 mm isotropic MNI space. Temporal artifacts were identified in each dataset by calculating framewise displacement (FD) from the derivatives of the six rigid-body realignment parameters estimated during standard volume realignment[82], as well as the root mean square change in BOLD signal from volume to volume (DVARS). Frames associated with FD > 0.25mm or DVARS > 2.5% were identified, however as no participants were identified with greater than 10% of the resting time points exceeding these values, no trials were excluded from further analysis. There were no differences in head motion parameters between the four sessions ($p > 0.500$). Following artifact detection, nuisance covariates associated with the 6 linear head movement parameters (and their temporal derivatives), DVARS, physiological regressors (created using the RETROICOR method) and anatomical masks from the CSF and deep cerebral WM were regressed from the data using the CompCor strategy[83]. Finally, in keeping with previous time-resolved connectivity experiments[84], a temporal band pass filter ($0.0071 < f < 0.125$ Hz) was applied to the data.

Brain Parcellation

Following pre-processing, the mean time series was extracted from 375 predefined regions-of-interest (ROI). To ensure whole-brain coverage, we extracted: 333 cortical parcels (161 and 162 regions from the left and right hemispheres, respectively) using the Gordon atlas[85], 14 subcortical regions from Harvard-Oxford subcortical atlas (bilateral thalamus, caudate, putamen, ventral striatum, globus pallidus, amygdala and hippocampus; http://fsl.fmrib.ox.ac.uk/), and 28 cerebellar regions from the SUIT atlas[86] for each participant in the study.

Time-Resolved Functional Connectivity and Network Analysis

Following pre-processing, the mean time series was extracted from 375 predefined regions-of-interest (ROI). To estimate functional connectivity between the 375 ROIs, we used the Jack-knife correlation approach (JC)[87]. Briefly, this approach estimates the static correlations between each pair of regions, and then recalculates the correlation between each pair after systematically removing each temporal 'slice' of data (i.e., each TR). By subtracting the jack-knifed correlation matrix from the original 'static' matrix, the difference in connectivity at each slice from the static connectivity value can be used as an estimate of time-resolved functional connectivity between each pair of regions at each TR in a way that does not require windowing.

Community Structure

The Louvain modularity algorithm from the Brain Connectivity Toolbox (BCT)[88] was used in combination with the JC to estimate both time-averaged and time-resolved community structure. The Louvain algorithm iteratively maximizes the modularity statistic, Q, for different community assignments until the maximum possible score of Q has been obtained (equation 1).

$$Q_T = \frac{1}{v^+}\sum_{ij}\left(w_{ij}^{+} - e_{ij}^{+}\right)\delta_{M_iM_j} - \frac{1}{v^+ + v^-}\sum_{ij}\left(w_{ij}^{-} - e_{ij}^{-}\right)\delta_{M_iM_j} \qquad (4)$$

Equation 1 – Louvain modularity algorithm, where v is the total weight of the network (sum of all negative and positive connections), w_{ij} is the weighted and signed connection between regions i and j, e_{ij} is the strength of a connection divided by the total weight of the network, and δ_{MiMj} is set to 1 when regions are in the same community and 0 otherwise. '+' and '–' superscripts denote all positive and negative connections, respectively.

For each subject, we calculated the mean adjacency matrix from 1 TR before tracking until the end of the tracking period. Afterwards, a consensus partition was estimated across subjects. Finally, to identify multi-level structure in our data, we repeated the modularity analysis for each of the modules identified in the first step[46,47]. With this final module assignment, we were afforded an estimate of the time resolved, multi-level modularity (Q_T) within each temporal window for each participant in the study.

Regional Integration

Based on the group consensus community assignments, we estimated between-module connectivity using the participation coefficient, B_T, which quantifies the extent to which a region connects across all modules (i.e. between-module strength; equation 2). In our experiment, we used two separate community assignments, one for each of

the modularity levels. In this manner we measure: 1) how the first hierarchical level (i.e., large scale) topology changed during tracking across the complete brain; and 2) how the topology of the sub-modules changed across the task. These values were calculated in each time point using the time-resolved adjacency matrix across each load condition.

$$B_{iT} = 1 - \sum_{s=1}^{n_M} \left(\frac{\kappa_{isT}}{\kappa_{iT}}\right)^2 \qquad (5)$$

Equation 2 - Participation coefficient B_{iT}, where κ_{isT} is the strength of the positive connections of region *i* to regions in module *s* at time *T*, and κ_{iT} is the sum of strengths of all positive connections of region *i* at time *T*. The participation coefficient of a region is therefore close to 1 if its connections are uniformly distributed among all the modules and 0 if all of its links are within its own module.

Neurotransmitter Receptor Mapping

To investigate the potential correlates of meso-scale integration, we interrogated the neurotransmitter receptor signature of each region of the brain. We used the Allen Brain Atlas micro-array atlas dataset (http://human.brain-map.org/)[55] to identify the regional signature of genetic expression of the α2a subtype of the adrenergic receptor (ADRA2A). This receptor has been *a priori* related to cognitive function and attention[89], and is one of the most abundant adrenergic subtypes expressed in the cerebral cortex[90]. This atlas contains postmortem samples of six donors that underwent microarray transcriptional characterization. The spatial map of α2a mRNA expression was obtained in volumetric 2mm isotropic MNI space, following improved nonlinear registration and whole-brain prediction using variogram modeling[91]. We used this data instead of the native sample-wise values in the AHBA database to prevent bias that could occur due to spatial inhomogeneity of the sampled locations. We projected the volumetric α2a expression data onto the Gordon atlas with linear interpolation and calculated the mean value within each parcel using custom MATLAB codes.

Statistical analysis

The Relationship Between Sympathetic Tone and Attentional Processing

We analysed the between subjects' effect of load on the behavioural, pupillometric and fMRI related variables by performing a two-level linear model analysis. In the first level, we used attentional load as a regressor (2 to 5) and -in independent models- the mean accuracy, reaction time, standard deviation of reaction time, drift rate, boundary criteria and non-decision time as dependent variables (i.e., 4 values per subject). From this, we ran a two-tailed t-test on the statistical effects (i.e., the β value

from the regression, one for each subject; N = 18). Similarly, to calculate the load effect on pupil diameter, we calculated the average pupil diameter on each load condition within each subject. Then, we performed a first-level analysis in which we ran a linear regression in each time frame (1600 frames in total, corresponding to 26.6 seconds). This procedure resulted in one β timeseries (i.e., the statistical load effect on pupil diameter) for each subject across the trial (Figure S1A). After this, we performed a right tailed t-test in each frame across subjects (n = 18 in each frame) to find the periods of time where the β value where higher than zero. Finally, we corrected by false discovery rate (FDR)[92] for multiple testing, which resulted in a period of time where the load effect was higher than 0 (light grey area in Figure 1A). The mean β values during this section was calculated in each subject and defined as 'βpupil'. Finally, following the same pipeline, we calculated the effect of attentional load on the brain related signals (i.e., BOLD, participation coefficient [PC] and modularity [Q]). The effect of load on BOLD was calculated running a separate linear model in each subject and region within each TR (18 subjects; 375 regions; 10 TRs; 4 load condition), resulting in a matrix of β values of 18 x 375 x 10.

To evaluate the statistical effect of pupil diameter on accuracy, we performed a logistic linear mixed effects model. We used the mean pupil diameter of the significant time period (Figure 1A) of the high load trials (Load 4 and 5), and the accuracy (i.e., correct or incorrect) as the predictor variable of each trial, grouping by subject as the random effect. The statistical model is described in the following equation:

$$\text{Accuracy} \sim \text{Pupil} + 1 + (\text{Pupil} + 1 | \text{Subject}) \quad (6)$$

Network meso-scale integration and adrenergic receptor density

To evaluate whether the modularity of the network we observed was higher than chance, we generated 100 random networks in each hierarchical level (300 random networks in total), with a preserved degree distribution (using the MATLAB *randmio_und_signed* function from the Brain connectivity toolbox[88]). We calculated the modularity value of each random network and used the resultant values to populate a null distribution (Figure 2D).

We analyzed the statistical effect of pupil diameter on the participation coefficient both within and between subjects by performing a linear mixed model using the time varying PC of the red sub-module (Figure 3A) of each load as a dependent variable

(N=72), and the respective pupil diameter as a regressor, with grouping by subject. The statistical model is described in the following equation:

$$PC \sim Pupil + 1 + (Pupil + 1 | Subject) \quad (7)$$

Network meso-scale integration and adrenergic receptor density

Expression of brain genetic atlas vary smoothly across the surface and thus is associated with non-trivial spatial autocorrelation that in turn violates the assumption of independence between samples[57,58,93]. To account for the spatial autocorrelation in these brain maps, we used spatial autocorrelation null maps as implemented in Brain Surrogate Maps with Autocorrelated Spatial Heterogeneity (BrainSMASH) python toolbox[57]. A geodesic distance matrix of the atlas parcels using the surface of the Gordon atlas was obtained to build the surrogates using BrainSMASH functions. We generated 5,000 null maps which were used to generate null distribution of the different statistics corrected by spatial autocorrelation.

We measure the statistical difference in the receptor density between sub-modules by a two-tailed t-test between each pair of modules. The same procedure was performed using the surrogate maps to generate a null distribution of t-statistics. To evaluate the effect of the density of each adrenergic receptor on the neural activity in the attentional task, we built a linear mixed model aimed at predicting regional differences in BOLD activity and participation coefficient. We created a model using the receptor density atlas of α2a receptor to predict parametric BOLD activity (i.e., linear increase of BOLD activity with task load) during tracking (Eq. 8). To evaluate the relationship between BOLD activity, adrenergic receptor expression and changes in participation coefficient as a function of attentional load, we tested two models: one using the adrenergic receptor density as independent factor (Eq. 9); and another using the parametric BOLD effect as an independent factor (Eq. 10). Additionally, we assessed the across-subject variability using the subjects ID as grouping variable in order to evaluate the random effects on the independent factor. We corrected the spatial autocorrelation by running the same model using 5,000 surrogate maps. Then we used the fixed effect null distribution to calculate the p_{SA} (i.e., the probability of finding the fixed effect within the 95th percentile of the null distribution). The deterministic part of the model is expressed in the following equations[94]:

$$\beta BOLD \sim \alpha 2a + 1 + (\alpha 2a + 1 | Subject) \quad (8)$$

$$\beta PC \sim \alpha 2a + 1 + (\alpha 2a + 1 | Subject) \quad (9)$$
$$\beta PC \sim BOLD + 1 + (BOLD + 1 | Subject) \quad (10)$$

Where *PC* is the parametric effect of meso-scale participation coefficient (i.e., βPC), BOLD is the parametric effect of load on BOLD activity during tracking for each region, and α2a are the regional densities of the respective adrenergic receptor atlas. We then correlated the random effects parameters to pupil diameter responses and behaviour and then compared these with the Pearson's correlation of the null distribution using the random effect of the surrogate maps. Finally, we performed a linear model within each subject with α2a as a regressor and βBOLD as dependent variable. Again, the statistical effect (i.e., β value) was compared against the null distribution when performing the regression using the surrogate maps (figure 4B-C).

Data and code availability

The anonymized preprocessed fMRI and pupillometry data can be found at https://figshare.com/articles/dataset/MOT_data_mat/13244504. The ADRA2A expression atlas can be downloaded from http://www.meduniwien.ac.at/neuroimaging/mRNA.html. All analysis of the fMRI and pupil diameter data were performed on MATLAB 2020a. The surrogate maps of the ADRA2A atlas were generated on python. Documented code for reproducing the analyses is provided in https://github.com/gabwainstein/MOT.

Acknowledgements, Funding and Disclosure

We thank P. Billeke for their thoughtful comments on our manuscript. JMS was supported by the University of Sydney Robinson Fellowship and NHMRC GNT1156536. GW was supported by 'Becas Chile' PhD scholarship. The authors declare no financial interests or conflicts of interest.

Author Contributions

GW and JS Analysed the data, interpreted the results and wrote the manuscript. DR: Interpreted the results and wrote the manuscript. KK, DA, BL and TE: Created the experimental design and contributed with the data acquisition. All authors reviewed, commented and edited the manuscript, and all authors gave final approval of the version to be published.

References

1. Shine, J. M. The thalamus integrates the macrosystems of the brain to facilitate complex, adaptive brain network dynamics. *Progress in Neurobiology* 101951 (2020) doi:https://doi.org/10.1016/j.pneurobio.2020.101951.
2. Shine, J. M. *et al.* The Dynamics of Functional Brain Networks: Integrated Network States during Cognitive Task Performance. *Neuron* **92**, 544–554 (2016).
3. Varela, F., Lachaux, J.-P., Rodriguez, E. & Martinerie, J. The brainweb: phase synchronization and large-scale integration. *Nature reviews neuroscience* **2**, 229–239 (2001).
4. Parvizi, J. & Damasio, A. Consciousness and the brainstem. *Cognition* **79**, 135–160 (2001).
5. Alnæs, D. *et al.* Pupil size signals mental effort deployed during multiple object tracking and predicts brain activity in the dorsal attention network and the locus coeruleus. *Journal of vision* **14**, 1–20 (2014).
6. Shine, J. M. *et al.* The low-dimensional neural architecture of cognitive complexity is related to activity in medial thalamic nuclei. *Neuron* **104**, 849–855 (2019).
7. Alnæs, D. *et al.* Attentional load modulates large-scale functional brain connectivity beyond the core attention networks. *Neuroimage* **109**, 260–272 (2015).
8. Munn, B., Müller, E. J., Wainstein, G. & Shine, J. M. The ascending arousal system shapes low-dimensional brain dynamics to mediate awareness of changes in intrinsic cognitive states. *bioRxiv* (2021) doi:10.1101/2021.03.30.437635.
9. Samuels, E. & Szabadi, E. Functional Neuroanatomy of the Noradrenergic Locus Coeruleus: Its Roles in the Regulation of Arousal and Autonomic Function Part II: Physiological and Pharmacological Manipulations and Pathological Alterations of Locus Coeruleus Activity in Humans. *Current Neuropharmacology* **6**, 254–285 (2008).
10. Bouret, S. & Sara, S. J. Network reset: A simplified overarching theory of locus coeruleus noradrenaline function. *Trends in Neurosciences* **28**, 574–582 (2005).

11. Sara, S. J. The locus coeruleus and noradrenergic modulation of cognition. *Nature reviews. Neuroscience* **10**, 211–223 (2009).
12. Shine, J. M. Neuromodulatory Influences on Integration and Segregation in the Brain. *Trends in Cognitive Sciences* **23**, 572–583 (2019).
13. Robbins, T. W. & Arnsten, A. F. T. The neuropsychopharmacology of fronto-executive function: monoaminergic modulation. *Annual Review of NeuroscienceNeuroscience* **32**, 267–289 (2009).
14. Aston-Jones, G. & Waterhouse, B. Locus coeruleus: From global projection system to adaptive regulation of behavior. *Brain Research* **1645**, 75–78 (2016).
15. Shine, J. M. *et al.* Computational models link cellular mechanisms of neuromodulation to large-scale neural dynamics. *Nature Neuroscience* **24**, 765–776 (2021).
16. Wang, X. J. Macroscopic gradients of synaptic excitation and inhibition in the neocortex. *Nature Reviews Neuroscience* **21**, 169–178 (2020).
17. Aston-Jones, G. & Cohen, J. D. An integrative theory of locus coeruleus-norepinephrine function: adaptive gain and optimal performance. *Annual Review of Neuroscience* **28**, 403–450 (2005).
18. Joshi, S., Li, Y., Kalwani, R. M. & Gold, J. I. Relationships between Pupil Diameter and Neuronal Activity in the Locus Coeruleus, Colliculi, and Cingulate Cortex. *Neuron* **89**, 221–234 (2016).
19. Liu, Y., Rodenkirch, C., Moskowitz, N., Schriver, B. & Wang, Q. Dynamic lateralization of pupil dilation evoked by locus coeruleus activation results from sympathetic, not parasympathetic, contributions. *Cell reports* **20**, 3099–3112 (2017).
20. van den Brink, R. L. *et al.* Catecholaminergic neuromodulation shapes intrinsic MRI functional connectivity in the human brain. *Journal of Neuroscience* **36**, 7865–7876 (2016).
21. Yüzgeç, Ö., Prsa, M., Zimmermann, R. & Huber, D. Pupil Size Coupling to Cortical States Protects the Stability of Deep Sleep via Parasympathetic Modulation. *Current Biology* **28**, 392-400.e3 (2018).

22. Gilzenrat, M. S., Nieuwenhuis, S., Jepma, M. & Cohen, J. D. Pupil diameter tracks changes in control state predicted by the adaptive gain theory of locus coeruleus function. *Cognitive, Affective and Behavioral Neuroscience* **10**, 252–269 (2010).
23. Wainstein, G. *et al.* Pupil size tracks attentional performance in attention-deficit/hyperactivity disorder. *Scientific reports* **7**, 1–9 (2017).
24. Kahneman, D. & Beatty, J. Pupil Diameter and Load on Memory. *Science* **154**, 1583–1585 (1966).
25. Mulder, G. The Concept and Measurement of Mental Effort. *Energetics and Human Information Processing* 175–198 (2012) doi:10.1007/978-94-009-4448-0_12.
26. Varazzani, C., San-Galli, A., Gilardeau, S. & Bouret, S. Noradrenaline and Dopamine Neurons in the Reward/Effort Trade-Off: A Direct Electrophysiological Comparison in Behaving Monkeys. *Journal of Neuroscience* **35**, 7866–7877 (2015).
27. Murphy, P. R., Boonstra, E. & Nieuwenhuis, S. Global gain modulation generates time-dependent urgency during perceptual choice in humans. *Nature communications* **7**, 1–15 (2016).
28. Reimer, J. *et al.* Pupil Fluctuations Track Fast Switching of Cortical States during Quiet Wakefulness. *Neuron* **84**, 355–362 (2014).
29. Joshi, S. & Gold, J. I. Pupil Size as a Window on Neural Substrates of Cognition. *Trends in Cognitive Sciences* **24**, 466–480 (2020).
30. Cazettes, F., Reato, D., Morais, J. P., Renart, A. & Mainen, Z. F. Phasic Activation of Dorsal Raphe Serotonergic Neurons Increases Pupil Size. *Current Biology* 192–197 (2020) doi:10.1016/j.cub.2020.09.090.
31. Zerbi, V. *et al.* Rapid reconfiguration of the functional connectome after chemogenetic locus coeruleus activation. *Neuron* **103**, 702–718 (2019).
32. Shenhav, A. *et al.* Toward a Rational and Mechanistic Account of Mental Effort. *Annual Review of Neuroscience* **40**, 99–124 (2017).

33. Shine, J. M., van den Brink, R. L., Hernaus, D., Nieuwenhuis, S. & Poldrack, R. A. Catecholaminergic manipulation alters dynamic network topology across cognitive states. *Network Neuroscience* **2**, 381–396 (2018).
34. Shine, J. M. *et al.* Human cognition involves the dynamic integration of neural activity and neuromodulatory systems. *Nature Neuroscience* **22**, 289–296 (2019).
35. de Gee, J. W. *et al.* Dynamic modulation of decision biases by brainstem arousal systems. *Elife* **6**, e23232 (2017).
36. Donner, T. *et al.* Involvement of the human frontal eye field and multiple parietal areas in covert visual selection during conjunction search. *European Journal of Neuroscience* **12**, 3407–3414 (2000).
37. de Gee, J. W., Knapen, T. & Donner, T. H. Decision-related pupil dilation reflects upcoming choice and individual bias. *Proceedings of the National Academy of Sciences* **111**, E618–E625 (2014).
38. Fornito, A., Arnatkevičiūtė, A., Fulcher, B. D., Fornito, A. & Arnatkevi, A. Bridging the gap between connectome and transcriptome. *Trends in Cognitive Sciences* **23**, 34–50 (2019).
39. Richiardi, J. *et al.* Correlated gene expression supports synchronous activity in brain networks. *Science* **348**, 1241–1244 (2015).
40. de Gee, J. W., Knapen, T. & Donner, T. H. Decision-related pupil dilation reflects upcoming choice and individual bias. *Proceedings of the National Academy of Sciences* **111**, E618–E625 (2014).
41. Ratcliff, R., Thompson, C. A. & McKoon, G. Modeling individual differences in response time and accuracy in numeracy. *Cognition* **137**, 115–136 (2015).
42. Ratcliff, R., Smith, P. L., Brown, S. D. & Mckoon, G. Diffusion decision model: Current issues and history. *Trends in cognitive sciences* **20**, 260–281 (2016).
43. Murphy, P. R., Vandekerckhove, J. & Nieuwenhuis, S. Pupil-Linked Arousal Determines Variability in Perceptual Decision Making. *PLoS Computational Biology* **10**, (2014).

44. Ratcliff, R., Thompson, C. A. & McKoon, G. Modeling individual differences in response time and accuracy in numeracy. *Cognition* **137**, 115–136 (2015).
45. Wagenmakers, E. J., Van Der Maas, H. L. J. & Grasman, R. P. P. P. An EZ-diffusion model for response time and accuracy. *Psychonomic Bulletin and Review* **14**, 3–22 (2007).
46. Meunier, D., Lambiotte, R. & Bullmore, E. T. Modular and hierarchically modular organization of brain networks. *Frontiers in Neuroscience* **4**, 1–11 (2010).
47. Meunier, D., Lambiotte, R., Fornito, A., Ersche, K. D. & Bullmore, E. T. Hierarchical modularity in human brain functional networks. *Frontiers in Neuroinformatics* **3**, 1–12 (2009).
48. Bassett, D. S. *et al.* Efficient physical embedding of topologically complex information processing networks in brains and computer circuits. *PLoS comput biol* **6**, e1000748 (2010).
49. McGinley, M. J. *et al.* Waking State: Rapid Variations Modulate Neural and Behavioral Responses. *Neuron* **87**, 1143–1161 (2015).
50. Reimer, J. *et al.* Pupil Fluctuations Track Fast Switching of Cortical States during Quiet Wakefulness. *Neuron* **84**, 355–362 (2014).
51. Wang, M. *et al.* α2A-adrenoceptors strengthen working memory networks by inhibiting cAMP-HCN channel signaling in prefrontal cortex. *Cell* **129**, 397–410 (2007).
52. Santana, N. & Artigas, F. Laminar and cellular distribution of monoamine receptors in rat medial prefrontal cortex. *Frontiers in neuroanatomy* **11**, 1–13 (2017).
53. Zilles, K. & Palomero-gallagher, N. Multiple Transmitter Receptors in Regions and Layers of the Human Cerebral Cortex. **11**, 1–26 (2017).
54. Arnsten, A. F. T., Wang, M. J. & Paspalas, C. D. Neuromodulation of Thought: Flexibilities and Vulnerabilities in Prefrontal Cortical Network Synapses. *Neuron* **76**, 223–239 (2012).
55. Hawrylycz, M. J. *et al.* An anatomically comprehensive atlas of the adult human brain transcriptome. *Nature* **489**, 391–399 (2012).

56. Gryglewski, G. *et al.* Spatial analysis and high resolution mapping of the human whole-brain transcriptome for integrative analysis in neuroimaging. *NeuroImage* **176**, 259–267 (2018).
57. Burt, J. B., Helmer, M., Shinn, M., Anticevic, A. & Murray, J. D. Generative modeling of brain maps with spatial autocorrelation. *NeuroImage* **220**, 117038 (2020).
58. Markello, R. D. & Misic, B. Comparing spatial null models for brain maps. *NeuroImage* **236**, 118052 (2021).
59. Mather, M., Clewett, D., Sakaki, M. & Harley, C. W. Norepinephrine ignites local hotspots of neuronal excitation: How arousal amplifies selectivity in perception and memory. *Behavioral and Brain Sciences* **39**, (2016).
60. Shine, J. M. The thalamus integrates the macrosystems of the brain to facilitate complex, adaptive brain network dynamics. *Progress in Neurobiology* **199**, 101951 (2021).
61. Lecrux, C. & Hamel, E. Neuronal networks and mediators of cortical neurovascular coupling responses in normal and altered brain states. *Phil. Trans. R. Soc. B* **371**, 20150350 (2016).
62. Bekar, L. K., Wei, H. S. & Nedergaard, M. The Locus Coeruleus-Norepinephrine Network Optimizes Coupling of Cerebral Blood Volume with Oxygen Demand. *J Cereb Blood Flow Metab* **32**, 2135–2145 (2012).
63. Logothetis, N. K. The Underpinnings of the BOLD Functional Magnetic Resonance Imaging Signal. **23**, 3963–3971 (2003).
64. Liu, Y., Rodenkirch, C., Moskowitz, N. & Schriver, B. Dynamic Lateralization of Pupil Dilation Evoked by Locus Coeruleus Activation Results from Article Dynamic Lateralization of Pupil Dilation Evoked by Locus Coeruleus Activation Results from Sympathetic , Not Parasympathetic , Contributions. *CellReports* **20**, 3099–3112 (2017).
65. Shine, J. M., Aburn, M. J., Breakspear, M. & Poldrack, R. A. The modulation of neural gain facilitates a transition between functional segregation and integration in the brain. *Elife* **7**, e31130 (2018).

66. Akiki, T. J. & Abdallah, C. G. Determining the Hierarchical Architecture of the Human Brain Using Subject-Level Clustering of Functional Networks. *Scientific Reports* **9**, 1–15 (2019).

67. Mohr, H. *et al.* Integration and segregation of large-scale brain networks during short-term task automatization. *Nature communications* **7**, 1–12 (2016).

68. Reimer, J. *et al.* Pupil fluctuations track rapid changes in adrenergic and cholinergic activity in cortex. *Nature Communications* **7**, 1–7 (2016).

69. Kaymak, H. *et al.* Short-term effects of low-concentration atropine eye drops on pupil size and accommodation in young adult subjects. *Graefe's Archive for Clinical and Experimental Ophthalmology* 2211–2217 (2018) doi:10.1007/s00417-018-4112-8.

70. Avery, M. C. & Krichmar, J. L. Neuromodulatory systems and their interactions: A review of models, theories, and experiments. *Frontiers in Neural Circuits* **11**, 1–18 (2017).

71. Smiley, J. F., Subramanian, M. & Mesulam, M. M. Monoaminergic-cholinergic interactions in the primate basal forebrain. *Neuroscience* **93**, 817–829 (1999).

72. Joshi, A. *et al.* An integrated modelling framework for neural circuits with multiple neuromodulators. *Journal of the Royal Society Interface* **14**, (2017).

73. Briand, L. A., Gritton, H., Howe, W. M., Young, D. A. & Sarter, M. Modulators in concert for cognition : Modulator interactions in the prefrontal cortex. **83**, 69–91 (2007).

74. Palomero-Gallagher, N. & Zilles, K. Cortical layers: Cyto-, myelo-, receptor- and synaptic architecture in human cortical areas. *NeuroImage* **197**, 716–741 (2019).

75. Douglas, R. J. & Martin, K. A. C. Neuronal Circuits of the Neocortex. *Annu. Rev. Neurosci.* **27**, 419–451 (2004).

76. Fornito, A., Arnatkevičiūtė, A., Fulcher, B. D., Fornito, A. & Arnatkevi, A. Bridging the gap between connectome and transcriptome. *Trends in Cognitive Sciences* **23**, 34–50 (2019).

77. Ratcliff, R. & Rouder, J. Modeling response times for two-choice decisions. *Psychological Science* **9**, 347–356 (1998).

78. Ratcliff, R., Smith, P. L., Brown, S. D. & Mckoon, G. Diffusion decision model: Current issues and history. *Trends in cognitive sciences* **20**, 260–281 (2016).

79. Wainstein, G. *et al.* Pupil size tracks attentional performance in attention-deficit/hyperactivity disorder. *Scientific reports* **7**, 1–9 (2017).

80. Rojas-Líbano, D. *et al.* A pupil size, eye-tracking and neuropsychological dataset from ADHD children during a cognitive task. *Scientific data* **6**, 25 (2019).

81. Campos-Arteaga, G. *et al.* Differential neurophysiological correlates of retrieval of consolidated and reconsolidated memories in humans: an ERP and pupillometry study. *Neurobiology of Learning and Memory* 107279 (2020) doi:10.1016/j.nlm.2020.107279.

82. Power, J. D. *et al.* Methods to detect, characterize, and remove motion artifact in resting state fMRI. *NeuroImage* **84**, 320–41 (2014).

83. Behzadi, Y., Restom, K., Liau, J. & Liu, T. T. A component based noise correction method (CompCor) for BOLD and perfusion based fMRI. *NeuroImage* **37**, 90–101 (2007).

84. Gu, S. *et al.* Controllability of structural brain networks. *Nature Communications* **6**, 1–10 (2015).

85. Gordon, E. M. *et al.* Generation and Evaluation of a Cortical Area Parcellation from Resting-State Correlations. *Cerebral Cortex* **26**, 288–303 (2016).

86. Diedrichsen, J., Balsters, J. H., Flavell, J., Cussans, E. & Ramnani, N. A probabilistic MR atlas of the human cerebellum. *NeuroImage* **46**, 39–46 (2009).

87. Thompson, W. H., Richter, C. G., Plavén-Sigray, P. & Fransson, P. Simulations to benchmark time-varying connectivity methods for fMRI. *PLoS Computational Biology* **14**, 1–23 (2018).

88. Rubinov, M. & Sporns, O. NeuroImage Complex network measures of brain connectivity : Uses and interpretations. *NeuroImage* **52**, 1059–1069 (2010).

89. Arnsten, A. F. T. & Haven, N. The Neurobiology of Thought : The Groundbreaking Discoveries of Patricia Goldman-Rakic 1937 – 2003. 2269–2281 (2013) doi:10.1093/cercor/bht195.

90. Perez, D. M. α1-Adrenergic Receptors in Neurotransmission, Synaptic Plasticity, and Cognition. *Frontiers in Pharmacology* **11**, 1–22 (2020).
91. Gryglewski, G. *et al.* Spatial analysis and high resolution mapping of the human whole-brain transcriptome for integrative analysis in neuroimaging. *NeuroImage* **176**, 259–267 (2018).
92. Benjamini, Y. & Yekutieli, D. The control of the false discovery rate in multiple testing under dependency. *Annals of Statistics* **29**, 1165–1188 (2001).
93. Vos de Wael, R. *et al.* BrainSpace: a toolbox for the analysis of macroscale gradients in neuroimaging and connectomics datasets. *Communications Biology* **3**, (2020).
94. Wilkinson, G. N. & Rogers, C. E. Symbolic Description of Factorial Models for Analysis of Variance. *Journal of Applied Statistics* **22**, 392–399 (1973).